



HAL
open science

Growth and characterization of metal silicides/SiGe-based quantum dots superlattices for thermoelectric applications

Sergio Silveira Stein

► **To cite this version:**

Sergio Silveira Stein. Growth and characterization of metal silicides/SiGe-based quantum dots superlattices for thermoelectric applications. Micro and nanotechnologies/Microelectronics. Université de Grenoble, 2014. English. NNT : 2014GRENT087 . tel-01228250

HAL Id: tel-01228250

<https://theses.hal.science/tel-01228250>

Submitted on 12 Nov 2015

HAL is a multi-disciplinary open access archive for the deposit and dissemination of scientific research documents, whether they are published or not. The documents may come from teaching and research institutions in France or abroad, or from public or private research centers.

L'archive ouverte pluridisciplinaire **HAL**, est destinée au dépôt et à la diffusion de documents scientifiques de niveau recherche, publiés ou non, émanant des établissements d'enseignement et de recherche français ou étrangers, des laboratoires publics ou privés.

THÈSE

Pour obtenir le grade de

DOCTEUR DE L'UNIVERSITÉ DE GRENOBLE

Spécialité : Nano électronique, Nano technologies

Arrêté ministériel : 7 août 2006

Présentée par

Sergio SILVEIRA STEIN

Thèse dirigée par **Laurent MONTES** et
codirigée par **Guillaume SAVELLI**

préparée au sein du laboratoire **LITEN/LTE (CEA)**
et du laboratoire **IMEP-LAHC (Minatec)**
dans l'**École Doctorale Électronique, Électrotechnique,
Automatique et Traitement du Signal (EEATS)**

Croissance et caractérisation de Super-Réseaux de Boîtes Quantiques à base de siliciures métalliques et SiGe pour des applications thermoélectriques

Thèse soutenue publiquement le **18 décembre 2014**
devant le jury composé de :

M. Laurent MONTES

Maître de Conférences à Grenoble INP, Directeur de thèse

Mme Isabelle BERBEZIER

Directrice de Recherche au CNRS, Rapporteuse

M. Armando RASTELLI

Professeur à l'Université Johannes Kepler, Rapporteur

M. Didier LECLERCQ

Professeur à l'Université de Lille, Examineur

M. Daniel Bourgault

Directeur de Recherche au CNRS, Examineur

M. Guillaume SAVELLI

Ingénieur de recherche au CEA-LITEN, Encadrant de thèse



Acknowledgements

The present work was made possible due to collaboration between the CEA/LTE and IMEP-LAHC laboratories. I would like to thank the actual LTE director Luc Aixala and the former director Emmanuelle Rouvière for receiving me in the laboratory and for their constant support. I would also like to thank the director of IMEP-LAHC, Jean-Emmanuel Broquin, for allowing me to employ the characterization tools available at the laboratory in order to characterize my samples.

I am thankful for my supervisor Laurent Montès for accepting to support my work and for his advices. I would like to thank very much my co-supervisor Guillaume Savelli for being available since the beginning of this work and along the 3 years it lasted. He demonstrated a great capacity of supervising my work and a sensibility to know to guide my steps and to help me accomplish the work. And last but not least, always with a great sense of humor and kindness.

I would like to thank my thesis reporters Mr. Armando Rastelli and Mrs Isabelle Berbezier for accepting to evaluate my thesis manuscript as well as the other members of the jury Mr. Didier Leclercq and Mr. Daniel Bourgault for their availability and their interest on my work.

I am very thankful to Pascal Faucherand for his constant support an availability to solve the technical problems arising from the CVD tool employed to growth my samples. Without him, it would be surely not possible to produce the samples for this thesis.

Another person that was fundamental for the accomplishment of this thesis is Guillaume-Bernard Granger. Thanks a lot for your help with the TEM characterization and for using a huge part of your time to help me.

I thank also Gilles Pernot and Stephan Dilhaire for allowing me to use the thermorefectance equipment at LOMA/Bordeaux.

I would like also to thank all of the LTE personal and the photovoltaic group for sharing with me their office.

A final thanks to my family and to my partner of life, Suzy, for their love.

Table of contents

ACKNOWLEDGEMENTS	1
TABLE OF CONTENTS	3
INTRODUCTION	7
CHAPTER I - THERMOELECTRICITY AND NANOSTRUCTURATION	11
1 - PRINCIPLES OF THERMOELECTRICITY	13
1.1 - HISTORY OF THERMOELECTRICITY	13
1.2 - THE THERMOELECTRIC EFFECTS.....	15
1.2.a - The Seebeck effect.....	15
1.2.b - The Peltier effect.....	20
1.2.c - The Thomson effect	22
1.2.d - The Kelvin Relationships	23
1.3 - PRINCIPLES OF THERMOELECTRIC CONVERTERS.....	24
1.4 - MAIN THERMOELECTRIC PARAMETERS	27
1.4.a - Electrical conductivity (σ).....	28
1.4.b - The thermal conductivity (λ).....	28
1.4.c - Seebeck Coefficient (S).....	30
1.4.d - Ideal carriers concentration.....	30
2 - THERMOELECTRIC APPLICATIONS	31
2.1 - STATE OF THE ART MATERIALS	31
2.1.a - Low and medium temperature materials	32
2.1.b - High temperature materials: Silicon-Germanium (SiGe).....	33
2.2 - BULK MATERIALS-BASED DEVICES.....	34
2.2.a - Generators	34
2.2.b - Cooling devices	36
2.2.c - Thermoelectric sensors	37

2.3 - THERMOELECTRIC THIN FILMS DEVICES.....	38
2.3.a - Thin film thermoelectric generators.....	38
2.3.b - Thin film cooling devices.....	39
2.3.c - Thin film thermoelectric sensors.....	40
<u>3 - INCREASING THE THERMOELECTRIC PROPERTIES VIA NANOSTRUCTURATION.....</u>	41
3.1 - POWER FACTOR IMPROVEMENT.....	42
3.2 - THERMAL CONDUCTIVITY REDUCTION.....	43
<u>4 - QUANTUM WELLS AND QUANTUM DOTS SUPERLATTICES.....</u>	46
4.1 - INTRODUCTION TO QUANTUM CONFINED STRUCTURES AND SUPERLATTICES.....	46
4.2 - GENERAL APPLICATIONS FOR QUANTUM WELLS AND QUANTUM DOTS.....	48
4.3 - THERMOELECTRIC APPLICATIONS FOR QWSL'S AND QDSL'S.....	49
<u>5 - CONCLUSION.....</u>	53
<u>REFERENCES.....</u>	55
<u>CHAPTER II - THE CVD GROWTH OF QUANTUM DOTS SUPERLATTICES.....</u>	59
<u>1 - INTRODUCTION.....</u>	61
<u>2 - THE CVD GROWTH.....</u>	61
2.1 - GENERALITIES.....	62
2.2 - NUCLEATION AND GROWTH MECHANISMS.....	63
2.3 - THE GROWTH RATE LIMITING FACTOR.....	65
2.4 - OUR CVD TOOL.....	66
2.5 - SI AND SiGe THIN FILM GROWTH.....	68
2.6 - TI AND MO PRECURSORS.....	72
2.7 - DELIVERY SYSTEM FOR NON-GASEOUS PRECURSORS.....	73
2.7.a - TiCl ₄ evaporation system.....	75
2.7.b - MoCl ₅ sublimation.....	76

<u>3 - THE GROWTH OF TI-BASED SILICIDE/SiGe QDSL.....</u>	<u>77</u>
3.1 - INTRODUCTION.....	77
3.2 - CVD DEPOSITION OF TI-BASED NANO-ISLANDS.....	79
3.2.a - The role of deposition temperature	82
3.2.b - The role of the substrate Ge content	86
3.2.c - The role of deposition duration	88
3.2.d - The role of the precursor partial pressure.....	90
3.2.e - Role of substrate crystallinity	91
3.2.f - Conclusion.....	92
3.3 - EMBEDDING THE NANO-ISLANDS AND FORMATION OF QUANTUM DOTS	94
3.3.a - Low temperature embedding: nanowires growth.....	94
3.3.b - High temperature embedding	97
3.4 - Ti/SiGe QDSL GROWTH	99
<u>4 - THE GROWTH OF MO-BASED SILICIDE/SiGe QDSL.....</u>	<u>102</u>
4.1 - INTRODUCTION.....	102
4.2 - CVD DEPOSITION OF MO-BASED NANO-ISLANDS.....	103
4.2.a - Role of deposition temperature.....	104
4.2.b - Role of Ge content	106
4.3 - Mo/SiGe QDSL GROWTH	107
<u>5 - CONCLUSION.....</u>	<u>108</u>
<u>REFERENCES.....</u>	<u>110</u>
<u>CHAPTER III - CHARACTERIZATION OF QDSL FOR THERMOELECTRIC APPLICATIONS.....</u>	<u>113</u>
<u>1 - INTRODUCTION.....</u>	<u>115</u>
<u>2 - STRUCTURAL CHARACTERIZATION.....</u>	<u>117</u>
2.1 - INTRODUCTION.....	117
2.2 - XRD	117
2.3 - TEM ANALYSIS	119
2.3.a - Ti-based QDSL: “n”-doped monocrystalline samples	119
2.3.b - Ti-based QDSL: “n”-doped polycrystalline samples.....	123

2.3.c - Ti-based QDSL: “p”-doped monocrystalline samples.....	126
2.3.d - Ti-based QDSL: “p”-doped polycrystalline samples.....	129
2.3.e - Mo-based QDSL: “n”-doped monocrystalline samples.....	130
2.3.f - Mo-based QDSL: “n”-doped polycrystalline samples.....	132
2.3.g - Mo-based QDSL: “p”-doped monocrystalline samples.....	134
2.3.h - Mo-based QDSL: “p”-doped polycrystalline samples.....	136
2.4 - CONCLUSION.....	138
<u>3 - THERMOELECTRICAL CHARACTERIZATION</u>	<u>142</u>
3.1 - INTRODUCTION.....	142
3.2 - TI-BASED QDSL: N-DOPED SAMPLES	146
3.2.a - Monocrystalline QDSL.....	146
3.2.b - Polycrystalline QDSL	150
3.3 - TI-BASED QDSL: P-DOPED SAMPLES.....	152
3.3.a - Monocrystalline QDSL.....	152
3.3.b - Polycrystalline QDSL	155
3.4 - DISCUSSION ABOUT THE THERMOELECTRICAL CHARACTERIZATION RESULTS OF THE TI-BASED QDSL.....	157
3.5 - MO-BASED QDSL: N-DOPED SAMPLES	159
3.5.a - Monocrystalline QDSL.....	159
3.5.b - Polycrystalline QDSL	161
3.6 - MO-BASED QDSL: P-DOPED SAMPLES.....	163
3.6.a - Monocrystalline QDSL.....	163
3.6.b - Polycrystalline QDSL	165
3.7 - DISCUSSION ABOUT THE THERMOELECTRICAL CHARACTERIZATION RESULTS OF THE MO-BASED QDSL ..	167
<u>4 - CONCLUSION.....</u>	<u>169</u>
<u>REFERENCES</u>	<u>174</u>
<u>CONCLUSION.....</u>	<u>175</u>
<u>APPENDIX A</u>	<u>179</u>

Introduction

The industrial revolution occurred during the last century produced profound changes in our society. An improvement of technological knowledge and production techniques allowed a great increase of human population and together with it an increase of consumption.

The main energy sources employed by humanity which allowed this great industrial and technological revolution have always been derived from carbon-based sources, initiated by the exploitation of wood and coal and later of petroleum. The latter, which is nowadays the main global energy source, is not an eternal resource.

Estimations suggest that oil production is on its historical maximum and during the rest of this century the sources will start to run out of petroleum. This theory is known as the “peak oil” period. It is not possible to know for sure when the “petroleum age” will end, but it appears clear that it will not last until the end of this century.

Together with these issues the use of fossil combustibles resulted on a great increase of CO₂ and other greenhouse effect gases emissions, producing the well accepted phenomenon of global warming and the prevision of catastrophes linked to it.

Both these facts illustrate the urgent need to develop and improve alternative energy conversion systems, such as solar, wind-power, hydroelectric, geothermal and finally thermoelectric energy, with is the core of this work. Efforts have been made in order to encourage the use of renewable energies by government institutions such as the European Commission, who proposed to fix an objective of 20 % of the global energy consumption to be derived from renewable sources until 2020 (against around 14 % nowadays).

Among the alternative energy conversion systems and methods known nowadays the ones based on the thermoelectricity appears as very versatile and interesting systems. The thermoelectric effect consists on the direct conversion of a temperature gradient into electrical current and vice-versa. Another feature of a thermoelectric conversion system is based on solid pieces with no moving parts.

Both these features are in the core of the advantages of this kind of system. First, the main energy source employed is heat. This opens the opportunity of applications in very different environments due to the omnipresence of heat losses in places such as industrial activities, transports, and others. Moreover, the heat loss can be thought as a “free” energy source, and the only cost related to the production of thermoelectric energy in this case is the cost of the device itself. As an example, for an automobile, more than 60 % of the available energy from the fuel is lost in the form of heat. In this case, thermoelectric modules could be coupled to engines to power the automobile

electrical components such as batteries, sensors and others, reducing the fuel consumption.

The second major interest of thermoelectric modules comes from its high reliability, precision and miniaturization possibility due to the device conception, which contains neither moving parts nor complex parts. Probably the most successful application of a thermoelectric module nowadays concern the RTG (Radioisotope Thermoelectric Generator) used to power some of the NASA space probes. It consists in a SiGe-based thermoelectric generator using as energy source the heat created from radiative decay. The reliability of these modules allows the use in probes where no maintenance work is possible.

The precision in temperature monitoring, local cooling and possibility of energy recuperation allow also considering applications in the microelectronics industry. Thermoelectric devices could be directed integrated in chips in order to avoid a device overheating by local cooling or to manage local temperature changes, for example. Also, small temperature differences could be employed to power small sensors and other devices used in locations where human access is difficult.

The major reason why thermoelectric modules are still not well spread in industrial applications concerns its low conversion efficiency, being of around 5 – 8 % for commercial modules. Moreover, at room and medium temperatures the main employed materials are based on Bi_2Te_3 and PbTe , which contains toxic, rare or expensive elements.

A possible solution is to improve the efficiency of SiGe based devices, which are only efficient at high temperatures. The main advantages of this material are its low toxicity, low cost and compatibility with microelectronic applications. If the global efficiency of this material could be sufficiently increased, it could be possible to employ it at lower temperatures.

In the early 90's a novel approach was proposed in order to improve the thermoelectrical efficiency of materials. At first, theoretical works were produced showing that by nanostructuring thermoelectric material considerable gains could be achieved.

These theoretical works motivated practical experiments and the new materials produced after this date proved that increases of the thermoelectric properties were possible, even though all the mechanisms involved are still not fully understood.

Several approaches exist to nanostructure the material and take advantage of its benefits. In the case of this work the inclusion of nanometric Ti and Mo silicides inside a SiGe matrix forming a thin film QDSL (Quantum Dots SuperLattice) was chosen.

The work performed consists at the same time in a fundamental experimental research and in a practical work related to possible industrial applications. This means that this work will test the theory showing that the inclusion of Quantum Dots (QD) increases the thermoelectric properties of a semiconductor matrix by producing

samples using an industrial CVD (Chemical Vapor Deposition) tool employed by the microelectronics industry.

In this context, the first chapter will be dedicated first to present the thermoelectric history and effects. Latter, the main physical properties of a thermoelectric material playing a role on the thermoelectrical conversion will be presented. A discussion will be performed presenting the state of the art materials and the possible applications for thermoelectric devices. The final part of this chapter considers the nanostructuration effects and how they may affect the thermoelectric properties. Together with these discussions, a bibliographic review will be presented showing the already obtained improvements reported in literature after the nanostructuration.

The second chapter consists in the growth of QDSL based on the inclusion of Ti and Mo silicides QD in a SiGe matrix. In order to understand the method employed to grow these materials, the thin film growth aspects and mechanisms using a CVD tool will be presented. The results of the growth of these nanoparticles on SiGe substrates will be presented as well as a discussion linking the growth parameters and the QD properties such as mean diameters and surface densities.

The information obtained from Chapter II will be employed to produce different QDSL, and parameters such as dopant nature and matrix crystallinity will be evaluated. In Chapter III the produced QDSL will be first characterized morphologically by using the TEM (Transmission Electronic Microscopy) technique. Thermoelectric characterizations will also be made and discussions linking the obtained results with the samples morphological properties will be performed. A comparison with literature works will be also done, in order to validate the obtained results and to evaluate the role of the inclusion of QD in doped SiGe matrixes. Finally, in conclusion, a synthesis of the obtained results will be made and suggestions of future works will be presented in order to optimize the obtained novel materials.

CHAPTER I

Thermoelectricity and nanostructuring

1 - PRINCIPLES OF THERMOELECTRICITY	13
1.1 - HISTORY OF THERMOELECTRICITY	13
1.2 - THE THERMOELECTRIC EFFECTS.....	15
1.2.a - The Seebeck effect.....	15
1.2.b - The Peltier effect.....	20
1.2.c - The Thomson effect	22
1.2.d - The Kelvin Relationships	23
1.3 - PRINCIPLES OF THERMOELECTRIC CONVERTERS	24
1.4 - MAIN THERMOELECTRIC PARAMETERS	27
1.4.a - Electrical conductivity (σ).....	28
1.4.b - The thermal conductivity (λ).....	28
1.4.c - Seebeck Coefficient (S).....	30
1.4.d - Ideal carriers concentration.....	30
2 - THERMOELECTRIC APPLICATIONS.....	31
2.1 - STATE OF THE ART MATERIALS.....	31
2.1.a - Low and medium temperature materials	32
2.1.b - High temperature materials: Silicon-Germanium (SiGe).....	33
2.2 - BULK MATERIALS-BASED DEVICES.....	34
2.2.a - Generators	34
2.2.b - Cooling devices	36
2.2.c - Thermoelectric sensors	37
2.3 - THERMOELECTRIC THIN FILMS DEVICES	38
2.3.a - Thin film thermoelectric generators.....	38
2.3.b - Thin film cooling devices.....	39
2.3.c - Thin film thermoelectric sensors.....	40

<u>3 - INCREASING THE THERMOELECTRIC PROPERTIES VIA NANOSTRUCTURATION</u>	<u>41</u>
3.1 - POWER FACTOR IMPROVEMENT	42
3.2 - THERMAL CONDUCTIVITY REDUCTION	43
<u>4 - QUANTUM WELLS AND QUANTUM DOTS SUPERLATTICES</u>	<u>46</u>
4.1 - INTRODUCTION TO QUANTUM CONFINED STRUCTURES AND SUPERLATTICES	46
4.2 - GENERAL APPLICATIONS FOR QUANTUM WELLS AND QUANTUM DOTS.....	48
4.3 - THERMOELECTRIC APPLICATIONS FOR QWSL'S AND QDSL'S.....	49
<u>5 - CONCLUSION</u>	<u>53</u>
<u>REFERENCES</u>	<u>55</u>

1 - Principles of Thermoelectricity

1.1 - History of Thermoelectricity

The thermoelectric effect is considered by the scientific world as being first observed and described by Thomas Johann Seebeck in 1821. His observations were published by the name of “Magnetische Polarisation der Metalle und Erze durch Temperatur-Differenz» in 1822-1823 [1]. In this article he described the deflection of a compass needle placed in the middle of a closed loop made of a heated junction of two different metals (Figure 1.1).

Seebeck noticed for the first time that a temperature gradient across a junction of two materials could lead to electromagnetic effects. Not knowing at that time the correlation of electricity and magnetism, he considered the phenomenon observed to have a purely magnetic origin and called it thermomagnetism.

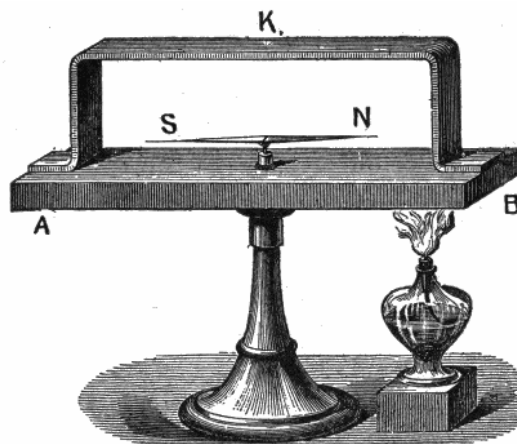


Figure 1.1: Seebeck apparatus. Image from [2].

Seebeck’s observations were further corrected by Hans Christian Oersted who at that time was working on finding a relationship between magnetism and electricity. He proposed the electrical origin of the effect and suggested a clear explanation for the phenomenon calling it *thermoelectricity* [3].

Later in the year of 1834 the French scientist Jean-Charles Peltier observed that thermal anomalies occurred at the junctions of two different conductors when an electrical current imposed to the materials. The effect at that time was not fully

understood and was wrongly described by Peltier, but four years later it was better explained by Heinrich Lenz.

By passing an electrical current through a junction of bismuth and antimony wires Lenz observed that depending on the direction of the current the junction was heated or cooled. This effect, which was further called the Peltier effect, can be seen as the reverse of the Seebeck effect.

It is interesting to notice that both of the Seebeck and Peltier effects were observed before the Joule effect (1841), which describes the heat created by an electrical current passing through a material.

In 1851 the English scientist William Thomson also known as Lord Kelvin made a synthesis of the thermoelectric effects. Together with the Seebeck and the Peltier effects, he introduced the Thomson effect and the mathematical formulation describing the three effects that is still employed nowadays. These three effects and their mathematical representation will be separately described in the next session of this chapter.

Even though a first prototype of a technological application based on the thermoelectric effect called thermomultiplier was developed by the Italian scientists Leopoldo Nobili and Macedonio Melloni in 1826, no relevant studies considering the efficiency of thermoelectric devices were conducted until the 20th century.

The work performed by Edmund Altenkirch during the years 1909-1911 fulfilled this lack of theoretical work and allowed a best understanding and improvement of the efficiency of thermoelectric devices. He proposed a theory based on the Seebeck effect to build a thermal generator and on the Peltier effect to make a cooler device. Both forms of devices had their maximum efficiency derived from his calculations. By doing this, he showed that a good thermoelectric material should have a high thermoelectric power (also called Seebeck coefficient), a low thermal conductivity as well as a high electrical conductivity.

After the work of Altenkirch, the possibility of using thermoelectricity to build generators and coolers led to an intensive research during the first and second World Wars period.

In 1949 Abram Fedorovich Ioffe developed the modern theory of thermoelectricity making several contributions to further development on the field. He developed the concept of the figure of merit “ ZT ”, an adimensional number that relates the intrinsic material properties such as the Seebeck coefficient, the electrical and the thermal conductivities with the thermoelectrical efficiency of a material used on a device as a cooler or a generator. Another great contribution of Ioffe’s work is the promotion of the use of doped semiconductor as thermoelectric materials, such as tellurides of antimony, bismuth and lead. His works were followed by those of H. Julian Goldsmid who did one of the first demonstrations of 0 °C cooling by using thermoelements based on bismuth telluride Bi_2Te_3 .

From 1960 to the 1990 decade, a few punctual achievements on successfully implementing thermoelectric generators were made, but none of them as a large scale production. The choice of using thermoelectric generators or coolers in these cases is certainly not driven by the efficiency of the device, but rather by the intrinsic reliability of solid-state generators. Indeed, thermoelectric devices have no moving parts, which make them well suited for using in situations where maintenance cannot be made and for continuous operation during long periods. The most remarkable of this successful application is called RTG (Radioisotope thermoelectric generator), a thermoelectric generator used for powering satellites and space probes (see section 2.2.a -).

Besides these achievements, not much improvement was made allowing the increasing of the energetic efficiency of thermoelectric devices, and the research on this field decreased.

This situation lasted until 1993 when L.D. Hicks and M. Dresselhaus published a theoretical work [4] showing that possible improvements could be achieved by using the nanostructuring of materials. Since then, a new interest emerged concerning thermoelectric materials, encouraged by the recent and continuous development of nanotechnologies.

In the following section, the origins and implications of the Seebeck and Peltier effects will be provided as well as a review on the possible applications of thermoelectric devices. Specific emphasis will be given to thin film devices as well as to the gains obtained by nano-structuring thermoelectric materials.

1.2 - The thermoelectric effects

1.2.a - The Seebeck effect

It will be first presented in this section a macroscopic view of the Seebeck coefficient (also called thermopower). Consider a piece of an electrical conductor, named "A" connected to two electrodes as represented in Figure 1.2.

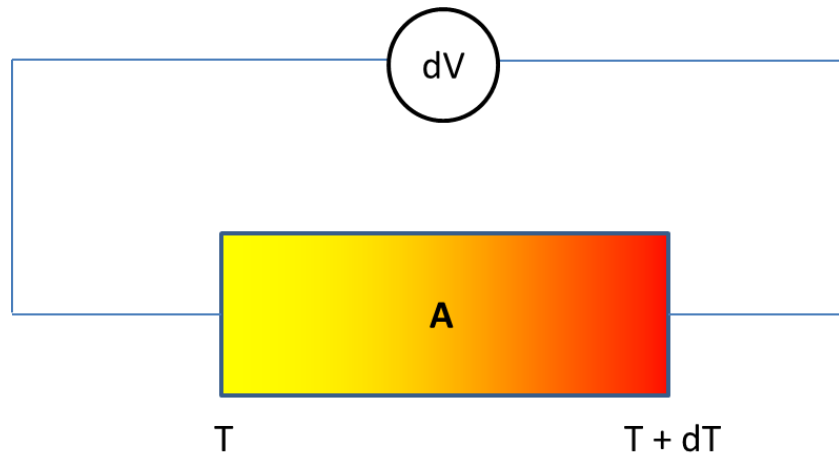


Figure 1.2: The ideal Seebeck coefficient measurement.

When heat is applied to one side of the material (represented as $T + dT$), an electrical potential difference is observed, noted as dV . The Seebeck coefficient S_A for the Material “A” is then defined as the proportionality coefficient linking these two quantities, as shown in Equation 1.1

$$S_A = \frac{dV}{dT} \quad \left[\frac{V}{K} \right] \quad 1.1$$

Where S_A is the Seebeck coefficient of the material “A”, “ dV ” is the measured potential difference and “ dT ” is the temperature difference between each side of the material. It should be noticed that the Seebeck coefficient is dependent on the temperature and is better represented by $S_A(T)$, but it can be approximately considered to be constant for the temperature interval ($T \rightarrow T + dT$).

This schematic representation presents however a problem. The electrodes used to measure “ dV ” are also electric conductors, and their Seebeck coefficient, even if in some cases can be neglected, is different from zero. In order to take into account the contribution of the electrodes, the representation of the Seebeck coefficient should be made as shown in Figure 1.3.

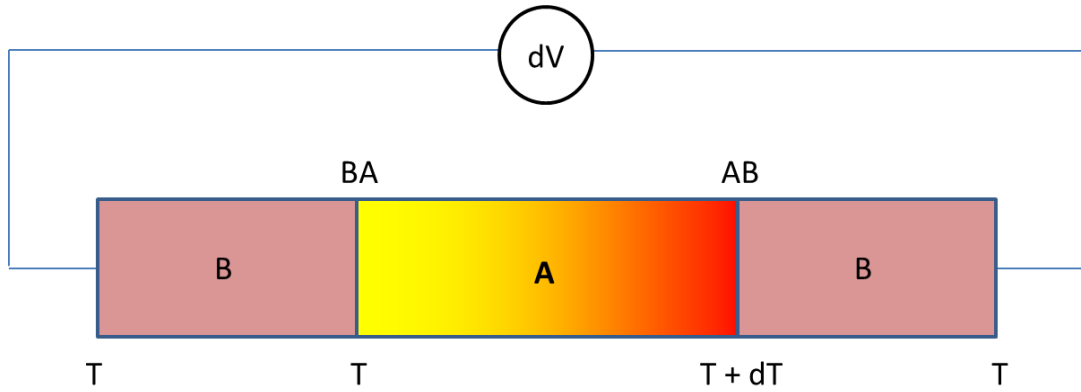


Figure 1.3: Measurement of the Seebeck coefficient of a junction of two materials.

In this case, the electrode material is represented as “B” and the potential difference “ dV ” is a sum of the potential drops due to contributions both for the “A” and “B” materials and can be defined as:

$$dV = S_B \cdot (T - T) + S_A \cdot dT + S_B \cdot (-dT) \quad 1.2$$

In this case, it is assumed that both the “BA” junctions as well as the exterior part of the electrodes are at the same temperature “ T ”. The Equation can then be written as:

$$S_A - S_B = S_{AB} = \frac{dV}{dT} \quad 1.3$$

This result means that in practice the Seebeck coefficient is always measured as a combination of the coefficient of two materials, S_{AB} . This statement demonstrates the importance to know the Seebeck coefficient of the electrodes (material “B”) employed to measure the Seebeck coefficient of material “A” precisely.

The results exposed in this section do not take into account the origin or the nature of the Seebeck effect. Different mathematical representations and theories explaining it are nowadays accepted, most of the time using non-equilibrium thermodynamics concepts, transport equations and some fundamentals of quantum mechanics.

However these equations are complex and for a non-specialist in the field it could be impossible to fully understand the origin of thermoelectric effects. Instead, in order to make the understanding of these phenomena more straight-forward, as long as possible the use of graphical representation such as band diagrams will be employed in this thesis.

The Seebeck coefficient of a material is considered to be related to the asymmetry of the concentration of charge carriers around the Fermi level. First consider the density of states of a material (DOS) represented as “ $N(E)$ ” and the Fermi function “ $f(E)$ ” described by the Equation 1.4:

$$f(E) = \frac{1}{1 + e^{(E-E_f)/k_B T}} \quad 1.4$$

Where “ E ” is the energy of a single carrier, “ E_f ” is the Fermi level, “ k_B ” is the Boltzmann constant and “ T ” is the absolute temperature. The Fermi-Dirac distribution represents the probability of occupation of a certain energy level by charge carriers as a function of the temperature.

By multiplying the density of states $N(E)$ (Figure 1.4-a) by the Fermi-Dirac distribution $f(E)$ it is possible to obtain the density of occupied states of the material. This new function represents the number of charge carriers per unit of energy and per unit of volume.

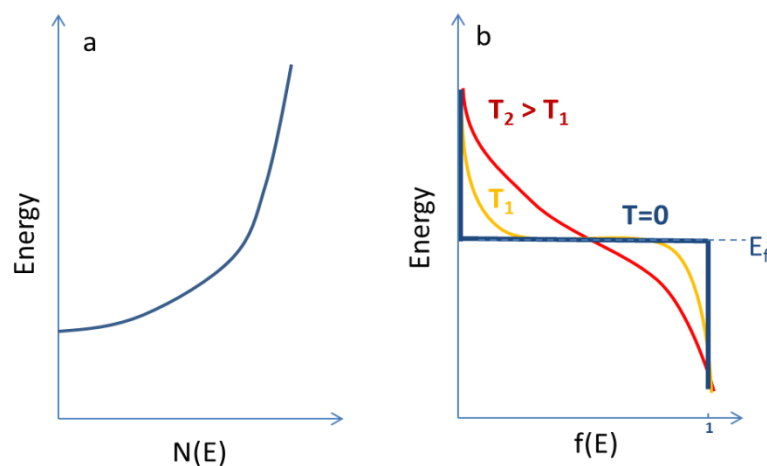


Figure 1.4: Density of states $N(E)$ of the conduction band (a) and $f(E)$ as a function of temperature (b)

At 0 K, only the states at the Fermi level are occupied. As the temperature of the material increases, the occupation probability at energies other than the Fermi energy becomes different from zero, as shown in Figure 1.4-b.

By integrating the function $N(E).f(E)$ over the energies of the conduction band the total number of carriers per unit volume in the conduction band is obtained.

In order to simplify the visualization of the phenomenon responsible for the origin of the Seebeck effect the examples presented here will be “n” type semiconductors (where electrons are the majority carriers). It should be noticed that the same is valid for “p” type materials (where holes are the majority carriers).

For a given temperature T_1 an average energy for the electrons occupying the conduction band can be obtained as represented in Figure 1.5.

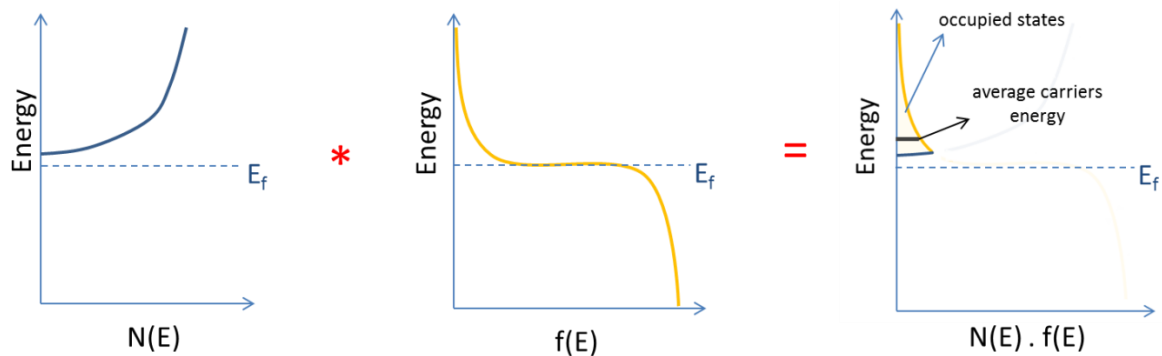


Figure 1.5: Density of occupied states $N(E).f(E)$ for a “n” type semiconductor showing the average energy of carriers at a temperature T_1 .

The same can be obtained for a temperature $T_2 > T_1$ (Figure 1.6).

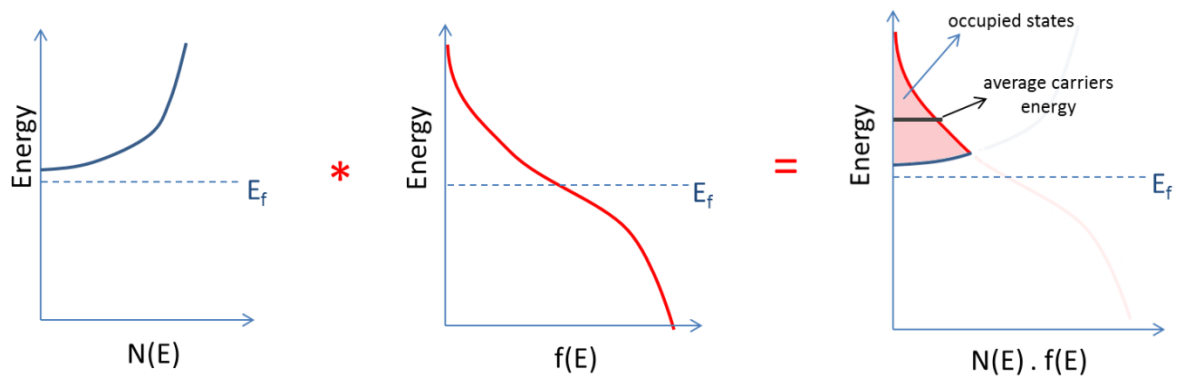


Figure 1.6: Density of occupied states $N(E).f(E)$ for a “n” type semiconductor showing the average energy of carriers at a temperature $T_2 > T_1$.

It is now easy to see that when each side of a material is kept at different temperatures the average energy of electrons in the conduction band will be different (Figure 1.7).

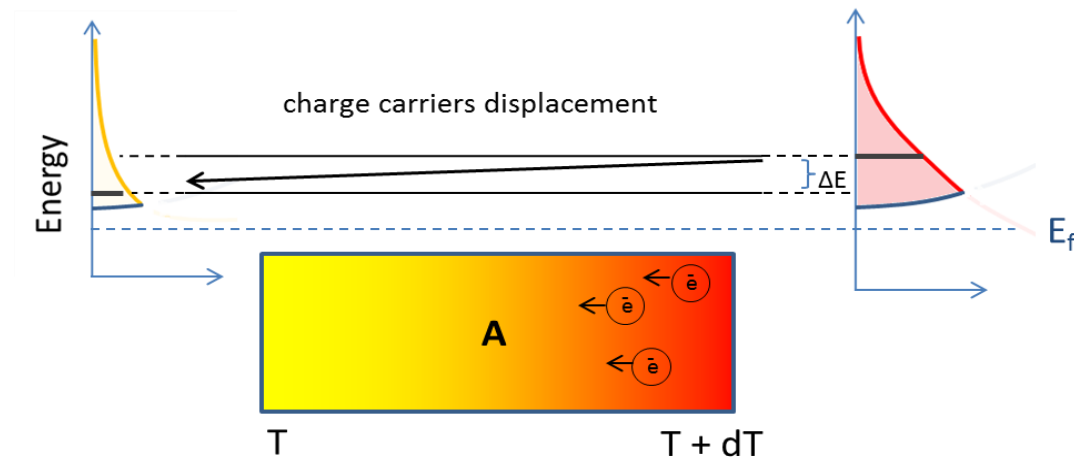


Figure 1.7: Schematic representation showing the movement of electrons in a "n" type semiconductor driven by the difference of average carriers energy ΔE .

To bring back the system to the thermodynamic equilibrium, the electrons will then move from the hot to the cold side, creating an electrical current.

To compensate this movement of charges, the Fermi level of the cold side will rise until the average charge carriers energy will be the same. The resulting difference of the Fermi levels between each side of the material is what causes the difference of electric potential as demonstrated in Figure 1.2 and Equation 1.1.

1.2.b - The Peltier effect

The Peltier effect can be thought as the opposite of the Seebeck effect. Consider a junction of two materials "A" and "B". An electrical current "I" is imposed through the materials as represented in Figure 1.8.

The current passing through the material will cause a heat absorption "dQ" in one junction as well as a heat release "-dQ" in the other junction. The heat absorbed or released is proportional to the current applied and the proportionality coefficient is called Peltier coefficient, Π .

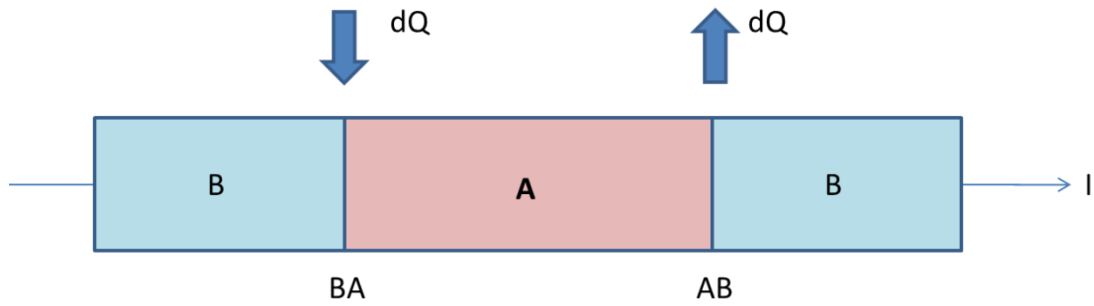


Figure 1.8: Macroscopic view of the Peltier effect.

Taking the BA junction as an example, the Peltier coefficient can be described by the Equation 1.5:

$$\Pi_{AB}(T) = \Pi_A(T) - \Pi_B(T) = \frac{dQ}{dT} \quad [V] \quad 1.5$$

Where Π_A is the Peltier coefficient of the material "A", Π_B for the material "B" and Π_{AB} the coefficient for the junction "BA" at temperature "T".

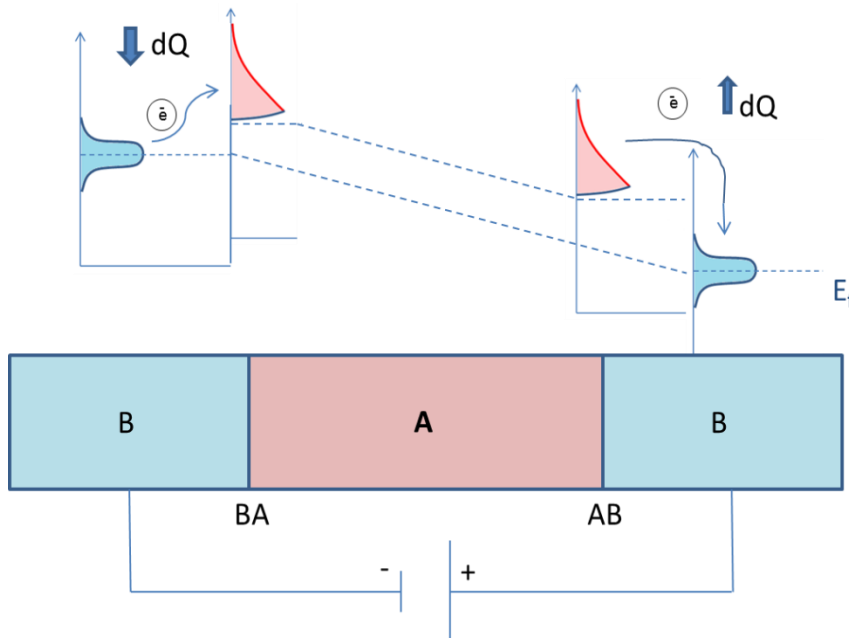


Figure 1.9: Schematic representation showing the heat absorption and release by the electrons moving from the conductor "B" to the semiconductor "A".

The origin of the Peltier effect can also be represented by band diagrams. Consider the material "B" as a metal and the material "A" as an "n" type semiconductor. A potential difference is applied to the materials as represented in Figure 1.9.

The applied voltage will cause a lowering of the Fermi level at the junction "AB". The electrons at the "B" conduction band in the "BA" junction (left side) will absorb energy (heat) in order to enter in the conduction band of the semiconductor "A". At the right side (junction "AB"), the electrons will release their energy in the form of heat in order to enter in the conduction band of the "B" material.

Once again, the same kind of representation can be made with a "p" type semiconductor as the material "A". The Peltier effect is used in calculations concerning the design of cooling systems.

1.2.c - The Thomson effect

The last of the thermoelectric effects is the Thomson effect, described by William Thomson, also known as lord Kelvin. It is however considered of low importance for practical applications [5], and it will be presented in a succinct manner. Consider a conductor having a temperature difference "dT" along its extremities and having a current "I" imposed through (Figure 1.10).

Providing small temperature differences, the amount of heat exchanged " $\frac{dQ}{dx}$ " is proportional to the thermic gradient " $\frac{dT}{dx}$ " and the current "I". The proportionality coefficient is called the Thomson coefficient, " β ", according to Equation 1.6.

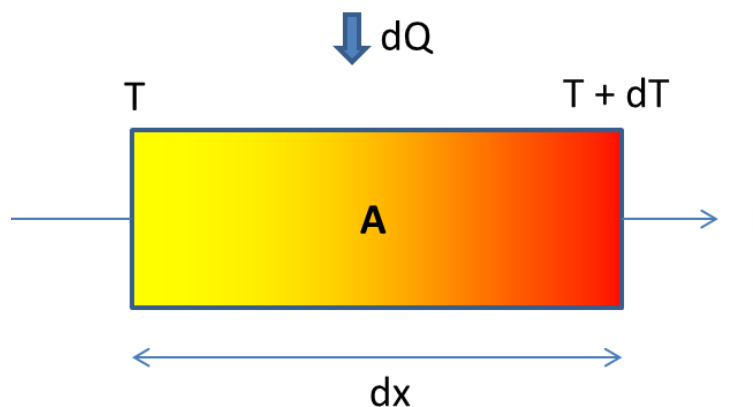


Figure 1.10: Macroscopic view of the Thomson effect.

The units of the Thomson coefficient are the same as for the Seebeck coefficient, [V/K].

$$\frac{dQ}{dx} = \beta \cdot I \cdot \frac{dT}{dx} \quad 1.6$$

1.2.d - The Kelvin Relationships

William Thomson also developed relationships between the coefficients cited above. They were further called the Kelvin relationships. The first one expresses the proportionality between the Seebeck coefficient “ S_{AB} ” and the Peltier coefficient “ Π_{AB} ” of a junction made with the materials “A” and “B” as showed in Equation 1.7.

$$S_{AB} = \frac{\Pi_{AB}}{T} \quad 1.7$$

The second Kelvin relationship relates the Seebeck coefficient of the junction to the Thomson coefficient of each material (Equation 1.8).

$$\frac{dS_{AB}}{dT} = (\beta_A - \beta_B)/T \quad 1.8$$

The validity of these equations was demonstrated for several materials and it is accepted that they are valid for all materials employed for thermoelectric applications.

1.3 - Principles of thermoelectric converters

A thermoelectric converter is a device that can be considered as a thermodynamic system allowing the direct transformation of thermic to electric energy and vice-versa.

The systems used as an example in this thesis are considered as ideal. This means that for the calculations no heat losses are included.

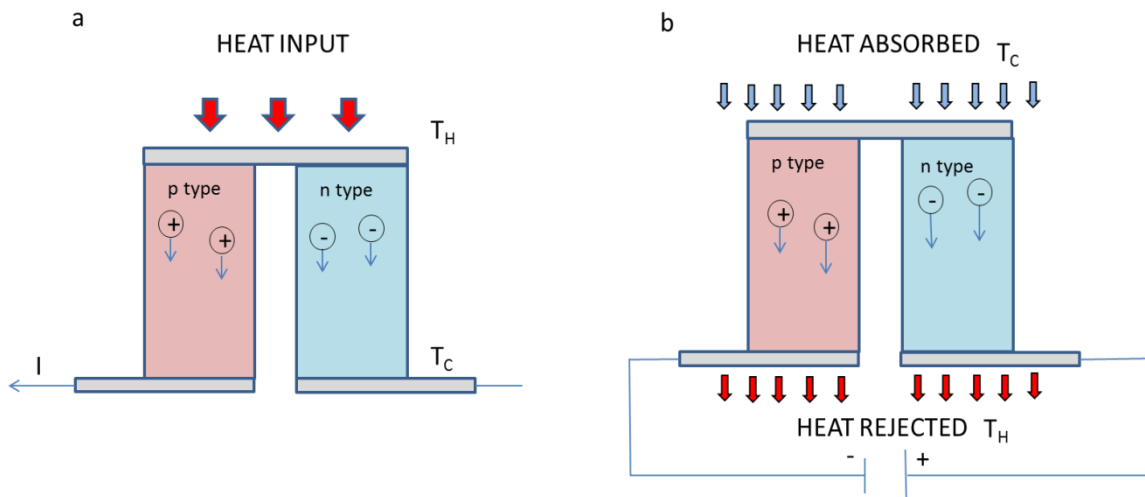


Figure 1.11: A thermoelectric generator (a) and a thermoelectric refrigerator (b).

Consider a junction of two materials (legs), a “p” and “n” type semiconductors linked by a metallic element, as represented in Figure 1.11. The device is called a “thermocouple” (TC) in this situation.

First consider the generator mode. When a heat input is applied to the upper side of the junction, a charge displacement will occur towards the lower part of the junction. Only the majority charge carriers are considered.

The temperature gradient created ($T_H - T_C$) applied to this type of junction will create by Seebeck effect a current “I”. The voltage created can be increased by increasing the number of legs by adding more junctions (thermally in parallel and electrically in series).

The same logic is valid for the thermoelectric refrigerator. When a current is imposed through the junction, the charge carriers will absorb energy in the upper side in order to enter the conduction band of the semiconductor as explained in section 1.2.b - . The carriers will then release the heat when they achieve the lower part of the junction.

This will cause a cooling in the surroundings of the upper part and inversely a heating in the lower part of the device. An increase of this effect is also obtained by increasing the number of legs.

In order to obtain a mathematical expression of the conversion yield, an ideal generator with no heat losses is assumed. The energetic yield (φ) is then expressed by the ratio between the energy supplied to the load (W) and the thermal energy supplied to the system, i.e., the heat absorbed on the hot side (Q_H), as stated by Equation 1.9.

$$\varphi = W/Q_H \quad 1.9$$

The electrical power W can be expressed as a function of the Seebeck effect of the p-n junction (S_{pn}) as:

$$W = (S_p - S_n) \cdot I \cdot \Delta T \quad 1.10$$

The absorbed heat on the cold side can be expressed as:

$$Q_H = S_{pn} \cdot I \cdot T_H + \lambda' \cdot \Delta T \quad 1.11$$

Where " λ " is the thermal conductance of the materials "n" and "p" (assuming that this value is approximately the same for both materials). By including Equations 1.10 and 1.11 in Equation 1.9, the following expression is obtained:

$$\varphi = \frac{S_{pn} \cdot I \cdot \Delta T}{S_{pn} \cdot I \cdot T_H + \lambda' \cdot \Delta T} \quad 1.12$$

The maximal efficiency of the system can be expressed by the product of Carnot efficiency " η_c " and the efficiency of the thermoelectric system " η_{th} ", where:

$$\eta_c = \frac{T_H - T_c}{T_H} \quad 1.13$$

and:

$$\eta_{th} = \frac{\sqrt{1 + Z_c \cdot T_m} - 1}{\sqrt{1 + Z_c \cdot T_m} + \frac{T_c}{T_H}} \quad 1.14$$

Where T_m is the mean temperature:

$$T_m = \frac{T_H + T_C}{2} \quad 1.15$$

“ Z_c ” is defined as the figure of merit of the couple “p” and “n” as follows:

$$Z_c = \frac{S_{pn}^2}{R \cdot \lambda'} \quad 1.16$$

Where “R” is the electrical resistance of the device. In practice, the two legs of the junction are made of materials with similar material constants and the figure of merit can be generalized for any material in the form of an adimensional number, “ZT”.

$$ZT = \left(S^2 \cdot \sigma / \lambda \right) \cdot T \quad 1.17$$

Where “ σ ” is the electrical conductivity and “ λ ” is the thermal conductivity of the material. The parameter “ $S^2 \cdot \sigma$ ” is also called the *electrical power factor*. The bigger is the figure of merit of a material, the higher is the energetic efficiency of a device made with it.

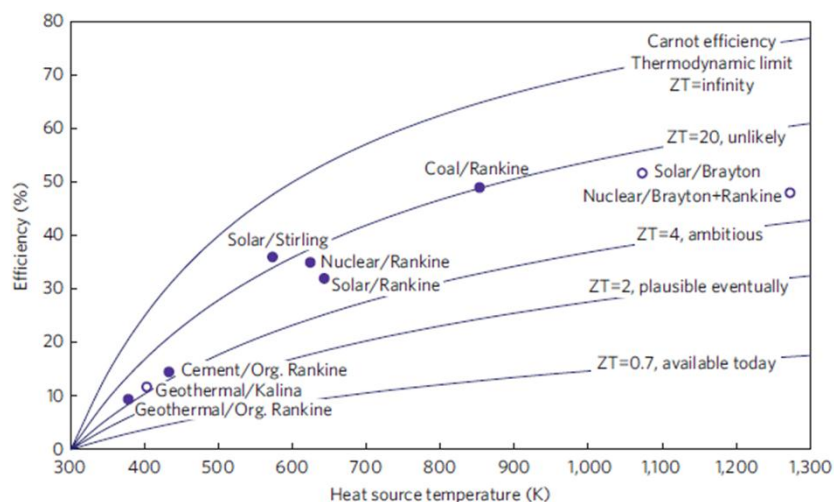


Figure 1.12: Conversion efficiency as a function of operating temperature difference and the thermocouple figure of merit "ZT". The cold side of the junction is maintained at 300K. Image from [6].

By analyzing Figure 1.12 some important information can be obtained concerning the energetic efficiency of thermoelectric devices. First of all, the role of the temperature difference between the cold and the hot side of the junction.

As demonstrated by Equation 1.13, the efficiency increases with the temperature difference. It can also be seen the role of the "ZT" of the thermocouple. For example, if a temperature difference of 100 K is applied to a device made of a thermocouple having a "ZT" of 2, the resulting efficiency would be similar to that of a geothermal organic Rankine device, i.e., around 10%.

These results support the fact that further research is necessary in order to obtain materials with the higher possible "ZT".

1.4 - Main thermoelectric parameters

It was demonstrated importance of using high "ZT" materials for having the maximum possible thermoelectric efficiency. However until now no information concerning how the "ZT" varies as a function of the chosen material was provided. In other words, when designing a thermoelectric device one should ask himself which class of materials would be the best.

Further in this section each one of the variables composing the "ZT", i.e., " σ ", " λ " and " S " will be explained and studied separately. These parameters will be considered primarily for the case of semiconductors, which are the materials employed in this work. One parameter that characterizes a semiconductor is its charge carriers

concentration, expressed in carriers $\times \text{cm}^{-3}$, and the role of this value on the variables composing the material's "ZT" will be demonstrated.

1.4.a - Electrical conductivity (σ)

The electrical conductivity of a semiconductor can be defined by:

$$\sigma = n \cdot q \cdot \mu \quad 1.18$$

Where "n" is the charge carriers concentration, "q" is the electron charge and " μ " is the carriers mobility. In this case, the conductivity is proportional to the dopants concentration.

The mobility of the charge carriers is also dependent on the dopants concentration. An increase in the number of dopants atoms causes a reduction of the mean free path and the collision time of carriers, reducing the mobility of the electrons by scattering. For high doping levels (more than 1×10^{18} atoms/cm³) however the mobility approaches a constant and the electrical conductivity increases almost linearly with dopants concentration.

1.4.b - The thermal conductivity (λ)

Heat transport in materials is mainly due to the displacement of electrons and phonons. Electrons, which act at the same time as charge and heat carriers are responsible for the most part of the conduction in metals. Phonons, on the other hand, are quasiparticles representing a vibration in a lattice made of atoms or molecules, and are the responsible for heat transport in insulating materials.

Heat transport in semiconductors has contributions of both of the two modes, i.e., electrons and phonons, as described by the equation 1.19.

$$\lambda = \lambda_l + \lambda_e \quad 1.19$$

Where " λ_e " is the electronic contribution and " λ_l " the lattice contribution (phonons) to the thermal conductivity. The electronic contribution can be

approximately expressed by the Wiedemann-Franz law, considering no inelastic collisions between electrons and phonons.

$$\lambda_e = L_0 \cdot \sigma \cdot T \quad 1.20$$

Where L_0 is the Lorentz number. For degenerate semiconductors it can be considered a constant number approximated to:

$$L_0 = \frac{\pi^2 \cdot k_B^2}{3 \cdot q^2} \approx 2,45 \cdot 10^{-8} \text{ V}^2 / \text{K}^2 \quad 1.21$$

The lattice contribution " λ_l " can be expressed as:

$$\lambda_l = \frac{C_v \cdot \langle v \rangle \cdot \tau}{3} \quad 1.22$$

Where " C_v " is the phonon's specific heat, " $\langle v \rangle$ " is the phonons average speed and " τ " is the phonons relaxation time. This equation is obtained from the kinetic gas theory applied to phonons and is valuable at low temperatures, where the phonons dispersion relation is negligible.

It can be seen from Equation 1.20 that the electronic contribution for the heat transport " λ_e " depends on the material's electrical conductivity. This is easily understood, since electrons are the particles responsible for heat transport. By increasing the number of charge carriers by further doping the material, the electrical conductivity is increased (Equation 1.18) but λ_e is increased as well, making this strategy not suitable for increasing the material's "ZT".

Equation 1.22 shows that the lattice contribution to heat transport is constant concerning the charge carriers. The reduction of the lattice thermal conductivity is the strategy chosen for the present work in order to increase the "ZT" of SiGe alloys. This is done by including quantum dots that will act as barriers for the phonon (and heat) transport inside a SiGe matrix (section 3.2 -).

1.4.c - Seebeck Coefficient (S)

For simplicity, only the case of degenerate semiconductors will be considered, which are the materials employed in this work. This coefficient can be determined via derivation of the Mott's formula [7]:

$$S = \frac{\pi^2 k_b^2 T}{3q} \left[\frac{1}{n(E)} \frac{dn(E)}{dE} + \frac{1}{\mu(E)} \frac{d\mu(E)}{\mu dE} \right]_{E=E_F} \quad 1.23$$

By approximating this equation using the Sommerfeld model for an electron gas [8] the effect of the charge carriers concentration “ n ” on the Seebeck coefficient is:

$$|S| \propto n^{-2/3} \quad 1.24$$

The Seebeck coefficient of a degenerate semiconductor thus decreases when increasing the dopant concentration.

1.4.d - Ideal carriers concentration

The results exposed in the last sections showed that both of “ λ ”, “ σ ” and “ S ” depend on the doping level. A summary of these results is represented in Figure 1.13.

The highest power factor is achieved by using semiconductors materials with doping levels around 1×10^{19} atoms.cm⁻³.

Moreover, for this carrier concentration, the larger contribution to the thermal conductivity comes from the lattice thermal conduction by phonons. For this work, a doping level around the optimal concentration was chosen.

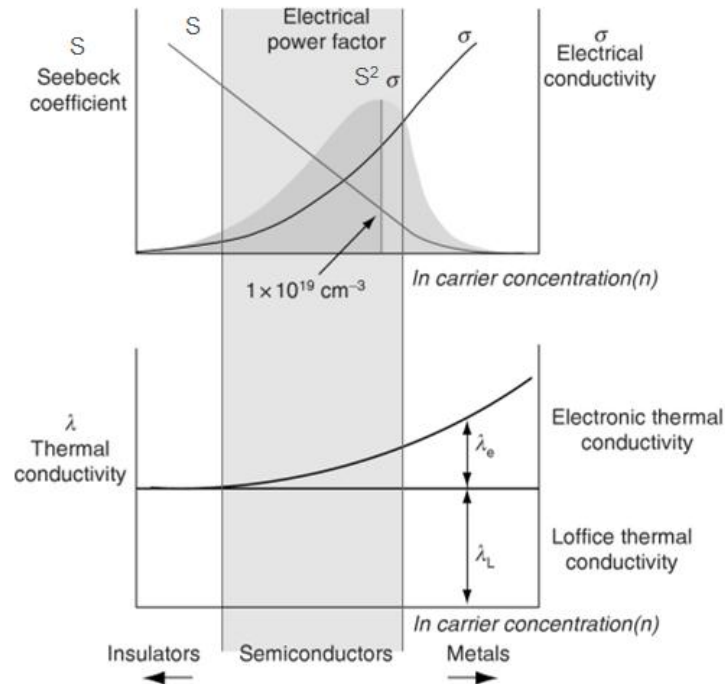


Figure 1.13: Power factor and thermal conductivity as a function of carriers concentration. Image modified from [5].

2 - Thermoelectric applications

First in this section a brief description of the best materials employed nowadays for thermoelectric applications will be performed, followed by traditional and new possible applications for devices made with these materials.

2.1 - State of the art materials

As discussed earlier, in general the best materials for thermoelectric applications are highly doped semiconductors, even though some exceptions exist such as intermetallic compounds. A convenient way to classify the materials is according to their working temperature, i.e., the temperature corresponding to their maximum “ZT”, as described in Figure 1.14.

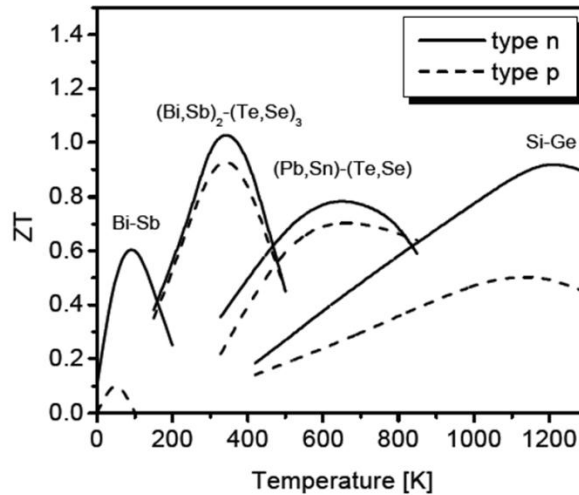


Figure 1.14: Figure of merit (ZT) for conventional materials as a function of temperature [9].

2.1.a - Low and medium temperature materials

For low temperatures (up to 450 K), the best materials employed are tellurium and bismuth compounds such as Bi_2Te_3 . By doping this material with antimony and selenium “p” and “n” materials are obtained, respectively. For medium temperatures, between 500 and 800 K, the reference material is PbTe with partial substitution of lead by tin and of tellurium by selenium. Even though it has a lower “ZT”, its higher melting point allows the using of it without chemical stability problems [10]. Doping can be obtained by a large choice of impurity atoms such as Na, Au, Ti, and O for “p” type and Zn, Cd, In, Bi, and Cl for “n” type.

It should be noticed that both tellurium and lead-based materials are highly toxic [11,12] and thus new materials should be developed for a safe usage of thermoelectric devices at low to medium temperatures.

Some other classes of materials are currently studied as being possibly well suited for low and medium temperatures having the advantage of being constituted of materials relatively abundant and presenting a low toxicity.

It can be cited for example some metals silicides such as CrSi_2 , FeSi_2 , $\text{MnSi}_{1.7}$ and $\text{Mg}_2(\text{Si},\text{Sn})$ [13]. The best performances were measured for the two latter. Solid solutions of Mg_2Si and Mg_2Sn were reported having an “n” type behavior with a “ZT” of 1.3 at around 700 K [14]. For the “p” type, the best performances were for $\text{MnSi}_{1.7}$, which presented for the same temperature range a “ZT” of 0.7 [15].

There are other materials for the medium temperature range having interesting properties, such as skutterudites and clathrates. Both of them share a possible low thermal conductivity due mostly to their complex crystalline structure, presenting

large voids that when filled with heavy atoms can establish local soft phonon modes causing a lowering of the thermal conductivity [16].

Skutterudites have the property of a glass-like lattice thermal conductivity because of the presence of loose atoms having more than one metastable position in the interior of the crystalline cell. They were reported having a “ZT” approaching 1 [10,17].

Similarly, clathrates have a very low thermal conductivity mostly due to the very large size of the lattice unit cell and consequently large open structure inside of it where guest atoms can be incorporated [10]. Theoretical studies for optimized clathrates compositions showed a possible “ZT” of 1.7 at 800 K [18]. However the high degree of complexity of these materials such as a large number of different atoms and possible stoichiometry make their synthesis and industrial application problematic.

2.1.b - High temperature materials: Silicon-Germanium (SiGe)

As illustrated in Figure 1.14, the last class of materials is those for high temperature applications, represented basically by Si-Ge alloys.

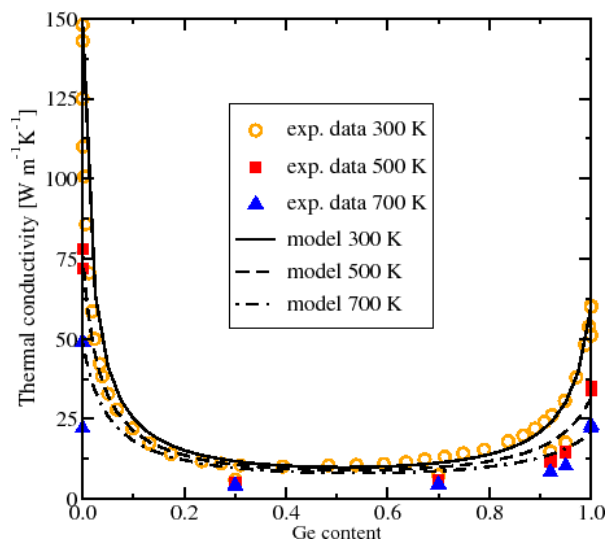


Figure 1.15: Thermal conductivity of SiGe as a function of Ge content [19].

Silicon, when doped, has a high electrical conductivity, but also a high thermal conductivity. Silicon and germanium form a solid solution with no intermetallic compounds, thus it is possible to mix the two atoms in any different concentrations. By mixing both atoms to form a solid solution a great reduction of the thermal

conductivity can be observed (Figure 1.15). Moreover, for high doping levels such as for degenerate SiGe, very little changes of the carriers mobility is observed [19].

These results imply that a relatively high figure of merit can be achieved by including Ge to Si. The state of the art values of “ZT” for conventional doped SiGe materials are around 1 for “n” type and 0.6 for “p” type materials using the composition $\text{Si}_{0.8}\text{Ge}_{0.2}$ at temperatures around 1200 K [20].

This material has the great advantage of being non-toxic. Moreover, silicon is the second more abundant element on earth [21]. Germanium however is much rarer and expensive. As a conclusion, further investigations should be made in order to improve the “ZT” of SiGe materials, allowing a further reduction of the Ge content. This issue is the core of this work. By including nanoparticles inside a SiGe matrix, a reduction on the thermal conductivity and an increase on the “ZT” are expected, and a possible reduction of the Ge content for the same figure of merit can be predicted.

2.2 - Bulk materials-based devices

Applications for thermoelectric devices will be grouped in this document in three major working modes. The first one, the generator mode, is based fundamentally on the Seebeck effect, where a temperature gradient is employed to produce electric power in the form of an electrical current. The second major application is the cooling mode, which is basically the reverse of the generator mode and can be also thought as a heat pump. It is generally described by the Peltier effect. The last mode of operation is the sensor mode, where changing of the heat flux in a certain spatial region can be detected also based on the Seebeck effect.

2.2.a - Generators

Although thermoelectric generators have been used since the 1950's, it always remained a “niche” application. The reason for the low-scale utilization of generators lays in its low efficiency (around 5 %), making it suitable for applications where the basic requirements are not the cost but rather their reliability [22]. This reliability is guaranteed mostly because of the simplicity of the operating mode of this type of device, which contains no moving parts.

The traditional applications for thermoelectric modules are basically concentrated on the field of military and spatial applications, such as the RTG.

RTG is the most successful application of thermoelectric generators using other materials than Bi_2Te_3 . This energy production system is considered to be the only one

capable of powering long-lasting spacecraft such as those employed for interplanetary missions [23,24].

RTG working principle is based by coupling a thermoelectric module with a heat source originated from the decay of radioactive isotopes, commonly Pu-238, which has a specific energy release of 0.57 W/g and a half-life period of 87.7 years [24]. Once again, the great advantage of this type of powering system is its high reliability (independent of solar radiation) and long life.

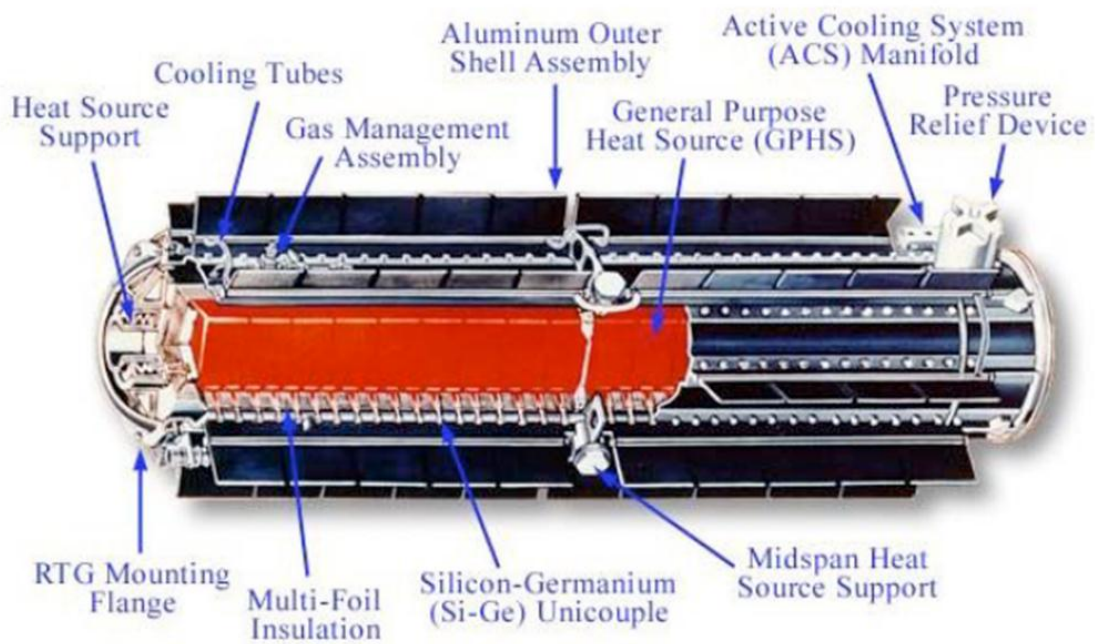


Figure 1.16: Representation of the GPHS-RTG. Image from [25].

Examples of well-known space probes that use RTG as powering system are the probes Pioneer, Voyager, Apollo 11, Galileo and more recently New Horizons.

Typically each RTG can provide power of around hundreds of watts. The general-purpose heat source-RTG (GPHS-RTG), which until 2006 was the current RTG employed by NASA nominally generates around 250 watts at the beginning of its mission [26].

The GPHS-RTG is considered of main importance in the context of this work. It employs doped SiGe as thermoelectric materials in a range of temperature of around 1273 K at the hot side and 566 K at the cold side [25]. This material will be further used as a reference material in order to evaluate the performance of the SiGe-based materials produced in this work.

Concerning potential future applications, both low and high power (microwatts for thin film applications and kilo watts for bulk materials) generators can be built, and the increase of the global concern of environmental issues can be considered a driving force for research on this field [27].

Others applications possibly viable from an economic point of view are those concerning heat waste. In these cases, where the heat is normally not re-used, the heat source can be considered as a “free” energy source, and cost considerations concern only the materials and the device production costs. For example, only 25% of the energy from the combustion in an automobile engine is used as mechanical work for moving the vehicle and 40% is lost in the form of hot exhaust gases [28].

2.2.b - Cooling devices

The world market concerning cooling thermoelectric devices is considered to be ten times more developed than the generator one [29].

Even though the energetic efficiency of the system remains low as compared to traditional fluid compressing systems, additional advantages exist for using thermoelectric coolers rather than traditional ones. Because thermoelectric devices use no compressors they are lighter, smaller and silent-operating. They also have the advantage of a more precise temperature control [27].

Several applications already exist nowadays, and in opposition to generators applications that are concentrated basically in the military and spatial domains, thermoelectric coolers are employed in more varied fields.

Some examples of commercially available products are: consumer products such as car refrigerators, portable picnic coolers, heated/cooled automobile seats (Figure 1.17), laboratory equipment (cold plates, cold chambers) and others [27].

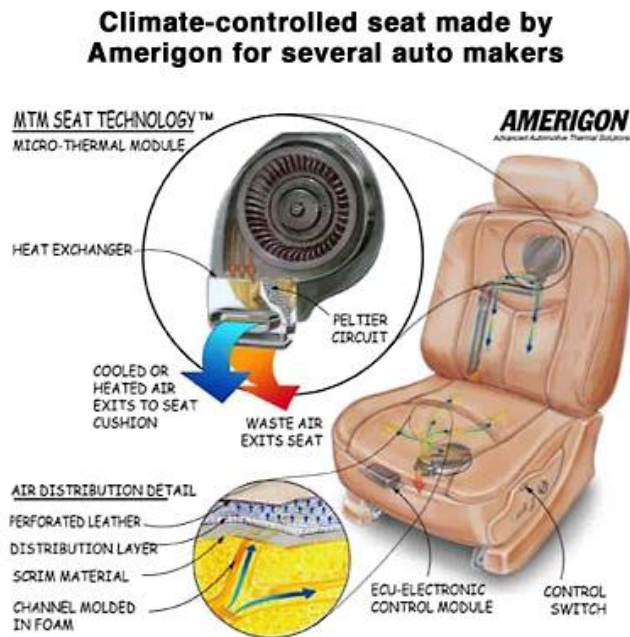


Figure 1.17: Schematic representation of the Amerigon climate-controlled seat.

2.2.c - Thermoelectric sensors

The most important example concerning macroscopic thermoelectric sensors in terms of applications is the thermocouples employed for temperature measurements (Figure 1.18). These systems have a big precision and are largely employed in industrial and laboratory applications. It is made basically of only one junction of two thermoelectric materials. Usually two metallic alloys are employed. There are several types of thermocouples, each one being more adapted for a specific temperature and for the ambient conditions.

The working mode is based on the Seebeck effect as demonstrated in Figure 1.3 and the reference temperature is the room temperature. The difference of temperature between the each sides of the junction produces a voltage drop that can be easily measured with a voltmeter. Calibration tables are widely available on internet with the Seebeck coefficient of both thermocouples materials with different temperatures.

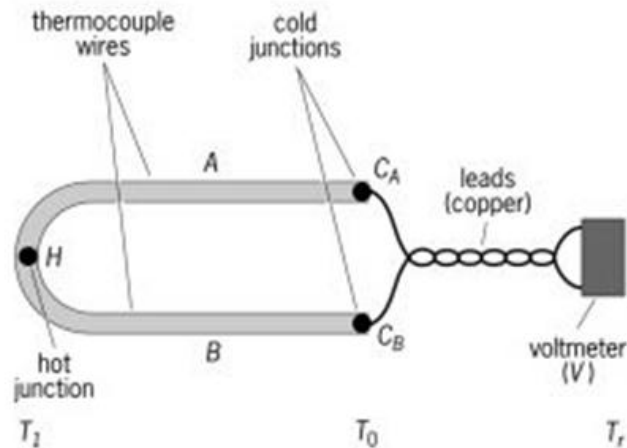


Figure 1.18: Representation of a thermocouple used for temperature measurements.

2.3 - Thermoelectric thin films devices

As for bulk applications, applications for thermoelectric thin films can also be divided in three major fields, i.e., generators, cooling devices and sensors. The expression “thin film thermoelectric generators” can lead to some misunderstanding and a more precise description of the type device is necessary. In the most part of the time it refers to any device where the thickness of the “p-n” thermoelectric junction is on the micrometer range. It can be produced by printing, sputtering, Molecular Beam Epitaxy (MBE) and Chemical Vapor Deposition (CVD), for example.

In this work a discussion will be presented concerning basically applications related to the microelectronics industry, which correspond to the materials and techniques employed during the production of our samples, i.e., silicon-based materials, CVD, lithography techniques and others.

2.3.a - Thin film thermoelectric generators

The main application of thin film thermoelectric generators related to the microelectronics industry is called “on-chip energy harvesting”. These devices could take advantage of the high energy density dissipated on the so-called hot spots of microprocessors, which could attain values up to $100\text{-}300\text{ W/cm}^2$. By integrating these devices into chips, the heat wasted could be directly converted and employed to power the microprocessor.

A simulation work has been reported using a superlattice structure of Bi_2Te_3 and Sb_2Te_3 as thermoelectric materials with a ZT larger than 2 (Figure 1.19). In this

reference the thermoelectric module was both considered to be directly grown on the Si substrate (die) and on an integrated heat spreader (IHS) [30]. The calculations showed that by using this material it is possible to harvest up to 30 mW of power from a heat flux of 200 W/cm².

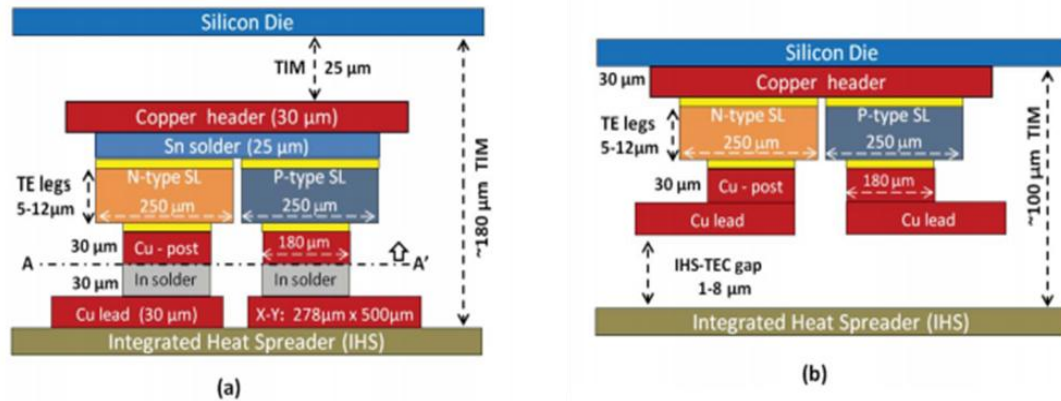


Figure 1.19: Example of a Bi₂Te₃ and Sb₂Te₃ thermoelectric module for “on-chip energy harvesting”. a) module integrated on the HIS. b) module integrated on the silicon die. Image from [31].

Some other references of integration of both BiSbTe and Si-based materials can be found in [31]. The Si-based materials however produced a lower conversion efficiency because of its lower ZT (considered to be 0.1–0.2 by the authors in the conditions of this work, i.e., at ambient temperatures).

All of these reported works are still in the research step, and some problems related to the integration of these devices in industrial applications exist. One of the major problems is related to the difficulty of integrating the BiSbTe-based materials on the silicon die because of the lack of compatibility between the two materials.

It can be seen here an example of the importance of obtaining a higher ZT at low and medium temperatures for Si-based materials, which is the goal of this thesis. The ways of increasing this material’s ZT will be presented and discussed in section 3 - .

2.3.b - Thin film cooling devices

Similarly to the “on-chip energy harvesting” applications, thermoelectric modules could be integrated in microelectronic devices to serve as an “on-chip cooling” device in order to keep the devices operation in the optimal temperature range thus reducing thermal noise and current leakage [27]. Due to size of these components, no other cooling systems are possible rather than those based on thermoelectricity. By using

thermoelectric devices, it should be possible to locally cool hot spots of hundreds of micrometers of diameter on chips [32].

A work has been published where a thermoelectric module was integrated on a state-of-the-art electronic package [33]. This was achieved using a Bi_2Te_3 superlattice-based material grown by metal-organic CVD (MOCVD) on GaAs substrates (Figure 1.20). It is interesting to notice that this was the same material studied for the “on-chip energy harvesting” devices. The authors reported a cooling of up to $15\text{ }^\circ\text{C}$ at a heat flux of $1,300\text{ W}\cdot\text{cm}^{-2}$.

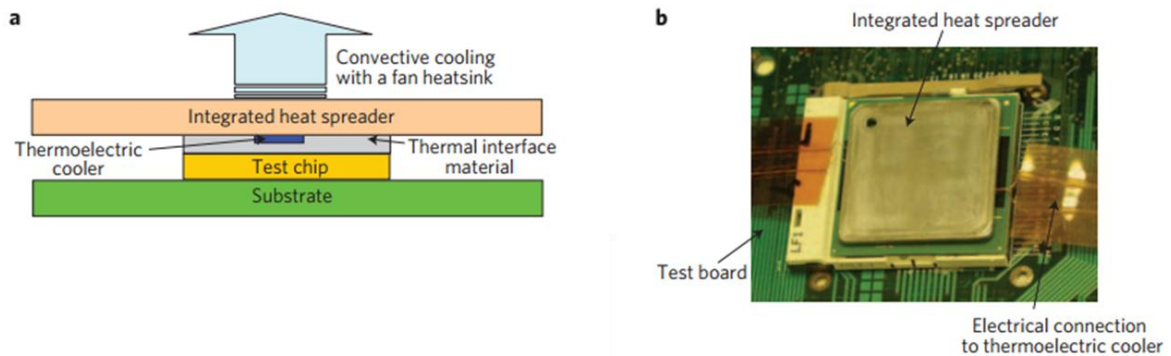


Figure 1.20: on-chip cooling device integrated on a silicon chip package. Image modified from [33].

In the case of this device also it could also be interesting for different reasons if the thermoelectric material employed was based on Si. To cite some of those, fewer production steps could be necessary, since the thermoelectric cooler could be grown directly on the chip. Also, it would be more interesting in terms of environmental care since no toxic elements would be employed (such as Bi and Te).

2.3.c - Thin film thermoelectric sensors

The last field of application for thermoelectric thin film devices is the one of thermal microsensors. These devices have the advantage of being reliable, inexpensive and produced using integrated circuit technology. Even though these devices work basically measuring the changings of the potential created by a changing of temperature via the Seebeck effect, they are often employed to measure non-thermal variables, such as radiation, pressure, position, flow and chemical reactions [34–36].

This is achieved by two transduction steps. The first one is the transduction of non-thermal to thermal signals, and the second one is the transduction of thermal to

electrical signals, which is accomplished through the thermoelectric device. Another advantage of this method is that the power needed for creating the electrical signal comes directly from the thermal signal, thus no external power is necessary [35].

Examples of already existing integrated thermoelectric microsensors include IR-radiation, vacuum, gas flow and heat flux sensors. Different materials have been proposed for these sensors, such as Bi_2Te_3 and Sb_2Te_3 films but also silicon, silicon/germanium and multi quantum wells structures (MQW). Lower performances were observed for Si-based devices, mostly because of their large thermal conductivity, but these materials are still interesting because of their technological potential [34].

The main problem cited (high thermal conductivity) could be avoided by reducing the material's thermal conductivity via nanostructuration, which is the next topic of this document.

As an example, a recent work has been published by Ziouche et al. in reference [37] showing the fabrication of a planar infrared microsensors (μSIR) using a CMOS technology employing as thermoelectric materials SiGe-based QDSL grown by CVD. Very interesting results were obtained, and the authors observed a sensitivity improvement of around 28% due to the material nanostructuration.

3 - Increasing the thermoelectric properties via nanostructuration

The establishment of thermoelectric materials science was accomplished in the middle of the XX century with the understanding of the figure of merit ZT and the development of functional thermoelectric devices and materials, mostly based on Bi_2Te_3 .

Even though niche applications were developed, only incremental gains were obtained on the ZT of the employed materials, without new breakthrough discoveries that could direct the scientific research towards a higher ZT.

In the 90's decade however new proposals were made, and a big hope of increasing the performance of thermoelectric materials was lied on the advent of nanotechnology. By nanostructuring the materials two major contributions to the increase of the ZT were thought to be possible, the first one is the increase of the thermoelectric power factor by quantum confinement effects and the second one is the decreasing of the thermal conductivity by phonon scattering.

3.1 - Power factor improvement

In the year of 1993 a work was published [4], containing theoretical studies showing that great increases of the ZT could be obtained by the nanostructuration of materials, providing the theoretical basis and encouraging further researches on this field.

The basic phenomenon allowing the increase of the Seebeck coefficient comes from the changing of the density of states (DOS) of the material when the size is reduced from a 3-D solid to quantum wells (2-D), nanowires (1-D) or quantum dots (0-D), as represented in Figure 1.21.

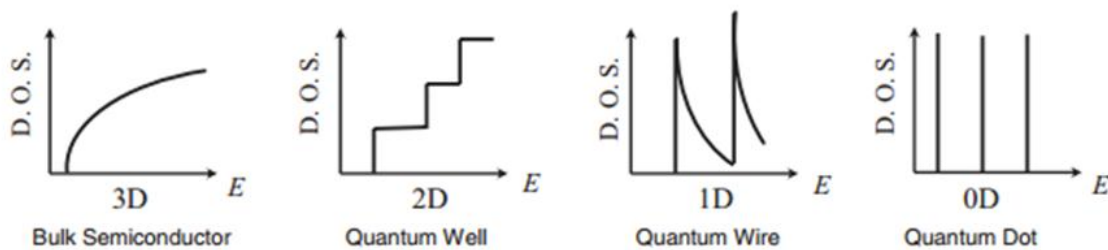


Figure 1.21: Electronic density of states for different structured materials. Image from [38].

A possible theory is that the changes on the material's density of states causes a higher asymmetry around the Fermi level between the hot and cold electrons energy, resulting on an higher average carriers energy and larger number of carriers, leading to an large Seebeck coefficient and electrical conductivity. However, until nowadays some controversy exists on whether the Seebeck coefficient improvement is possible or not by nanostructuring the material, with the possible mechanisms for that not being fully understood [39].

Several groups attempted to validate this theory by producing Quantum Well SuperLattices (QWSL) structures of different thermoelectric materials such as $\text{Bi}_2\text{Te}_3/\text{Sb}_2\text{Te}_3$, $\text{PbTe}/\text{PbSe}_x\text{Te}_{1-x}$, $\text{GaAs}/\text{Al}_x\text{Ga}_{1-x}\text{As}$ and others [39]. For example, for the materials PbTe/Te and PbTe/PbSe , claims were made of a measured increase of the Seebeck coefficient [40]. However, some discussions have been made stating that actually no increasing was observed and the observed values came actually from calculation errors. Some results have also been published concerning the observations of electron filtering, but at the same time a reduction of the electronic conductivity was observed, canceling the effect over the global figure of merit of the material [39].

Even if some controversy exist related to the changes on the Seebeck coefficient when nanostructuring occurs, when researchers begun trying to verify these theories by creating experimental low-dimensional materials, an interesting factor was observed, the reduction of the thermal conductivity when compared to bulk materials.

This phenomenon, which was not the initial motivation for nanostructuring thermoelectric materials became the core of one of the major research field nowadays for increasing the materials figure of merit.

3.2 - Thermal conductivity reduction

The basic idea of the research on the increase of the materials' ZT is to decouple the thermal conductivity to the electrical conductivity. In order to do this, a further study on the thermal conductivity is made. On Equation 1.22 it was shown the contribution of the phonons relaxation time " τ " to the lattice thermal conductivity " λ_l ". The relaxation time depends on the collision mechanisms, which scatter the phonons responsible for the heat transport.

The relaxation time can be divided in different parts, corresponding to the different scattering sources present in a material, as described by the Matthiesen law:

$$\tau^{-1} = \tau_a^{-1} + \tau_d^{-1} + \tau_{np}^{-1} + \tau_{gb}^{-1} \quad 1.25$$

Where τ_a is the intrinsic inharmonic contribution, τ_d is the solid solution contribution, τ_{np} is the contribution from nanoparticles inside the matrix and τ_{gb} is the contribution due to grain boundaries.

By nanostructuring the material it can thus be possible to change the thermal conductivity by creating new interfaces with the matrix.

It should be noticed that the relative size of each one of these defects will cause a different interaction with different frequency phonons. Long wavelength phonons will mostly interact with grain boundaries and nanometric inclusions and short wavelength phonons will interact mostly with atomic defects such as alloying and dopant atoms (Figure 1.22).

In the case of polycrystalline materials, the grain boundary acts as a natural scattering site for phonons but also for electrons. This explains why polycrystalline materials have typically a smaller thermal and electrical conductivity than a monocrystalline solid with the same doping level and stoichiometry.

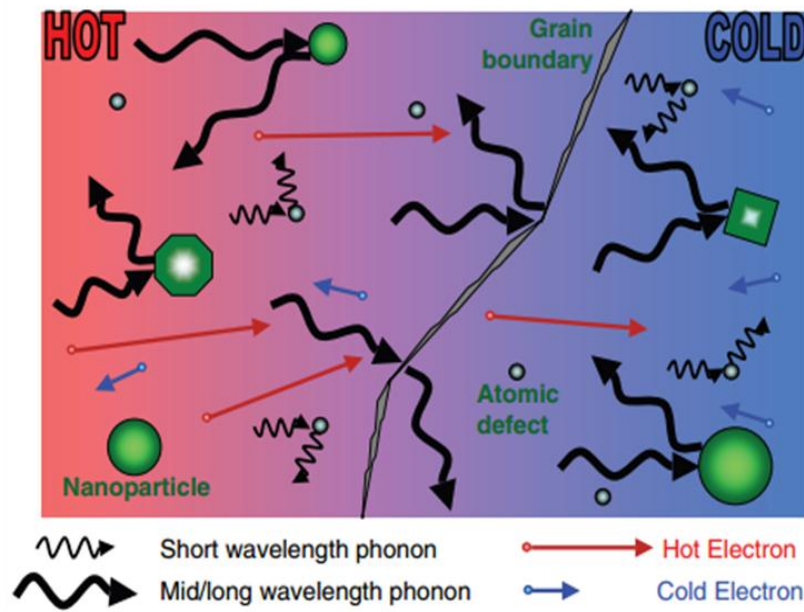


Figure 1.22: Schematic representation of the movement of phonons and electrons inside a thermoelectric material. Image from [39].

In 2008, two studies [41,42] were published showing a reduction of the room temperature thermal conductivity of up to two-fold for silicon-germanium alloys having nano-sized grains when compared to the RTG material. These results were observed both for “p” and “n” materials (Figure 1.23). By decreasing the grain size, more grain boundaries per volume of material exist, and thus more scattering sites. Moreover, no important changes on the electrical conductivity or Seebeck coefficient were observed, leading to a substantial increase of the materials “ZT”.

Still considering polycrystalline solids, a further reduction of the thermal conductivity have been reported by including nanoparticles inside a thermoelectrics materials matrix.

Two examples can be cited, the first one is the reduction of up to 1.5-fold of the room temperature thermal conductivity of sodium-doped PbTe with the incorporation of nanometric SrTe [43].

Considering silicon-germanium, a theoretical work was published [44] where the authors demonstrated that by including silicide quantum dots (QD) inside a monocrystalline $\text{Si}_{50}\text{Ge}_{50}$ matrix a reduction of up to four-fold on the thermal conductivity of the matrix could be obtained without changing the electrical conductivity (Figure 1.24).

3 - Increasing the thermoelectric properties via nanostructuring

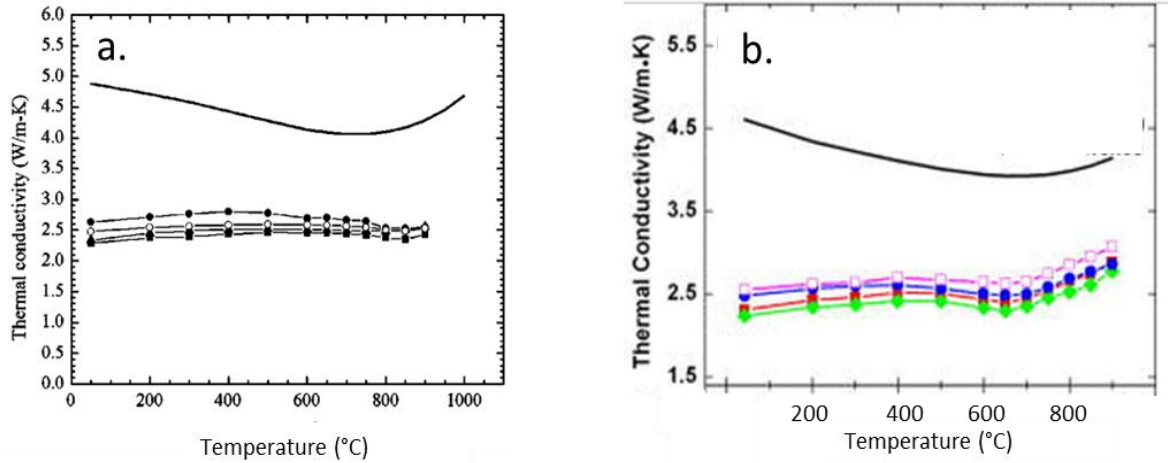


Figure 1.23: Thermal conductivity of nanostructured Si-Ge alloys (lower curves) and the RTG reference (upper curve) for “p” type material (a) and “n” type (b). Images modified from [41] for (a) and [42] for (b).

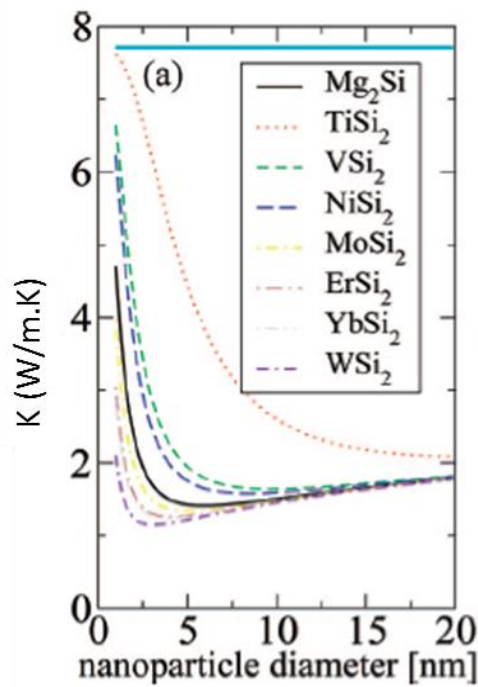


Figure 1.24: Reduction of the thermal conductivity of polycrystalline $Si_{50}Ge_{50}$ with the inclusion of around a volumetric fraction of 3.4% of silicide nanoparticles. The blue line corresponds to the conductivity of pure SiGe. Image modified from [44].

A recent work was published by Favier et al. [45], inspired by the works of Mingo et al. The author evaluated the role of the inclusion of nanometric particles of metal

silicides (MoSi_2) both for a “p” and “n” doped polycrystalline $\text{Si}_{91}\text{Ge}_{09}$ matrix. Even though the Ge content and the matrix crystallinity were not the same as those for the theoretical works, the authors observed a reduction of the thermal conductivity for the composite materials leading to an increase on the material’s ZT.

The strategy adopted for the present thesis was the same employed by Favier, i.e., the inclusion of nanometric metal silicides particles inside the Si-Ge matrix. The basic difference is that Favier studied this material using bulk (polycrystalline) structures and for this work a thin film (mono and polycrystalline) approach was employed. However, due to the lack of references and works similar to ours, these results will serve as a comparison to the results presented in Chapter 3.

4 - Quantum wells and quantum dots superlattices

In the present thesis the strategy employed in order to include silicides QD in a thin film SiGe matrix was to produce a superlattice material, more precisely a quantum dot superlattice (QDSL). A description of the techniques employed to grow this material is presented in Chapter 2.

In order to better understand what these structures are, a description of the fundamentals of confined semiconductors structures will be presented. Next, examples of general applications will be presented and latter a review concerning materials produced for thermoelectric applications.

4.1 - Introduction to quantum confined structures and superlattices

Basically a quantum confined structure consists in one in which the movement of electrons or holes is restricted in certain directions [46]. The simplest model for treating this situation is the “particle in a box” solution for one dimension semiconductors.

First consider a particle inside an infinite potential well. By solving the Schrödinger equation, only certain discrete energies states are allowed for the particle, corresponding to each one of the permitted wavenumbers (Figure 1.25).

This model represents an isolated quantum well, in which the particle is confined in only one direction (2-D system). Further confinement is obtained for a nanowire (1-

D system) and for a quantum box (0-D), where the particle is confined along the three directions.

The most important feature from an application point of view for semiconductor quantum wells is the possibility of new electronic transitions between the confined discrete levels (Figure 1.26).

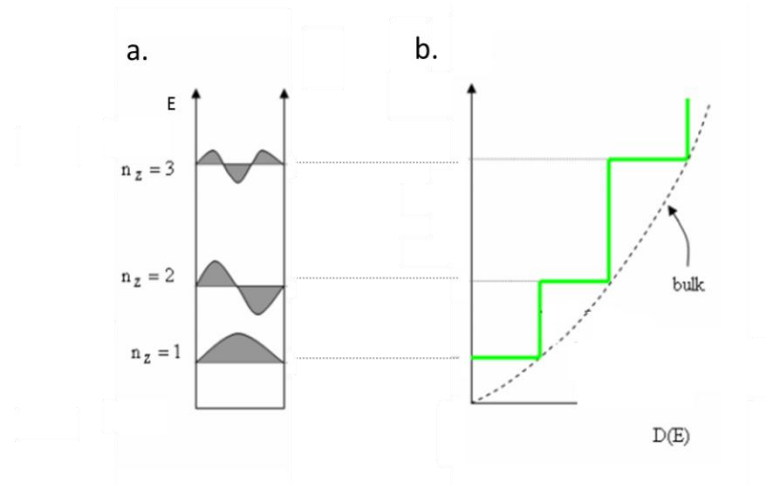


Figure 1.25: An ideal (infinite) quantum well from the “particle in a box” model. The quantization of the wave function (a) and the DOS compared to a bulk material (b) are also represented. Image modified from [47].

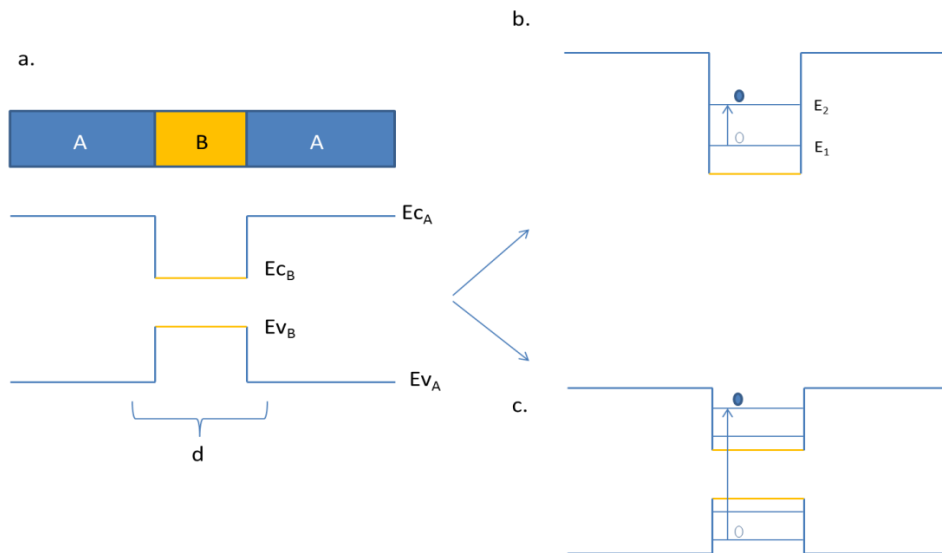


Figure 1.26: Schematic representation of a Quantum well made of materials “A” and “B” showing the resulting band diagram (a). An inter-sub-band transition (b) and an inter-band transition (c).

In order to take advantage of these features for practical applications, a quantum well superlattice (QWSL) is more suitable, formed by repeating the quantum well structure successively. This type of structure using a semiconductor material was first proposed by Esaki and Tsu [48] in 1970.

By further confining the material's charge carriers over the three dimensions, a quantum dot is obtained. This is practically achieved by the growth of crystals in the nanometer size.

As shown in Figure 1.21, confining the electrons in a quantum dot will cause the apparition of discrete possible energy values for the charge carriers, much like the energy values for an atom. By the same mechanism that for quantum wells, it is possible to tailor up to a certain point the position of the permitted energy levels of the material by controlling the size of the quantum dot. Quantum dots are generally employed on the form a dispersion of the particles in a solvent or in a similar way of quantum well superlattices. In this case, the material is called quantum dot superlattice (QDSL) and is obtained by successively stacking quantum dots inside a matrix.

In the case of this thesis, QDSL structures were produced. There is however a difference compared to "classical" QDSL in the sense that the expected effect of the inclusion of QD inside the SiGe matrix is not related to the possible energy transitions but rather to the effect of the QD on the thermal conductivity and on the Seebeck effect as already discussed. Even if the materials produced were referred as QDSL, the thin films can also be thought as a composite material with nanometric inclusions.

4.2 - General applications for quantum wells and quantum dots

In this section the traditional optoelectronic applications of quantum wells and quantum dots will be explained. The main feature allowing this kind of applications is, as cited before, the particular band structure and allowed electronic transitions of these structures.

As examples we could cite the laser and light emitting diodes based on interband transitions. Among these applications the vertical-cavity surface emitting laser (VCSEL) is considered to have several advantages over conventional devices, such as simpler fabrication, enhanced coupling with optical fibers and low threshold currents. Another type of laser that employs QWSLs is the quantum cascade laser.

It has been suggested that by using a QDSL instead of QWSL, an increase of the device properties could be obtained by eliminating the movement of charge carriers along the quantum well plane [49].

In opposition to quantum wells, quantum dots can be also employed in the form of “free” nano-materials, i.e., not necessarily in the form of a superlattice. Possible applications are the use of QD markers for biological labeling, low-energy photons infra-red detectors [50] and for qubit memories for storing information via quantum states [51]. An example is the CdSe nanocrystals used as biological marker (Figure 1.27). By controlling the size of these nanoparticles dispersed in a suspension (colloid) and thus controlling the energy of electronic transitions, these particles can be detected by fluorescence methods [52,53].

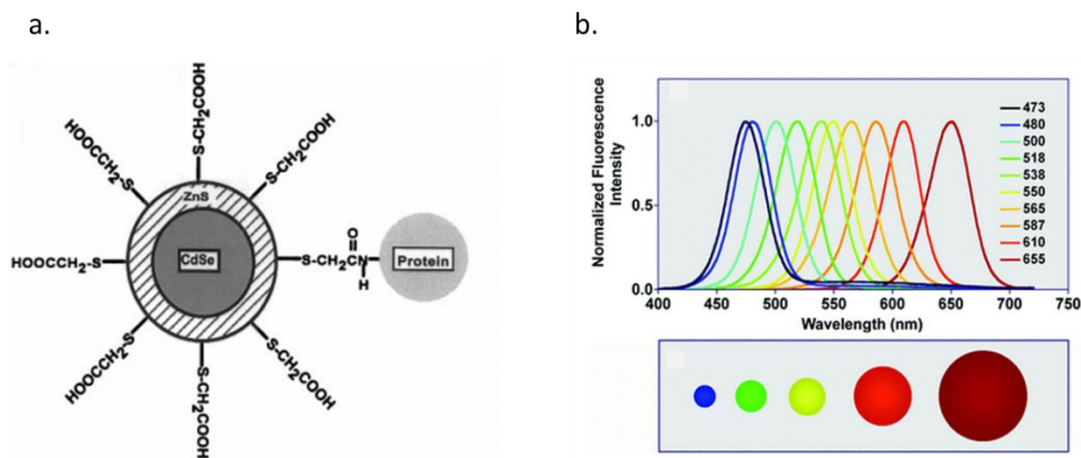


Figure 1.27: A core shell quantum dot for biomolecules detection (a) and the fluorescence energy as a function of the quantum dot size (b). Images modified from [52] and [54].

Different growth methods exist for QD and QW. For growing superlattices of QW and QD similar growing devices are employed, and the most commonly employed techniques are the MBE and CVD. QD can also be employed and grown in an isolated form rather than inside a superlattice. In this case they are typically grown by colloidal synthesis in a liquid medium.

4.3 - Thermoelectric applications for QWSL's and QDSL's

As it has been discussed in section 3 - , two major contributions are expected when a thermoelectric material is nanostructured: an increase of the power factor due

to the increase of the asymmetry of the differential conductivity and a reduction of the material's thermal conductivity due to phonon scattering.

Actually there exist a spectrum of phonons of different frequencies and mean free paths [55]. These phonons will preferably scatter in impurities of the same size magnitude, and thus an optimal configuration should present different size of defects, such as nanoparticles, interfaces and impurities atoms. Moreover, ideally these defects should not disturb the electrical conduction.

Optoelectronic applications for QW and QDSL take advantage on the possible energy transitions due to quantification effects. Thus, all materials employed are semiconductors. For thermoelectric applications, however, as the main goal is to reduce the thermal conductivity or increase the power factor, other materials can be employed, in particular in the case of QDSL. In this case, nanodots from other natures can be used, such as metallic and semi metallic materials. Because of the growth techniques, restrictions exist concerning the thickness of the devices. In practice, QWSL and QDSL are only employable for building thin films thermoelectric devices (section 2.3 -).

In recent years, different authors have published results showing an effective reduction of the materials lattice thermal conductivity both for QWSL and QDSL structures. Published results often report thermal conductivities beyond the alloy limit. This limit consists on the reduction of the thermal conductivity by introducing a different size atom in the structure (alloying). Considering the changes on the Seebeck coefficient, the role of the quantum confinement have not yet been clearly demonstrated in practice and the main improvements observed by nanostructuring materials came from the reduction of the thermal conductivity [39].

It should be noticed that for QWSL the reduction of the thermal conductivity is related do the cross plane component, i.e., along the direction perpendicular to the thin film surface.

A very complete revue work has been published by Vineis et al in [39] where discussions are presented considering the possible effects on the thermoelectric properties when the materials are structured as a QWSL or a QDSL. The authors also present a description of the most interesting QWSL and QDSL materials in terms of thermoelectric properties, represented in Figure 1.28.

A description of the growth methods, type of structure and reduction on the thermal conductivity for some of the materials discussed by Vineis et al are presented in Table 1.1.

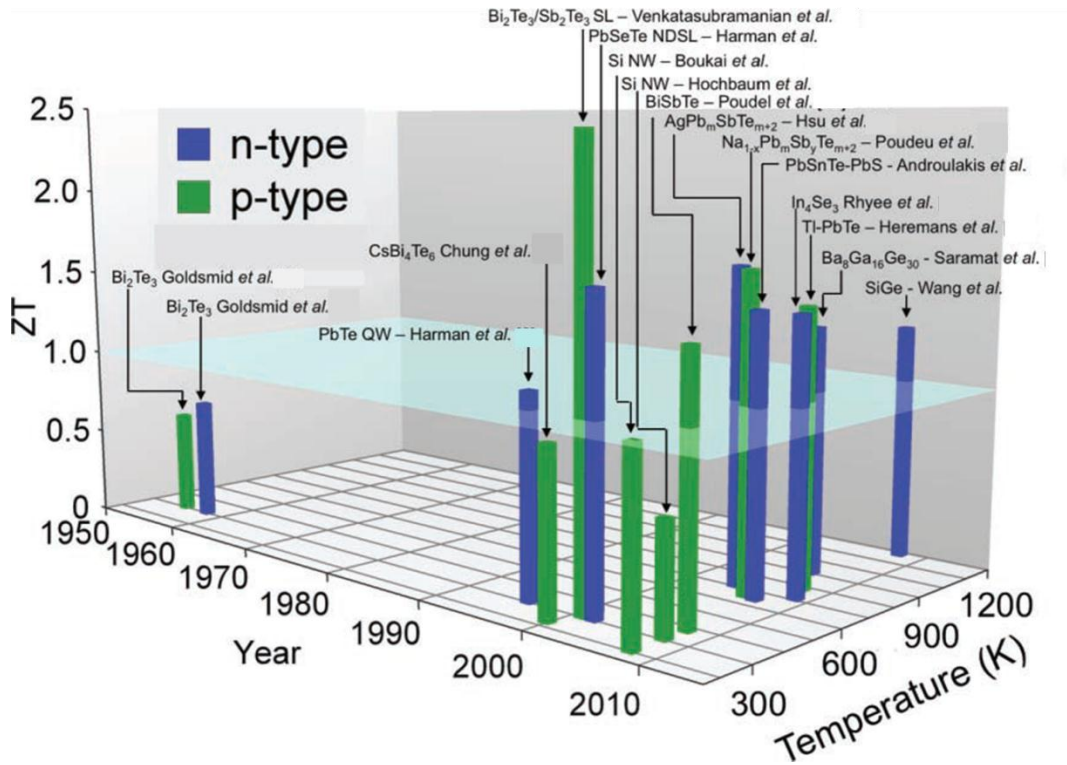


Figure 1.28: Thermoelectric figure of merit ZT as a function of temperature and year. According to Vineis et al, all the materials presenting a ZT >1 present some form of nanostructuration. Image modified from [39].

Table 1.1: The thermal conductivity, growth method and nanostructures size for different superlattices for thermoelectric applications.

Materials	Type of structure	Thermal conductivity (W.m ⁻¹ K ⁻¹)	reduction factor ($\lambda_{\text{alloy}}/\lambda_{\text{SL}}$)	Growth method	Reference
Bi ₂ Te ₃ /Sb ₂ Te ₃	QWSL	0,2	2,2	MOCVD	[56]
PbTe/PbTe _{0.75} Se _{0.25}	QWSL	0,5	2,0	evaporation	[57]
AlAs/GaAs	QWSL	3,1	4,0	MBE	[58]
Si/Ge	QWSL	3,0	2,5	CVD	[59]
SiGe/Si	QWSL	2,8	1,1	CVD	[60]
PbTe/PbSe	QDSL	0,3	6,0	MBE	[61]
ErAs/In _{0.53} Ga _{0.47} As	QDSL	3,0	2,0	MBE	[62]
GeSi/Si	QDSL	10	13,0	MBE	[63]

The higher ZT obtained to my knowledge concerning nanostructured materials was obtained by Venkatasubramanian et al. in reference [56]. The studied material was a thin film composed of Bi_2Te_3 / Sb_2Te_3 superlattices grown on GaAs by metallorganic chemical vapor deposition (MOCVD) [64]. A ZT of 2.4 was obtained at 300 K for the “p” type material, with a thermal conductivity of $0.22 \text{ W} \cdot (\text{m} \cdot \text{K})^{-1}$ for a $10 \text{ \AA} / 50 \text{ \AA}$ superlattice. This represents a reduction of around 2.2 times compared to the $\text{Bi}_{0.5}\text{Sb}_{1.5}\text{Te}_3$ alloy and can be compared to the minimum theoretical thermal conductivity for Bi_2Te_3 material.

Even if this material presented a remarkable ZT, there are still controversies among the research community concerning the validity of the presented results. Moreover, it is still a variation of the “classical” thermoelectric materials, based on the toxic/rare elements Bi and Te.

Considering thin films based on Si and SiGe materials, the first work on the measurement of the thermal properties of Si and SiGe QWSL was the study [59] published by Lee et al.

The authors produced a QWSL structure made of alternating Si and Ge layers using the CVD method. The best obtained results concerned a measured cross-plane thermal conductivity of around $3 \text{ W} \cdot (\text{m} \cdot \text{K})^{-1}$ at room temperature for layers of 140 and 275 \AA thick against around $7.5 \text{ W} \cdot (\text{m} \cdot \text{K})^{-1}$ for a reference $\text{Si}_{0.85}\text{Ge}_{0.15}$, i.e., a reduction factor of around 2.5 times. For this work, however, no information concerning the electrical conductivity and the Seebeck coefficient was provided.

Savelli et al. have also published a work [60] showing the effect of the nanostructuration via the production of a QWSL composed of alternating SiGe and Si layers, both mono and polycrystalline. The best obtained results were consisted on a polycrystalline sample with SiGe and Si periods of 8 nm. In this case, a thermal conductivity of $2.8 \text{ W} \cdot (\text{m} \cdot \text{K})^{-1}$. Concerning the monocrystalline sample, the best result was a QWSL with a Si and SiGe periods of 4 and 8 nm respectively and a thermal conductivity of $5 \text{ W} \cdot (\text{m} \cdot \text{K})^{-1}$.

A similar work [63] was produced by Bao et al. but focused on the production of QDSL. It consisted in the inclusion of $\text{Ge}_x\text{Si}_{1-x}$ in a silicon matrix grown by Molecular Beam Epitaxy (MBE) using a silicon wafer as substrate. The quantum dots density was about $3 \times 10^9 \text{ cm}^{-2}$ and the average measured base diameter was 40 nm. Considering the carriers mobility, a decrease was observed using Hall effect measures compared to bulk Si and Ge, probably due to charging effects, surface disorder or alloy scattering effects. However the authors consider the overall mobility high enough for the material to be considered a good candidate for thermoelectric applications. It should be pointed however that no Seebeck coefficient measurements were performed. Considering the thermal conductivity, the authors measured values of around $10 \text{ W} \cdot (\text{m} \cdot \text{K})^{-1}$ using the 3ω technique, which is around 13 times slower than the values for bulk silicon.

These two works show clearly an improvement of the thermoelectric properties when the materials are nanostructured, whether by producing QWSL or QDSL. It should be noticed however that for the QDSL work a pure Si reference sample was not produced by the authors, which would have been interesting in order to compare the thermoelectric properties of samples grown and measured using the same techniques.

These two works can be considered as the inspiration of a few other works on the growth of Si and Ge or SiGe QWSL and QDSL. Other published works concerning variations on these theme can be found in [65,66]

It is interesting to notice from the works described above and in Table 1.1 that different materials and types of nanostructuration produced a reduction on the materials thermal conductivity and thus a possible improvement on the thermoelectric properties.

However, for a study to be considered complete two main features are important, and were performed during the present thesis. First, the electrical conductivity and the Seebeck coefficient should also be measured along with the thermal conductivity in order to evaluate if the reduction of the last will not disturb the formers. Second, a reference sample without nanostructuration should be produced and characterized using the same techniques in order to minimize possible variations.

5 - Conclusion

In this chapter the fundamentals of thermoelectricity were presented, along with an explanation of the different thermoelectric phenomenon such as the Seebeck, Peltier and Thomson effects. Along with these, the role of the charge carriers concentration was discussed when semiconductors are employed as thermoelectric materials. This type of materials has advantages as thermoelectric materials because of their relative low thermal conductivity and possible high electrical conductivity obtained by doping. A brief discussion was performed in order to present the state-of-the-art materials and the actual and potential thermoelectric applications, both considering thin films and bulk devices.

Further, the nanostructuration was presented as a way of improving the material's ZT, due to possible effects both on the Seebeck coefficient and on the thermal conductivity. The nanostructuration can be employed both for bulk materials (by including nanoparticles inside the matrix) and for thin films, particularly by producing QWSL and QDSL.

A review was presented on the principles and applications for QWSL and QDSL, with an emphasis on thermoelectric applications. Different authors reported

improvements on the thermoelectric properties of thin films where a nanostructuration of this kind was performed.

In this it was chosen to deepen the study on SiGe-based materials, due to their low toxicity and compatibility with the microelectronics industry. To my knowledge, it is the first time thin films QDSL are produced using silicides as inclusions. If the obtained results are compatible with theoretical work of Mingo et al in reference [44], an increase of up to a factor 4 of the material's ZT could be obtained.

This material will be produced using an industrial CVD tool, which has the advantage of allowing an industrial production.

The materials obtained will be compared to references produced and characterized using the same techniques. The results of the thin films SiGe-based materials produced by Lee et al. and Bao et al. will be employed in order to compare the results of this thesis with literature references, even if the nature of the nanostructuration is not the same.

Bulk materials will also be employed as a reference to the performed measurements. Some relevant works concerning bulk SiGe materials are the ones presented by Wang et al in [42] and Joshi et al. in [41]. The work of Favier et al. in [45] is of great importance because it is the only reported practical work where the inclusion of metallic silicides are studied as inclusion in a SiGe matrix for thermoelectrical applications.

In the next chapter, the growth of metals silicides/SiGe QDSL using a CVD tool will be presented, as well as a complete study relating the obtained quantum dots size and densities with the growth parameters.

REFERENCES

- [1] T. J. Seebeck and A. v (Arthur) Oettingen, *Magnetische Polarisation der Metalle und Erze durch Temperatur-Differenz, 1822-1823. Hrsg. von A.J. v. Oettingen.* Leipzig W. Engelmann, 1895.
- [2] "The Project Gutenberg eBook of Hawkins Electrical Guide, Number One, by Nehemiah Hawkins." [Online]. Available: <http://www.gutenberg.org/files/38384/38384-h/38384-h.htm>. [Accessed: 04-Mar-2014].
- [3] E. Velmer, "Thomas Johann Seebeck (1770-1831).," *Est. J. Eng.*, vol. 13, no. 4, 2007.
- [4] L. D. Hicks and M. S. Dresselhaus, "Effect of quantum-well structures on the thermoelectric figure of merit," *Phys. Rev. B*, vol. 47, no. 19, pp. 12727–12731, May 1993.
- [5] D. Rowe, Ed., *CRC Handbook of Thermoelectrics*. CRC Press, 1995.
- [6] C. B. Vining, "An inconvenient truth about thermoelectrics," *Nat. Mater.*, vol. 8, no. 2, pp. 83–85, 2009.
- [7] H. Fang and Y. Wu, "Telluride nanowire and nanowire heterostructure-based thermoelectric energy harvesting," *J. Mater. Chem. A*, vol. 2, no. 17, p. 6004, 2014.
- [8] D. Hauser, "Elaboration de super-réseaux de boîtes quantiques à base de SiGe et développement de dispositifs pour l'étude de leurs propriétés thermoélectriques," *UNIVERSITE DE GRENOBLE*, 2011.
- [9] A. Jacquot, "Ingénierie des Matériaux et des Microgénérateurs Thermoélectriques," *Institut National Polytechnique de Lorraine - INPL*, 2003.
- [10] H. J. Goldsmid, *Introduction to thermoelectricity*, vol. 121. Springer, 2009.
- [11] M. Lippmann, *Environmental Toxicants: Human Exposures and Their Health Effects*. John Wiley & Sons, 2009.
- [12] M. C. Yarema, "Acute Tellurium Toxicity From Ingestion of Metal-Oxidizing Solutions," *PEDIATRICS*, vol. 116, no. 2, pp. e319–e321, Aug. 2005.
- [13] M. I. Fedorov, "Thermoelectric silicides: past, present and future," *J. Thermoelectr.*, pp. 51–60, 2009.
- [14] W. Liu, X. Tan, K. Yin, H. Liu, X. Tang, J. Shi, Q. Zhang, and C. Uher, "Convergence of conduction bands as a means of enhancing thermoelectric performance of n-type Mg₂Si(1-x)Sn(x) solid solutions," *Phys. Rev. Lett.*, vol. 108, no. 16, p. 166601, Apr. 2012.
- [15] V.K. Zaitsev, "Thermoelectric Properties of Anisotropic MnSi_{1.75}," in *CRC Handbook of Thermoelectrics*, CRC Press, 1995.
- [16] G. J. Snyder and E. S. Toberer, "Complex thermoelectric materials," *Nat Mater*, vol. 7, no. 2, pp. 105–114, février 2008.
- [17] G. Savelli, "Etude et développement de composants thermoélectriques à base de couches minces," *Université Joseph-Fourier-Grenoble I*, 2007.
- [18] G. Nolas, "Structure, Thermal Conductivity, and Thermoelectric Properties of Clathrate Compounds," in *Thermoelectrics Handbook*, D. Rowe, Ed. CRC Press, 2005, pp. 33–1–33–8.
- [19] M. Wagner, "Simulation of Thermoelectric Devices," 2007. [Online]. Available: <http://www.iue.tuwien.ac.at/phd/mwagner/> [Accessed: 10-Mar-2014]
- [20] A. J. Minnich, M. S. Dresselhaus, Z. F. Ren, and G. Chen, "Bulk nanostructured thermoelectric materials: current research and future prospects," *Energy Env. Sci*, vol. 2, no. 5, pp. 466–479, Feb. 2009.
- [21] "Abundance of elements in Earth's crust," [Online]. *Wikipedia, the free encyclopedia*. Available: http://en.wikipedia.org/wiki/Abundance_of_elements_in_Earth's_crust/ [Accessed: 14-Mar-2014]

- [22] D. M. Rowe, "Thermoelectrics, an environmentally-friendly source of electrical power," *Renew. Energy*, vol. 16, no. 1–4, pp. 1251–1256, Jan. 1999.
- [23] G. L. Bennett, "Space nuclear power: opening the final frontier," in *4th International Energy Conversion Engineering Conference and Exhibit (IECEC)*, 2006, pp. 26–29.
- [24] A. A. Pustovalov, "Role and prospects of application of RTG on base of plutonium-238 for planetary exploration," in *Proceedings of the 5th European Conference on Thermoelectrics, Odessa, Ukraine, 2007*.
- [25] G. L. Bennett, J. J. Lombardo, R. J. Hemler, G. Silverman, C. W. Whitmore, W. R. Amos, E. W. Johnson, A. Schock, R. W. Zocher, and T. K. Keenan, "Mission of daring: the general-purpose heat source radioisotope thermoelectric generator," in *Proceedings of the 4th International Energy Conversion and Engineering Conference*, 2006, pp. 26–29.
- [26] R. Abelson, "Space Missions and Applications," in *Thermoelectrics Handbook*, D. Rowe, Ed. CRC Press, 2005, pp. 56–1–56–29.
- [27] S. B. Riffat and X. Ma, "Thermoelectrics: a review of present and potential applications," *Appl. Therm. Eng.*, vol. 23, no. 8, pp. 913–935, juin 2003.
- [28] S. Kumar, S. D. Heister, X. Xu, J. R. Salvador, and G. P. Meisner, "Thermoelectric Generators for Automotive Waste Heat Recovery Systems Part I: Numerical Modeling and Baseline Model Analysis," *J. Electron. Mater.*, vol. 42, no. 4, pp. 665–674, Apr. 2013.
- [29] H. Hachiuma and K. Fukuda, "Activities and future vision of Komatsu thermo modules," in European Conference on Thermoelectrics", *ECT2007*, [Online]. Available: <http://ect2007.its.org/system/files/u1/pdf/01.pdf>.–2007, 2007.
- [30] S. H. Choday, C. Lu, V. Raghunathan, and K. Roy, "On-chip energy harvesting using thin-film thermoelectric materials," in *2013 29th Annual IEEE Semiconductor Thermal Measurement and Management Symposium (SEMI-THERM)*, 2013, pp. 99–104.
- [31] S. H. Choday, M. S. Lundstrom, and K. Roy, "Prospects of Thin-Film Thermoelectric Devices for Hot-Spot Cooling and On-Chip Energy Harvesting," *IEEE Trans. Compon. Packag. Manuf. Technol.*, vol. 3, no. 12, pp. 2059–2067, Dec. 2013.
- [32] A. Shakouri, "Nanoscale Thermal Transport and Microrefrigerators on a Chip," *Proc. IEEE*, vol. 94, no. 8, pp. 1613–1638, Aug. 2006.
- [33] I. Chowdhury, R. Prasher, K. Lofgreen, G. Chrysler, S. Narasimhan, R. Mahajan, D. Koester, R. Alley, and R. Venkatasubramanian, "On-chip cooling by superlattice-based thin-film thermoelectrics," *Nat. Nanotechnol.*, vol. 4, no. 4, pp. 235–238, Apr. 2009.
- [34] A. Meier and F. Volklein, "Thermoelectric Microelectromechanical Systems," in *Thermoelectrics Handbook*, D. Rowe, Ed. CRC Press, 2005, pp. 47–1–47–18.
- [35] S. van Herwaarden, "Sensor applications of thermoelectric thin films," in *XVI International Conference on Thermoelectrics, 1997. Proceedings ICT '97*, 1997, pp. 47–55.
- [36] A. Hierlemann and H. Baltes, "CMOS-based chemical microsensors," *The Analyst*, vol. 128, no. 1, pp. 15–28, Dec. 2003.
- [37] K. Ziouche, G. Savelli, Z. Bougrioua, D. Hauser, P. Lejeune, P.-M. Michon, T. Lasri, and D. Leclercq, "Thermoelectric infrared microsensors based on a periodically suspended thermopile integrating nanostructured Ge/SiGe quantum dots superlattice," *J. Appl. Phys.*, vol. 116, no. 4, p. 043701, Jul. 2014.
- [38] M. S. Dresselhaus, G. Chen, M. Y. Tang, R. G. Yang, H. Lee, D. Z. Wang, Z. F. Ren, J.-P. Fleurial, and P. Gogna, "New Directions for Low-Dimensional Thermoelectric Materials," *Adv. Mater.*, vol. 19, no. 8, pp. 1043–1053, Apr. 2007.
- [39] C. J. Vineis, A. Shakouri, A. Majumdar, and M. G. Kanatzidis, "Nanostructured Thermoelectrics: Big Efficiency Gains from Small Features," *Adv. Mater.*, vol. 22, pp. 3970–3980, Sep. 2010.

- [40] T. C. Harman, D. L. Spears, and M. P. Walsh, "PbTe/Te superlattice structures with enhanced thermoelectric figures of merit," *J. Electron. Mater.*, vol. 28, no. 1, pp. L1–L5, Jan. 1999.
- [41] G. Joshi, H. Lee, Y. Lan, X. Wang, G. Zhu, D. Wang, R. W. Gould, D. C. Cuff, M. Y. Tang, M. S. Dresselhaus, G. Chen, and Z. Ren, "Enhanced thermoelectric figure-of-merit in nanostructured p-type silicon germanium bulk alloys," *Nano Lett.*, vol. 8, no. 12, pp. 4670–4674, Dec. 2008.
- [42] X. W. Wang, H. Lee, Y. C. Lan, G. H. Zhu, G. Joshi, D. Z. Wang, J. Yang, A. J. Muto, M. Y. Tang, J. Klatsky, S. Song, M. S. Dresselhaus, G. Chen, and Z. F. Ren, "Enhanced thermoelectric figure of merit in nanostructured n-type silicon germanium bulk alloy," *Appl. Phys. Lett.*, vol. 93, no. 19, p. 193121, Nov. 2008.
- [43] K. Biswas, J. He, I. D. Blum, C.-I. Wu, T. P. Hogan, D. N. Seidman, V. P. Dravid, and M. G. Kanatzidis, "High-performance bulk thermoelectrics with all-scale hierarchical architectures," *Nature*, vol. 489, no. 7416, pp. 414–418, Sep. 2012.
- [44] N. Mingo, D. Hauser, N. P. Kobayashi, M. Plissonnier, and A. Shakouri, "'Nanoparticle-in-Alloy' Approach to Efficient Thermoelectrics: Silicides in SiGe," *Nano Lett*, vol. 9, no. 2, pp. 711–715, 2009.
- [45] K. Favier, G. Bernard-Granger, C. Navone, M. Soulier, M. Boidot, J. Leforestier, J. Simon, J.-C. Tedenac, and D. Ravot, "Influence of in situ formed MoSi₂ inclusions on the thermoelectrical properties of an N-type silicon–germanium alloy," *Acta Mater.*, vol. 64, pp. 429–442, Feb. 2014.
- [46] M. Fox and R. Ispasoiu, "Quantum Wells, Superlattices, and Band-Gap Engineering," in *Springer Handbook of Electronic and Photonic Materials*, S. K. Prof and P. C. Dr, Eds. Springer US, 2007, pp. 1021–1040.
- [47] B. M. Rai, Quantum Confinement of Nanostructured Systems. *Central Michigan University*, 2005.
- [48] L. Esaki and R. Tsu, "Superlattice and Negative Differential Conductivity in Semiconductors," *IBM J Res Dev*, vol. 14, no. 1, pp. 61–65, Jan. 1970.
- [49] R. A. Suris and I. A. Dmitriev, "Quantum-dot based quantum cascade lasers: Arguments in favor," in *2011 IEEE Winter Topicals (WTM)*, Jan., pp. 43–44.
- [50] A. Lakhtakia, Ed., *The Handbook of Nanotechnology. Nanometer Structures: Theory, Modeling, and Simulation*. 1000 20th Street, Bellingham, WA 98227-0010 USA: SPIE, 2004.
- [51] M. Bayer, P. Hawrylak, K. Hinzer, S. Fafard, M. Korkusinski, Z. R. Wasilewski, O. Stern, and A. Forchel, "Coupling and Entangling of Quantum States in Quantum Dot Molecules," *Science*, vol. 291, no. 5503, pp. 451–453, Jan. 2001.
- [52] W. C. W. Chan and S. Nie, "Quantum Dot Bioconjugates for Ultrasensitive Nonisotopic Detection," *Science*, vol. 281, no. 5385, pp. 2016–2018, Sep. 1998.
- [53] M. Bruchez Jr, M. Moronne, P. Gin, S. Weiss, and A. P. Alivisatos, "Semiconductor nanocrystals as fluorescent biological labels," *Science*, vol. 281, no. 5385, pp. 2013–2016, Sep. 1998.
- [54] A. M. Smith and S. Nie, "Chemical analysis and cellular imaging with quantum dots," *Analyst*, vol. 129, no. 8, pp. 672–677, Jul. 2004.
- [55] A. Shakouri, "Recent Developments in Semiconductor Thermoelectric Physics and Materials," *Mater. Res.*, vol. 41, no. 1, p. 399, 2011.
- [56] R. Venkatasubramanian, E. Siivola, T. Colpitts, and B. O'Quinn, "Thin-film thermoelectric devices with high room-temperature figures of merit," *Nature*, vol. 413, no. 6856, pp. 597–602, Oct. 2001.

- [57] J. C. Caylor, K. Coonley, J. Stuart, S. Nangoy, T. Colpitts, and R. Venkatasubramanian, "Developing PbTe-based superlattice structures with enhanced thermoelectric performance," in *International Conference on Thermoelectrics, ICT, Proceedings*, 2005, vol. 2005, pp. 492–494.
- [58] W. S. Capinski and H. J. Maris, "Thermal conductivity of GaAs/AlAs superlattices," *Phys. B Condens. Matter*, vol. 219–220, no. 1–4, pp. 699–701, 1996.
- [59] S.-M. Lee, D. G. Cahill, and R. Venkatasubramanian, "Thermal conductivity of Si–Ge superlattices," *Appl. Phys. Lett.*, vol. 70, no. 22, pp. 2957–2959, Jun. 1997.
- [60] G. Savelli, M. Plissonnier, V. Remondière, J. Bablet, and J.-M. Fournier, "An innovating technological approach for Si–SiGe superlattice integration into thermoelectric modules," *J. Micromechanics Microengineering*, vol. 18, no. 10, p. 104002, Oct. 2008.
- [61] T. C. Harman, P. J. Taylor, M. P. Walsh, and B. E. LaForge, "Quantum Dot Superlattice Thermoelectric Materials and Devices," *Science*, vol. 297, no. 5590, pp. 2229–2232, Sep. 2002.
- [62] W. Kim, S. L. Singer, A. Majumdar, D. Vashaee, Z. Bian, A. Shakouri, G. Zeng, J. E. Bowers, J. M. O. Zide, and A. C. Gossard, "Cross-plane lattice and electronic thermal conductivities of ErAs:InGaAsInGaAlAs superlattices," *Appl. Phys. Lett.*, vol. 88, no. 24, 2006.
- [63] Y. Bao, W. L. Liu, M. Shamsa, K. Alim, A. A. Balandin, and J. L. Liu, "Electrical and Thermal Conductivity of Ge / Si Quantum Dot Superlattices," *J. Electrochem. Soc.*, vol. 152, no. 6, pp. G432–G435, Jun. 2005.
- [64] R. Venkatasubramanian, "Lattice thermal conductivity reduction and phonon localizationlike behavior in superlattice structures," *Phys. Rev. B*, vol. 61, no. 4, pp. 3091–3097, Jan. 2000.
- [65] S. T. Huxtable, A. R. Abramson, C.-L. Tien, A. Majumdar, C. LaBounty, X. Fan, G. Zeng, J. E. Bowers, A. Shakouri, and E. T. Croke, "Thermal conductivity of Si/SiGe and SiGe/SiGe superlattices," *Appl. Phys. Lett.*, vol. 80, no. 10, pp. 1737–1739, Mar. 2002.
- [66] Z. Aksamija and I. Knezevic, "Reduced Thermal Conductivity in SiGe Alloy-Based Superlattices for Thermoelectric Applications," in *Silicon-Germanium Technology and Device Meeting (ISTDM), 2012 International*, 2012, pp. 1–2.

CHAPTER II

The CVD growth of Quantum Dots SuperLattices

1 - INTRODUCTION	61
2 - THE CVD GROWTH	61
2.1 - GENERALITIES	62
2.2 - NUCLEATION AND GROWTH MECHANISMS	63
2.3 - THE GROWTH RATE LIMITING FACTOR	65
2.4 - OUR CVD TOOL	66
2.5 - SI AND SiGe THIN FILM GROWTH	68
2.6 - TI AND MO PRECURSORS	72
2.7 - DELIVERY SYSTEM FOR NON-GASEOUS PRECURSORS	73
2.7.a - TiCl ₄ evaporation system.....	75
2.7.b - MoCl ₅ sublimation.....	76
3 - THE GROWTH OF TI-BASED SILICIDE/SiGe QDSL	77
3.1 - INTRODUCTION	77
3.2 - CVD DEPOSITION OF TI-BASED NANO-ISLANDS	79
3.2.a - Role of deposition temperature.....	82
3.2.b - Role of the substrate Ge content.....	86
3.2.c - Role of deposition duration.....	88
3.2.d - Role of the precursor partial pressure.....	90
3.2.e - Role of substrate crystallinity	91
3.2.f - Conclusion.....	92
3.3 - EMBEDDING THE NANO-ISLANDS AND FORMATION OF QUANTUM DOTS	94
3.3.a - Low temperature embedding: nanowires growth.....	94
3.3.b - High temperature embedding	97
3.4 - TI/SiGe QDSL GROWTH	99

4 - THE GROWTH OF MO-BASED SILICIDE/SiGe QDSL	102
4.1 - INTRODUCTION	102
4.2 - CVD DEPOSITION OF MO-BASED NANO-ISLANDS	103
4.2.a - Role of deposition temperature.....	104
4.2.b - Role of Ge content	106
4.3 - Mo/SiGe QDSL GROWTH.....	107
5 - CONCLUSION	108
REFERENCES	110

1 - Introduction

As presented in the previous chapter, the main objective of this work is to produce QDSL of metallic silicides quantum dots embedded in a doped SiGe matrix. An improvement of the thermoelectric properties of the material is theoretically expected, both by the increase of the power factor and the reduction of the thermal conductivity.

In Chapter 2 the aspects of the QDSL growth using a Chemical Vapor Deposition (CVD) tool will be presented. First, a description of the CVD method and growth mechanisms is given. The CVD tool employed during this work and the basics of SiGe growth will be presented followed by the modifications needed to introduce non-gaseous precursors. These precursors, TiCl_4 and MoCl_5 , were employed to provide Ti and Mo atoms to directly grow silicide quantum dots onto silicon wafers. Several studies were performed in order to determine the role of the different deposition parameters (deposition temperature, partial pressure of employed gases) as well as the substrate Ge content on the morphology of the obtained quantum dots.

The choice of the deposition parameters was essential to control the size and distribution of the obtained quantum dots. The control of these parameters is important in order to produce QDSL similar to those theoretically studied by Mingo et al. [1], and thus to compare the thermoelectric properties of the obtained materials with the theory.

The final part of this chapter presents the QDSL grown using the in-situ deposition of quantum dots embedded with doped SiGe. The results of the physical and thermoelectrical characterizations as well as discussions linking the measured properties to the growth of the obtained materials will be further presented in Chapter 3.

2 - CVD growth

The chosen method employed to grow QDSL in this work was the CVD process. This method is the most common one employed to grow high quality thin films (2-D structures) on different substrates, but can also be used to produce 1-D materials such as nanowires [2] and 0-D such as quantum dots and their superlattices [3–5].

Other methods typically employed to produce nanostructured materials are the Molecular Beam Epitaxy (MBE), which produces the higher quality materials but is a slow and expensive process, the Physical Vapor Deposition (PVD), the

electrodeposition technique and variations of the CVD method such as metallorganic CVD (MOCVD) and Plasma Enhanced CVD (PECVD).

There are two main advantages for using the CVD process in the case of the materials employed in this work: the first one is its versatility and the second is the possibility to transfer the experimental results to an industrial-scale production. Moreover, this method is less expensive and needs less deposition time compared to MBE.

By using a modified industrial CVD, all the steps employed to grow and dope the QDSL were made in-situ. By changing the process recipes, different Ge contents of the SiGe matrix can be studied, as well as different doping levels. Moreover, both mono and polycrystalline materials can be produced. Finally, the CVD tool employed in this work was fully automatized.

2.1 - Generalities

CVD process can basically be described as the growth of a solid phase on a surface using a gas phase precursor as source of atoms. Several variants of the CVD process exist, and the most common classification is based on the pressure used inside the reaction chamber. In this work a Reduced Pressure CVD (RP-CVD) apparatus was employed, with pressures ranging from 10^2 to 10^5 Pa. Other CVD types normally used are the Atmospheric Pressure CVD (AP-CVD) and Ultra High Vacuum CVD (UHV-CVD).

In this work, commercial CVD equipment was employed. The main advantage of this type of tool is the precise control of different parameters such as chamber temperature, pressure and gas flow rates, allowing to perform a reproducible process.

In a traditional CVD system, as described here, the chamber configuration is set in order to provide a horizontal laminar flow of the precursor gases. The laminar flow is characterized by the formation of a boundary layer, where the gas velocity varies from zero (near the substrate) to a constant value (“the main gas flow” region).

A carrier gas (H_2) is employed to dilute the precursor gases and deliver them to the process chamber. While the gases cross the chamber, reactions between the carrier, the precursor gases and the substrate take place.

During the deposition and solid phase growth, several non-equilibrium reactions take place inside the chamber. The overall process can be described by different independent steps, as illustrated in Figure 2.1.

Step “1” corresponds to the diffusion of precursor gases through the boundary layer to reach the substrate surface. Once they reach the surface, gas molecules are adsorbed onto the surface (step “2”) and diffuse until a reaction site is reached (3).

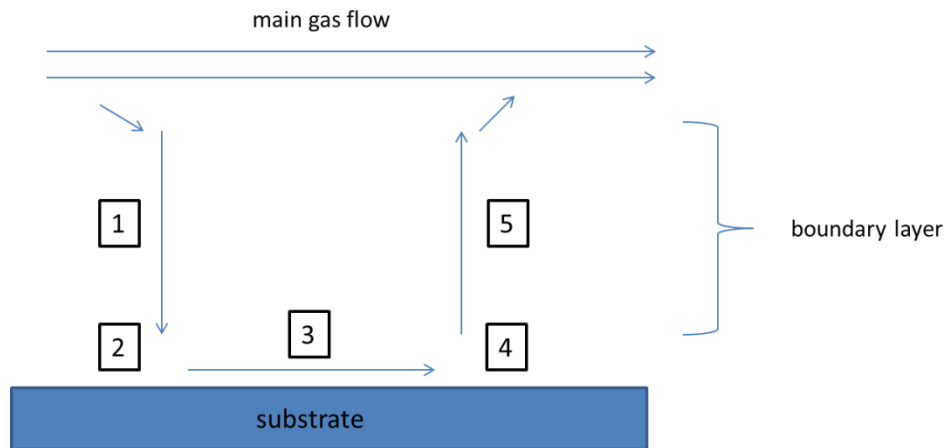


Figure 2.1: Overall view of the different steps of the CVD deposition.

Latter, chemical reactions take place leading to the formation of a solid phase and gaseous products (step “4”). These species diffuse through the boundary layer until they reach the main gas flow and are evacuated from the chamber (step “5”).

2.2 - Nucleation and growth mechanisms

A more precise description of the growth mechanisms is presented in Figure 2.2. Actually several simultaneous phenomena occur when atoms/molecules arrive at the substrate surface. First, they can adsorb on the surface (“a”) or re-evaporate (“b”). The adsorbed species will then diffuse on the surface (“c”). The surface diffusion can be described by the diffusion coefficient of the species (Equation 2.1).

$$D_s(T) = D_0 \cdot e^{-E_{diff}/kT} \quad 2.1$$

Where D_s is the surface diffusion coefficient, D_0 is a constant, E_{diff} is the potential barrier for the adatoms to move from one adsorption site to another, k is the Boltzmann constant and T the temperature.

By surface diffusion the mobile species can then form metastable clusters (“d”), which will disintegrate or can form stable nucleus bigger than the critical size, also called islands (“e”). Further diffusion of adsorbed species will result on an increase of the islands size.

The role of temperature is of great importance for the diffusion of atoms. The higher is the temperature, the higher is the mobility of the species on the surface.

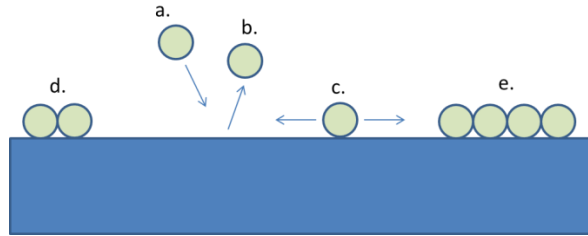


Figure 2.2: Possible reactions taking place at the substrate surface during the CVD process.

Another important parameter that controls the solid phase growth is the interaction of the deposited species with the substrate atoms. Assuming that sufficient temperature is given to the system to assure surface diffusion, species presenting a high interaction (for example, the growth of Si on Si), will grow layer by layer. This is described by the *Franck van der Merwe* model [6] and is shown in Figure 2.3-a).

The opposite situation, where the interaction between the deposited atoms is higher than the interaction between the growing species and the substrate, the growth will be characterized by an island growth, also called the *Volmer-Weber* growth (Figure 2.3-b).

The third growth mechanism, also called the *Stranski-Kastanov* model is characterized by a layer-by-layer growth until a critical thickness " h_c " is reached and then by an island growth.

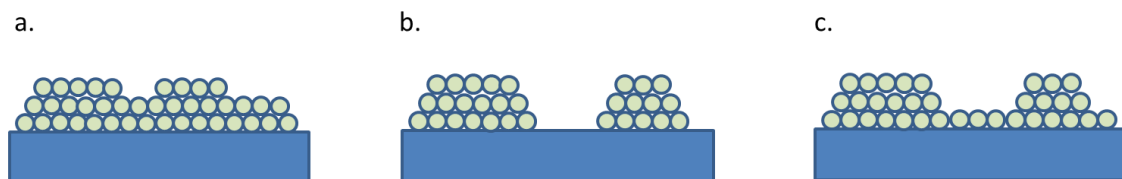


Figure 2.3: The three main possible growth mechanisms. Franck der Merwe (a), Volmer-Weber (b) and Stranski-Kastanov(c).

In the case of the *Volmer-Weber* growth, if the deposition continues up to the formation of a thin film, a polycrystalline material will be produced.

For a *Franck van der Merwe* growth type, the growth can occur epitaxially, i.e., the grown film will follow the substrates crystalline orientation resulting on a monocrystalline film. If the temperatures employed are low (resulting on a small diffusion of surface atoms and larger number of nucleation points) or if the substrate has defects or impurities, a polycrystalline film will be produced. The same is true for the *Stranski-Kastanov* growth type.

Polycrystalline materials can be interesting in thermoelectric applications because the presence of grain boundaries can act as barriers for phonons diffusion. At the same time, they present typically a lower electrical conductivity due to the reduction of the atoms mobility compared to monocrystalline materials, which can annul the beneficial effect of the thermal conductivity reduction.

In this work, when monocrystalline SiGe films were grown on Si wafers a previous step consisting in sending a HCl flow at 1100 °C was employed in order to clean the surface to allow the epitaxy.

It is important to notice that the *Volmer-Weber* growth type, if well controlled, can result on the formation of quantum dots. This mechanism is typical for metallic growth on insulating substrate and was observed in the present work, where Ti and Mo-based nano-islands were grown onto SiGe substrates. By controlling the deposition temperature and duration, the islands remained isolated without forming a continuous layer and acted as quantum dots precursors.

The *Stranski-Kastanov* type occurs when the grown material and the substrate have a similar crystalline structure but a different lattice parameter. An example is the case of SiGe grown onto silicon substrates, explained in more details in section 2.5 - .

2.3 - The growth rate limiting factor

In this section a brief discussion on how the growth rate changes as a function of temperature will be presented. The growth of thin films rather than quantum dots will be employed as an example in order to make the understanding of these aspects simpler.

Actually the steps presented in Figure 2.2 can be resumed in two major parts. The first one is the diffusion of gaseous species through the boundary layer and the second is the surface diffusion and reactions of the adsorbed species on the substrate surface.

By plotting the growth rate of a thin film as a function of the temperature, *Arrhenius plots* are obtained as shown in Figure 2.4. Commonly it is possible to identify and separate in these graphics two distinct regions corresponding to two growth regimes.

By analyzing these two regimes it is possible to determine if the process is limited by gaseous diffusion through the boundary layer or by surface diffusion and reactions.

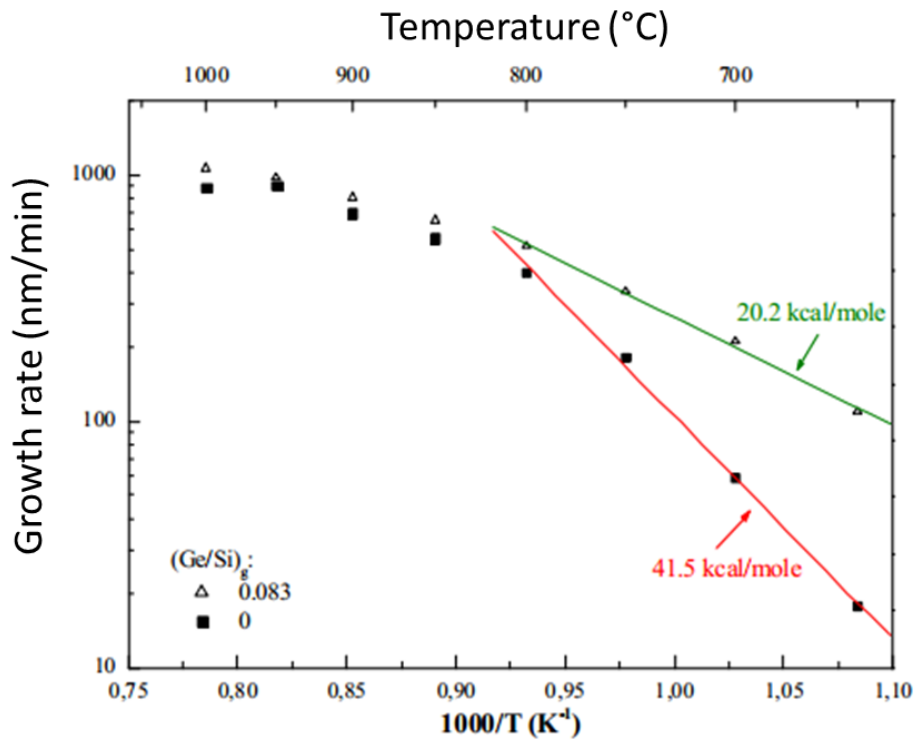


Figure 2.4: Arrhenius plot of the CVD growth of Si (red curve) and of SiGe (green curve). Under 800 °C, the growth rate is limited by surface reactions. Above this temperature, it is limited by mass transport. Image from [7].

At low temperatures, the growth is limited by surface reactions. The growth rate “ R ” can be approximated to $R \propto e^{-E_a/kT}$. In this case, both surface diffusion mechanisms and chemical reactions are considered.

At higher temperatures, the surface reactions take place faster and the limiting step is the mass transport through the boundary layer. In this case the growth rate approaches to a constant value.

2.4 - CVD tool

The equipment employed for this work is the RPCVD *Centura 5200* from *Applied Materials*. This equipment is currently employed by the microelectronics industry in order to grow doped Si and SiGe thin films onto silicon wafers. It is equipped with a cleaning system allowing to epitaxially grow thin films.

The deposition chamber is isolated from the atmosphere and the heating for the reactions is provided by a set of lamps situated both on top of the chamber and below it, allowing a homogeneous heating (Figure 2.5).

The substrate lies under a support which is equipped with a rotation system (20 turns/min.). The whole system is covered by quartz dome, allowing the light from lamps to reach and heat the sample. The temperature is controlled by a pyrometer positioned on the lower part of the chamber. The reaction gases are delivered to the chamber providing a horizontal laminar flow using H_2 as the carrier gas.

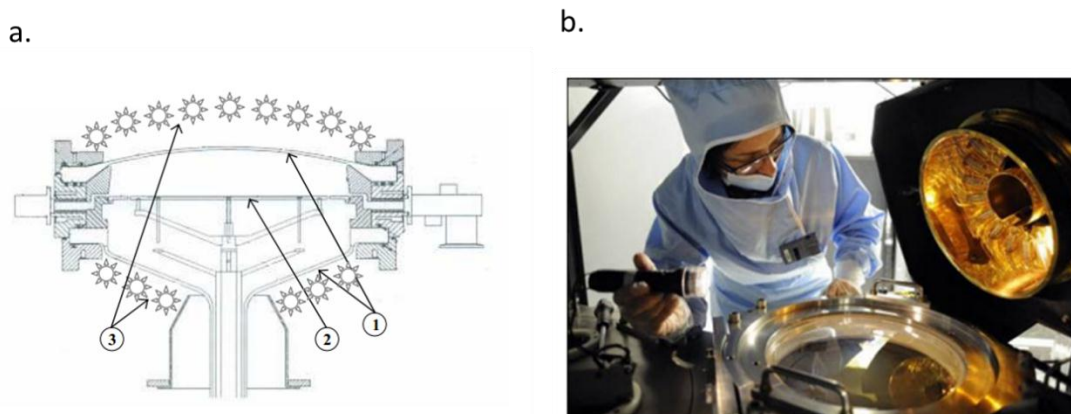


Figure 2.5: (a):Representation of the reaction chamber with its main parts. 1=the quartz dome, 2=the substrate support and 3= the heating lamps. (b): A view of the chamber during maintenance.

The CVD apparatus is equipped with SiH_4 as a precursor for silicon deposition and GeH_4 for germanium, as well as with dopant gases PH_3 for *n*-type doping and B_2H_6 for *p*-type. Both dopants precursors are pre-diluted in H_2 in order to achieve the low concentrations necessary.

The typical parameters ranges for this type of equipment are listed above.

- Working pressure: 5 – 500 Torr
- Temperature: 550 – 1100 °C
- Precursor gas flow rate: 10 – 300 standard cubic centimeter per minute (sccm)
- Carrier gas flow rate (H_2): 10 – 30 standard liter per minute (slm)

2.5 - Si and SiGe thin film growth

In this section some considerations concerning the growth of Si and SiGe using the CVD tool employed to grow the QDSL are presented. First of all, the growth mechanisms are detailed, as well as the differences between the growth of pure Si and of SiGe.

When only SiH_4 is employed to grow a monocrystalline thin film onto a silicon wafer, the process is called homoepitaxy and the *Franck van der Merwe* growth type is observed. This is achieved if the temperature inside the chamber is sufficient to provide the mobility necessary for the atoms to arrange themselves according to the substrate crystalline structure.

It should be noticed that both the chamber and the substrate should be clean enough not to disturb the growth. In this case, growth with no defects and thin films with no internal stress can be obtained.

Both silicon and germanium have the same cubic “diamond” crystalline structure (Figure 2.6), forming a homogenous solid solution with no intermetallic compounds (Figure 2.7). This feature makes it straightforward to produce SiGe materials with different Ge contents.

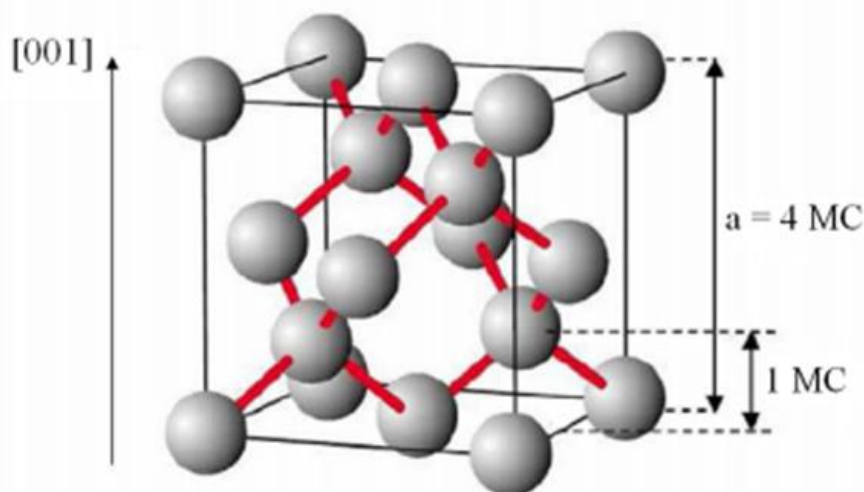


Figure 2.6: Crystalline structure of Si and Ge.

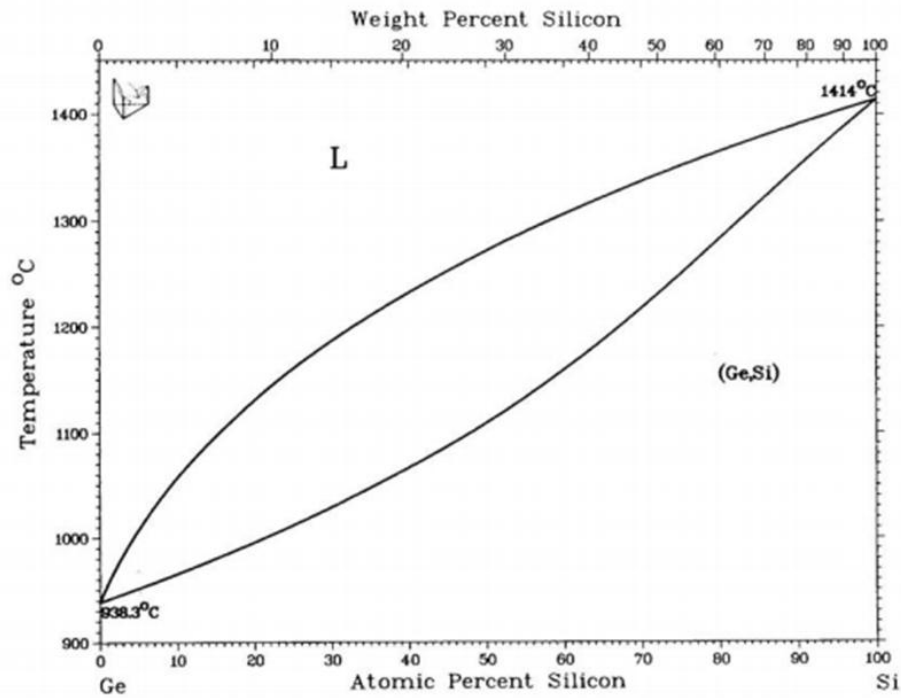


Figure 2.7: Phase diagram of Si and Ge. Image from [8].

The difference between the two materials crystalline structure is the lattice parameter, named “ a ”. For silicon, $a_{Si} = 5,431 \text{ \AA}$ and for germanium $a_{Ge} = 5,646 \text{ \AA}$. The difference between the two lattice parameters is defined by the lattice mismatch, showed in Equation 2.2, and is around 4% for silicon and germanium.

$$\frac{\Delta a}{a} = \frac{a_{Ge} - a_{Si}}{a_{Si}} \quad 2.2$$

In the case of SiGe, the representation $Si_{1-x}Ge_x$ can be adopted, where “ x ” correspond to the atomic fraction of Ge atoms in the binary compound.

By adding Ge to Si, the lattice parameter changes linearly with the Ge content and can be calculated by the equation 2.3.

$$a_{Si_{1-x}Ge_x} = a_{Si} + x \cdot (a_{Ge} - a_{Si}) \quad 2.3$$

For polycrystalline thin films, the lattice parameter can be measured by the shifting of the diffraction spectrum peaks and the Ge content of the material can be estimated.

Consider a SiGe thin film epitaxially grown onto a silicon wafer. In this case, the difference on the lattice parameter of the two materials can disturb the growth. In order to accommodate the atoms according the silicon substrate's lattice, the lattice parameter of the SiGe is reduced along the horizontal direction and increased along the vertical direction (Figure 2.8). The higher the Ge content of the SiGe, the more this effect is noticed.

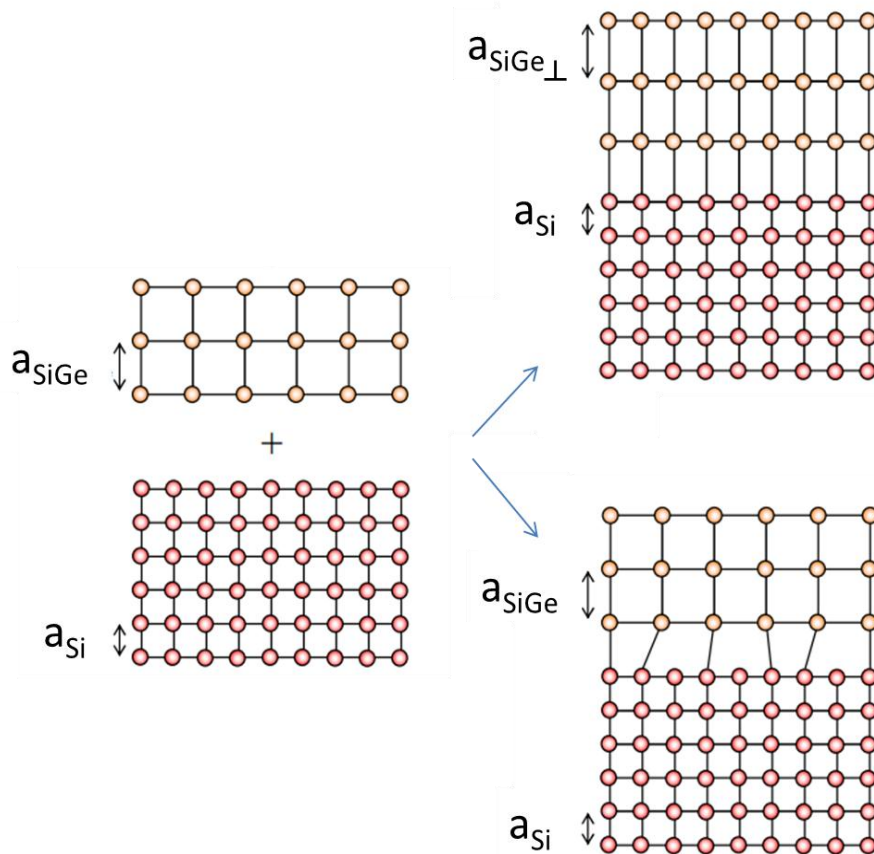


Figure 2.8: Representation of the modifications of the lattice parameter when SiGe is grown onto (100) Si. Left: the lattice parameter for both materials. Up right: epitaxial growth with distortion of the SiGe lattice parameter. Low right: relaxation of the SiGe film to the original lattice parameter by the creation of dislocations.

This phenomenon will result on an increase of the internal elastic energy of the material. The thicker the film is, the higher is the stored energy. A further increase on the elastic energy of the system will lead to the creation of dislocations and relaxing of

the structure. In this case, the lattice parameter of the SiGe thin film will no longer match the Si substrate, but it will be rather the one of a bulk material. A further growth of the film will then result on the formation of dome-like structures, resulting on a *Stranski-Kastanov*-like growth. This feature can be employed to create quantum dots/nano-islands structures based on SiGe/Si [9,10]. The shape of the obtained nano-islands can thus be further tailored by annealing the obtained material [11].

The thickness where the system will relax and form dislocations is called the critical thickness h_c and is dependent on the Ge content of the grown SiGe film (Figure 2.9).

In the present work the produced QDSL had Ge contents ranging from 2 – 10 % and a total thickness of round 1000 nm, and both poly and monocrystalline samples were produced. It can thus be expected that for the monocrystalline samples a metastable growth exists, with the possible presence of relaxed layers with dislocations. Further discussion on this subject will be presented in Chapter 3.

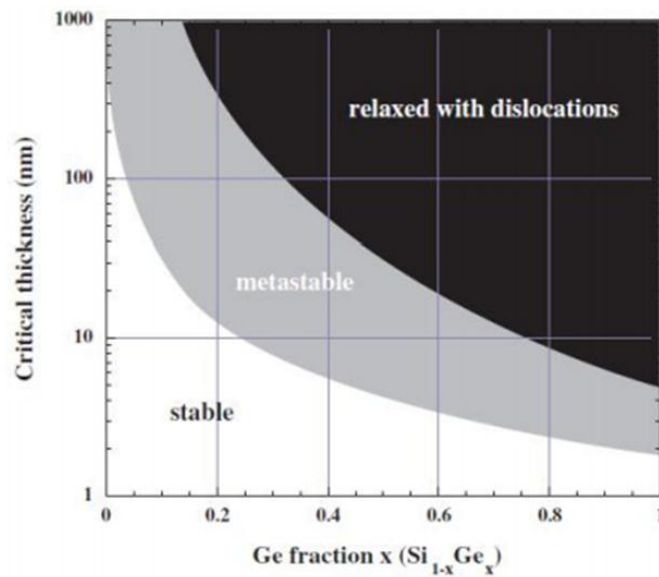


Figure 2.9: Critical thickness as a function of the Ge fraction. The metastable zone corresponds to conditions where the creation of dislocations depends on the experimental conditions. Image from [12].

Another important point to be considered in this section concerns the chemical reactions taking place when SiGe is grown. In the case of the precursors employed in this work, the following reactions can be cited.





And for the dopants:



Both reactions are pyrolysis, i.e., the molecules bonds are broken using the energy from the heat source.

In order to produce SiGe thin films, both gases are mixed during the deposition, and by varying the gas flow rates, different concentrations of Ge are obtained. Similarly, different doping levels can be obtained by varying the dopant gases flow rates.

2.6 - Ti and Mo precursors

The first step in order to produce silicide-based QDSL is to select the appropriate precursors. Several restrictions exist, and the choice of using Ti and Mo among the silicides studied by Mingo et al in reference [1] was mainly due to the possibility of using precursors for these atoms on the CVD tool available for this work.

The main characteristics of a candidate precursor are:

- High vapor pressure (in the case of non-gaseous precursors)
- Low toxicity
- Low reactivity with the gas lines
- Molecules with no oxygen
- Molecules producing gaseous products after decomposition
- Stability of the molecule up to deposition temperatures
- Availability
- Compatibility with a technological transfer

Generally, the precursor must be able to supply a gas phase that will stay inert until it reaches the reaction chamber. When the deposition takes place, the byproducts of the reactions occurring in the chamber must be evacuated and must not interfere with the growth.

Once all of these parameters were evaluated, the chosen precursors were $TiCl_4$ for Ti and $MoCl_5$ for Mo.

The chemical reactions using chloride compounds are not governed by the same mechanisms as for SiH_4 and GeH_4 . In this case, the main reaction is the reduction of the metal atoms by the carrier gas H_2 , as presented in equations 2.8 and 2.9.



In pyrolysis reactions, the carrier gas H_2 acts only as a diluting agent. For the same precursor gas flow rate, increasing the carrier gas flow rate reduces the partial pressure of the precursor, and thus reduces the deposition rate.

For reduction reactions, however, more attention has to be given to the carrier gas, since it is fundamental and takes part of the reactions.

2.7 - Delivery system for non-gaseous precursors

The main inconvenient of the $TiCl_4$ and $MoCl_5$ precursors is that they are non-gaseous and thus cannot be directly delivered to the deposition chamber. To solve this problem, a system has been conceived to allow the separation between the gas and liquid phase (for the Ti precursor) and between the gas and solid phase (for the Mo precursor). A second function of this system is to deliver the gas phase to the reaction chamber.

This system is schematically represented in Figure 2.10. The apparatus is adapted both for the use of the liquid ($TiCl_4$) and solid precursors ($MoCl_5$), with changes only in the inner part of the container.

The system consists in an isolated container charged with the precursor. Two mass flows controllers (MFC) are employed, one for the H_2 carrier gas (MFC1) entering the container and one for controlling the flow rate of the metallic precursor and the H_2 carrier gas coming from the container (MFC2).

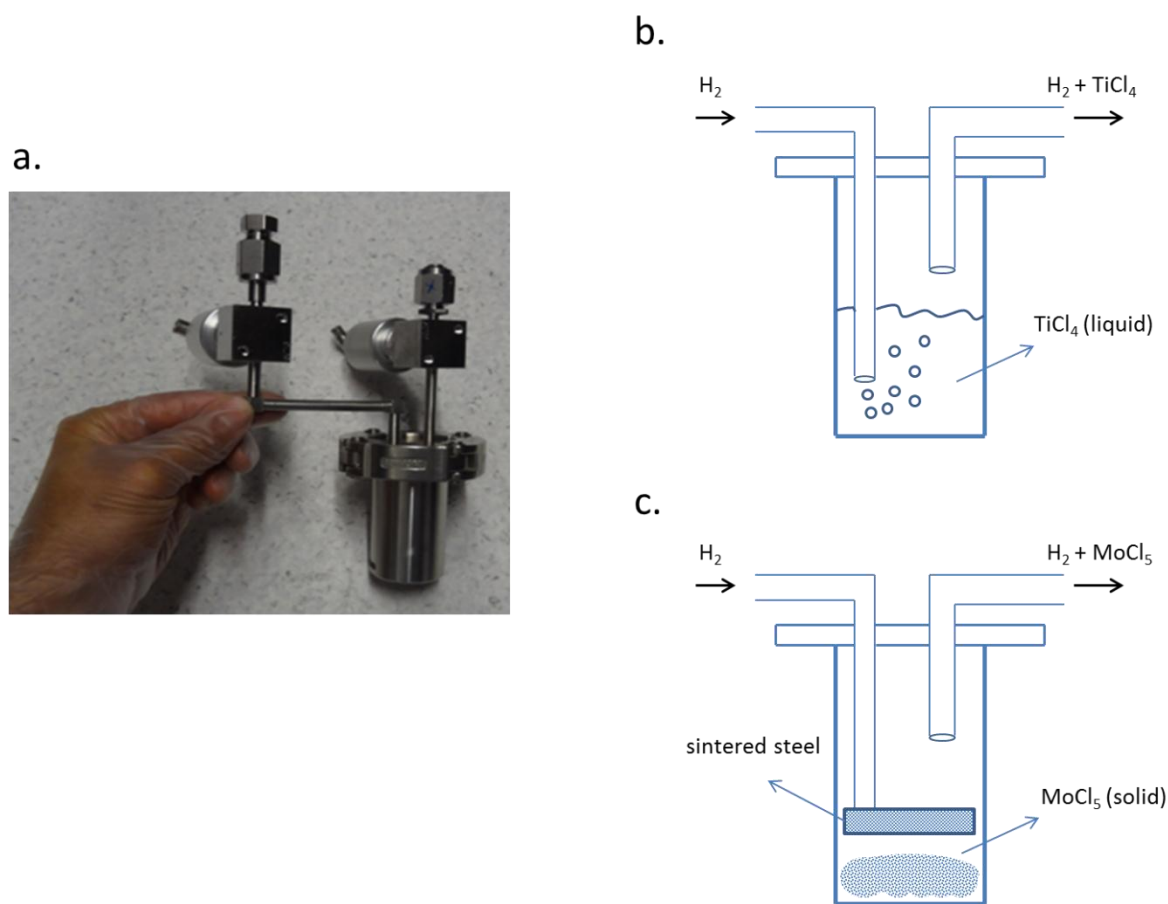


Figure 2.10: The precursor container of the evaporation system. (a): a view of the outside of the piece. (b): schematic representation of the inside of the container for the use of TiCl_4 . (c) schematic representation of the inside of the container employed for the MoCl_5 precursor.

All the parameters (gas flow rate, pressure, temperature) were controlled using specific software (Figure 2.11). A PID (Proportional Integral Derivative) control system is employed to maintain the pressure inside the container constant by controlling the MFC1 to regulate the intake of carrier gas.

A heating mechanism was conceived allowing to heat independently three different zones of the system. The first one, named T_1 corresponds to the temperature inside the container. T_2 is the temperature of the zone above the container, consisting on the beginning of the gas lines and MFC2. T_3 corresponds to the rest of the gas line until the deposition chamber. The heating is performed in such a way that $T_3 > T_2 > T_1$, assuring that no condensation occurred inside the gas lines even if small temperature drops exists.

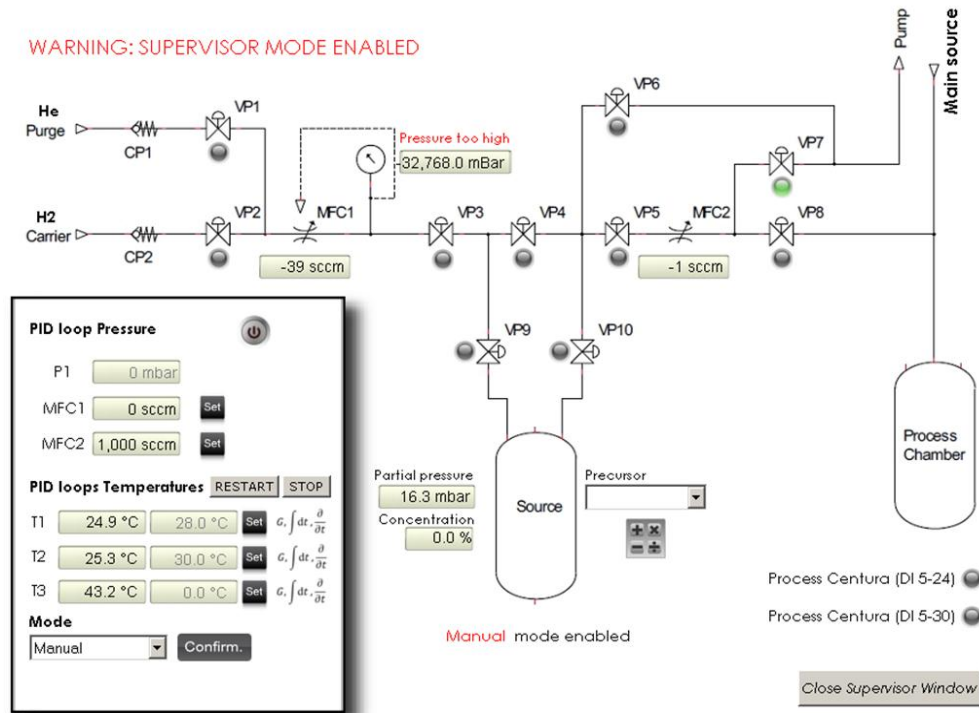


Figure 2.11: The evaporation system software interface.

2.7.a - TiCl₄ evaporation system

For the Ti precursor, which is liquid at ambient conditions, the system consists in a bubbler apparatus (Figure 2.10-b).

In this case the container is filled so that the carrier gas bubbles inside the precursor, forming a TiCl₄-rich gaseous phase. This gas is then pumped to the chamber. In order to estimate the TiCl₄ flow rate, the following procedure was adopted. First, the vapor pressure of TiCl₄ as a function of temperature is determined by Equation 2.10 [13].

$$\log P_{TiCl_4} = 6,79 - \frac{1346,56}{T + 208,52} \quad 2.10$$

This equation, also called “Antoine equation” is empirically determined and allows to determine approximately the vapor pressure of the gaseous phase of a liquid/gas system in equilibrium. The pressure is given in Torr and the temperature in °C.

For further calculating the real flow coming from the evaporating apparatus, equation 2.11 is used.

$$Q_{TiCl_4} = \frac{P_{TiCl_4}}{P_{meas}} Q_{out} \quad 2.11$$

Where “ Q_{TiCl_4} ” is the flow rate of the $TiCl_4$ precursor, “ P_{TiCl_4} ” is the pressure obtained from equation 2.10, “ P_{meas} ” is the pressure inside the container and “ Q_{out} ” is the flow rate coming from the evaporation system, controlled by MFC2.

In this work the temperature inside the evaporator is fixed to 30 °C. This choice was done in order to provide the minimum precursor as possible but still at a slightly higher temperature compared to the room temperature, allowing a better stabilization of the temperature.

The chosen container temperature produced a vapor pressure of around 1,1 Torr. The pressure inside the container is set to 700 Torr, and the flow rate was set to the range of 50 to 200 sccm, leading to a real $TiCl_4$ flow of 0,08 to 0,3 sccm. During these calculations it was assumed that the system is in equilibrium.

2.7.b - MoCl₅ sublimation

A similar method is employed to deliver the $MoCl_5$ to the deposition chamber. As the precursor is solid up to high temperatures, the carrier gas is only directed onto the solid precursor surface through a sintered steel piece (Figure 2.10-c).

The Antoine equation used for $MoCl_5$ is [14]:

$$\log P_{MoCl_5} = 9,465 - \frac{3504}{T} \quad 2.12$$

Where T is the temperature (in K) and P is the pressure (in Torr). The chosen temperature was the maximum allowed to our system, i.e., 135 °C, producing a vapor pressure of approximately 0,87 Torr and gas flow rate of 0,06 to 0,25 sccm, which are similar to those used for $TiCl_4$.

These results were useful to guide the first experiments to calibrate the evaporation/sublimation system. Care should be taken in order to estimate the real gas flow rate during the depositions, as these calculations are approximated and

consider that the system is in equilibrium. The case of MoCl_5 is even more critical, because there is no bubbling of the carrier inside the precursor.

3 - Growth of Ti-based silicide/SiGe QDSL

3.1 - Introduction

Titanium silicide is a well-studied material for using in the microelectronic industry as electrical contacts. The traditional way to form the silicide is the *Salicide* process, where a thin Ti film is deposited either by evaporation, sputtering or CVD directly onto the Si wafer. A latter heat treatment provides the energy for the reactions between Ti atoms and Si atoms from the substrate, forming the silicide [13].

The main phase of interest for the microelectronics industry is the TiSi_2 C54 phase, due to its low electrical resistivity, and it is normally obtained by annealing the wafer at temperatures between 600 – 800 °C. Even if different phases exist for the Si-Ti system (Figure 2.12), during the *salicide* process the more thermodynamically stable phases obtained are the C49 and C54 TiSi_2 phases.

TiSi_2 is also the phase studied as nano-inclusions inside a SiGe matrix for reducing the thermal conductivity in reference [1], the main inspiration for the present work.

In this work, a similar process to the *salicide* process using CVD was employed to deposit the Ti nano-islands and further form the QDSL. The first step was the deposition of Ti onto a wafer where a SiGe thin film was previously grown. The process was then stopped before a continuous film was formed, taking advantage of the *Stranski-Kastanov* growth type. By doing this, the deposition of Ti nano-islands was achieved.

Some studies have been published showing the deposition of Ti silicides onto a Si wafer by CVD [15], and a correlation between the formed phases with the partial pressure of the precursor gases (TiCl_4 and SiH_4) was identified. The authors found that several silicide phases exist and depend strongly on TiCl_4 and SiH_4 partial pressures.

In the case of the present work, different mechanisms are expected, since the Ti deposition does not form a continuous film and since there is no SiH_4 added to the Ti deposition. However as the employed TiCl_4 deposition temperatures varied between 750 – 900 °C, which corresponds to the same range of temperatures of the *salicide* process, it can be expected that during the deposition, reactions between the Ti atoms and Si atoms take place in-situ forming silicide phases.

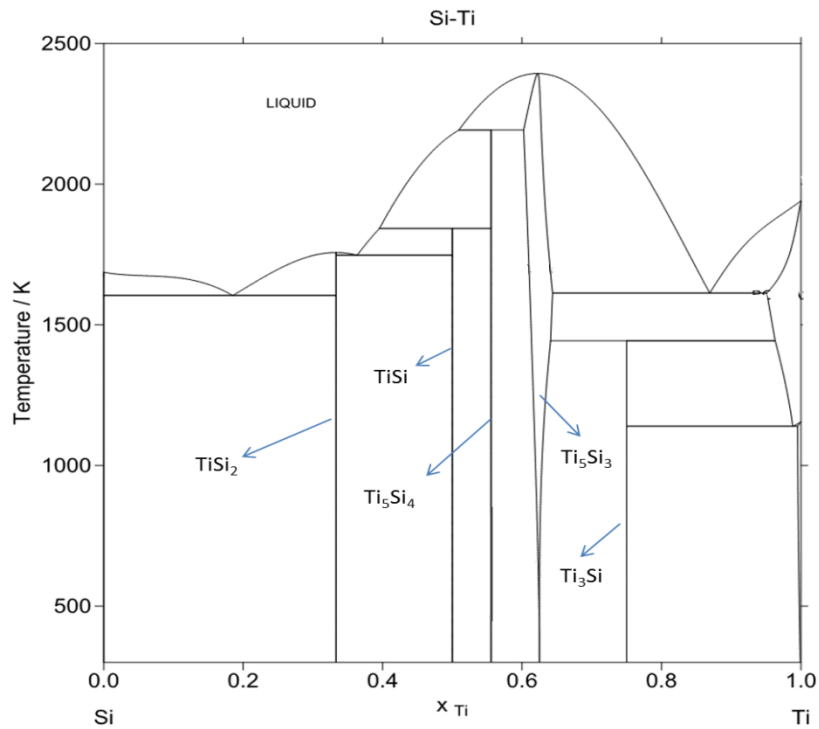


Figure 2.12: The Si-Ti phase diagram. The arrows indicate the composition of the different stable phases.

The deposition of QDSL by CVD employed in this work can be divided in three steps, represented in Figure 2.13. The first one is the deposition of Ti nano-islands onto a SiGe thin film. The nano-islands are further embedded by the deposition of a SiGe thin film, forming simultaneously quantum dots by the reaction of the Ti atoms with the Si atoms. These steps were then repeated in order to produce a QDSL.

In this work the expression “nano-island” is differentiated from “quantum dot” in the sense that the former is related to the first steps of the growth, where the deposited Ti atoms form quasi-planar nanometric structures. Once they react with the Si atoms and form the silicides, spherical crystalline structures are formed, called quantum dots.

For convenience, when the Ti deposition on SiGe surface is being treated, they will be called nano-islands and when the QDSL is formed and the nano-islands will react with Si atoms to form silicides, they will be called quantum dots.

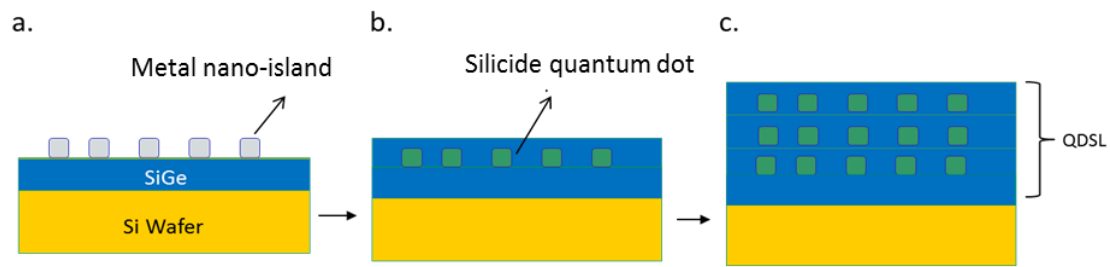


Figure 2.13: Strategy for the growing QDSL by CVD. Metal nano-islands are grown onto a SiGe thin film (a). A SiGe layer is deposited to embed the islands and form the quantum dots (b). Steps “a” and “b” are repeated to produce a QDSL, represented in (c).

3.2 - CVD deposition of Ti-based nano-islands

The surface growth of Ti silicide quantum dots has already been reported using different methods. For instance, this was achieved by depositing a Ti thin film onto a Si wafer with further annealing in order to nucleate and form nano islands [16] or by the direct CVD deposition [17,18]. In both works, the authors achieved the formation of Ti silicide nano-islands onto silicon substrates at temperatures as low as 630 °C.

In this work, no annealing step was used, and the system employed (coupled evaporator and CVD chamber) allowed to directly deposit quantum dots.

In reference [1] the optimal reduction of the thermal conductivity was obtained for a SiGe matrix containing approximately 3 % (in volume) of silicide quantum dots. In the case of Ti and Mo-based quantum dots, the best calculated diameters were around 20 - 40 nm for Ti and of 10 - 40 nm for Mo. In the present work, an effort was made in order to produce QDSL with a similar volumetric density of quantum dots and with inclusions having diameters of the same order of magnitude of those studied in the reference.

To accomplish this, the first step was the calibration of the nano-islands deposition parameters. *Scanning electronic microscope* (SEM) images were employed in order to determine the mean diameter and the surface coverage. The final volume fraction of the quantum dots inside the SiGe matrix was calculated from the surface coverage measures taking into account the following assumptions:

- the quantum dots were considered to be spherical and having the same diameter as the nano-islands;
- the thickness (t_{SiGe}) of the embedding SiGe thin film was set to be $t_{\text{SiGe}} = 2 \cdot D_{\text{NI}}$, where “ D_{NI} ” is the nano-islands mean diameter.

By using these assumptions, the relationship between the volumetric fraction and the surface coverage can be approximated to:

$$\%_v = \%_s/3 \tag{2.13}$$

Where “%_v” is the volumetric fraction and “%_s” is the surface coverage of the nano islands calculated by image treating (Figure 2.14). From equation 2.13, the optimal surface coverage calculated in order to obtain the reference values is 9 %.

The surface coverage can be related to the nano-islands mean diameter “D_{NI}” and the nano-islands surface density “d_s”, i.e., the number of particles per surface unit by the equation:

$$\%_s = \pi \left(\frac{D_{NI}}{2} \right)^2 \cdot d_s \cdot 100 \tag{2.14}$$

The following calibration table can be created:

Table 2.1: Nano-islands diameter and related surface density in order to obtain a final volumetric fraction of around 3% in the final QDSL.

nano-islands mean diameter "D _{NI} " (nm)	nano-islands surface density "d _s " (μm ⁻²)
10	764
20	191
30	85
40	48

The choice of the SiGe thin film thickness $t_{SiGe} = 2 \cdot D_{NI}$ was made in order to insure that the quantum dots were covered and embedded inside the matrix before the next quantum dots deposition. In order to simplify the calculations the nano-islands diameter was considered to be approximately equal to the silicides quantum dots diameter.

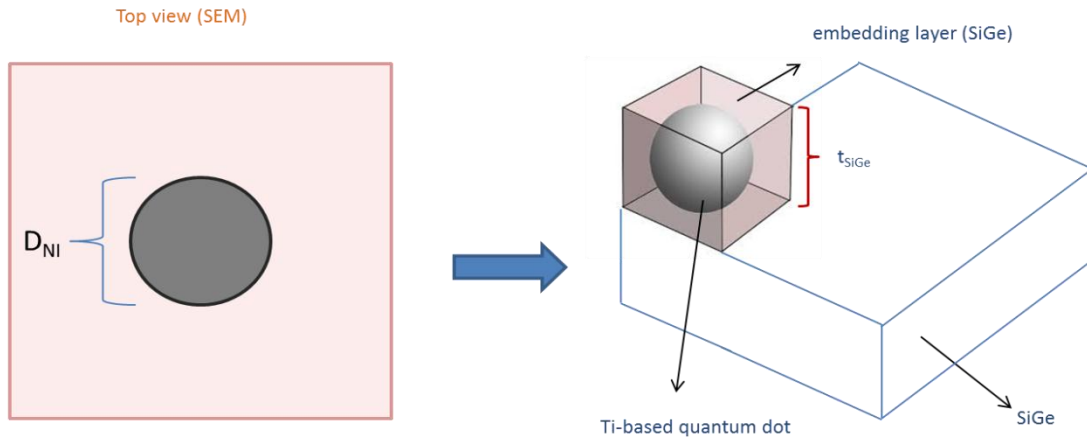


Figure 2.14: Schematic view of SEM image of a nano-island showing the measured diameter " D_{NI} " (left). Right: Embedding the nano-island with a SiGe thin film of thickness " t_{SiGe} " and formation of a quantum dot.

Another parameter that can be approximately calculated is the total volume of the deposited nano-islands, which is proportional to the quantity of deposited Ti. By approximating the nano-islands to spherical particles, the total volume v_{tot} per surface unit is defined by:

$$v_{tot} = \frac{4}{3} \cdot \pi \cdot \left(\frac{D_{NI}}{2}\right)^3 * d_s \quad 2.15$$

This value can be employed to calculate the growth rate of the Ti deposition. The growth rate can be defined by the dividing " v_{tot} " by the deposition time and can be plotted as a function of the deposition temperature in order to create *Arrhenius* plots (Figure 2.4).

Different studies were performed in order to determine the role of the parameters involved in the process concerning the size and distribution of the quantum dots obtained, such as the deposition temperature, the role of the Ge content of the SiGe substrate, the deposition duration and the partial pressure of the gases employed. The main results are presented in the following sections.

3.2.a - Role of deposition temperature

The first performed experiments consisted in the Ti deposition directly onto the monocrystalline silicon wafer, without a previous deposition of a SiGe thin film.

Different temperatures were employed as shown in Figure 2.15. The other deposition parameters were kept constant, with the deposition duration set to 15 s, the chamber pressure to 10 Torr (1 Torr = 133,3 Pa), the H₂ gas flow rate to 30 standard liters per minute (SLM) and the TiCl₄ gas flow rate to 50 standard cubic centimeters per minute (sccm). This value was the flow rate measured by the MFC2, constituted by the TiCl₄ plus the carrier gas. In equilibrium, the real flow rate of TiCl₄ is around 1 sccm (equation 2.11).

The calculated values of the nano-islands properties after the images were treated are presented in Table 2.2.

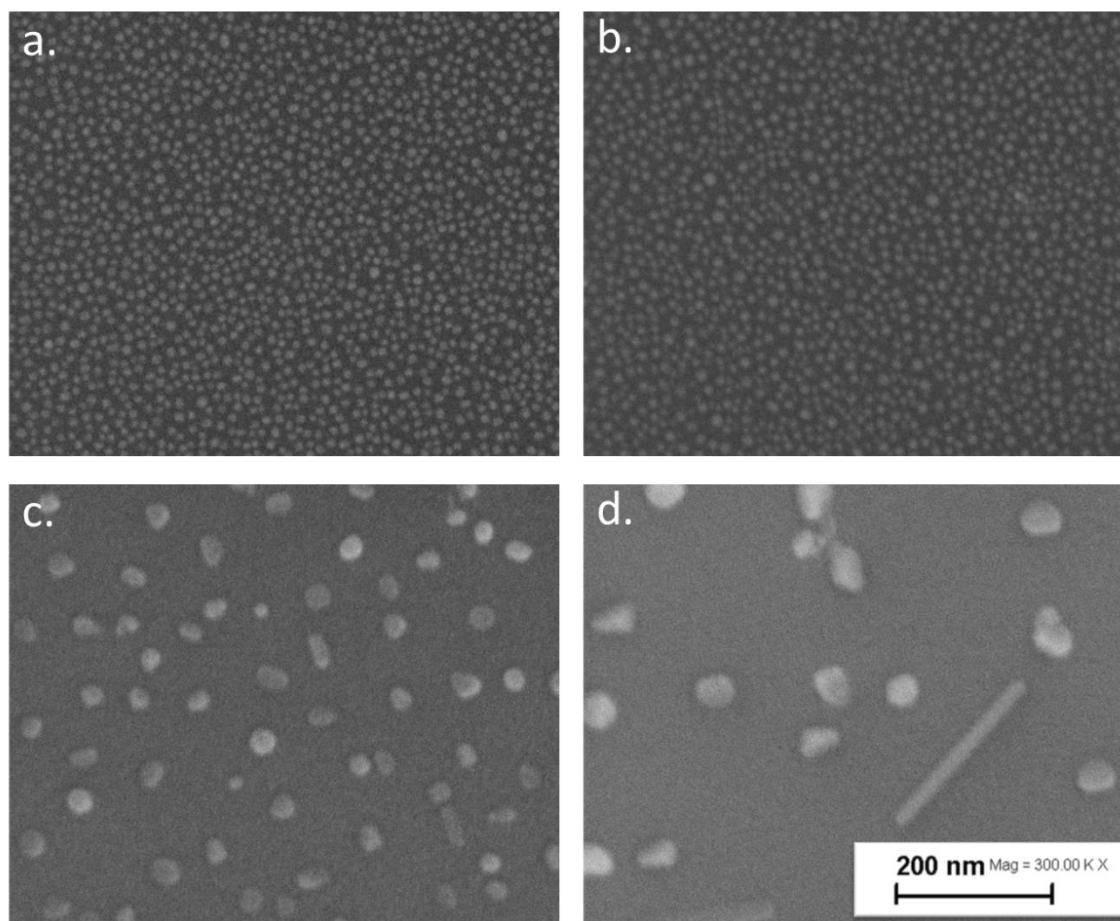


Figure 2.15: Top view SEM images of nano-islands grown on monocrystalline silicon as a function of deposition temperature. a) T = 750 °C. b) T = 800 °C. c) T = 850 °C. d) T = 900 °C.

Table 2.2: Measured nano-islands properties as a function of the deposition temperature onto a monocrystalline Si substrate.

<u>Deposition Temperature (°C)</u>	<u>750</u>	<u>800</u>	<u>850</u>	<u>900</u>
surface coverage (%)	32	32	11	8
mean diameter (nm)	10	11	31	58
islands density (μm^{-2})	3752	3296	131	31
total islands volume ($10^{-3} \mu\text{m}^3$)	2,0	2,3	2,0	3,2

The growth rate was calculated by taking into account the total islands volume and the deposition duration. By plotting the growth rate as a function of the deposition temperature the *Arrhenius* plot was obtained (Figure 2.16).

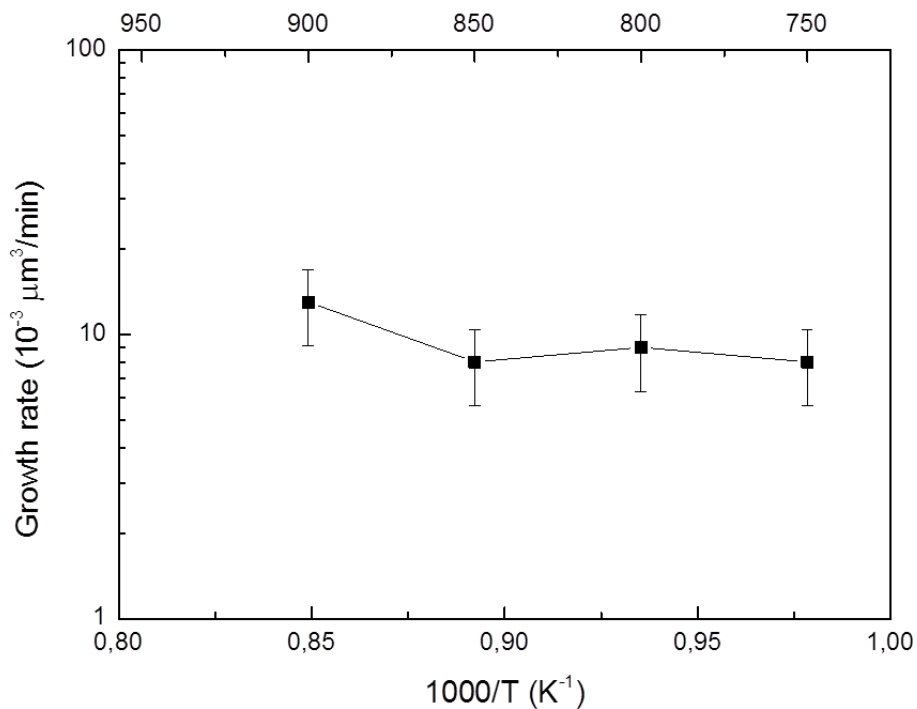


Figure 2.16: Arrhenius plot relating the growth rate to the deposition temperature for Ti-based nano-islands grown onto a monocrystalline Si substrate. An error of 10 % on the growth rate was calculated based on the error of the particles' diameter measurements.

Several conclusions can be taken from these initial results. Considering the growth rate, no significant difference was observed in the temperatures range employed during this work. As it was demonstrated in Figure 2.4, normally two domains can be identified in CVD *Arrhenius* plots. In the first one, at low temperatures, the growth rate varies exponentially with the temperature. In this case the limiting factor is the surface reactions. In the second domain (higher temperatures), the growth rate is almost constant and the deposition is limited by the mass transport.

It can be thus concluded that in the temperatures employed in this work the system is in the mass transport-limited domain. An increase on the deposition temperature has very low influence on the quantity of deposited atoms.

Even though the same quantity of mater is deposited onto the substrate, the behavior of the deposited species differs with the temperature. The main factor playing a role in this case is the surface diffusion of the deposited species (Equation 2.1). Here two main different temperature domains can also be identified. The first one consists in the deposition temperatures of 750 and 800 °C. In this case, the temperatures are not high enough to provide sufficient surface diffusion resulting on the growth from a large number of small islands. The second domain is related to depositions at 850 and 900 °C. Here the diffusion is highly dependent on the deposition temperature, resulting on a variation of the particles diameter and density.

A similar study was performed onto a monocrystalline SiGe substrate. This substrate was produced by growing a SiGe thin film onto the Si wafer. The Ge content of the substrates was kept constant and the gas flow rates were set to $\text{SiH}_4 = 70$ sccm and $\text{GeH}_4 = 30$ sccm. Earlier studies were made in order to calibrate the Ge content of the SiGe films by coupling XRD analysis with equation 2.3. The flow rates employed here provided a Ge concentration of around 10 % (atomic fraction).

These values were chosen for this work in order to produce materials with a similar Ge content to the samples studied in [19]. In this reference, the authors studied the role of the inclusion of silicide quantum dots in doped SiGe bulk samples for thermoelectric applications, which makes this the only similar study to the present work published to date. It should be noted that in the reference the authors studied bulk samples and in this work thin films were produced, which can contribute to a difference on the obtained results.

The deposition parameters were the same as those for the deposition onto the Si substrate, except the deposition duration that in this case was set to 10 s. SEM images of the samples are presented in Figure 2.17 and the calculated properties are presented in Table 2.3. The *Arrhenius* plot obtained from the calculated growth rate is presented in Figure 2.18.

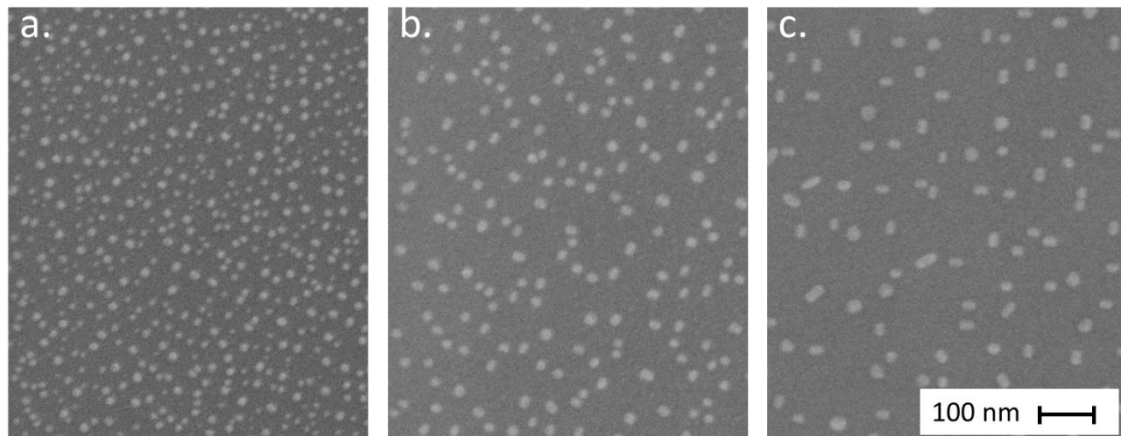


Figure 2.17: Top view SEM images of nano-islands grown on a monocrystalline $\text{Si}_{0.90}\text{Ge}_{0.10}$ thin film employed as substrate as a function of deposition temperature. a) $T = 800$ °C. b) $T = 850$ °C. c) $T = 900$ °C.

A similar behavior was found both for the deposition onto a pure Si and onto a SiGe thin film as substrate. Both depositions were limited by mass transport phenomena, and no significant variation on the growth rate was observed over the studied temperatures.

Table 2.3: Measured nano-islands properties as a function of the deposition temperature onto a monocrystalline $\text{Si}_{0.90}\text{Ge}_{0.10}$ thin film substrate.

<u>Deposition Temperature (°C)</u>	<u>800</u>	<u>850</u>	<u>900</u>
surface coverage (%)	14	9	8
mean diameter (nm)	14	22	27
islands density (μm^{-2})	841	256	135
total islands volume ($10^{-3} \cdot \mu\text{m}^3$)	1,2	1,4	1,4

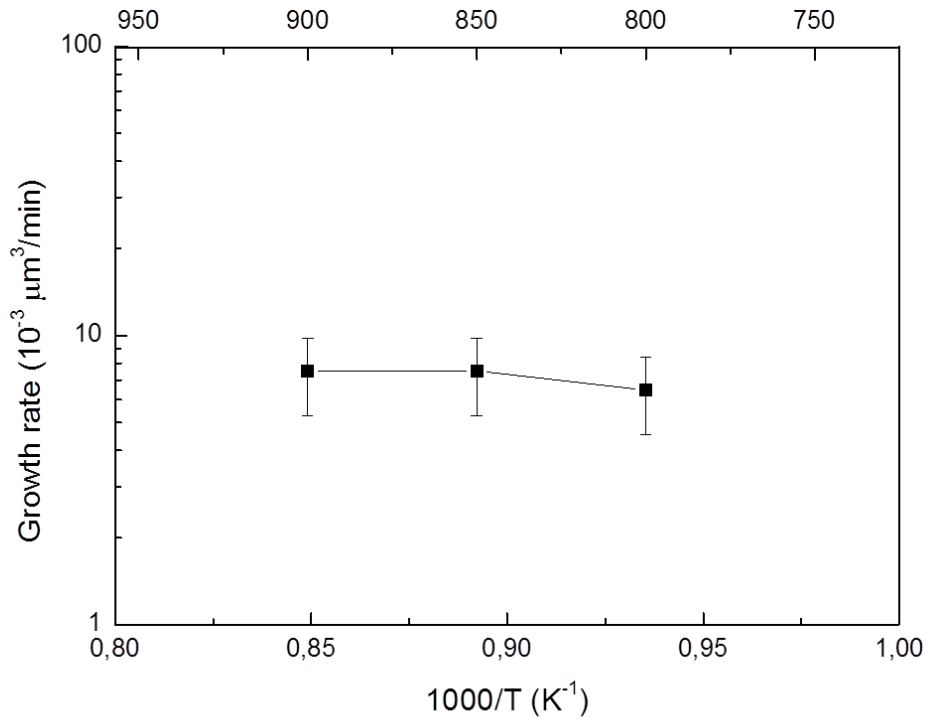


Figure 2.18: Arrhenius plot relating the growth rate to the deposition temperature for Ti-based nano-islands grown onto a monocrystalline SiGe substrate.

The most important conclusion for this part of the work is the determination of the role of temperature on the diameter and density of the obtained nano-islands. It can be seen that by changing the deposition temperature a precise control of the nano-islands density and diameter can be obtained. For instance, the growth of Ti-based nano-islands onto SiGe substrates at 850 °C resulted on particles with ideal sizes and surface densities for the production of QDSL, as it can be seen when the results are compared to Table 2.1.

3.2.b - Role of the substrate Ge content

In order to further understand the growth mechanisms, other depositions were made at the optimal chosen temperature (850 °C) but onto substrates with different Ge contents (Figure 2.19).

The Ge content was expressed by the ratio of the SiH_4 and GeH_4 gas flow rates employed for growing the substrate. The ratios studied were: 100/0, corresponding to 0 % Ge; 70/30, corresponding to a content of around 10 %, and 50/50, corresponding to a Ge content of 15 %. The Ge content has been measured by x-ray diffraction (see chapter 3).

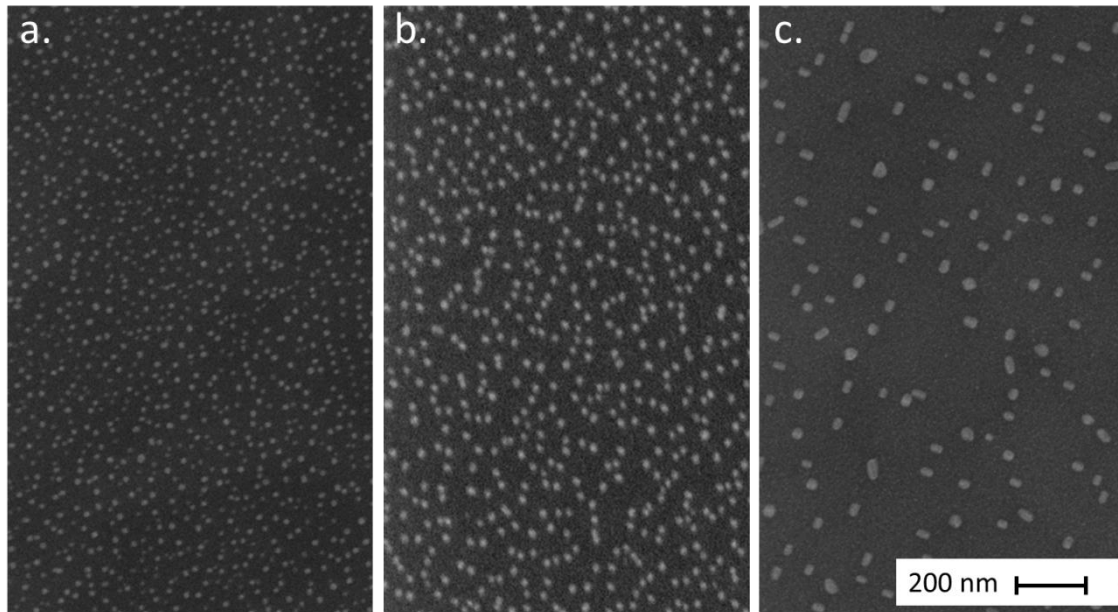


Figure 2.19: Top view SEM images of nano-islands grown on monocrystalline SiGe substrate as a function of the Ge content expressed as the $\text{SiH}_4/\text{GeH}_4$ gas flow rates. a) $\text{SiH}_4/\text{GeH}_4 = 100/0$. b) $\text{SiH}_4/\text{GeH}_4 = 70/30$. c) $\text{SiH}_4/\text{GeH}_4 = 50/50$.

By analyzing the images of Figure 2.19 it can be seen that the Ge content of the substrate has an important role on the morphology of the deposited nano-islands.

The results of the growth results for these samples are presented in Table 2.4. By comparing these with those presented in Table 2.3, it is observed that both the substrate Ge content and the deposition temperature play a similar role.

Table 2.4: Measured nano-islands properties as a function of the substrate Ge content (expressed as the gas flow rates ratio).

<u>$\text{SiH}_4/\text{GeH}_4$ ratio</u>	<u>100/0</u>	<u>70/30</u>	<u>50/50</u>
surface coverage (%)	12	9	6
mean diameter (nm)	16	22	36
islands density (μm^{-2})	604	256	59
total islands volume ($10^{-3} \cdot \mu\text{m}^3$)	1,3	1,4	1,4

It has been already shown that the main difference between the samples grown at different temperatures come from the difference on the surface diffusion of the deposited species. At higher temperatures, the diffusion is increased resulting on fewer and bigger nano-islands.

It can be thus concluded that a similar mechanism plays a role when the substrate Ge content is changed. The fact that a pure silicon substrate produces a larger number of smaller nano-islands than a Ge-rich substrate shows that Ti and Si atoms present a higher chemical interaction than Ti and Ge atoms. In the case of the Ge-rich substrates, it can be assumed that the potential barrier to surface diffusion E_{diff} is smaller (see equation 2.1). By increasing the substrate Ge content, a higher number of islands with bigger diameters is obtained.

It should be noted that here again the estimated total quantity of deposited atoms (and the growth rate) remained the same, thus the substrate Ge atoms did not change the $TiCl_4$ reduction by the H_2 carrier gas.

3.2.c - Role of deposition duration

In Figure 2.20 the role of the deposition duration “t” of Ti nano-islands on a $Si_{0.90}Ge_{0.10}$ substrate performed at 850 °C is presented. Three different deposition times were studied: 5, 10 and 15 s. The measured properties for these samples are presented in Table 2.5.

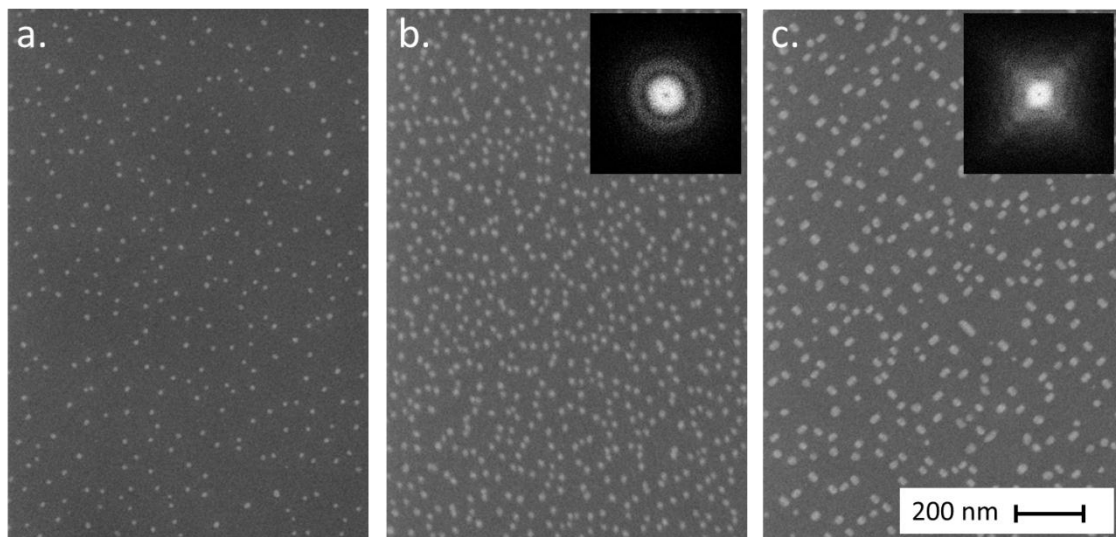


Figure 2.20: Top view SEM images of nano-islands grown on monocrystalline SiGe as a function of deposition duration “t”. a) t = 5 s. b) t = 10 s. c) t = 15 s. Inset: Fourier transform of the images.

By analyzing the results presented in Table 2.5, the following description of the growth mechanisms is obtained. After 5 seconds of deposition, only a few stable nucleus are formed onto the substrate. After 10 seconds, the increase of the mass transport results on an increase of the nucleus sizes and on the apparition of others (evidenced by the two-fold increase on the islands density). After 15 seconds, the coalescence phenomenon takes place, represented by the increase of the calculated total islands volume.

Table 2.5: Measured nano-islands properties as a function of the deposition duration.

<u>deposition duration (s)</u>	<u>5</u>	<u>10</u>	<u>15</u>
surface coverage (%)	2,5	9	11
mean diamater (nm)	16	22	30
islands density (μm^{-2})	115	256	158
total islands volume ($10^{-3} \mu\text{m}^3$)	0,2	1,4	2,2
growth rate ($10^{-3} \mu\text{m}^3/\text{min}$)	2,4	8,4	8,8

The growth rate did not change once the deposition duration was higher than 10 seconds. However, for 5 seconds the growth rate was considerably smaller, which confirms that at 5 seconds deposition the growth is not yet stabilized. As a conclusion, deposition times smaller than 10 seconds should not be employed for this system in order to produce reproducible results.

An interesting feature that can be observed in Figure 2.20 “b” and “c” is the Fourier transform of the images. Clearly the 15 seconds deposition resulted on an oriented growth of the nano-islands along the two main axis of the (100) plan of the substrate. For the 10 seconds deposition, not enough matter was available and the nano-islands present no preferential orientation.

3.2.d - Role of the precursor partial pressure

As it has been shown in the previous sections, the studied system is governed by the mass transport. In this case, the growth rate is known to be proportional to the precursor partial pressure [13].

The partial pressure of the TiCl_4 precursor " P_{TiCl_4} " is defined by:

$$P_{\text{TiCl}_4} = \frac{Q_{\text{TiCl}_4}}{Q_{\text{TiCl}_4} + Q_{\text{H}_2}} * P_{\text{Chamber}} \quad 2.16$$

Where " Q_{TiCl_4} " and " Q_{H_2} " are the TiCl_4 and H_2 flow rate respectively and " P_{Chamber} " is the pressure inside the deposition chamber. As " Q_{TiCl_4} " is small compared to " Q_{H_2} ", the precursor partial pressure can be approximated to " $P_{\text{TiCl}_4} \propto \frac{Q_{\text{TiCl}_4}}{Q_{\text{H}_2}}$ ".

In order to study the role of the precursors' partial pressure, it was chosen in this work to vary the carrier gas H_2 flow rate. While the TiCl_4 flow rate remained constant, the H_2 was set to 10, 20 and 30 SLM. The SEM images for this study are presented in Figure 2.21 and the measured results in Table 2.6.

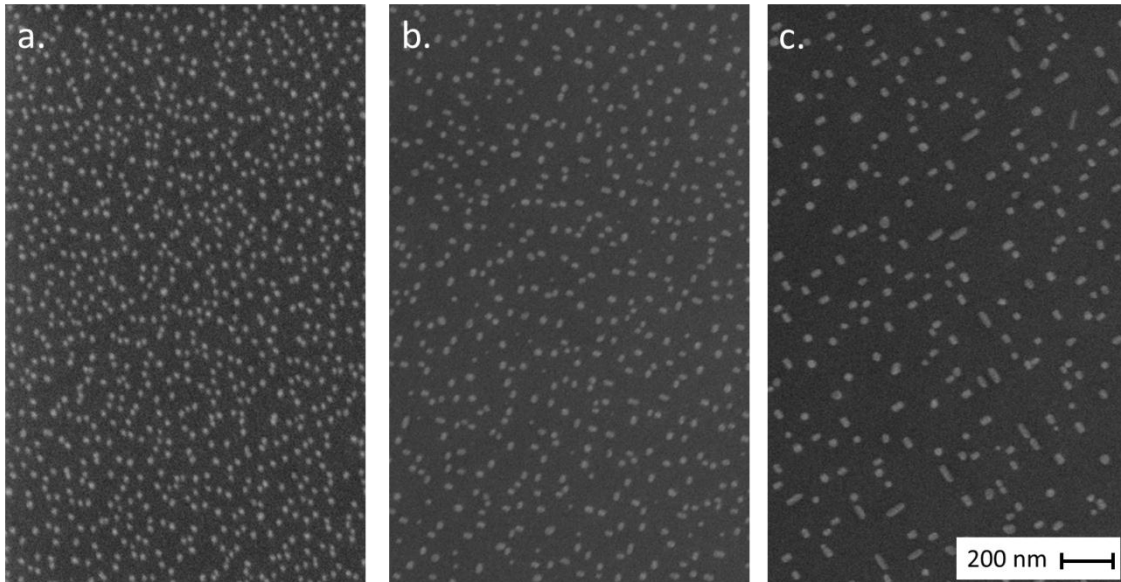


Figure 2.21: Top view SEM images of nano-islands grown on monocrystalline SiGe as a function of H_2 flow rate. a) $Q_{\text{H}_2} = 30$ SLM. b) $Q_{\text{H}_2} = 20$ SLM. c) $Q_{\text{H}_2} = 10$ SLM.

By analyzing the results from Table 2.6, it can be seen that the reduction of the H₂ flow rate from 30 to 20 SLM and further to 10 SLM produced the expected results, i.e., the dilution of the TiCl₄ precursor gas was reduced and the growth rate was increased.

The islands density was reduced and the mean diameter was increased because a higher mass transport and total deposited matter produced the coalescence of nucleus close to each other. Similar results were obtained by changing the TiCl₄ flow rate and keeping the H₂ flow rate constant.

Table 2.6: Measured nano-islands properties as a function of H₂ flow rate.

H₂ mass flow rate (SLM)	<u>30</u>	<u>20</u>	<u>10</u>
surface coverage (%)	9	10	7,5
mean diameter (nm)	22	28	35
islands density (μm⁻²)	256	159	92
total islands volume (10⁻³ μm³)	1,4	1,8	2,1
growth rate (10⁻³ μm³/min)	8,4	10,8	12,6

3.2.e - Role of substrate crystallinity

Until now all the presented studies consisted in growing the nano-islands onto monocrystalline substrates. The main reason for this is because it is simpler to treat the images and obtain consistent measures of the particles density and mean diameters. Treating images of polycrystalline samples would not be possible because of contrast differences caused by the material's grains.

However, as the substrate crystallinity is an important parameter to be considered when the thermoelectric properties are studied, it was essential to verify if the growth of the nano-islands onto polycrystalline substrates occurred in a similar way than onto monocrystalline substrates.

In Figure 2.22 a comparison between both substrates is presented. The substrates are composed of a Si₉₀Ge₁₀ thin film previously grown by CVD.

It can be seen that at least qualitatively the growth seems to be similar and the size of the particles is of the same order of magnitude. The particles density seems to

be smaller for the polycrystalline substrate, however it is difficult to evaluate this statement since some nano-islands can be hidden behind the material grains.

Another important observation from the SEM images is that the nano-islands seem to grow preferentially near the grain boundaries in polycrystalline samples. This fact will be further discussed in Chapter 3.

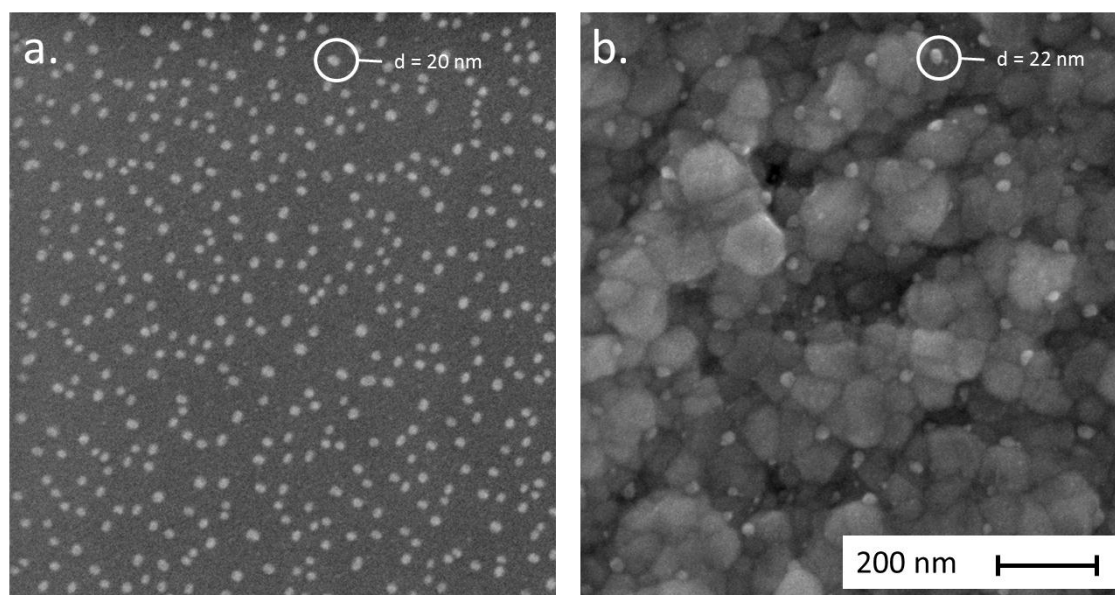


Figure 2.22: Top view SEM images of nano-islands grown on monocrystalline (a) and polycrystalline (b) $\text{Si}_{90}\text{Ge}_{10}$ thin films.

For the growth of QDSL, no changes were done on the growth parameters as function of the substrate crystallinity, as it was assumed that only slight differences occurred.

3.2.f - Conclusion

In the previous sections, the role of the different growth parameters was highlighted. The performed studies allowed a better comprehension of the growth mechanisms and the determination of the growth rate limiting factor for the Ti deposition onto Si and SiGe substrates, which is the mass transport. By adjusting the growth parameters a precise control of the nano-islands diameter and surficial density can be obtained. The studied variables can be divided in two main groups (see Table 2.7).

The first one contains the variables playing a role on the surface diffusion of the adsorbed species, such as the growth temperature and the substrate Ge content. By increasing the temperature or the Ge content, a higher surface diffusion occurs resulting on a smaller number of bigger nano-islands.

The second group is composed by the variables playing a role on the quantity of deposited matter, such as the deposition duration and the gases partial pressure. Logically, by increasing the deposition duration a higher amount of atoms is deposited, leading to an increase of the nano-islands size. If enough time is provided, the nano-islands will grow up to a point where coalescence will occur, and a reduction of the surface density will occur.

The partial pressure of gases is, on the other hand, responsible for the growth rate. By increasing the TiCl_4 precursor or reducing the H_2 carrier gas flow rate, a higher partial pressure of the precursor is obtained and the deposition growth rate is increased. The consequences are similar to increasing the deposition duration, i.e., an increase on the nano-islands diameter and reduction of surface density by coalescence.

By taking into account all these parameters, an example with suggested steps in order to produce controlled nano-islands onto a SiGe thin film substrate is presented:

1. Choice of the Ge content of the substrate;
2. Deposition on different temperatures in order to adjust the surface density;
3. Controlling the nano-islands diameter by adjusting the precursor partial pressure and/or deposition duration.

Table 2.7: Measured nano-islands properties as a function of H_2 flow rate.

	variables	nano-islands mean diameter	nano-islands surface density
group 1: surface diffusion	- growth temperature - substrate Ge content	↑	↓
group 2: quantity of deposited matter	- TiCl_4 partial pressure - deposition duration	↑	-

3.3 - Embedding the nano-islands and formation of quantum dots

In order to study the mechanisms occurring when the nano-islands are embedded (Figure 2.13-b), two different temperature ranges were employed, a low temperature embedding (650 – 700 °C) and a high temperature embedding (800 – 850 °C). These values were chosen based on the temperature where the growth rate limiting factor changes for the Si and SiGe system, i.e., around 750 – 800 °C (Figure 2.4). For the low temperature range, the deposition is limited by surface reactions while for the high temperature range the deposition is limited by mass transport.

3.3.a - Low temperature embedding: nanowires growth

When the first tests in order to embed the nano-islands with pure silicon were performed, the growth of nanowires instead of a continuous layer was observed.

The growth of Si nanowires catalyzed by Ti nano-islands has already been described elsewhere [20] at similar temperatures. The growth mechanism is known as a variant of the Vapor-Liquid-Solid (VLS) mechanism, known as Vapor-Solid-Solid (VSS) [2]. This method has often been employed in the context of CVD processes in order to grow semiconductor nanowires [21]. Here, the Ti nano-islands act as a catalyst for the deposition reactions. After the SiH_4 pyrolysis, silicon atoms diffuse inside the Ti particles. When the saturation point is reached, Si precipitates forming nanowires (Figure 2.23).

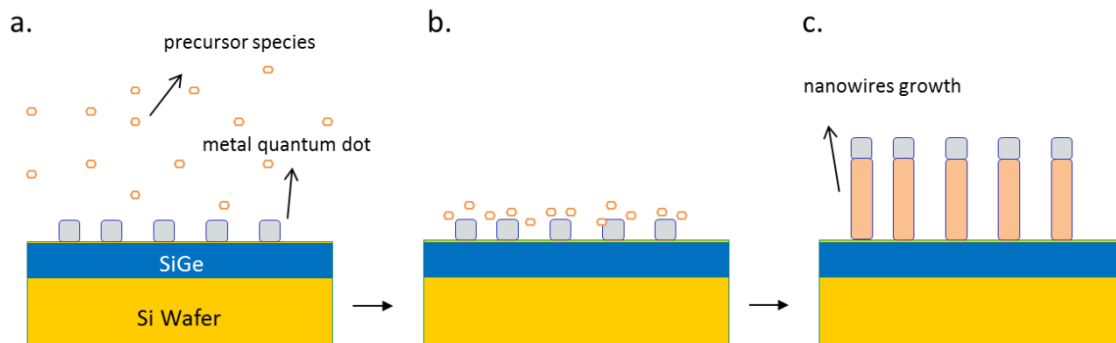


Figure 2.23: Representation of the VSS growth. a) Adsorption of the precursor species onto the Ti nano-islands. b) decomposition and diffusion of Si atoms inside the Ti forming a solid solution. c) saturation of the system and precipitation of silicon as nanowires.

As the deposition reactions are faster because of the catalysis effect, even if some growth occurs onto the substrate in the zones without nano-islands, the growth of the nanowires is faster and dominates the process. In Figure 2.24 SEM images are presented showing nanowires grown during 5, 10 and 50 seconds at 700 °C.

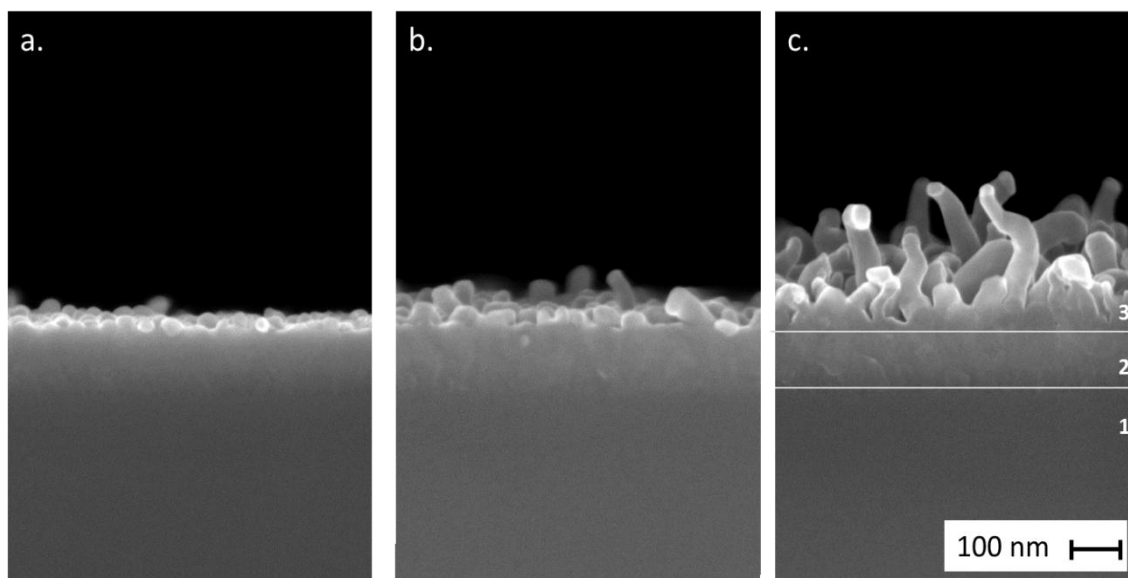


Figure 2.24: Cross section SEM images of nano-islands instead of a continuous layer after the deposition using SiH_4 as precursor gas. a) deposition duration “t” = 5 s. b) t = 10 s. c) t = 50 s. The zone “1” corresponds to the Si wafer, zone “2” to the SiGe thin film substrate and “3” to the embedding layer.

In order to avoid the growth of nanowires, a study was performed by adding GeH_4 to the gases employed for embedding the nano-islands, represented by changing the $\text{SiH}_4/\text{GeH}_4$ gas flow ratios.

In Figure 2.25 are presented the results of the embedding tests performed at 700 °C. First of all it can be observed in Figure 2.25-a the presence of the quantum dots at the top of the wires, which confirms the growth mode as being the VSS. The increase of GeH_4 ratio to 30 % (Figure 2.25-b) reduced the nanowires growth and a further increase to 50% (Figure 2.25-c) provided a homogeneous growth without the formation of nanowires, with the effective embedding of the quantum dots.

A similar study was made at 650 °C (Figure 2.26). It can be seen that a higher proportion of GeH_4 in the embedding gases ($\text{SiH}_4/\text{GeH}_4 = 30/70$) should be employed in order to provide a homogeneous growth instead of the production of nanowires. Moreover, when the embedding layer was deposited at temperatures $T \geq 800$ °C, no nanowires growth was observed, even without GeH_4 additions.

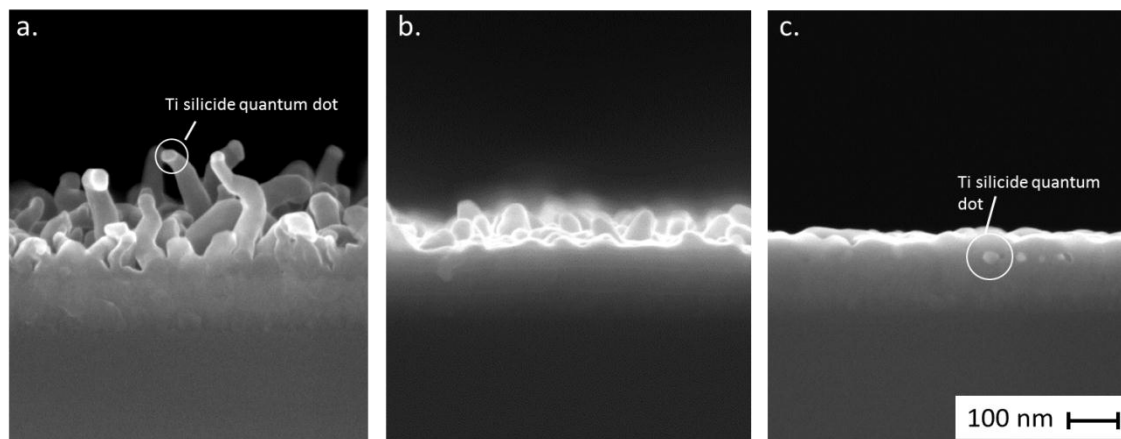


Figure 2.25: Cross section SEM images of nano-islands after the deposition of an embedding layer at 700 °C as a function of the Ge content (expressed as the $\text{SiH}_4/\text{GeH}_4$ gas flow rates of the embedding gases). a) $\text{SiH}_4/\text{GeH}_4 = 100/0$ (pure SiH_4). b) $\text{SiH}_4/\text{GeH}_4 = 70/30$. c) $\text{SiH}_4/\text{GeH}_4 = 50/50$.

Clearly there is a correlation between the deposition temperature and quantity of GeH_4 necessary to provide a homogeneous growth.

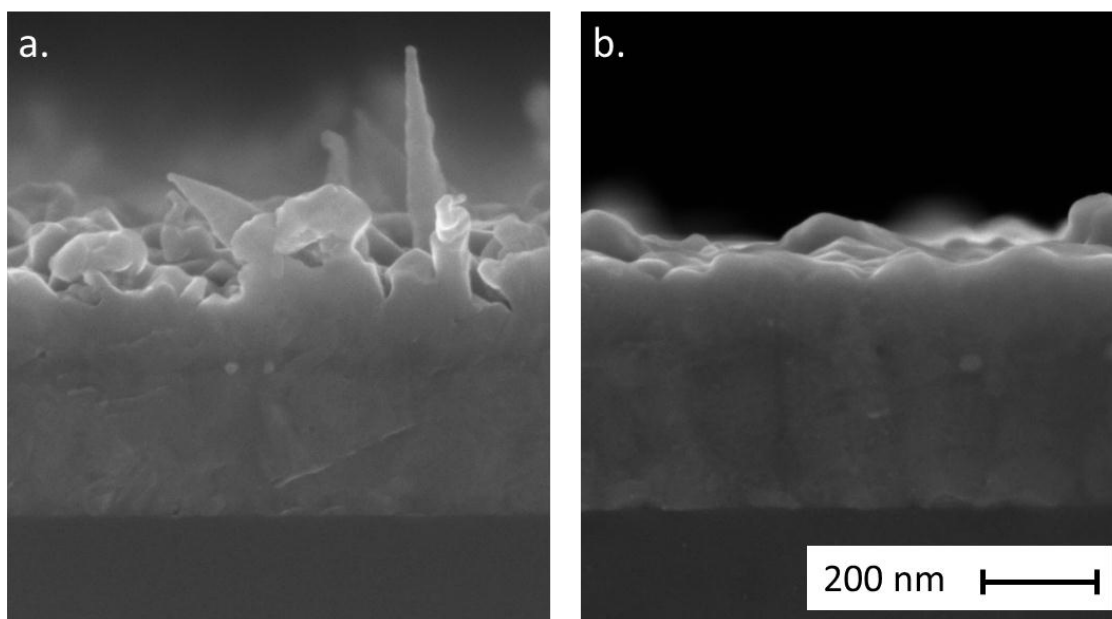


Figure 2.26: Cross section SEM images of nano-islands after the deposition of an embedding layer at 650 °C as a function of the Ge content (expressed as the $\text{SiH}_4/\text{GeH}_4$ gas flow rates of the embedding gases). a) $\text{SiH}_4/\text{GeH}_4 = 50/50$. b) $\text{SiH}_4/\text{GeH}_4 = 30/70$.

A possible mechanism to explain these observations can be provided by a further analysis of Figure 2.4. At low temperatures (growth limited by surface reactions) the energy necessary to activate these reactions is represented by the slope of the right part of the graphic. When GeH_4 is added, a significant decrease of the activation energy is obtained (20,2 against 40,1 kcal/mol for pure SiH_4 in the example). Thus, by adding GeH_4 to the precursor gases employed to embed the nano-islands a reduction of the energy needed to produce the reactions is obtained and the catalysis effect (which can be thought as a local reduction of the activation energy for the reactions) becomes less important. The lower is the deposition temperature, the higher is the difference between the speed of deposition catalyzed by the nano-islands and the deposition on the substrate, and the more GeH_4 is needed to compensate this difference.

3.3.b - High temperature embedding

At high temperatures, no nanowires growth was observed even when pure SiH_4 was employed. The main reason for this is that the reactions take place faster making the deposition speed high enough to compensate the catalyst effect. However another phenomenon was observed, a fraction of the quantum dots migrated to the surface of the embedding layer instead of remaining inside the material (Figure 2.27).

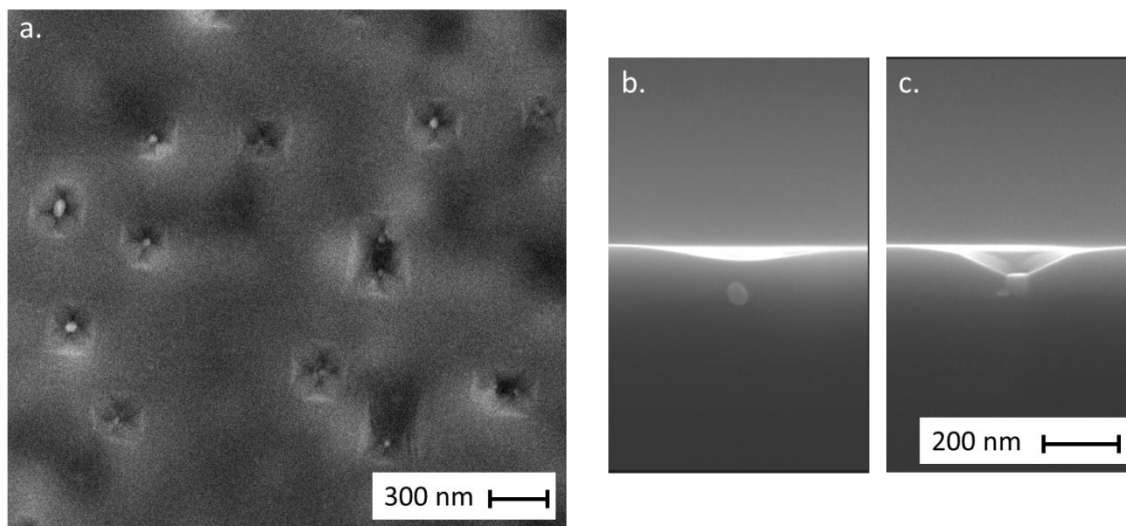


Figure 2.27: Top view SEM images (a) and cross section SEM images (“b” and “c”) of the samples after an embedding deposition at 850 °C. For the same sample, some dots were embedded inside the material (b) while others remained “opened” to the surface (c).

A possible explanation for this phenomenon relies on the diffusion of Ti inside Si and vice-versa. At high temperatures, the mobility of the atoms is high enough to provide enough diffusion and the “movement” of the quantum dots inside the SiGe matrix.

A large number of experimental tests were performed in order to better understand these mechanisms and to prevent the migration of the quantum dots inside the material. Some examples of the variables studied are the Ge content of the embedding layer, the deposition temperature and the deposition duration (thickness of the embedding layer). None of these studies provided conclusive results, and for all the conditions tested a fraction of the quantum dots remained at the surface of the material.

It was observed, however, that when the deposition of Ti and embedding layer was repeated in order to provide the growth of a QDSL, the fraction of quantum dots in the surface was reduced (Figure 2.28 and Table 2.8).

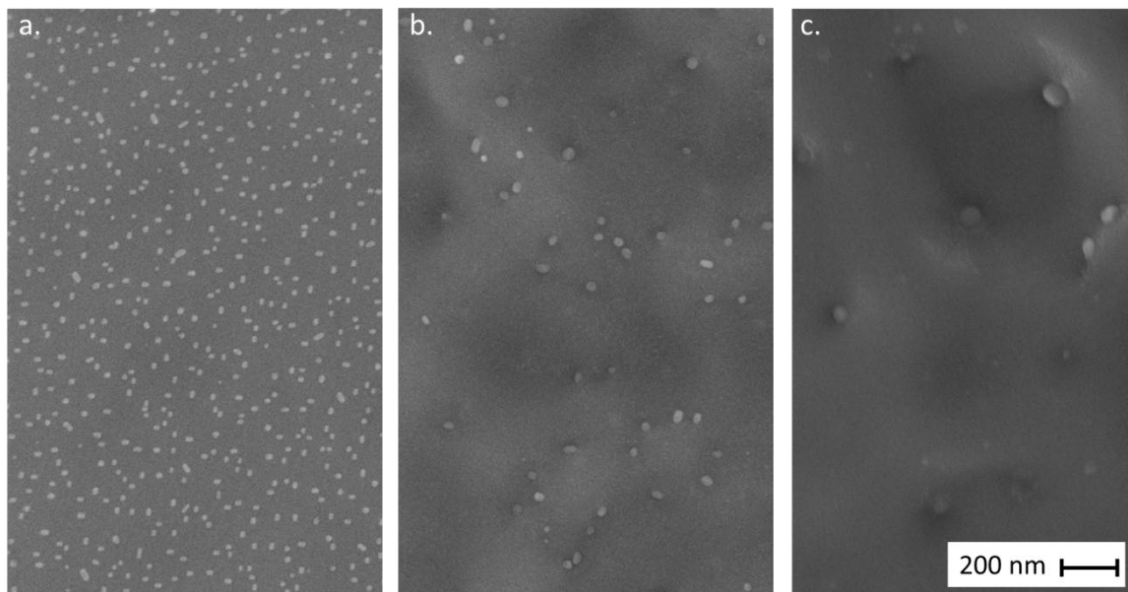


Figure 2.28: Top view SEM images with no embedding layer (a), with 3 nano-islands + 3 embedding layers (b) and with 16 repetitions.

After 16 repetitions of Ti deposition and embedding SiGe layers, the density of quantum dots was reduced from 125 to only 3 μm^{-2} , with an increase of the particles mean diameter, from 26 nm to 65 nm. The probable reason is that while the 16 stacking layers are being grown, the quantum dots coalesce inside the material, increasing their diameter.

The increase of their diameter will then reduce their mobility and at the end fewer quantum dots reach the material surface. Further detailed discussion will be presented in Chapter 3.

Table 2.8: Measures of surface quantum dots as a function of the number of deposited layers.

Number of repetitions	0	3	16
surface coverage (%)	7	4	2
mean diameter (nm)	26	30	65
dots density (μm^{-2})	125	50	3

3.4 - Ti/SiGe QDSL growth

Once the Ti deposition was calibrated and the layer stacking with SiGe embedding was validated, the last step of the work was performed, i.e., the growth of QDSL. The main parameters and aimed properties of the produced QDSL are presented in Table 2.9.

The number of layers was set to 16 and the thickness of each embedding SiGe layer to around 40 - 50 nm. As commented before, the layer thickness was $t_{SiGe} = 2 \cdot D_{NI}$ in order to assure better coverage of the quantum dots.

The number of layers was set then to 16 in order to provide a material with total thickness of approximately 1 μm . A first buffer layer of 200 nm was deposited before the growth of the QDSL for different reasons. The first one is linked to the final Ge content of the layer. As an inter-diffusion between the Ge atoms from the QDSL and the Si atoms from the substrate exists, the final Ge content of the first QDSL layer can be different from the rest of the material. The buffer layer serves in this case in order to lower this effect and produce results similar to those tested during the surface studies. Another expected effect of the buffer layer is to eventually accommodate dislocations produced due to the lattice mismatch between the SiGe thin films and the Si substrate, preventing these dislocations to occur inside the QDSL.

The Ge content of the SiGe layers inside the QDSL was set to around 10 % in order to produce a similar material to those in reference [13]. The deposition temperature for the SiGe layers was chosen to be the same of the Ti deposition, i.e., 850 °C. The

doping level was based on the optimal dopants concentration in order to produce a thermoelectric material with the higher possible power factor, i.e., around 10^{19} - 10^{20} atoms.cm⁻³.

Table 2.9: Correlation between the aimed values and the chosen parameters for the growth of Ti-based QDSL.

<u>variables</u>	<u>aimed values</u>	<u>chosen parameters</u>
Ge content	10 %	SiH ₄ /GeH ₄ = 70/30 sccm
quantum dots properties	D _{Ni} = 20 nm %S = 9 %	TiCl ₄ deposition at 850 °C for 10 seconds H ₂ = 30 SLM
doping	10^{19} to 10^{20} atoms.cm ⁻³ ("n" and "p")	addition of PH ₃ or B ₂ H ₆ during SiGe deposition
SiGe embedding layer thickness	t _{SiGe} = 40 - 50 nm	deposition duration = 20 - 40 seconds
number of layers	n = 16	repetition of Ti and SiGe deposition 16 times

Both mono and polycrystalline QDSL were produced. In order to produce the conditions to the epitaxial growth, an in-situ HCl cleaning step was performed prior to the QDSL deposition. For the polycrystalline growth, no cleaning step was performed. Moreover, the substrate was not the same for both type of QDSL (Figure 2.29). For the polycrystalline growth, a silicon wafer with a 200 nm SiO₂ layer on the surface was employed. The oxide layer was necessary in order to insulate the QDSL from the Si substrate for the electrical characterizations. For the monocrystalline QDSL, a Silicon-on-Insulator (SOI) substrate was chosen. This type of substrate allows the epitaxial growth onto a monocrystalline layer of Si and at the same time to isolate the QDSL from the bulk substrate by a SiO₂ layer.

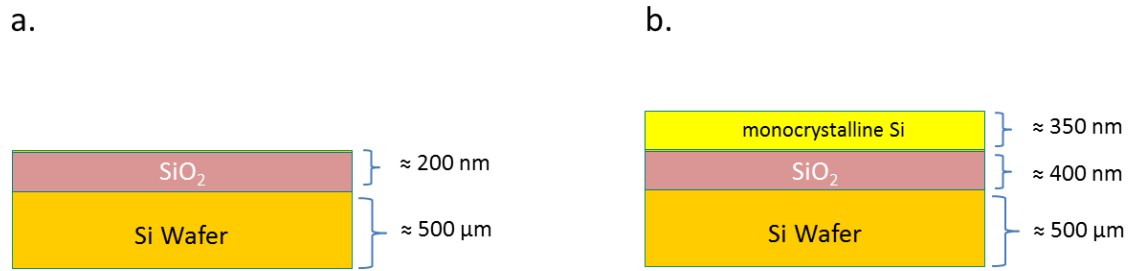


Figure 2.29: Representation of the substrates employed in this work. (a) Substrate employed for the growth of polycrystalline QDSL and (b) the SOI employed for the monocrystalline QDSL.

For each produced QDSL, a reference sample of pure SiGe was grown using the same Ge content and doping level, serving as reference for the thermoelectric characterizations.

In Figure 2.30 are presented SEM images of two QDSL, a monocrystalline and a polycrystalline. Detailed analyses and discussion of the QDSL produced will be presented in Chapter 3.

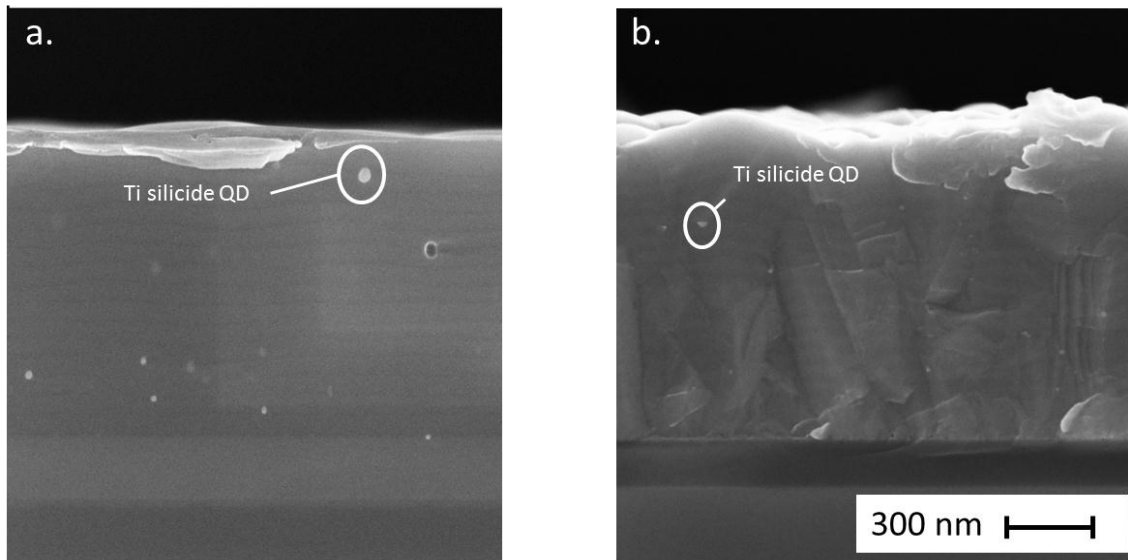


Figure 2.30: Cross section SEM images of a monocrystalline Ti-based QDSL (a) and of a polycrystalline sample (b).

4 - The growth of Mo-based silicide/SiGe QDSL

4.1 - Introduction

Similarly to titanium silicides, molybdenum silicides have also been studied in the literature to produce electrical contacts on solid state chips and can be formed by the *Salicide* process as well [22]. Typically a Mo layer is deposited onto a silicon substrate and a heat treatment with temperatures on the range of 800 – 1000 °C will allow the reaction between the two materials to form preferentially the MoSi₂ phase [23].

The reactions between Mo and Si can produce only three intermetallic stable phases, Mo₃Si, Mo₅Si₃ and MoSi₂ (Figure 2.31). As for Ti-based silicide quantum dots, our presented studies were based on the theoretical works of Mingo et al. in [1] where the inclusion of MoSi₂ quantum dots into a SiGe matrix was studied in order to reduce the materials thermal conductivity.

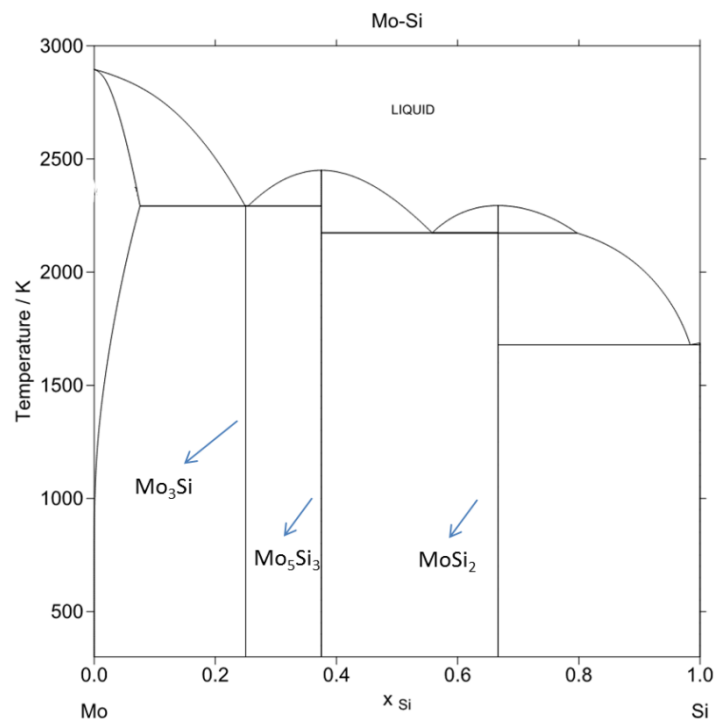


Figure 2.31: The Mo-Si phase diagram. The arrows indicate the composition of the different stable phases.

The strategy employed to grow these QDSL is the same employed for the Ti-based, described in Figure 2.13. The temperature range employed in this thesis for the deposition of the quantum dots coincides with the temperatures employed in the *Salicide* process, thus the reactions between the deposited dots and the substrate are expected to happen during the deposition.

4.2 - CVD deposition of Mo-based nano-islands

Even though there exists fewer references in literature concerning the CVD deposition of MoSi_2 when compared to TiSi_2 , there are some studies reporting the growth of these phase using the same precursor as the one employed in this work, the molybdenum(V) chloride, MoCl_5 .

In reference [24] the authors accomplished the formation of the silicides at temperatures $900\text{ }^\circ\text{C} < T < 1400\text{ }^\circ\text{C}$ using chamber pressures of 37 – 300 Torr. The growth of MoSi_2 by the CVD method was also reported for different temperatures and pressures, namely $520\text{ }^\circ\text{C} < T < 800^\circ\text{C}$ and $0,6\text{ Torr} < P < 2,0\text{ Torr}$ followed by an annealing at $700\text{ }^\circ\text{C} - 1000\text{ }^\circ\text{C}$ [25]. From the last reference, it appears that films deposited at temperatures higher than $800\text{ }^\circ\text{C}$ directly produced the MoSi_2 phase.

It should be noticed that in both references, the authors employed as precursor gas a silicon source (SiH_4 or SiCl_4) at the same time of MoCl_5 to provide Si atoms for the reaction. In the present work, as it was made with the Ti deposition, no silicon precursor was employed during the Mo deposition. As it will be seen in Chapter 3, the atoms from the SiGe layers between the quantum dots reacted with the Mo atoms producing an in-situ silicide phase.

Even if some references exist reporting the CVD deposition of Mo silicide thin films on Si substrate, no publications were found concerning the growth of Mo nano-islands or quantum dots by this method.

Thus, the method employed for the deposition of Mo-based nano-islands was performed in a similar way compared to Ti-based particles. However, some problems were identified during the studies employed to calibrate the deposition parameters. It was observed that the sublimation system (Figure 2.10-c) did not provide reproducible results in a large scale of time, i.e., when results were compared with a time difference of around 30 days.

The main origin of this problem is the conception and operating mode of the sublimation system. Contrary to the evaporator system employed for the Ti precursor, where the carrier gas is bubbled inside the precursor, in the sublimation method the carrier gas only touches the solid Mo precursor surface. It can be assumed that slight variation such as the precursor level inside the container can greatly change the

quantity of sublimated precursor. For future experiments, a modification of the apparatus should be performed in order to provide more reproducible results.

In the present work two studies considering the growth of these Mo-based nano-islands were performed and are presented in the next sections.

4.2.a - Role of deposition temperature

Because of the low quantity of precursor provided by the sublimation system, the Mo-based nano-islands deposition duration was set to 210 seconds and the H_2 carrier gas flow rate was set to 10 SLM in order to minimize the precursor dilution.

The SiGe substrate was grown using a SiH_4/GeH_4 precursor gases ration of 70/30, providing a Ge content of approximately 10%.

Three temperatures were tested, and the results are showed in Figure 2.32 and Table 2.10.

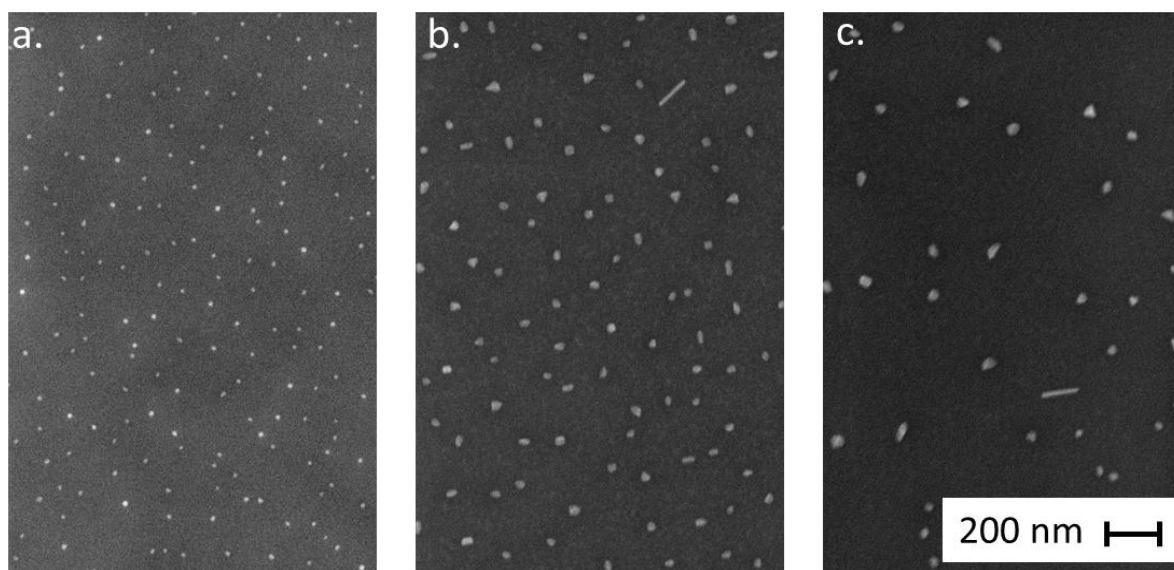


Figure 2.32: Top view SEM images of Mo-based nano-islands grown on monocrystalline $Si_{0.92}Ge_{0.08}$ as a function of deposition temperature. a) $T = 800$ °C. b) $T = 850$ °C. c) $T = 900$ °C.

Table 2.10: Measured Mo-based nano-islands properties as a function of the deposition duration.

Deposition Temperature (°C)	800	850	900
surface coverage (%)	1,7	2,6	1,7
mean diameter (nm)	20	36	51
islands density (μm^{-2})	42	24	8
total islands volume ($10^{-3} \mu\text{m}^3$)	0,2	0,6	0,6
growth rate ($10^{-3} \mu\text{m}^3/\text{min}$)	0,06	0,2	0,2

The deposition was successfully achieved for all the three temperatures tested, even though the growth rate is smaller than the one for Ti deposition. A behavior similar to the one for Ti deposition was observed, i.e., the deposition at higher temperatures lead to a smaller number of larger nano-islands.

The growth rate was smaller at 800 °C and remained constant when the deposition was made at 850 and 900 °C. This could be an evidence of a deposition rate limited by mass transport. In reference [24,25] however, the authors had different results, showing that at these temperatures the growth rate was still dependent on the deposition temperature and concluded that the growth was limited by the surface reactions.

The origin of these differences could be that in the system employed in this thesis all the MoCl_5 entering the chamber was consumed at both 850 °C and 900 °C, and thus a similar growth rate is obtained, i.e., the process is limited by the reactant availability.

These results were sufficient to the determination of the optimal deposition temperature, which was 800 °C. Even if this temperature provided the nano-islands with the diameter closest to the goals of this work (20 nm), the density of particles and surface coverage remained far from the optimal values, with values of 2,6 % against the goal of 9 %.

A further study on the role of the substrate Ge content was essential to increase the particles density and is presented in the next section.

4.2.b - Role of Ge content

In Figure 2.33 are presented the results of the Mo-based nano-islands grown on substrates with two different contents chosen as a function of the $\text{SiH}_4/\text{GeH}_4$ ratio. The studied values were 70/30, producing a Ge content of around 10 % and 85/15, producing a Ge content of around 3 %.

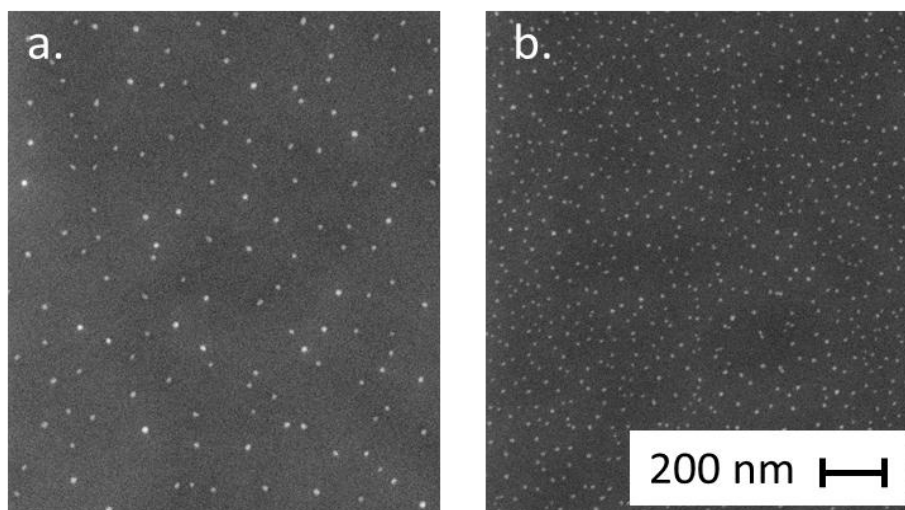


Figure 2.33: Top view SEM images of Mo-based nano-islands grown on monocrystalline SiGe at 800 °C as a function of the substrate Ge content (expressed as the $\text{SiH}_4/\text{GeH}_4$ gas flow rates employed for the substrate growth. a) $\text{SiH}_4/\text{GeH}_4 = 70/30$. b) $\text{SiH}_4/\text{GeH}_4 = 85/15$.

When the Ge content of the substrate was decreased, a higher potential barrier for the surface diffusion of the adsorbed species was obtained, producing a larger number of smaller nano-islands (Table 2.11). The quantity of deposited matter (and the growth rate) did not change, in a similar way to the one observed for the Ti deposition.

The 85/15 precursor ratio produced thus a surface coverage closer to the values needed to meet the requirements assumed for this work, and this Ge content was so chosen for the production of the QDSL.

No phenomenon such as nanowires growth or migration of the particles to the surface were encountered for the embedding of the Mo-based nano-islands, probably because of lower mobility of Mo atoms due to their higher atomic mass compared to Ti atoms.

Table 2.11: Measured Mo-based nano-islands properties as a function of substrate Ge content.

<u>SiGe ratio</u>	<u>70/30</u>	<u>85/15</u>
surface coverage (%)	1,7	4
mean diameter (nm)	22	15
islands density (μm^{-2})	46	247
total islands volume ($10^{-3} \mu\text{m}^3$)	0,2	0,3
growth rate ($10^{-3} \mu\text{m}^3/\text{min}$)	0,06	0,06

4.3 - Mo/SiGe QDSL growth

In Table 2.12 the main parameters employed for the growth of the QDSL are presented.

Table 2.12: Correlation between the aimed values and the chosen parameters for the growth of Mo-based QDSL.

<u>variables</u>	<u>aimed values</u>	<u>chosen parameters</u>
Ge content	3 %	SiH ₄ /GeH ₄ = 85/15 sccm
quantum dots properties	D = 15 nm %S = 4 %	MoCl ₅ deposition at 800 °C for 210 seconds H ₂ = 10 SLM
doping	10^{19} to 10^{20} atoms.cm ⁻³ ("n" and "p")	addition of PH ₃ or B ₂ H ₆ during SiGe deposition
SiGe embedding layer thickness	t _{SiGe} = 30 - 40 nm	deposition duration = 10 - 30 seconds
number of layers	n = 25	repetition of Ti and SiGe deposition 25 times

The main differences compared to Ti-based QDSL were the Ge content of the SiGe matrix, the Mo deposition duration, the SiGe thickness and the number of layers. The number of layers composing the QDSL was changed because as the mean diameter of the particles was smaller (15 nm), the embedding layer thickness was also smaller. To compensate this difference, a higher number of layers was produced in order to obtain a sample with a total thickness similar to the one employed for Ti-based QDSL, i.e., around 1 μm .

In Figure 2.34 are presented SEM images of a mono and polycrystalline samples produced according to the parameters described in Table 2.12. Detailed analysis of these QDSL will be presented in Chapter 3.

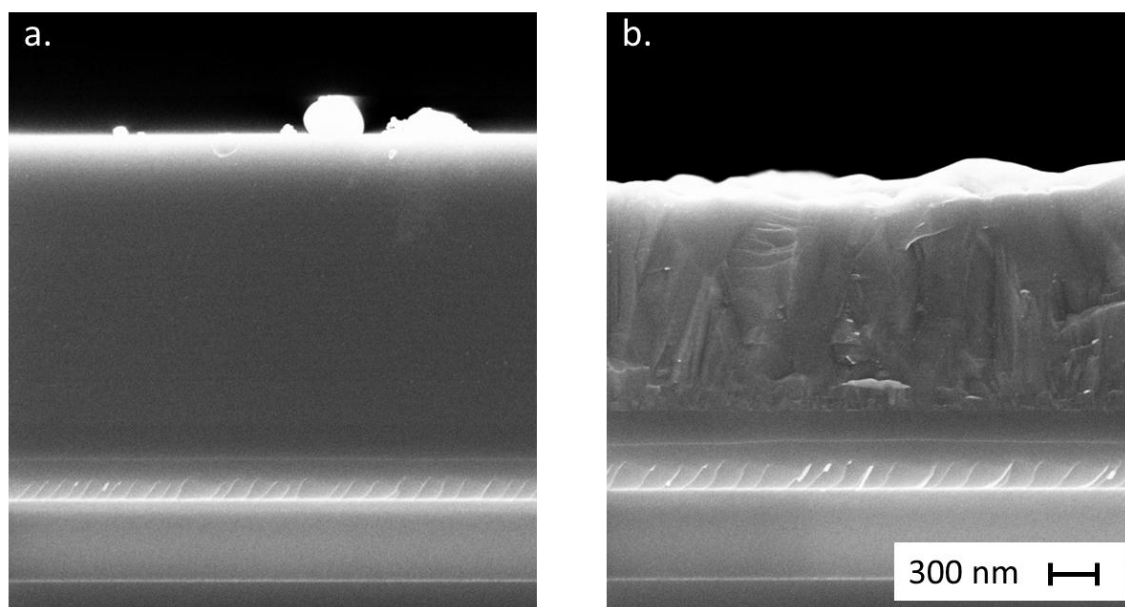


Figure 2.34: Cross section SEM images of a monocrystalline Mo-based QDSL (a) and of a polycrystalline sample (b).

5 - Conclusion

In this chapter the parameters concerning the deposition and growth of metallic (Si and Mo) nano-islands on SiGe surfaces were presented. Both materials were successfully deposited by using a specific evaporation/sublimation apparatus coupled to an industrial CVD tool.

The role of the different deposition parameters was evaluated and the comprehension of the growth mechanisms allowed to produce nano-islands with controlled diameter and surface density. The deposited nano-islands were embedded

with a doped SiGe layer and these steps were repeated in order to successfully produce both mono and polycrystalline QDSL structures.

The structural and thermoelectric characterization of these new nanostructured materials are going to be presented in the following chapter.

REFERENCES

- [1] N. Mingo, D. Hauser, N. P. Kobayashi, M. Plissonnier, and A. Shakouri, “‘Nanoparticle-in-Alloy’ Approach to Efficient Thermoelectrics: Silicides in SiGe,” *Nano Lett*, vol. 9, no. 2, pp. 711–715, 2009.
- [2] D. Kohen, Etude des nanofils de silicium et de leur intégration dans des systèmes de récupération d’énergie photovoltaïque. *Institut National Polytechnique de Grenoble- INPG*, 2012.
- [3] D. Hauser, G. Savelli, M. Plissonnier, L. Montès, and J. Simon, “Growth of heavily doped monocrystalline and polycrystalline SiGe-based quantum dot superlattices,” *Thin Solid Films*, vol. 520, no. 13, pp. 4259–4263, Apr. 2012.
- [4] G. Savelli, D. Hauser, H. Michel, and J. Simon, “Growth, electrical and thermal properties of doped mono and polycrystalline SiGe-based quantum dot superlattices,” in *AIP Conference Proceedings*, 2012, vol. 1449, pp. 275–278.
- [5] L. Masarotto, J. M. Hartmann, G. Bremond, G. Rolland, A. M. Papon, and M. N. Séméria, “Reduced pressure–chemical vapor deposition of high Ge content Si/SiGe superlattices for 1.3 μm photo-detection,” *J. Cryst. Growth*, vol. 255, no. 1–2, pp. 8–18, Jul. 2003.
- [6] E. Bauer, “Phänomenologische Theorie der Kristallabscheidung an Oberflächen. II,” *Z. Krist.*, vol. 110, pp. 395–431, Jan. 1958.
- [7] G. Savelli, “Etude et développement de composants thermoélectriques à base de couches minces,” *Université Joseph-Fourier-Grenoble I*, 2007.
- [8] J. S. Christensen, “Dopant diffusion in Si and SiGe,” *KTH Microelectronics and Information Technology*, 2004.
- [9] D. Hauser, “Elaboration de super-réseaux de boîtes quantiques à base de SiGe et développement de dispositifs pour l’étude de leurs propriétés thermoélectriques,” *Université de Grenoble, UNIVERSITE DE GRENOBLE*, 2011.
- [10] I. Berbezier and A. Ronda, “SiGe nanostructures,” *Surf. Sci. Rep.*, vol. 64, no. 2, pp. 47–98, Feb. 2009.
- [11] J. J. Zhang, A. Rastelli, H. Groiss, J. Tersoff, F. Schäffler, O. G. Schmidt, and G. Bauer, “Shaping site-controlled uniform arrays of SiGe/Si(001) islands by in situ annealing,” *Appl. Phys. Lett.*, vol. 95, no. 18, p. 183102, Nov. 2009.
- [12] D. J. Paul, “Si/SiGe heterostructures: from material and physics to devices and circuits,” *Semicond. Sci. Technol.*, vol. 19, no. 10, p. R75, 2004.
- [13] D. Maury, Siliciuration par depot en phase vapeur pour les technologies cmos avancees : tisi#2 selectif et drain/source sureleves. *INSA TOULOUSE*, 1997.
- [14] R. M. Y. Saeki, “Contributions to the Chemistry of Chlorides of Molybdenum. II. Thermodynamic Properties of Molybdenum Pentachloride,” *Journal of the Electrochemical Society of Japan*, pp. 59–60, 1965.
- [15] P. Gouy-Pailler, Procédé de depot selectif par cvd pour la micro-electronique silicium applications au tungstene et au disiliciure de titane. *INP GRENOBLE*, 1994.
- [16] W. Yang, F. . Jedema, H. Ade, and R. . Nemanich, “Correlation of morphology and electrical properties of nanoscale TiSi₂ epitaxial islands on Si (001),” *Thin Solid Films*, vol. 308–309, no. 0, pp. 627–633, Oct. 1997.
- [17] G. A. D. Briggs, D. P. Basile, G. Medeiros-Ribeiro, T. I. Kamins, D. A. A. Ohlberg, and R. Stanley Williams, “The incommensurate nature of epitaxial titanium disilicide islands on Si(001),” *Surf. Sci.*, vol. 457, no. 1–2, pp. 147–156, Jun. 2000.

-
- [18] T. I. Kamins, D. a. A. Ohlberg, and R. S. Williams, "Deposition and structure of chemically vapor deposited nanoscale Ti-Si islands on Si," *J. Appl. Phys.*, vol. 96, no. 9, pp. 5195–5201, Nov. 2004.
- [19] K. Favier, G. Bernard-Granger, C. Navone, M. Soulier, M. Boidot, J. Leforestier, J. Simon, J.-C. Tedenac, and D. Ravot, "Influence of in situ formed MoSi₂ inclusions on the thermoelectrical properties of an N-type silicon–germanium alloy," *Acta Mater.*, vol. 64, pp. 429–442, Feb. 2014.
- [20] T. . Kamins, R. Stanley Williams, T. Hesjedal, and J. . Harris, "Chemically vapor deposited Si nanowires nucleated by self-assembled Ti islands on patterned and unpatterned Si substrates," *Phys. E Low-Dimens. Syst. Nanostructures*, vol. 13, no. 2–4, pp. 995–998, Mar. 2002.
- [21] I. Berbezier, J. P. Ayoub, L. Favre, A. Ronda, L. Morresi, and N. Pinto, "Vapor–solid–solid growth of Ge nanowires from GeMn solid cluster seeds," *Surf. Sci.*, vol. 605, no. 1–2, pp. 7–11, Jan. 2011.
- [22] J. P. Gambino and E. G. Colgan, "Silicides and ohmic contacts," *Mater. Chem. Phys.*, vol. 52, no. 2, pp. 99–146, février 1998.
- [23] K. . Gesheva, T. Ivanova, D. Gogova, and G. Beshkov, "Formation of MoSi₂ by rapid thermal annealing in vacuum of CVD – Mo films on silicon substrate," *Vacuum*, vol. 58, no. 2–3, pp. 502–508, août 2000.
- [24] J. L. Bobet, G. Vignoles, F. Langlais, and J. L. Bobet, "On the CVD of MoSi₂: an experimental study from the MoCl₄–SiCl₄–H₂–Ar precursor with a view to the preparation of C/MoSi₂/SiC and SiC/MoSi₂/SiC microcomposites," *J. Mater. Sci.*, vol. 33, pp. 4461–4473, Sep. 1998.
- [25] S. Inoue, N. Toyokura, T. Nakamura, M. Maeda, and M. Takagi, "Properties of Molybdenum Silicide Film Deposited by Chemical Vapor Deposition," *J. Electrochem. Soc.*, vol. 130, no. 7, pp. 1603–1607, juillet 1983.

CHAPTER III

Characterization of QDSL for thermoelectric applications

<u>1 - INTRODUCTION</u>	<u>115</u>
<u>2 - STRUCTURAL CHARACTERIZATION.....</u>	<u>117</u>
2.1 - INTRODUCTION	117
2.2 - XRD.....	117
2.3 - TEM ANALYSIS	119
2.3.a - Ti-based QDSL: “n”-doped monocrystalline samples	119
2.3.b - Ti-based QDSL: “n”-doped polycrystalline samples.....	123
2.3.c - Ti-based QDSL: “p”-doped monocrystalline samples.....	126
2.3.d - Ti-based QDSL: “p”-doped polycrystalline samples.....	129
2.3.e - Mo-based QDSL: “n”-doped monocrystalline samples.....	130
2.3.f - Mo-based QDSL: “n”-doped polycrystalline samples	132
2.3.g - Mo-based QDSL: “p”-doped monocrystalline samples.....	134
2.3.h - Mo-based QDSL: “p”-doped polycrystalline samples	136
2.4 - CONCLUSION	138
<u>3 - THERMOELECTRICAL CHARACTERIZATION</u>	<u>142</u>
3.1 - INTRODUCTION	142
3.2 - Ti-BASED QDSL: N-DOPED SAMPLES	146
3.2.a - Monocrystalline QDSL.....	146
3.2.b - Polycrystalline QDSL	150
3.3 - Ti-BASED QDSL: P-DOPED SAMPLES.....	152
3.3.a - Monocrystalline QDSL.....	152
3.3.b - Polycrystalline QDSL	155
3.4 - DISCUSSION ABOUT THE THERMOELECTRICAL CHARACTERIZATION RESULTS OF THE Ti-BASED QDSL ..	157
3.5 - MO-BASED QDSL: N-DOPED SAMPLES.....	159
3.5.a - Monocrystalline QDSL.....	159
3.5.b - Polycrystalline QDSL	161

3.6 - MO-BASED QDSL: P-DOPED SAMPLES	163
3.6.a - Monocrystalline QDSL.....	163
3.6.b - Polycrystalline QDSL	165
3.7 - DISCUSSION ABOUT THE THERMOELECTRICAL CHARACTERIZATION RESULTS OF THE MO-BASED QDSL	167
<u>4 - CONCLUSION</u>	<u>169</u>
<u>REFERENCES</u>	<u>174</u>

1 - Introduction

In this chapter the results of the characterizations performed in order to evaluate the physical and thermoelectrical properties of the Ti and Mo-based QDSL will be presented.

The studied samples were produced using the growth parameters (such as temperature and deposition duration) discussed in Chapter 2. These parameters were chosen in order to produce QDSL with QD diameters d_{QD} and volumetric fraction $\%_V$ as close as possible to the values studied by Mingo et al. [1], i.e., $d_{QD} \approx 15-40$ nm and $\%_V \approx 2-3$ %. For the Ti-based QDSL, the chosen values were $d_{QD} = 20$ nm, and the layer thickness $e = 40-50$ nm. For the Mo-based QDSL, the chosen values were $d_{QD} = 15$ nm, and $e = 30-40$ nm.

There was a difference however between the samples produced in this work and those in the literature concerning the Ge content of the QDSL. Mingo et al. studied samples with 50 % Ge, but for our samples the Ge range varied between 3 and 13 %. As Ge is an expensive material, in this work it was chosen to test samples with a slower Ge content.

The QDSL were produced in such a way so that the role of the dopant (“p” and “n” doping), crystallinity (mono and polycrystalline) and QD material (Ti or Mo-based) were evaluated independently. This was accomplished by varying only one physical quantity and maintaining the other parameters constant, as long as possible.

As it has already been discussed, the materials studied during this thesis have never been produced or reported on the literature (to our knowledge), making it complicated to compare our results and evaluate the role of the QD inclusions inside the SiGe matrix. Even though a relatively similar material was reported made of inclusions of MoSi₂ in a bulk SiGe matrix [2], some problems arise when comparing the literature results with the samples produced during this thesis. First of all, the nature of the material itself is not the same. In the case of polycrystalline thin films, often there is a preferential grain growth along the vertical direction (texture), where for bulk samples the grains tend to be more homogeneous. Moreover, depending on the thin film thickness quantum and surface effects can become visible. The second difficulty when thin films and bulk samples are compared is related to the measurement techniques, which are completely different and sometimes based on different physical phenomena.

In order to bypass these issues, for each QDSL produced, a similar pure SiGe sample was also grown in order to serve as a reference. The reference samples were produced once the electrical conductivity and Ge content of the QDSL were already measured, and an effort was made in order to produce SiGe samples with similar values of electrical conductivity and Ge content for the QDSL. By doing this, it was

possible to evaluate the role of the QD inclusion on the materials Seebeck coefficient and on the thermal conductivity.

Moreover, a large series of calibration studies was performed in order to calculate the growth rate, the role of SiH_4 and GeH_4 on the Ge content and of the dopant gases on the doping level for each sample. The information obtained from them was essential for the production of the characterized QDSL. The Ge content for the Ti-based QDSL was set to around 10 %, which are close to the values studied in reference [2]. For the Mo-based samples, it was not possible to obtain this Ge content and a lower Ge percentage (3%) was necessary in order to produce a $\%_V$ not too low (see Chapter 2).

A description of the QDSL evaluated in this chapter is presented in Table 3.1.

Table 3.1: Description of the produced QDSL.

<u>sample</u>	<u>QD inclusion</u>	<u>dopant</u>	<u>crystallinity</u>
Ti-n-MONO	Ti	n (PH_3)	monocrystalline
Ti-n-POLY			polycrystalline
Ti-p-MONO		p (B_2H_6)	monocrystalline
Ti-p-POLY			polycrystalline
Mo-n-MONO	Mo	n (PH_3)	monocrystalline
Mo-n-POLY			polycrystalline
Mo-p-MONO		p (B_2H_6)	monocrystalline
Mo-p-POLY			polycrystalline

2 - Structural characterization

2.1 - Introduction

The first results concerning the QDSL characterizations consisted on structural analysis such as X-Ray Diffraction (XRD), Scanning Electronic Microscopy (SEM) and Transmission Electronic Microscopy (TEM).

SEM images were very useful during the initial depositions performed to measure the samples thickness and calibrate the growth rate for each QDSL. This technique requires no complex sample preparation, is relatively cheap and the equipment is easy to operate compared to TEM analysis. This technique was also employed to measure the final thickness of the QDSL, a necessary parameter for the electrical resistivity measurement.

However, these images lack of magnification and contrast to serve as a tool to analyze the QD inclusions. For this reason, in this chapter only TEM images will be presented, since they provide similar results but with a much greater quality.

2.2 - XRD

The X-Ray Diffraction (XRD) technique employed in this work consisted on the Grazing Incidence Diffraction mode, which results on a smaller penetration of the X-rays inside the sample due to the low incidence angle employed. By doing this, the noise from the substrate is reduced and only the thin film on the surface is analyzed.

XRD analyses were employed in this work for two main reasons. The first one was to determine the phases of the deposited QD. In Figure 3.1 is provided an example of an XRD analysis. It concerns the XRD of two samples, one with Ti QD deposited only on the surface of SiGe and another one concerning a sample where the Ti nanoparticles were embedded inside the SiGe matrix using the same method as the one employed for growing QDSL.

It can be seen that when the QD are deposited on the surface, the main phase present is metallic Ti. When this deposition is followed by the growth of an embedding layer of SiGe, the reaction between Si and Ti atoms take place and the QD form silicide phases. This confirms our expectations discussed in Chapter 2, where the metallic atoms were expected to react with Si during the QDSL growth.

It is important to notice however that the results presented in Figure 3.1 concern initial tests, with different conditions than those employed for growing the QDSL.

These depositions were made at a lower temperature (750 °C) than the temperature employed for the Ti QDSL growth (850 °C). Moreover, the QD had bigger diameters and the surface coverage was higher. When similar XRD analyses were performed on the samples containing the optimal QD sizes and distribution, no signal was observed, even when 36 hours analyses were performed.

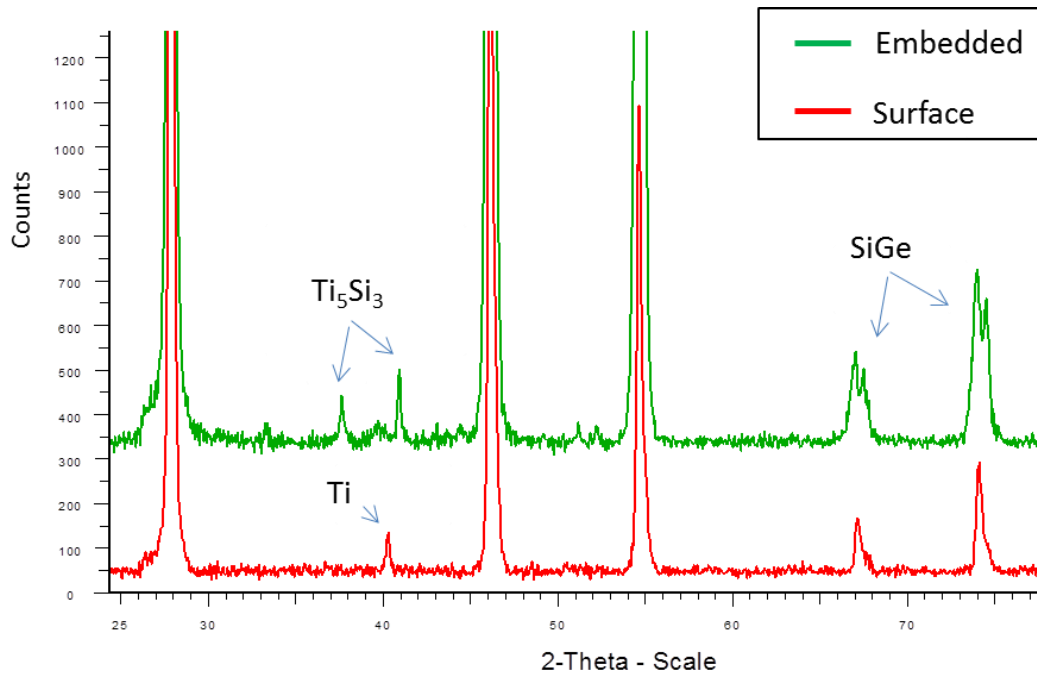


Figure 3.1: XRD analysis of two samples. The lower spectrum (red) corresponds to a surface deposition of Ti QD. The upper one (green) corresponds to a similar sample but in this case the QD were embedded inside the SiGe matrix.

Because of this, it is not clear if at 850 °C the deposited QD react directly with the substrate or if they react with the embedding SiH₄ to form the silicide phases. Anyway, the presence of silicide phases on the final QDSL materials was observed on the SEM images (section 2.3 -).

The second reason why XRD analyses were important for this work was in order to calibrate the Ge content of the samples. It was shown in Chapter II that Si and Ge mixtures produce a solid solution for any Ge content and the final lattice parameter is proportional to the Ge content. The difference on the lattice parameter causes a shift of the Si peaks on the XRD spectrum, and the Ge content can be extracted.

The limitation of this technique is that it can only be employed for polycrystalline samples. In this work, thus, the calibration of the Ge content for the QDSL and the reference samples was performed using the XRD technique for the polycrystalline

materials. This allowed determining the necessary $\text{SiH}_4 / \text{GeH}_4$ ratio to obtain the desired final Ge content. For the monocrystalline samples growth, the same behavior was assumed and the same $\text{SiH}_4 / \text{GeH}_4$ ratio was maintained.

2.3 - TEM analysis

The TEM analysis were performed with a 200 kV equipment including a Scanning mode (STEM) which allows to acquire both high resolution images and chemical mapping using the Energy-dispersive X-ray spectroscopy (EDX) technique. The samples were prepared using the tripod polishing technique.

These features made possible the acquisition of three types of images. The first one consisted on global cross-plane views of the QDSL, allowing to measure the QD diameters, each layer thickness and the total thickness of the samples.

The second mode employed were the high resolution images, made to analyze individual QD in order to determine the distance between the crystallographic planes and to determine the phase of the particle.

Finally, the third class of images obtained with the TEM equipment was the chemical mappings obtained with the EDX technique coupled with the STEM mode. This technique is based on the X-ray emission due to the relaxation of excited electrons which assume discrete and particular energy values for each element of the periodic table. The obtained chemical mapping produced then high spatial resolution images showing the position of the different elements forming the material, and was very useful to estimate the Ge content of the samples, as well as to confirm the phase of the QD.

Following the results of these analyses will be presented for each one of the QDSL described on Table 3.1. At the end of this section a discussion will be performed concerning the obtained results and comparing the growth for each one of the presented samples.

2.3.a - Ti-based QDSL: “n”-doped monocrystalline samples

As a starting point, the results of the n-doped Ti-based QDSL structural analyses will be discussed. In Figure 3.2 the overall view of the “Ti-n-MONO” mono sample is presented.

By analyzing this image different informations can be obtained. First, inside the zone named “1” in Figure 3.2-a some dislocations between the SOI substrate and the sample buffer layer can be identified. These dislocations indicate that the SiGe thin film is relaxed, with the lattice parameter of QDSL corresponding to the Ge content of the material.

Another interesting information obtained from this image is that the particles of the lower layers appear to be smaller than the ones of the upper layers.

By further magnifying zone “2” (Figure 3.2-b) it is possible to measure the QD diameter “ d ” and the layer thickness “ e ”. A statistical measurement of this image provide the mean value of $d_{QD} = 66$ nm and $e = 70$ nm. The aimed values were $d_{QD} = 20$ nm and $e = 40 - 50$ nm.

It is important to notice that the value of the QD diameter is around three times higher than the measured mean value of the nano-islands diameters deposited on the SiGe surface (Chapter 2). This indicates that some coalescence occurred between the QD during the QDSL growth.

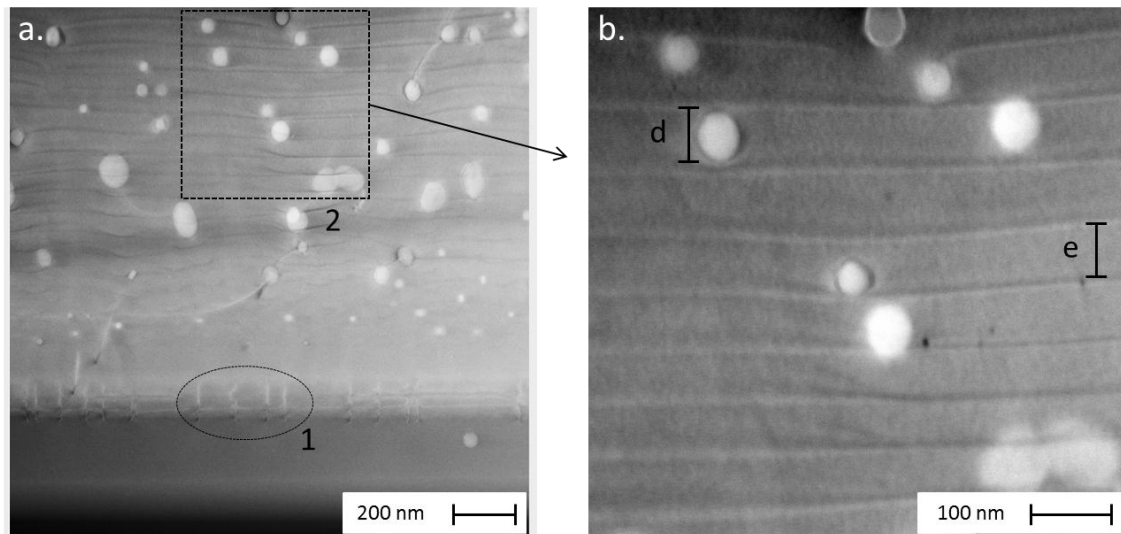


Figure 3.2: Cross-section TEM image of the “Ti-n-MONO” sample. a) global view showing the Ti-based QD and dislocations between the substrate and the buffer layer (1). b) higher magnification of zone “2” showing a QD diameter of $d = 66$ nm and a layer thickness $e = 65$ nm.

The explanation for this phenomenon is the high mobility of the QD inside the SiGe matrix. It was demonstrated on Chapter 2 when the embedding of the nano-islands was discussed that a percentage of the particles migrated to the surface of the sample during the embedding with SiGe. The same mechanism is observed here, but

instead of migrating up to the surface, the QD coalesce inside the material, resulting on particles with higher diameters.

Surface images of the finished QDSL showed no QD on the surface, thus it can be concluded that when the QD reach a critical diameter their mobility inside the SiGe matrix is lowered and they remain inside the material.

It should be pointed that the increase on the QD diameter produced by the coalescence effect results on a reduction of the volumetric fraction $\%_v$ of the QD inside the SiGe matrix. Both the increase of the QD diameter and the reduction of the volumetric fraction can reduce the expected effect on the phonons diffusion (and on the reduction of the thermal conductivity), since the values obtained are not those studied by reference [1].

In Figure 3.3 is presented a high resolution image of one QD inside the “Ti-n-MONO” sample.

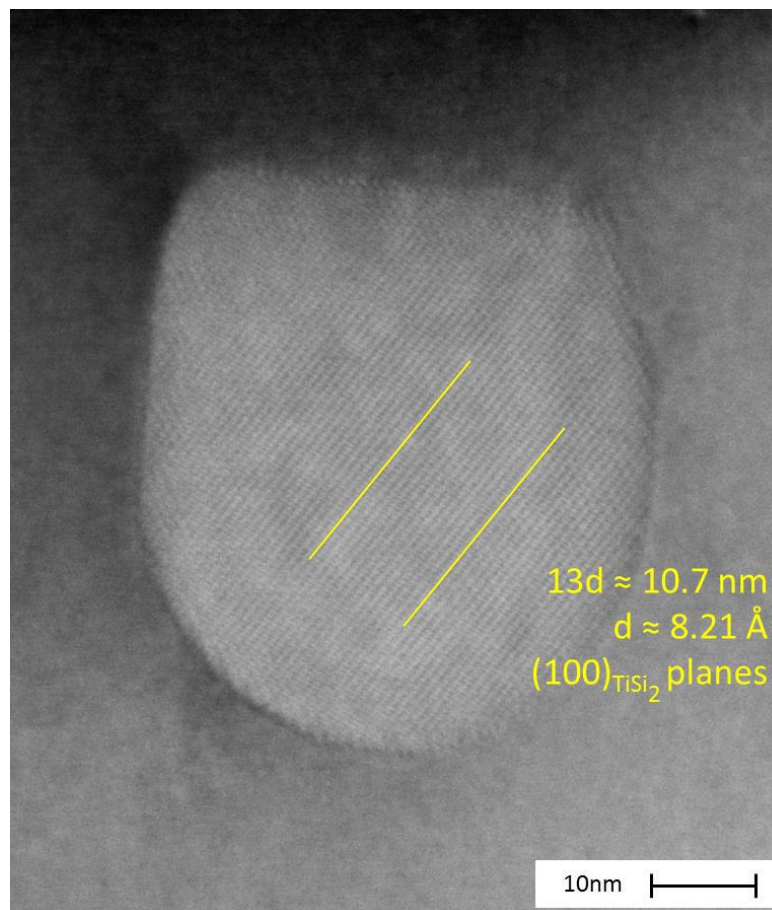


Figure 3.3: High resolution TEM image of a QD inside the “Ti-n-MONO” sample. The planes distances correspond to the (100) planes of the TiSi₂ phase.

In the case of this QD, the measure of the planes distance resulted on $d \approx 8.21 \text{ \AA}$, which corresponds to the (100) TiSi_2 planes, which is the expected phase for this material. As no statistical studies were performed, however, it is possible that other QD with different crystalline phases could also exist inside this sample.

The EDX chemical mapping of the sample is presented in Figure 3.4. Two basic informations can be obtained from these images. First, by looking at the Ti signal (Figure 3.4-d), it is clear that the QD are rich in Ti atoms, confirming the measurements discussed above.

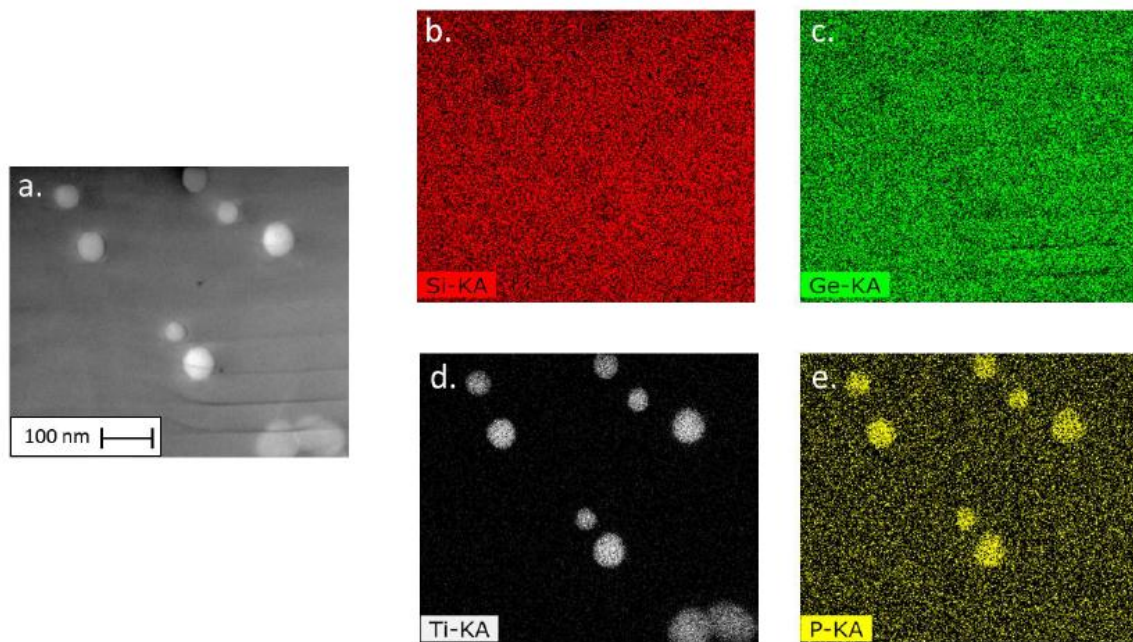


Figure 3.4: EDX chemical mapping of the sample “Ti-n-MONO”. a) STEM image. b) Si signal. c) Ge signal. d) titanium signal and e) phosphorus signal. Note the correspondence between the QD, the Ti and P signals.

The second important information can be obtained by analyzing the dopant (phosphorus) signal (Figure 3.4-e). An accumulation of phosphorus is observed in the zones corresponding to the QD, probably due to a chemical affinity between the two materials. A similar result was observed by [2]. In this reference, however, the inclusions were Mo-based QD. The accumulation of dopant could affect the thermoelectric properties in a few ways, which will be further discussed in this chapter.

A punctual EDX analysis inside the SiGe embedding layer resulted on a Ge content of 12.7 % (atomic fraction), which is close to the 10 % goal, considering the

measurement errors. The same analysis was performed inside a QD, and a Ti content of 31 % was obtained, confirming that the QD phase is TiSi_2 .

2.3.b - Ti-based QDSL: “n”-doped polycrystalline samples

Considering the polycrystalline “n”-doped Ti-based QDSL, a global cross-section TEM image is presented in Figure 3.5-a. Two distinct zones were selected, named “1” and “2”. It can be seen that a difference on the QD density between these two zones exist, the zone “2” being richer in QD than the zone “1”.

By looking at the Figure 3.5-b it is observed that actually zone “2” corresponds to an individual grain and the particles tend to agglomerate in the grain boundaries. This effect was already observed during the studies considering the surface growth described in Chapter 2 and could affect the expected effect on the reduction of the thermal conductivity, since there is an inhomogeneity of QD inside the material. The probable reason for the preferential growth near the grain boundaries is that these highly disordered sites lower the energy for the nucleation of the Ti phase.

By measuring statistically the particles and the layers of this sample, a mean QD diameter of $d_{QD} = 42$ nm and a thickness $e = 54$ nm are obtained. It should be remembered that for the polycrystalline sample the mean diameter when the surface growth was performed was also around 20 nm (Chapter 2).

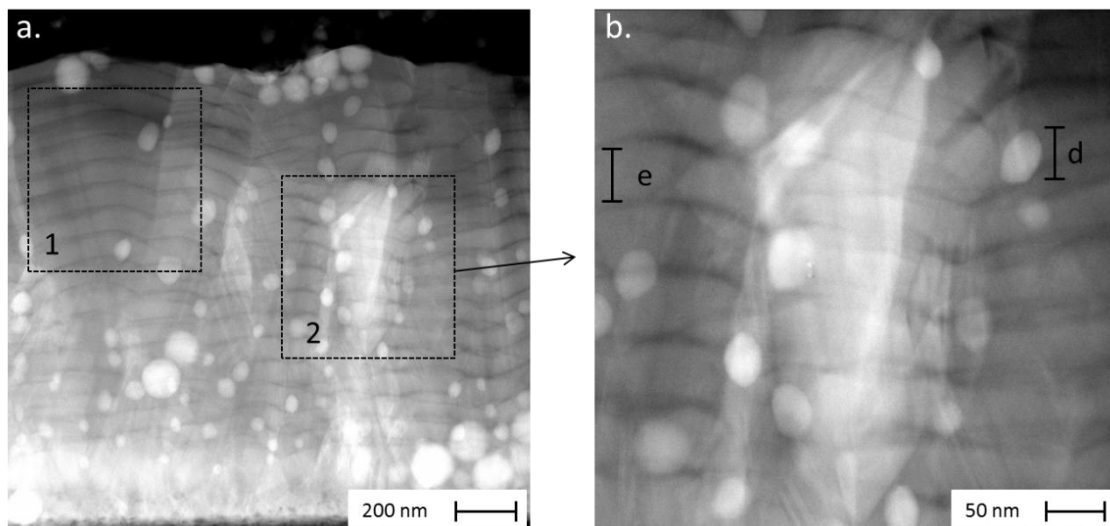


Figure 3.5: Cross-section TEM image of the “Ti-n-POLY” sample. a) global view showing the Ti-based QD and two zones with different QD densities, “1” and “2”. b): higher magnification of the image showing a SiGe grain and a QD with diameter $d = 44$ nm and a layer thickness $e = 50$ nm.

Once again, it is observed that the particles of the lower layers corresponding to the first stages of the QDSL growth are smaller than the upper QD. These two features indicate that in the polycrystalline sample there is also a coalescence occurring during the growth, but in a smaller scale than for the monocrystalline sample, since the mean diameter in this case (42 nm) is smaller than for the monocrystalline QDSL (66 nm). It is probable that the grain boundaries act as barriers for the diffusion of the QD inside the matrix, reducing the coalescence effect.

In Figure 3.6 is presented the high resolution image of an individual QD inside the Ti-n-POLY sample. In this image two set of planes were identified, corresponding to the distances of the $(1\bar{1}0)$ and (210) planes of the Ti_3Si tetragonal phase. A different phase is thus obtained when a polycrystalline material is produced. In this case, the obtained phase (Ti_3Si) is much richer in Ti than the expected phase ($TiSi_2$), suggesting that the reaction between Si and Ti was slower.

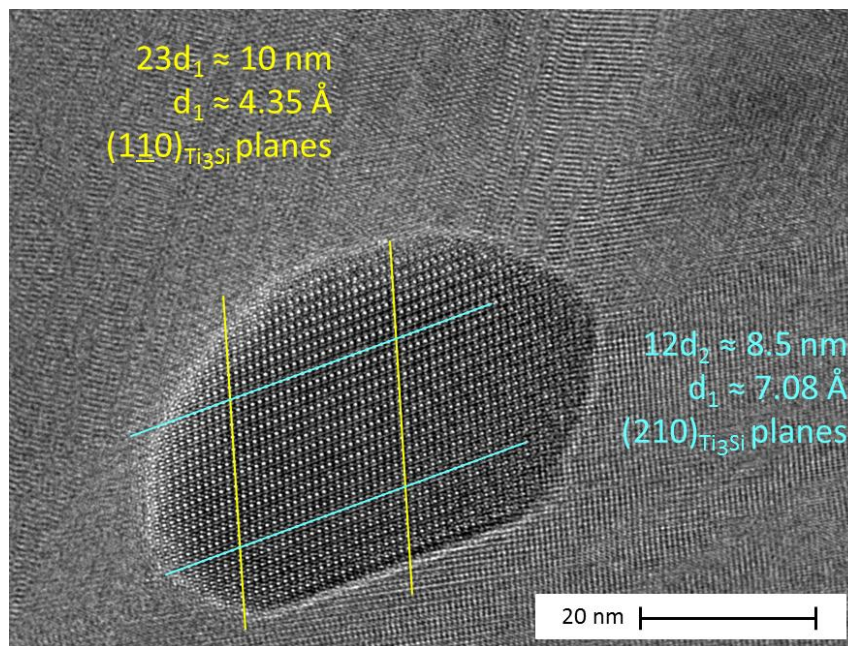


Figure 3.6: High resolution TEM image of a QD inside the “Ti-n-POLY” sample. The planes distances correspond to the $(1\bar{1}0)$ and (210) planes of the Ti_3Si tetragonal phase.

However, as a statistical study was not possible in order to determine if all the QD of the polycrystalline QDSL corresponded to this phase this assumption should be taken with caution and further studies should be performed to better understand the mechanisms leading to the formation of Ti silicides during the growth of polycrystalline QDSL.

The EDX chemical mapping for this sample is presented in Figure 3.7. The informations obtained from these analyses are very similar to those for the “Ti-n-MONO” sample, i.e., the correspondence between the QD, the Ti and the P dopant signals.

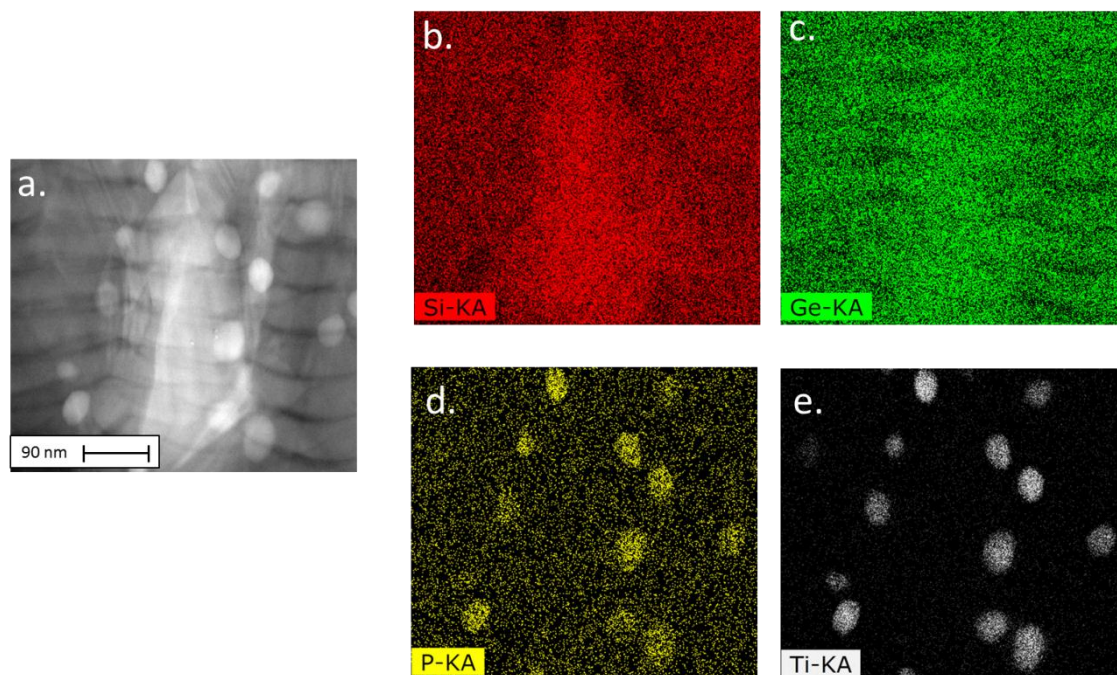


Figure 3.7: EDX chemical mapping of the sample “Ti-n-POLY”. a) STEM image. b) Si signal. c) Ge signal. d) phosphorus signal and e) titanium signal. Note the accumulation of the P dopant in the QD zone.

Quantitative EDX analysis of the matrix provided a Ge content of 12 %, which is the same value obtained for the monocrystalline sample. This result validates the methodology of calibrating the Ge content using XRD for polycrystalline samples and using the same $\text{SiH}_4/\text{GeH}_4$ ratios for producing monocrystalline SiGe materials with the same Ge content. It was also performed a quantitative analysis of a single QD, and a Ti content of 70 % was obtained, which is close to the value corresponding to the Ti_3Si phase (Ti =75 %).

2.3.c - Ti-based QDSL: “p”-doped monocrystalline samples

In this section the results of the structural characterization of the Ti-based “p”-doped samples will be presented. In Figure 3.8 are presented the TEM images of the monocrystalline sample.

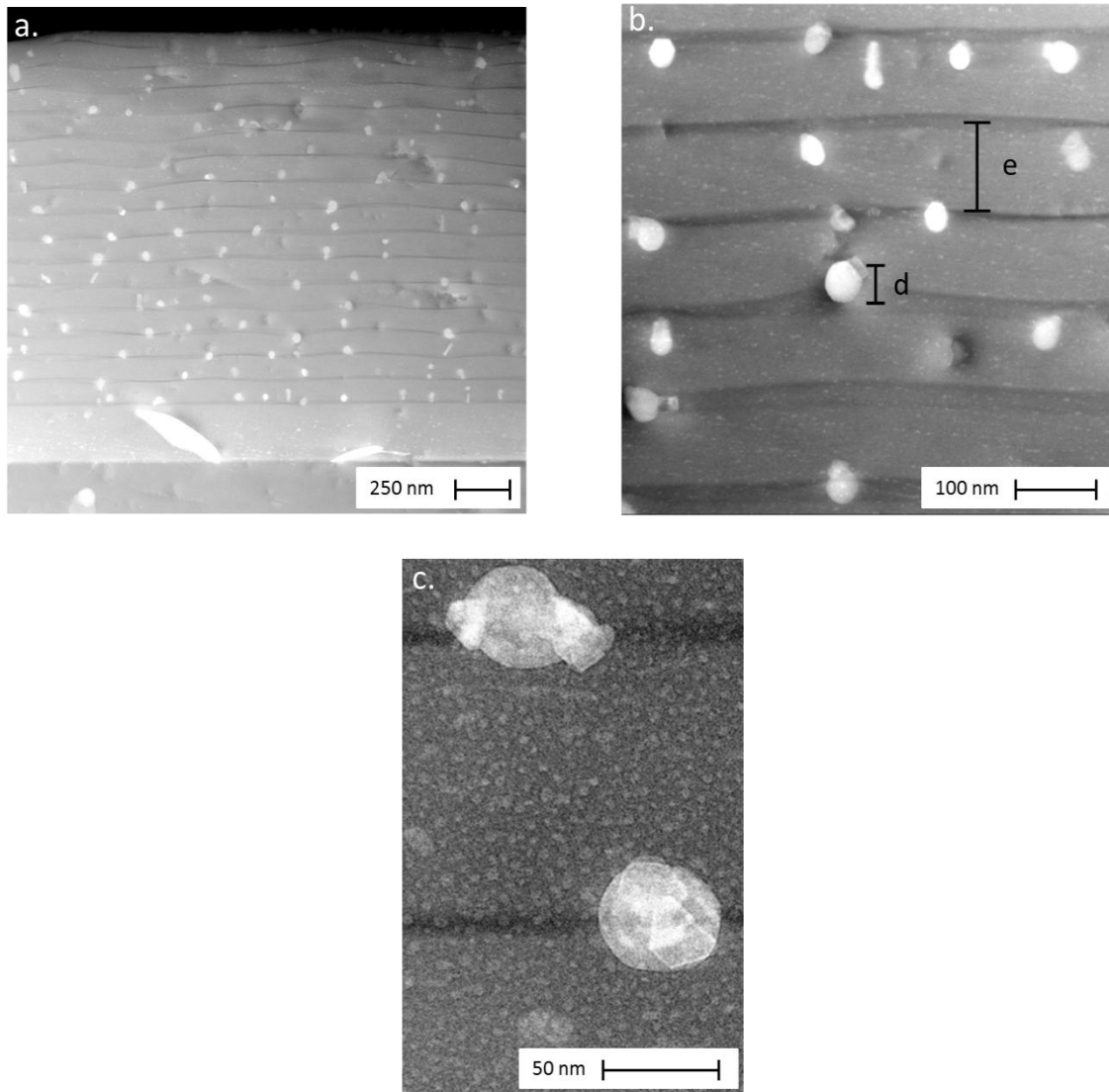


Figure 3.8: Cross-section TEM image of the “Ti-p-MONO” sample. a) global view showing the Ti-based QD . b) higher magnification of the image showing a QD diameter of $d = 50$ nm and a layer thickness $e = 108$ nm. c) high magnification image showing the position of the QD on the SiGe layers.

By analyzing the obtained images and statistically calculating the mean QD diameters and layers thickness, values of $d_{QD} = 34$ nm and $e = 110$ nm are obtained.

The high variation between the aimed thickness (40 - 50 nm) and the obtained (110 nm) comes from the difference of the growth rate when the sample is doped with boron ("p"-doping) rather than with phosphorous ("n"-doping). In the case of this sample no or only little coalescence occurs, since the values of 30 nm are close to the surface measurements. This can be visually confirmed by analyzing the difference between the QD diameters on the lower and on the upper layers in Figure 3.8-a.

Two possible reasons exist to explain why in this case the coalescence is not observed. The first one is due to the higher layer thickness "e" obtained (110 nm) compared to the "n"-doped sample (70 nm). This results on a greater distance for the QD to travel inside the material in order to reach another QD of the upper layer and coalesce.

However, a further look at Figure 3.8-c shows that the QD appear to be exactly on the beginning of a new SiGe layer, i.e., the QD probably did not migrate inside the material during the growth. This fact leads to another possible explanation, that the boron dopant atoms could reduce the QD diffusion inside the material. Further experiments should be performed, in particular reducing the layers thickness to values comparable to those of the "n"-doped sample in order to understand the differences obtained on the coalescence for the two samples.

Another information obtained by further looking at Figure 3.8-a concerns the absence of dislocations between the buffer layer and the substrate. In this case no dislocations are visible, contrary to the "n"-doped sample. By looking at Figure 2.9 (Chapter 2) it can be seen that both samples (with total thickness > 1 μm) fall inside the metastable zone, where dislocations may or may not be present. However, the "n"-doped sample have a higher Ge content (around 13 %) compared to the "p"-doped (around 10 %). This higher Ge content causes thus an increase of the internal stress up to the point of the creation of dislocations.

In Figure 3.9 is presented the high resolution image of a QD inside the "Ti-p-MONO" sample. No difference was noticed comparing this QDSL to the "Ti-n-MONO" sample in terms of obtained Ti phase (TiSi_2).

In Figure 3.10 is presented the chemical mapping of the sample. Here again a good correspondence between the QD and the Ti signal exists. Moreover, there is also an accumulation of the dopant near the QD, even if in this case it concerns boron atoms instead of phosphorus.

Additional information can be obtained from these images. For instance, by looking at Figure 3.10-c it can be seen that there exists a zone with a deficiency of Ge, which corresponds to the beginning of each layer forming the QDSL.

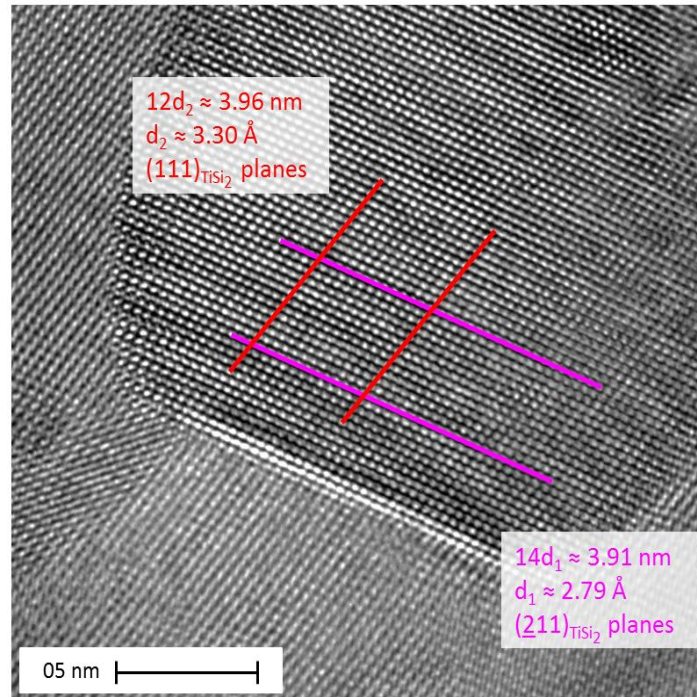


Figure 3.9: High resolution TEM image of a QD inside the “Ti-p-MONO” sample. The planes distances correspond to the (111) and (211) planes of the TiSi_2 phase.

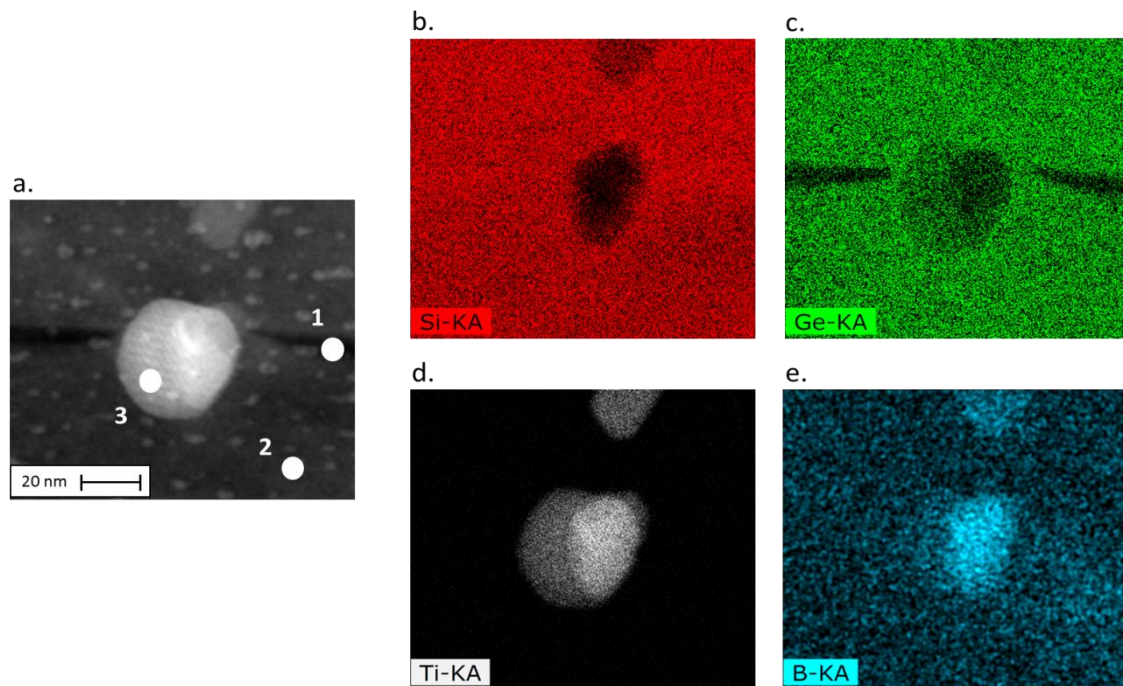


Figure 3.10: EDX chemical mapping of the sample “Ti-p-MONO”. a) STEM image. The points “1”, “2” and “3” correspond to the zones where a relative atomic percentage was measured b) Si signal. c) Ge signal. d) titanium signal and e) boron signal. Note the accumulation of the B dopant in the QD zone.

This indicates that when the QDSL are grown there is also the formation of a Multiple Quantum Well (MQW) structure with quantum wells of around 15 nm thick. Both the quantum wells and the intermediate layers are formed of SiGe phases, but with a different Ge content.

Local EDX analysis showed that the Ge content of point “1” (Figure 3.10-a), which corresponds to a point inside the quantum well, is 3 % where the content of point “2” is 10 %. Point “3”, corresponding to the QD presents a Ti content of 31 %, which is very close to the content expected of the measured phase TiSi_2 .

Some hypotheses exist to explain the formation of a MQW structure. One could imagine that possibly the reaction between Si atoms from surroundings with Ti nano-islands could lead to a reduction of Si from these zones. However in the present work the opposite occurs, the QW zones being richer in Si than the intermediate areas.

Probably the phenomenon taking place during the growth is related to the catalytic properties of the QD, evidenced by the growth of Si nanowires as demonstrated in Chapter 2. It was concluded that the Ti QD catalyzing effect was only observed for the SiH_4 precursor, and for the GeH_4 gas it was either inexistent or occurred in a lower rate. Thus at the beginning of the growth of each layer forming the QDSL the catalytic effect can be seen until the Ti QD are fully embedded inside the material, producing a film that is richer in Si. Once the QD are no longer on the surface, the catalyst effect is no longer present and the “normal” Ge content is obtained, i.e., a higher Ge content.

Concerning the expected thermoelectric properties for this sample, some comments will be at the end of this section. Even though in the case of this sample a QD diameter close to the values studied by the literature were obtained, the layers thickness was almost 2 times bigger than the layer thickness necessary to produce a volumetric fraction $\%_v$ of 3 % (60 nm), the value studied in reference [1].

It can thus be expected in the case of this sample that the reduction on the thermoelectric conductivity will be lower than the predicted by the theory.

2.3.d - Ti-based QDSL: “p”-doped polycrystalline samples

It was not possible to obtain TEM images and EDX chemical mapping of the “Ti-p-POLY” due to lack of availability of the microscope. The SEM image of the sample is presented in Figure 3.11.

Even if it is not possible to visually identify and analyze the QD for this sample, the thermoelectrical properties were measured and will be presented in the second half of this chapter.

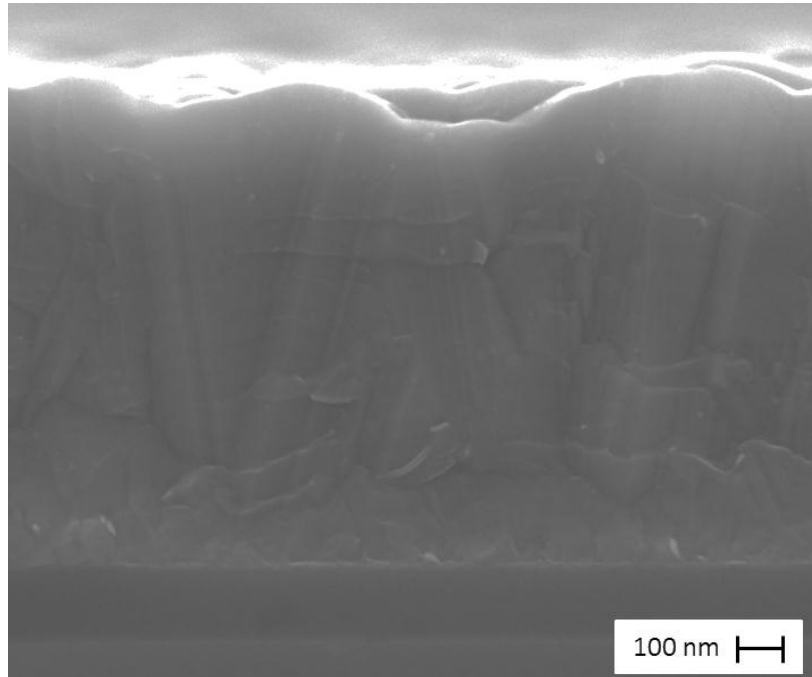


Figure 3.11: Cross-section SEM image of the “Ti-p-POLY” sample.

2.3.e - Mo-based QDSL: “n”-doped monocrystalline samples

In Figure 3.12 are presented the TEM images of the monocrystalline “n”-doped Mo-based sample. A measurement of the QD diameters in Figure 3.12-b provided a mean value of $d_{QD} = 5$ nm and a layer thickness $e = 50$ nm. This indicates that no coalescence effects took place in the case of this sample.

It should be noticed that the “ d_{QD} ” value is around 3 times smaller than the value obtained from the surface studies (Chapter 2), the reason for this being the instability of the sublimation apparatus. Also the layer thickness “ e ” is also bigger than the aimed range of 30 – 40 nm. This variation comes from the difficulty of precisely measuring the layer thickness during the calibration tests and thus to have a precise growth rate. If more time was expended during the calibration tests, a more precise growth rate value could be obtained.

Even if the obtained “ d_{QD} ” of 5 nm still falls inside the optimal range studied in reference [1], the big difference between the “ d_{QD} ” and the “ e ” results on a lower volumetric density “ $\%_v$ ”, which can reduce the expected reduction of the thermal conductivity. Ideally, in order to obtain the aimed “ $\%_v$ ” of around 3 %, “ e ” should be equal to $2 \times d_{QD}$ (see Chapter II).

Another information that can be obtained by looking at Figure 3.12-a is that there is a considerable variation of the QD sizes and densities when different layers are compared. Here again the main reason for this fact is that the sublimation system employed to deliver gaseous MoCl_5 was not as reproducible and stable as the evaporation system employed for the Ti-based samples.

In the case of this sample it was not possible to perform a high resolution analysis due to difficulties to obtain an analysis angle allowing a diffraction condition. Thus, the QD phase determination was relied solely on EDX analysis.

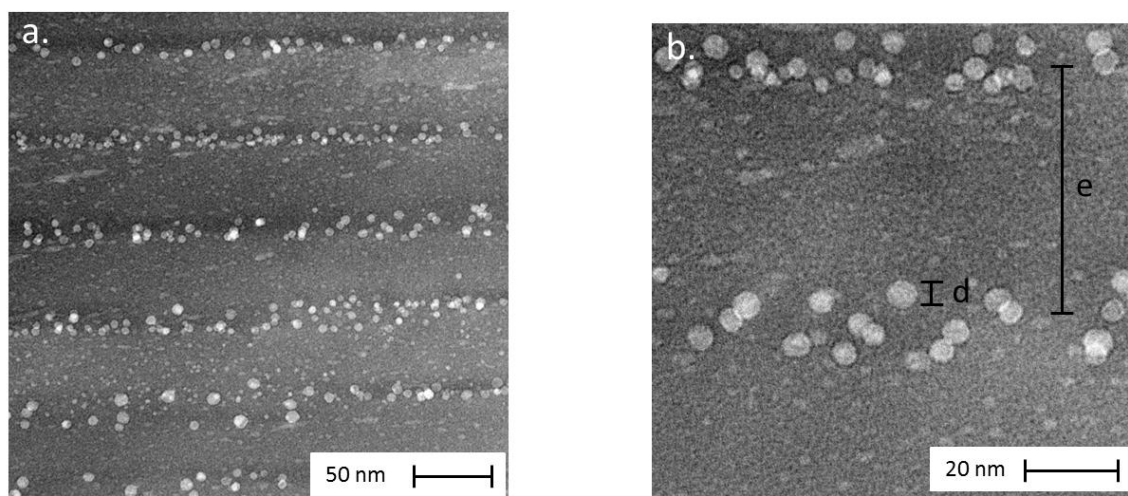


Figure 3.12: Cross-section TEM image of the “Mo-n-MONO” sample. a) global view showing the Mo-based QD . b) higher magnification of the image showing a QD diameter of $d = 5 \text{ nm}$ and a layer thickness $e = 50 \text{ nm}$.

In Figure 3.13 is presented the EDX chemical mapping for this QDSL. Similarly to Ti-based samples, a clear correspondence between the QD and the Mo signal is observed. Moreover, a small phosphorus accumulation can be observed in Figure 3.13-e, even if little contrast is obtained compared to the noise.

A MQW structure can also be identified in this sample (with the QW thickness “ e_{QW} ” of around 5 nm), appearing clear on the Ge signal image (Figure 3.13-c). This thickness corresponds to the QD diameter “ d_{QD} ” and indicates that Ge-based QD also selectively catalyze the SiH_4 pyrolysis.

The results of the measurement of the SiGe layers Ge content and the QD Mo content were not considered here because of the high sample thickness, which results in an inaccurate measure.

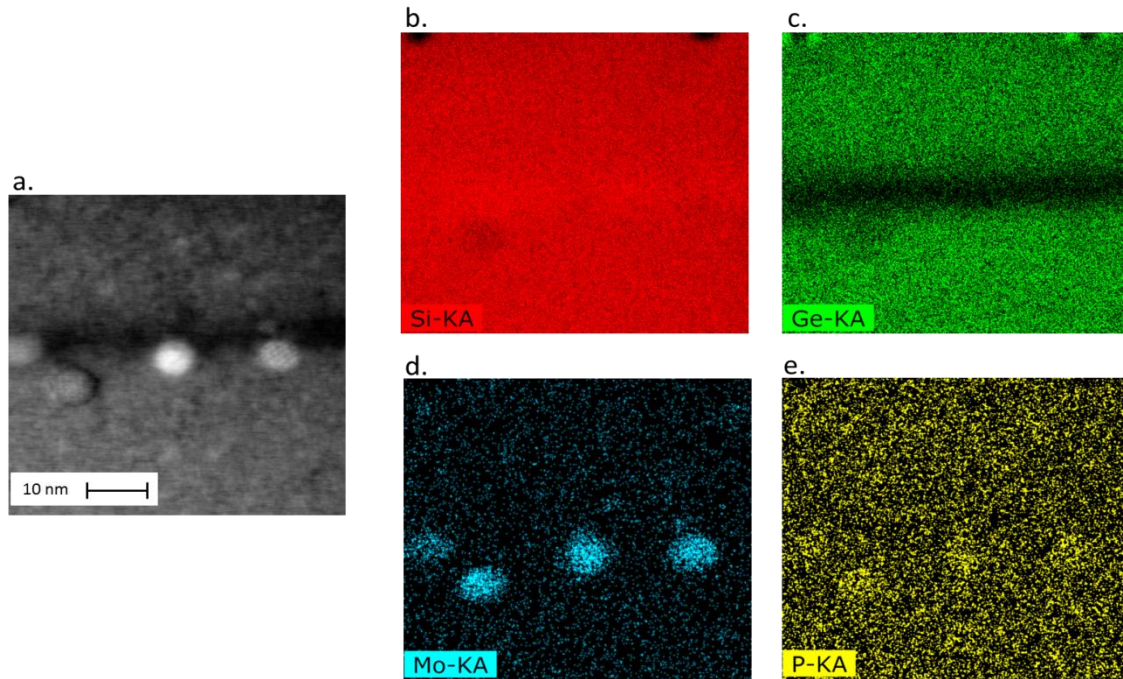


Figure 3.13: EDX chemical mapping of the sample “Mo-n-MONO”. a) STEM image. b) Si signal. c) Ge signal. d) molybdenum signal and e) phosphorus signal. Note the accumulation of the P dopant near the QD zone.

2.3.f - Mo-based QDSL: “n”-doped polycrystalline samples

Concerning the polycrystalline sample, TEM images are presented in Figure 3.14.

In the global cross-section image presented in Figure 3.14-a, the presence of the QD and the MQW structure can be observed, as well as the buffer layer. By measuring the particles on Figure 3.14-b, a mean QD diameter $d_{QD} = 7$ nm and a layer thickness $e = 43$ nm are obtained. These results are very close to those obtained for the monocrystalline sample, thus in the case of Mo-based samples it appears that the grain boundaries have no effects on the QD growth.

Moreover, no accumulation of the QD near the grain boundaries is observed when this sample is compared to the Ti-based QDSL, confirming the lower mobility of the Mo-based QD inside the SiGe matrix.

A high resolution image (Figure 3.15) was obtained and it was possible to measure the planes distance of a single QD, corresponding to the $(1\bar{1}1)$ planes of the MoSi_2 phase.

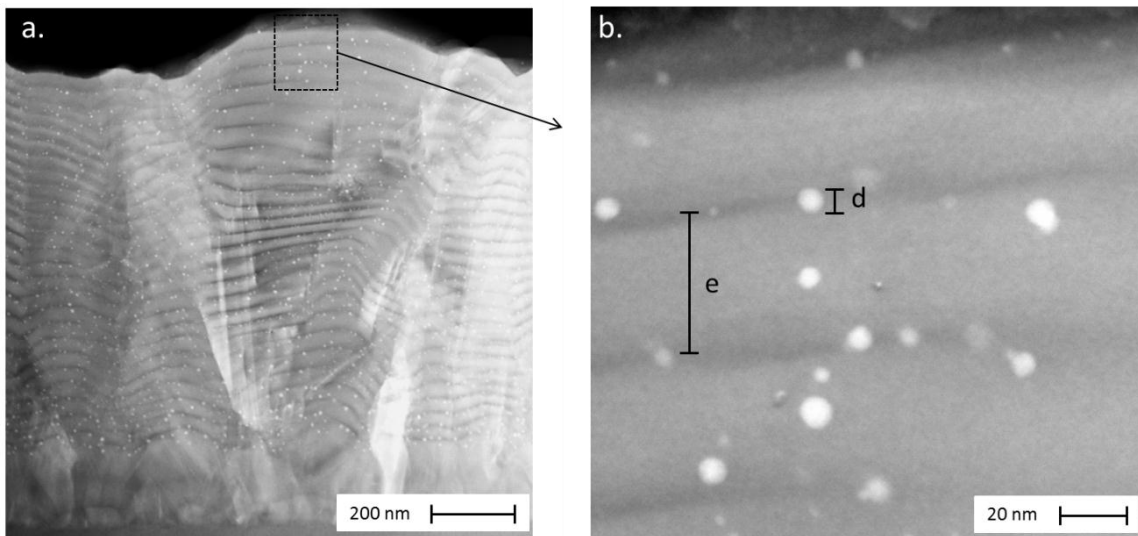


Figure 3.14: Cross-section TEM image of the “Mo-n-POLY” sample. a) global view showing the QDSL . b) higher magnification of the image showing a QD diameter of $d = 7$ nm and a layer thickness $e = 43$ nm.

In the case of this sample, the expected phase was obtained, contrary to the Ti-based polycrystalline sample. A possible reason for this is that in the case of the Mo-based QDSL, the smaller size of the QD facilitated the reaction with the Si atoms, forming the Si-rich phase during the QDSL growth.

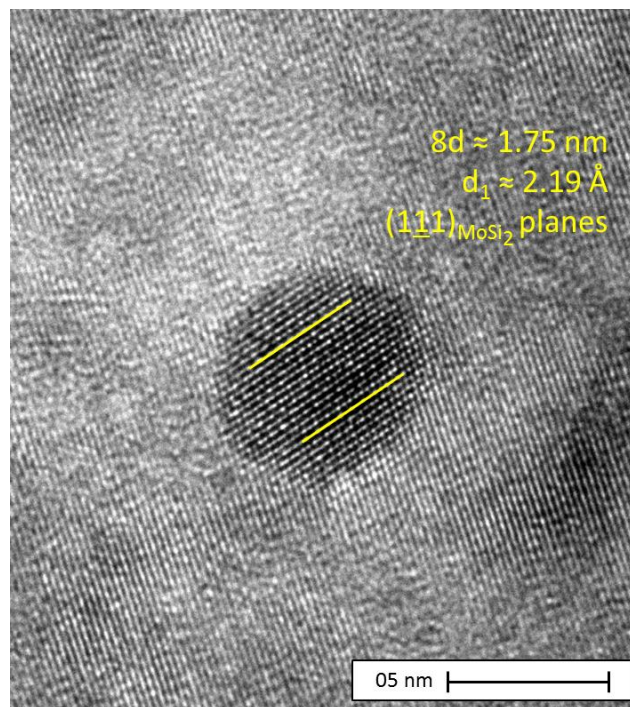


Figure 3.15: High resolution TEM image of a QD inside the “Mo-n-POLY” sample. The measured distance correspond to the (111) planes of the MoSi_2 phase.

In Figure 3.16 is presented the chemical mapping of the QDSL. The obtained results are very similar to those for the monocrystalline sample, with a phosphorus accumulation visible near the QD zone. Also, no significant differences were found relative to the QD diameter and the layers thickness compared to the monocrystalline sample.

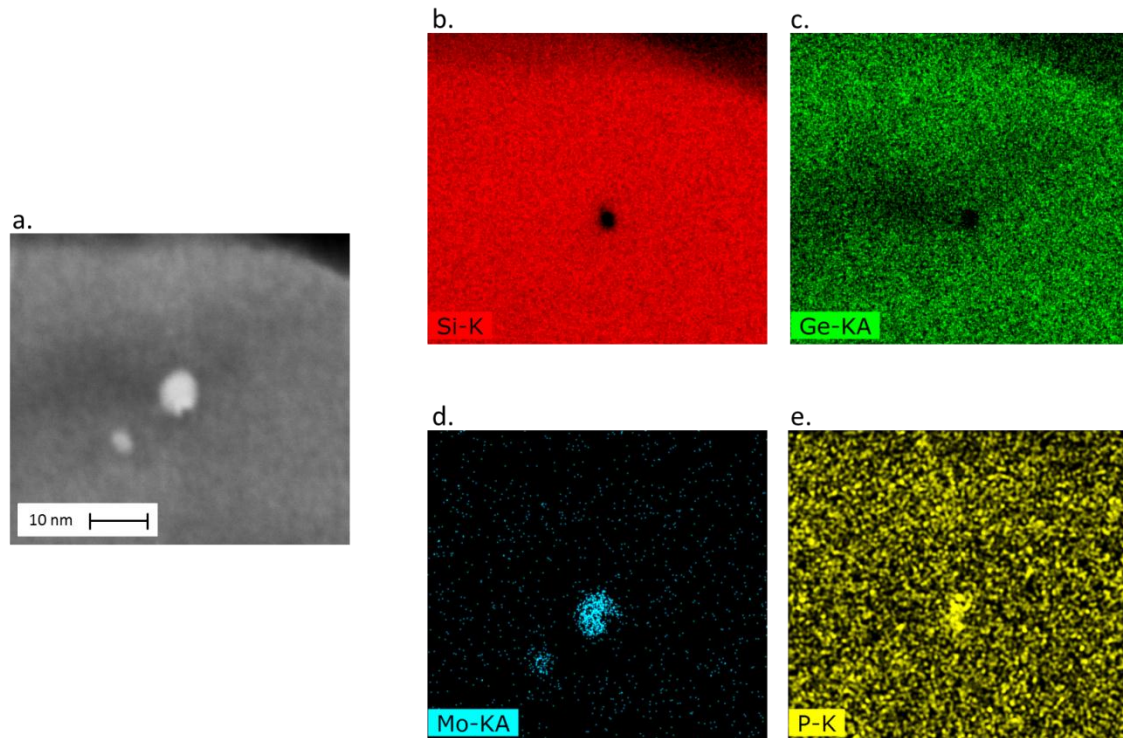


Figure 3.16: EDX chemical mapping of the sample “Mo-n-POLY”. a) STEM image. b) Si signal. c) Ge signal. d) molybdenum signal and e) phosphorus signal. Note the accumulation of the P dopant near the QD zone. The black spot visible in “b” and “c” is due to a hole caused by the electron beam.

2.3.g - Mo-based QDSL: “p”-doped monocrystalline samples

The last samples studied by TEM microscopy are the “p”-doped, Mo-based QDSL. In Figure 3.17 are presented the TEM images of the monocrystalline sample. The measured values presented in Figure 3.17-b produced values of $d_{QD} = 7$ nm and $e = 50$ nm, very close to the values obtained for the “n”-doped QDSL. A similar behavior is also seen when Figure 3.17-a is analyzed, where a considerable variability of the QD sizes and densities within the different layers forming the QDSL is observed.

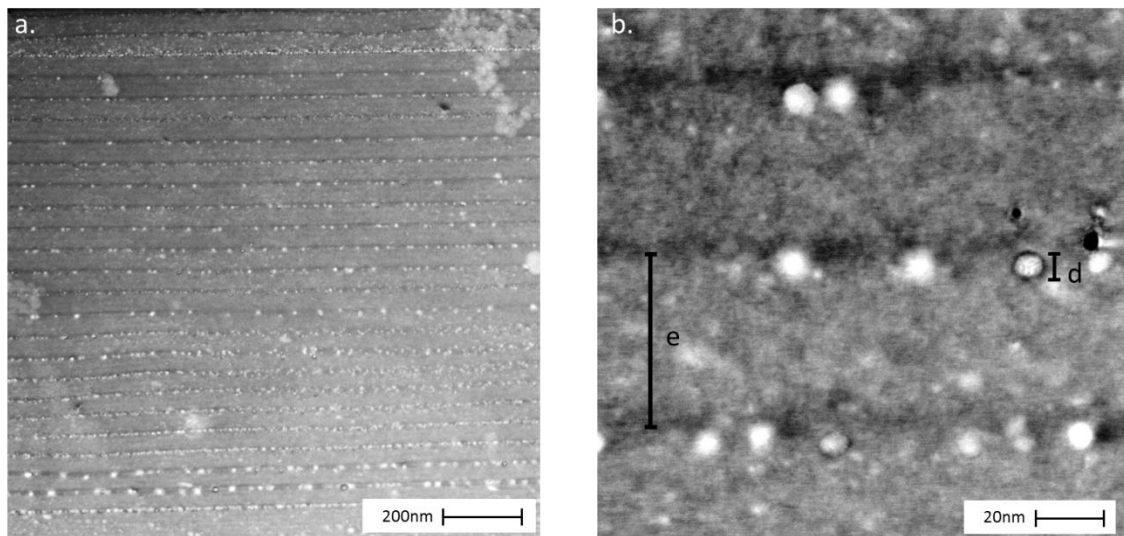


Figure 3.17: Cross-section TEM image of the “Mo-p-MONO” sample. a) global view showing the QDSL . b) higher magnification of the image showing a QD diameter of $d = 7$ nm and a layer thickness $e = 50$ nm.

The measurement of the crystallographic planes distance in the high resolution image (Figure 3.18) showed that in the case of this sample the expected phase MoSi_2 was obtained.

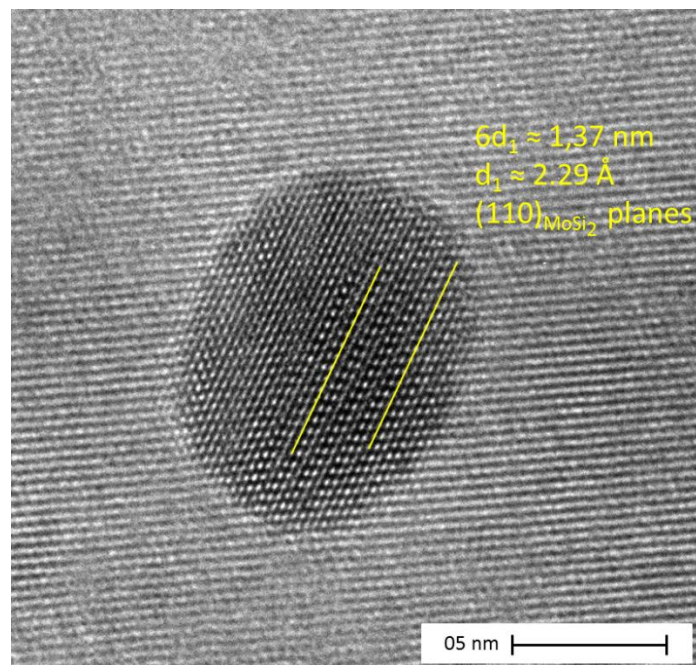


Figure 3.18: High resolution TEM image of a QD inside the “Mo-p-MONO” sample. The measured distance corresponds to the (110) planes of the MoSi_2 phase.

Considering the chemical mapping (Figure 3.19), a good correlation between the Mo signal and the QD position was found (Figure 3.19-a and d). The boron dopant signal was not high enough to provide a relevant contrast due to the large thickness of the sample, so this image was omitted.

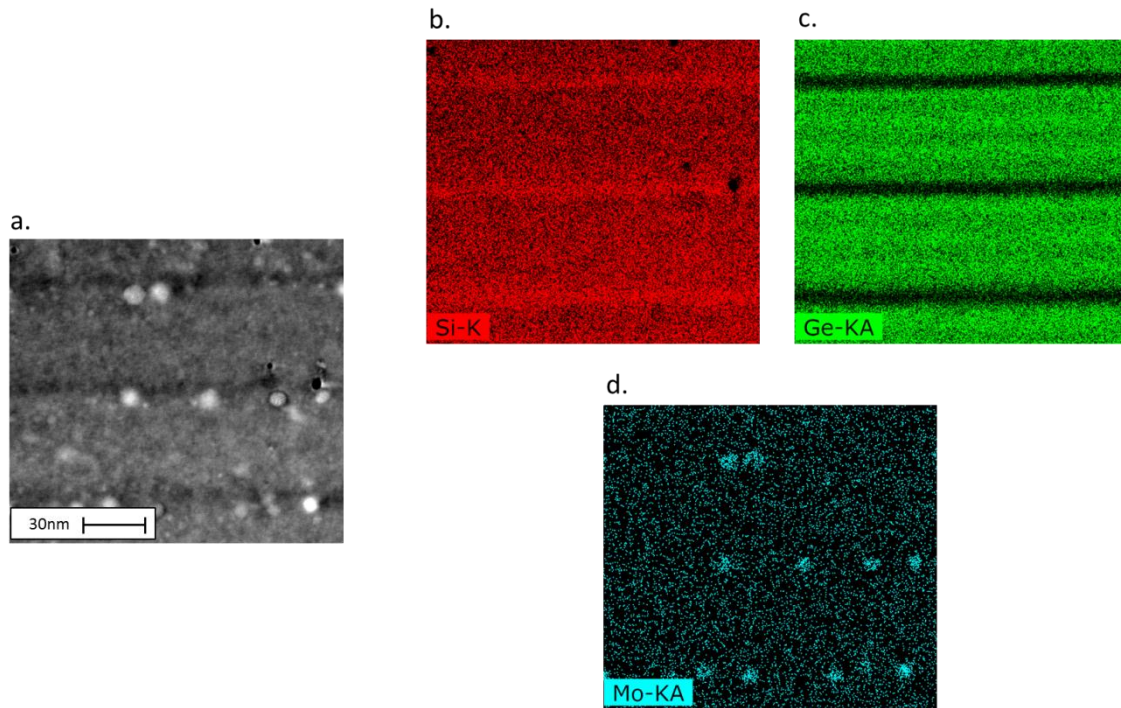


Figure 3.19: EDX chemical mapping of the sample “Mo-p-MONO”. a) STEM image. b) Si signal. c) Ge signal. d) molybdenum signal. Note the quantum well structures in images “b” and “c”.

Again the MQW structure was obtained, and can be clearly observed in Figure 3.19-b and c. The mean thickness measured for the QW was the same as for the “n”-doped samples, i.e., around 5 nm. The obtained atomic content measured by EDX was 3 % of Ge of the thick layer and 0,7 % of Ge for the QW.

2.3.h - Mo-based QDSL: “p”-doped polycrystalline samples

Consider now the TEM images obtained for the polycrystalline sample (Figure 3.20). A QD mean diameter mean value of around 5 nm was obtained, with a layer thickness of 43 nm. Here again no accumulation near the grain boundaries was observed.

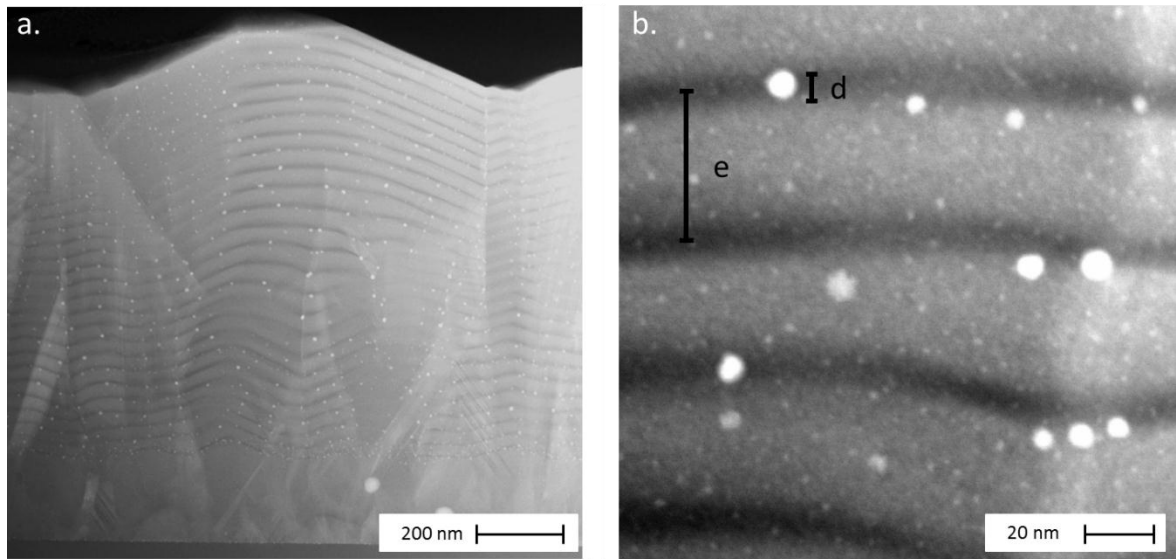


Figure 3.20: Cross-section TEM image of the “Mo-p-POLY” sample. a) global view showing the QDSL . b) higher magnification of the image showing a QD of 8 nm of diameter and a layer thickness of 44 nm.

The EDX chemical mapping is presented in Figure 3.21.

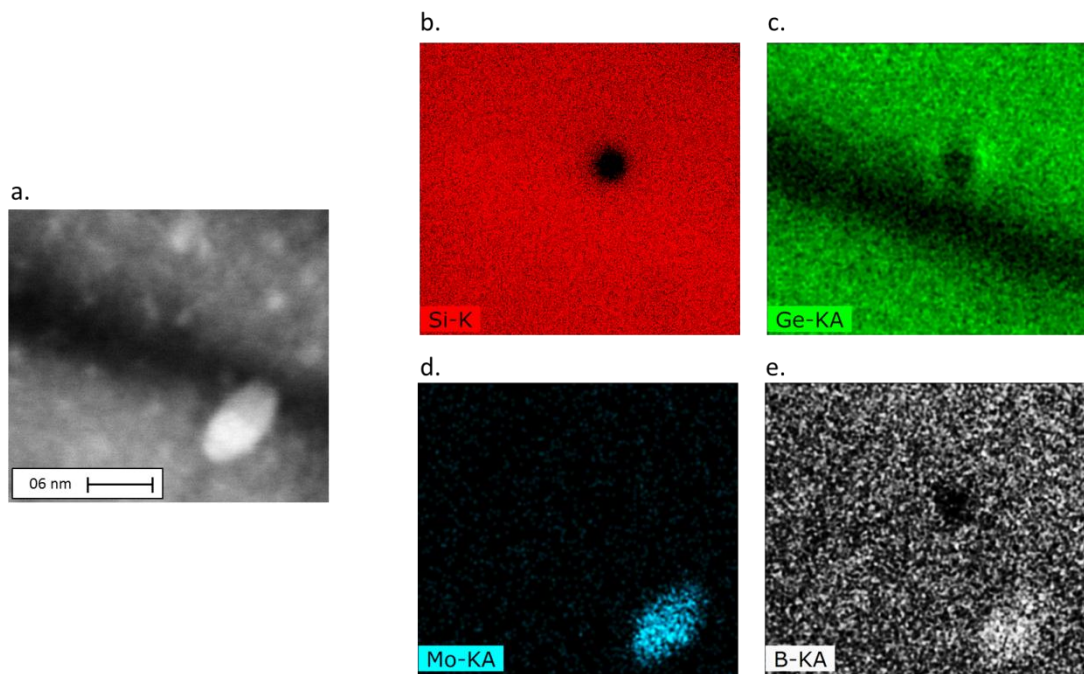


Figure 3.21: EDX chemical mapping of the sample “Mo-p-POLY”. a) STEM image. b) Si signal. c) Ge signal. d) molybdenum signal and e) boron signal. Note the accumulation of the B dopant near the QD zone. The black spot visible in “b” and “c” is due to a hole caused by the electron beam. Note the quantum well structures in image “c”.

Similar results were obtained compared to the other Mo-based QDSL, but in the case of this sample it was possible to identify the boron signal, and the accumulation of the dopant near the QD was observed (Figure 3.21-e).

The measured Ge content provided a value inside the QW of around 4 % and in the thicker layer of 6 %. A diffraction condition was obtained during the TEM analysis and the planes distance was compatible with the (111) planes of the MoSi₂ phase.

2.4 - Conclusion

In Table 3.2 it can be seen the fundamental and most important information obtained from the TEM and EDX measurements.

As no similar materials have been reported in the literature, only a comparison between the obtained samples will be performed.

Following a global conclusion of this part of the work will be presented together with some discussion relating the obtained properties and their expected effect on the thermoelectric properties of the materials.

Table 3.2: Summary of the QDSL structural information obtained by TEM and EDX analyses.

<u>sample</u>	<u>QD phase</u>	<u>mean QD diameter</u>	<u>mean layer thickness</u>	<u>QW thickness</u>	<u>layer Ge content</u>	<u>QW Ge content</u>
Ti-n-MONO	TiSi ₂	66 nm	70 nm	15 nm	13%	-
Ti-n-POLY	Ti ₃ Si	42 nm	54 nm	-	12%	-
Ti-p-MONO	TiSi ₂	34 nm	110 nm	15 nm	10%	3%
Ti-p-POLY	-	-	-	-	-	-
Mo-n-MONO	-	5 nm	50 nm	5 nm	-	-
Mo-n-POLY	MoSi ₂	7 nm	43 nm	-	-	-
Mo-p-MONO	MoSi ₂	7 nm	50 nm	5 nm	3%	0,7%
Mo-p-POLY	MoSi ₂	5 nm	43 nm	5 nm	6%	4%

- **QD phase :**

It can be seen that for the majority of the samples the expected silicide phases (TiSi_2 and MoSi_2) was obtained. Considering the Ti samples, the “n”-doped polycrystalline QDSL resulted on a phase richer in Ti (Ti_3Si), indicating that the reaction between Si and Ti is slower and was not completed during the QDSL growth. It was not possible to measure the phase of the polycrystalline “p”-doped sample, however.

For the Mo-based samples all the measured QD corresponded to the MoSi_2 phase, even the polycrystalline QDSL. This is probably due to the smaller size and thus higher surface/volume ratio of the Mo-based QD, which increase the reaction rate between Si and Mo atoms.

It should be remembered that the phase measurements were performed for only few (if not one) QD, and a complete study should include a statistical measurement of the QD phases inside the material.

Further annealing studies could also be performed in order to determine which the stable phase is for each QDSL at different temperatures.

- **QD diameter :**

Let's consider first the Ti-based QDSL. For both “p” and “n” doping and both mono and polycrystalline materials the surface deposited nano-islands measured in Chapter 2 presented a mean diameter of approximatively 20 nm.

For the “n”-doped samples, it is clear that a coalescence phenomenon is observed for these particles. For the “p”-doped monocrystalline sample, it is not possible to determine if the smaller coalescence is due to the thicker SiGe layer or if the boron dopant atoms change the QD diffusion inside the material.

Even if the particles diameter is bigger than the expected for these samples, it can be seen from reference [1] that their diameters still correspond to the minimum of the thermal conductivity obtained with QD inclusions. However, the coalescence also modifies the QD volumetric fraction “%_v”, and this can lead to a reduction of the expected effect of the QD on the thermal conductivity.

Considering the Mo-based samples, it appears that no coalescence took place, and the particles remained small. However, the final measured diameter (around 5 nm) did not correspond to the surface measurements of 15 nm (Chapter 2). This can be explained by the lack of long-term reproducibility of the MoCl_5 sublimation system. Further changes on the geometry of the apparatus should be performed in order to allow more rigorous studies.

Similarly to the Ti-based QDSL, the difference on the Mo-based particles diameter should not reduce their effect on the thermal conductivity, since this diameter also corresponds to the minima presented by Mingo et al. But here again a smaller volumetric fraction “%_v” is expected for these QDSL.

- **layer thickness :**

It was determined that in order to obtain the desired volumetric fraction “%_v” of around 3 %, the optimal layers thickness “*e*” should be $e = 2d$, where “*d*” is the QD diameter (Chapter 2).

Considering the Ti-based samples, this value should be around 40-50 nm. For the “n”-doped samples, values close to the expected were obtained, with some variations due to the errors on the calculated growth rate. This variation comes from the error of the sample thickness measurements using cross-section SEM images.

In theory, thus, no negative effect should be expected considering the layer thickness on the increase of the thermoelectric properties for these samples due to a reduction of the thermal conductivity.

For the “p”-doped monocrystalline sample an “*e*” value almost 2 times higher was obtained. In this case, a reduction of the phonons diffusion on the QD can be expected, since the volumetric fraction “%_v” is reduced.

Considering the Mo-based samples, no problems were encountered and all the samples had a layer thickness of the same order of magnitude as the one expected (30-40 nm), with a small difference coming from the precise determination of the SiGe growth rate.

Finally, the measured QW thickness for the Mo-based samples corresponds perfectly with the QD diameters, proving the catalysis theory already exposed. For the Ti-based QDSL, the difference between the QW thickness and the QD diameters exposes the coalescence phenomenon.

- **Ge content :**

For the Ti-based samples, all the measured QDSL had a Ge content of around 10 % (considering the measurement inaccuracy), which was the desired value.

The Mo-based samples presented a much lower Ge content, but as it has been reported in Chapter 2, these lower values were necessary in order to obtain QD with appropriate sizes and distributions.

The difference between the Ge contents measured for the “Mo-p-MONO” and “Mo-p-POLY” samples came probably from errors on the polycrystalline sample EDX measurements. The presence of different crystals causes the layers composing the QDSL to be distorted along the horizontal direction. Thus, due to the penetration of the electron beam employed to measure the EDX signal inside the material, a Ge signal coming both from the quantum wells and from the thick layers is obtained, affecting the results.

- **accumulation of QD on grain boundary :**

This phenomenon was observed for the Ti-based polycrystalline sample only. There are two possible effects happening to explain this observation. The first one is related to a preferential surface growth of the Ti-based nano-island on the grain boundary region, as observed in Chapter 2. This occurs because the high disorder of the atoms of the grain boundary favors the nucleation of the solid phase.

The second possible effect taking place during the QDSL growth is related to the high mobility of the Ti-based QD inside the SiGe matrix. It can be possible that while diffusion inside the matrix, the QD reaching the grain boundaries are “trapped” in these regions.

This accumulation causes an inhomogeneity of the QD density inside the material, and can reduce the expected thermal conductivity reduction due to phonons diffusion by the QD.

For the Mo-based samples this accumulation was not observed, probably due to the lower mobility of these QD inside the SiGe matrix.

- **the presence of QW structures :**

This type of structure was observed for all the samples analyzed using the TEM technique. Depending on different factors such as the material’s thickness after the sample preparation for the TEM analysis and the sample crystallinity these QW were more or less visible.

As discussed in section 2.3.c - the origin of these structures comes probably from the catalyzing effects of the both the Ti and Mo QD on the decomposition of the SiH₄ precursor, since the zones near the QD are richer in Si. This effect is also the responsible of the nanowires growth observed for the low-temperature embedding of Ti-based QD (Chapter 2).

The presence of these QW results on a hybrid final structure, composed both of a QDSL and a QWSL. This can be benefic to the increase of the thermoelectric properties, since both types of structures are known to produce notably a reduction of the material’s thermal conductivity. For more informations, see reference [3].

- **dopant accumulation near the QD :**

This effect was observed for the all of the analyzed samples, except for the “p”-doped monocrystalline Mo-based QDSL due to lack of contrast between the QD zones and the noise coming from the SiGe zones.

This accumulation has already been reported in the literature by Favier et al. in reference [2] for bulk phosphorous-doped SiGe samples with Mo-based inclusions. No explanations were provided in this reference for this phenomenon, but it probably

comes from a high affinity between the metal silicide and the dopant atoms, causing a precipitation around the QD.

This feature can interfere on the material's power factor, as demonstrated by Yu et al. in reference [4]. The authors observed an increase of the material's electrical conductivity due to an increase of the carriers' mobility without changes on the Seebeck coefficient. This effect is called modulation doping and is obtained by spatially separating carriers from their parent atoms.

In the case of the QDSL produced during this thesis, it is thus possible that a similar effect occurs.

- **presence of dislocations :**

Dislocations between the substrate and the QDSL were observed for the "n"-doped monocrystalline Ti-based QDSL, indicating that the thin film is relaxed. This was not observed for the "p"-doped monocrystalline Ti-based sample, probably due to the lower Ge content of the last.

For the Mo-based samples, as the TEM images did not show the interface between the QDSL and the substrate, it is not possible to determine if dislocations are present or not. However, due to the low Ge content of the Mo-based samples, it is probable that the thin films are not relaxed.

3 - Thermoelectrical characterization

3.1 - Introduction

In this section will be presented the results concerning the measurement of the different parameters composing the material's thermoelectric figure of merit, ZT (see Chapter 1).

Consider first the upper part of the ZT equation, also known as the thermoelectric power factor, which is composed of the electrical conductivity and the Seebeck coefficient. The *ULVAC ZEM-3* tool (Figure 3.22) was employed to measure both parameters from room temperature up to 200 °C. This equipment being conceived to measure bulk samples, some modifications were made in order to measure the thermoelectric power factor for thin films.

A schematic representation of the measurement system is presented in Figure 3.23. The first step is to evaporate two rectangular strips of first Al and then Au onto the thin film surface. The 200 nm Al metal deposition by evaporation was chosen in

order to provide an ohmic contact with the SiGe-based material. A further 100 nm Au deposition was also performed using the same equipment in order to protect the surface against oxidation.

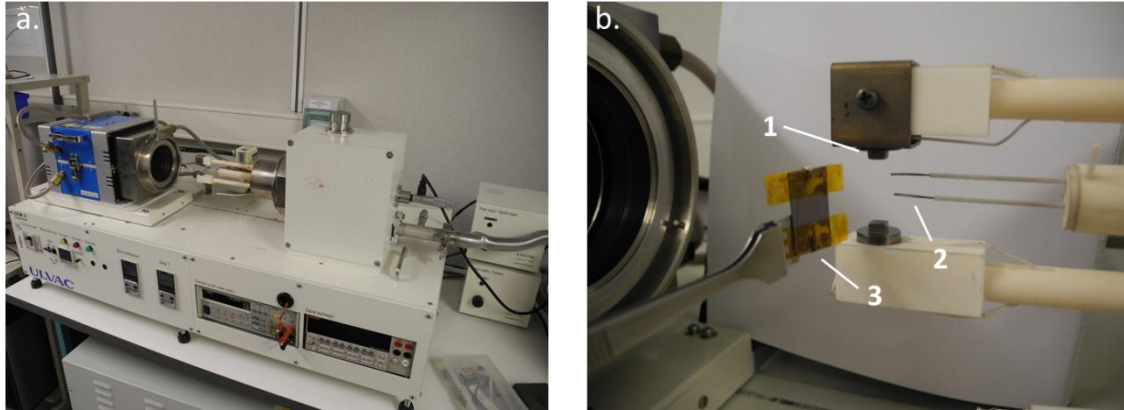


Figure 3.22: The ULVAC ZEM-3 tool. a) global view. b) view of the electrode/heater (1), the thermocouples (2) and the insulated sample prepared to be placed between the electrodes (3).

The sample was placed between the electrodes from the measurement equipment (Figure 3.23-a). The upper electrode serves also as a heating element. A polyimide electrical insulating film was put between the sample edge and the electrode and a copper wire was positioned in order to electrically connect the electrodes and the Al/Au strips on the samples surface. By doing this, the Si (or SOI) substrate did not interfere on the electrical measurements, and the electrical contact was established only between the electrodes and the thin film.

The equipment works simultaneously on two modes, the first employed to measure the electrical conductivity and the second one to measure the Seebeck coefficient. The first is represented in Figure 3.23-b and can be thought as a 4-point probes method apparatus. An electrical current “ I ” is imposed trough the sample and the resulting voltage “ V ” is measured using the thermocouples as electrodes. Using the ohm’s law (equation 3.1) the thin film electrical resistance can be obtained.

The electrical conductivity can thus be calculated using the sample length “ l ”, width “ w ” and the thin film thickness “ e ” (equation 3.2).

$$R = V/I \quad 3.1$$

$$\sigma = \frac{l}{R.w.e} \quad 3.2$$

The Seebeck coefficient was measured according to the scheme represented in Figure 3.23-c. A temperature difference “ ΔT ” is imposed through the sample by the upper electrode, which also act as a heater element.

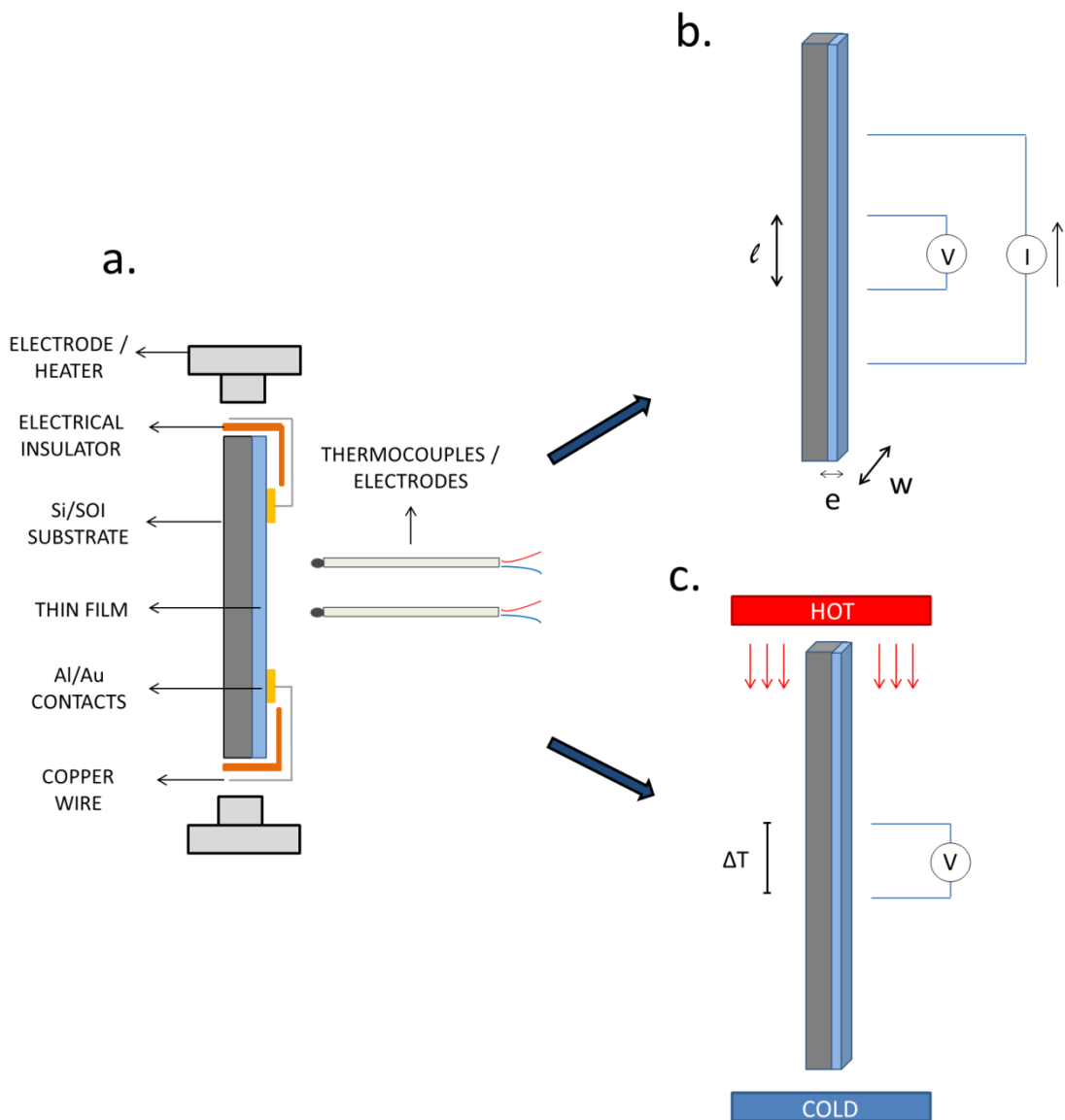


Figure 3.23: Representation of the ZEM-3 apparatus measurement system. a) schematic view of the sample inside the machine. b) representation of the electrical conductivity measurement. c) representation of the Seebeck coefficient measurement.

The thermocouples placed in the center of the sample are employed in a first time to measure the temperature difference ΔT . Instantaneously after it the equipment software switches the thermocouples measuring mode and they serve as electrodes to measure the voltage created by the temperature gradient.

The employed equipment is capable of measuring the samples parameter at temperatures up to 900 °C, but in the case of the thin films produced in this work the maximum temperature allowed was around 200 °C, because the electrical insulator employed degrades at temperatures higher than these.

The main advantage of this technique is that the temperature gradient and the voltage drop are measured exactly at the same point by the thermocouples, reducing the measurement errors.

The sign of the measured Seebeck coefficients presented in the next sections was intentionally omitted. It should be noticed however that for convention the Seebeck coefficient for “n”-doped samples is negative and for “p”-doped samples is positive.

The electrical conductivity was also measured with another tool (Figure 3.24) using the Van der Pauw technique [5] coupled with a Hall effect measurement. Further information on this technique can be found in [6].

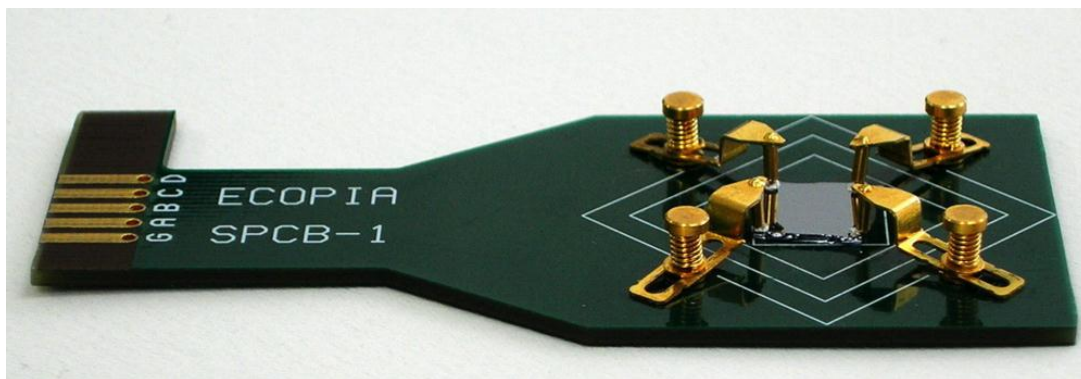


Figure 3.24: Spring clip board sample holder of the equipment employed to perform the van der Pauw and Hall effect analyses.

These techniques allowed to measure at room temperature the QDSL carriers concentration and the electrical resistivity. The fact that the electrical resistivity was measured using two different techniques allowed to increase the reliability of the obtained results.

It is important to notice that both techniques measure the properties along the “in-plane” direction, i.e., parallel to the thin film surface.

The thermal conductivity of the samples was measured at room temperature by the thermo-reflectance method, at the LOMA laboratory at Bordeaux/France. It should be noticed that this technique allows to measure the cross-plane thermal conductivity component of thin films.

This technique consists in exciting the samples surface with a laser pulse during a few hundreds of femtoseconds. A thermal perturbation is created, along with an elastic stress. This stresses produce a variation on the sample reflectivity. Another laser pulse called probe is then sent to the samples surface in order to follow the variation of the samples reflectivity. By employing a physical model of this variation it is possible to obtain the material's thermal conductivity. Further information can be found in references [7,8]

Due to the lack of availability of the thermo-reflectance equipment, it was not possible to characterize all of the produced QDSL.

In the next sections the results for the thermoelectric characterization will be presented. Latter, a discussion comparing the obtained results and the results from literature will be performed.

3.2 - Ti-based QDSL: n-doped samples

3.2.a - Monocrystalline QDSL

Consider the monocrystalline Ti-based "n"-doped sample. In Figure 3.25 the results of the evolution of the Seebeck coefficient and the electrical resistivity with the temperature are presented, both for the QDSL and the corresponding SiGe reference sample.

It can be seen that the behavior of the electrical resistivity was exactly the same for both samples, with an increase of this value with the temperature. It should be remembered that the reference samples were produced in order to have an electrical resistivity similar to its corresponding QDSL.

The main reason for this increase is the reduction of the charge carriers mobility at higher temperatures due to the increase of carrier's scattering by phonons, which is coherent with the metallic characteristic of these high-doped semiconductors.

For the same samples, a surprising result concerning the Seebeck coefficient was observed, with an increase of the Seebeck coefficient with the addition of QD in the matrix, i.e., of the QDSL. This resulted logically on an increase of the material's power factor (Figure 3.26).

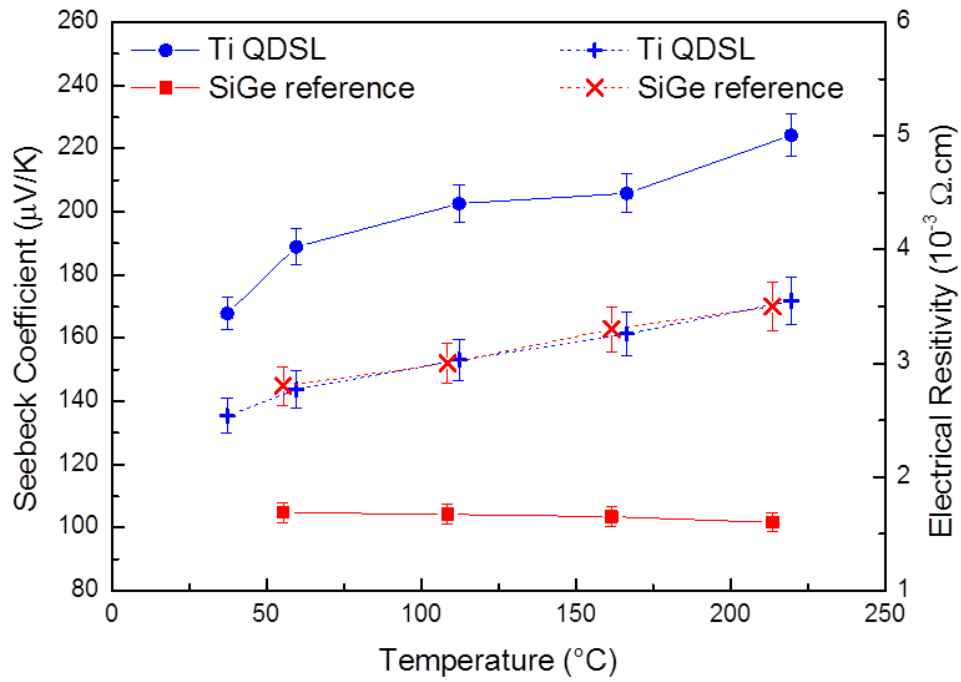


Figure 3.25: left axis: Seebeck coefficient of the n-doped monocrystalline Ti-based QDSL (blue circles) and of the SiGe reference (red squares). Right axis: Electrical resistivity of the n-doped monocrystalline Ti-based QDSL (blue crosses) and of the SiGe reference (red "X").

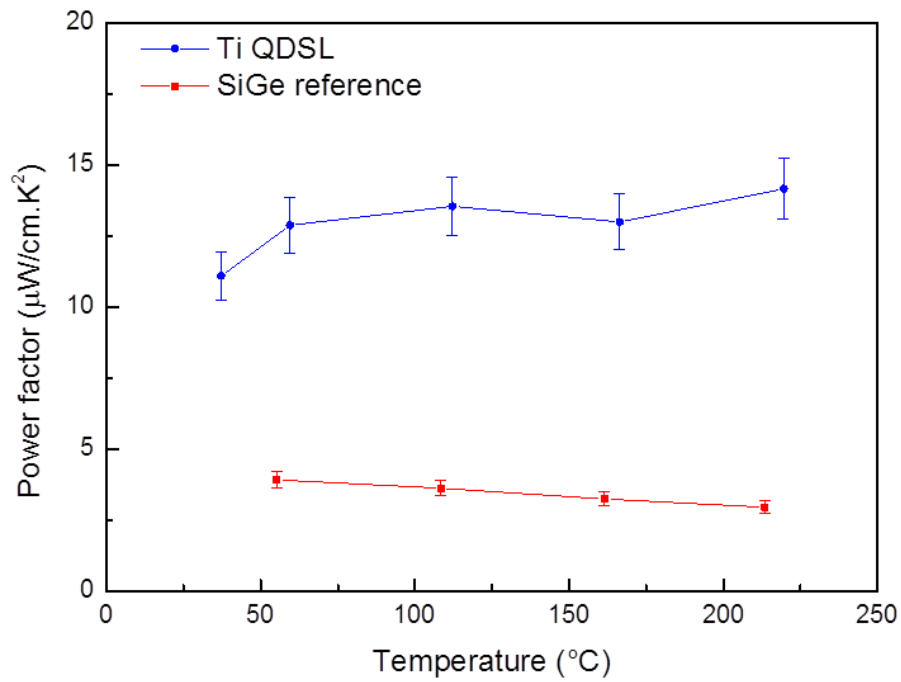


Figure 3.26: Evolution of the thermoelectric power factor with the temperature for the monocrystalline Ti-based "n"-doped QDSL (blue circles) and for its SiGe reference (red squares).

Different considerations should be made considering these results. First, consider the Seebeck coefficient values for the QDSL and the sample. At 50 °C, the SiGe reference Seebeck coefficient is around 100 $\mu\text{V}/\text{K}$ and the QDSL value is around 190 $\mu\text{V}/\text{K}$, resulting in an almost 2-fold increase with the inclusion of the QD. The behavior of this coefficient with an increasing temperature is according to the expected, i.e., an increase of the Seebeck coefficient is observed by increasing the temperature.

The same behavior is observed for the power factor measurements, and values at 50 °C of around 13 $\mu\text{W}/\text{cm}\cdot\text{K}^2$ are obtained for the QDSL and around 3 $\mu\text{W}/\text{cm}\cdot\text{K}^2$ for the SiGe reference, i.e., around a 4-fold increase.

It is not clear however why the SiGe reference sample Seebeck coefficient and power factor remain almost constant in the tested temperature ranges, and no literature references exists reporting Seebeck coefficient measurements for monocrystalline SiGe thin films with similar Ge contents and dopant levels. It is possible that the error bar employed for the obtained curves (calculated by taking into account the variance of the measure equipment) is bigger and the increase on the Seebeck coefficient is masked by it.

If these results are compared with n-doped bulk samples, the values with the same magnitude are found. Wang et al. studied in reference [9] the $\text{Si}_{80}\text{Ge}_{20}$ material doped with phosphorous and having a carrier concentration of around $2.2 \times 10^{20} \text{ cm}^{-3}$ and compare their results with RTG values.

The Seebeck values obtained both for the RTG and for the authors' samples were around 120 $\mu\text{V}/\text{K}$ at room temperature and 160 $\mu\text{V}/\text{K}$ at 200 °C and the power factor values varied from 10 to 20 $\mu\text{W}/\text{cm}\cdot\text{K}^2$ for the temperature range considering the room temperature up to 200 °C.

This comparison indicates that the values obtained for the QDSL and reference measurements are coherent and are of the same order of magnitude with reference results. Moreover, there is no doubt that the inclusion of Ti-based QD produced an increase on the material's power factor, since both samples were produced and measured using the same equipment and methods.

Further studies should be performed notably by producing samples with different Ge contents and doping levels in order to understand the anomalous behavior of the SiGe sample.

More information can be obtained by looking at Table 3.3, which presents the results obtained by Hall Effect measurements (carriers' concentration and mobility), the dopant gas flow employed during the QDSL growth, and the cross-plane thermal conductivity measured by thermo-reflectance. The electrical resistivity measurements results obtained using the Van de Pauw equipment are not presented. These results were intentionally omitted because all the measured values corresponded to the results from the *ZEM-3* measurements presented in Figure 3.25, validating the measured values.

Table 3.3: Additional measured properties of the Ti-based monocrystalline “n”-doped QDSL and its SiGe reference.

	carriers concentration. (cm ⁻³)	carriers mobility (cm ² /V.s)	dopant flow rate (sccm)	thermal conductivity (W/m.K)
QDSL	3,20E+19 ± 0,2	73 ± 5	20	6,8 ± 0,7
Ref.	3,20E+19 ± 0,2	56 ± 3	10	8,5 ± 0,8

It can be seen that a higher dopant partial pressure (expressed as the dopant flow rate) was necessary to obtain a QDSL with the same dopant concentration as the reference.

This can be explained due to the dopant accumulation near the QD (section 2.3 -). As a considerable part of the dopant accumulates, further dopant atoms are necessary in solid solution to produce a carrier concentration equal to the reference. This dopant accumulation is probably the origin of the higher mobility observed for the QDSL, due to the modulation doping phenomenon (discussed at the end of this section).

The mobility values for both the reference samples and for the QDSL are of the same order of magnitude as for the expected by theory. By using an *on-line* tool (accessible at [10]) for calculating the mobility of monocrystalline Si samples as a function of dopant nature and doping concentration a value of 89 cm²/V.s is obtained for the same carrier concentration as those showed at Table 3.3. Since the samples produced during this work, were composed of an alloy of SiGe, it is normal that lower values are obtained due to the alloy scattering effects.

The same tool can be employed to compare the room temperature electrical resistivity values obtained of $3 \times 10^{-3} \Omega \cdot \text{cm}$ with the one for a silicon sample with the same doping level ($2,2 \cdot 10^{-3} \Omega \cdot \text{cm}$). These results being very similar, this fact validates the obtained results and the measurement techniques employed for this work.

It is also presented in Table 3.3 the thermal conductivity obtained by thermo-reflectance. Here again an improvement of the thermoelectric properties of the material was observed by the reduction of the thermal conductivity due to the inclusion of QD inside the material. These results prove the effect of the nanostructuration by the inclusion of silicide QD on the reduction of the material's thermal conductivity. The measured reference value for the reference SiGe sample of 8,5 W/m.K is coherent with literature values. For instance, Savelli et al. in [11] reported

a value of 6,1 W/m.K for a monocrystalline $\text{Si}_{0.85}\text{Ge}_{0.15}$ thin film and Mingo et al. in reference [1] a value of around 8 W/m.K for a $\text{Si}_{50}\text{Ge}_{50}$ monocrystalline bulk sample.

3.2.b - Polycrystalline QDSL

The results of the Seebeck coefficient and electrical resistivity for “n”-doped polycrystalline Ti-based QDSL are presented in Figure 3.27.

First consider the electrical resistivity. Both the reference and the QDSL samples presented the same electrical resistivity, as aimed. Moreover, both samples behaved in the same way with an increase of the temperature. Contrary to the monocrystalline samples, the electrical resistivity practically does not change, an even a light reduction is observed as the temperatures is increased.

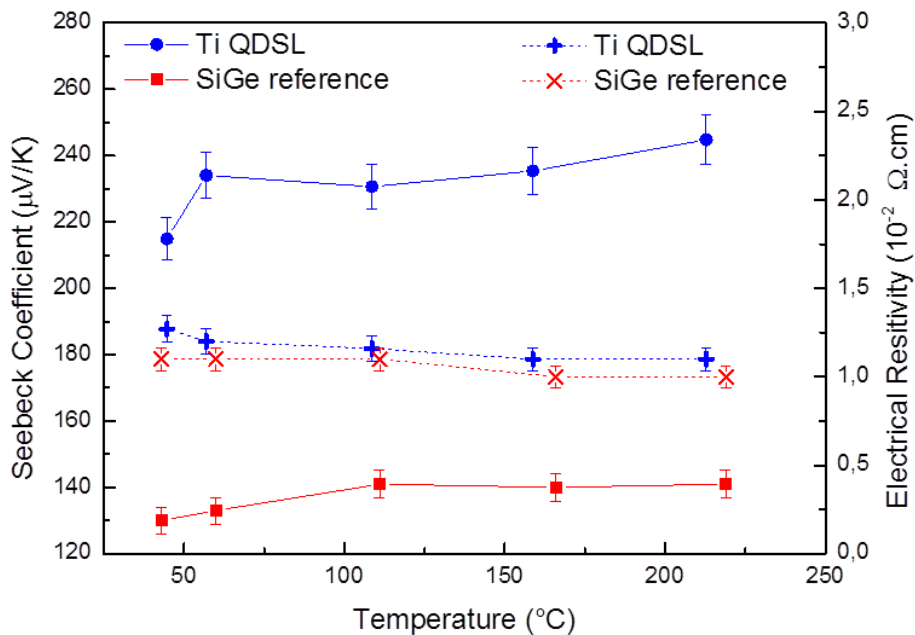


Figure 3.27: left axis: Seebeck coefficient of the “n”-doped polycrystalline Ti-based QDSL (blue circles) and of the SiGe reference (red squares). Right axis: Electrical resistivity of the n-doped polycrystalline Ti-based QDSL (blue crosses) and of the SiGe reference (red X).

The explanation for this observation comes from the fact that for polycrystalline materials the scattering at grain boundaries is the main scattering mechanism [12]. Moreover, its effect is higher than other scattering modes such as alloy scattering, thus the observed mobility values are much lower (13 $\text{cm}^2/\text{V.s}$ for the polycrystalline SiGe reference than 56 $\text{cm}^2/\text{V.s}$ for the monocrystalline reference sample). As the grain

boundaries can act as trapping sites for the carriers, their accumulation results on the creation of a potential energy barrier for the carrier transport [13]. By increasing the material temperature, more energy is available for the carriers to cross the potential barrier and thus the mobility is increased.

Moreover, the value of the room temperature electrical resistivity is considerably higher for the polycrystalline samples (around $1 \times 10^{-2} \Omega \cdot \text{cm}$) compared to the monocrystalline (around $1 \times 10^{-3} \Omega \cdot \text{cm}$), due to reduction of the electronic carriers' mobility (Table 3.3 and Table 3.4).

The inclusion of the QD in the polycrystalline sample produced also very interesting results, with the improvement of the material Seebeck coefficient. A similar effect on the obtained Seebeck coefficient compared to the monocrystalline samples, i.e., an increase from around $130 \mu\text{V/K}$ to $230 \mu\text{V/K}$ was observed at $50 \text{ }^\circ\text{C}$. This resulted on an increase of the material's power factor, presented in Figure 3.28.

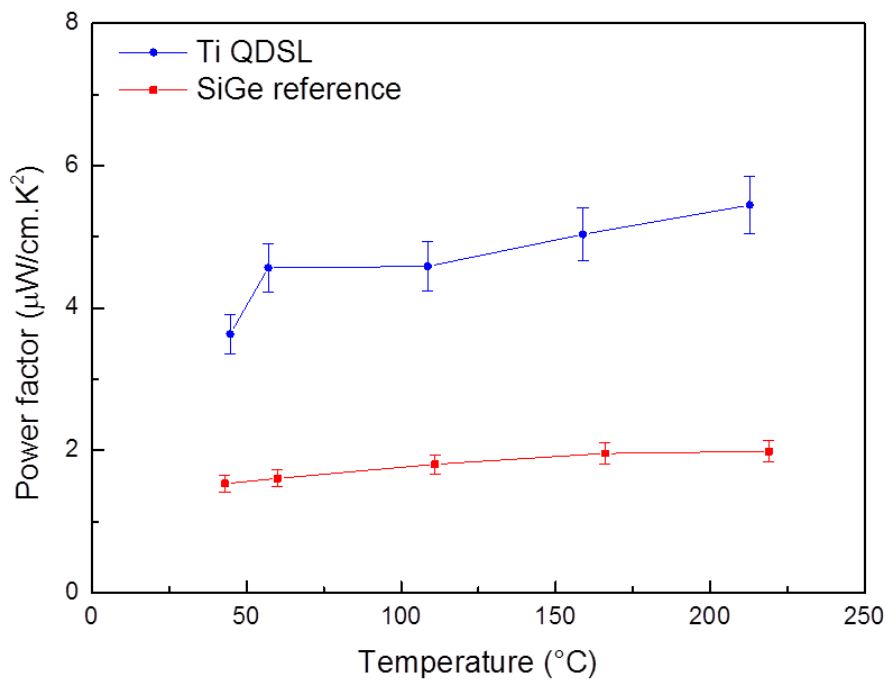


Figure 3.28: Evolution of the thermoelectric power factor with the temperature for the polycrystalline Ti-based "n"-doped QDSL (blue circles) and for its SiGe reference (red squares).

An increase on the dopant gas flow rate was also necessary in order to produce a QDSL with similar carriers' concentration compared to the reference (Table 3.4).

The main difference on the behavior of the mono and polycrystalline QDSL concerned the thermal conductivity. In the case of the polycrystalline samples, no changes were observed when QD were included inside the SiGe matrix (Table 3.4).

Table 3.4: Additional measured properties of the Ti-based polycrystalline “n”-doped QDSL and its SiGe reference.

	carriers conc. (cm^{-3})	carriers mobility ($\text{cm}^2/\text{V}\cdot\text{s}$)	dopant flow rate (sccm)	thermal conductivity ($\text{W}/\text{m}\cdot\text{K}$)
QDSL	$2,80\text{E}+19 \pm 0,2$	18 ± 1	20	$4,6 \pm 0,5$
Ref.	$4,40\text{E}+19 \pm 0,3$	13 ± 1	5	$4,2 \pm 0,4$

Two hypotheses exist to explain this observation. The first and most probable one is that the grain boundaries already act as sites for phonon diffusion, thus the phonons diffusion on the QD is “masked” by this effect.

Compare the thermal conductivity of both SiGe reference samples, which have the same Ge content (Table 3.2) and a similar carrier concentration. By observing the difference on their thermal conductivities which are 8,5 and 4,2 W/m.K for mono and polycrystalline samples respectively, the hypothesis of the grains boundary effect is supported.

Another possible source of difference on the thermal conductivity is the obtained phase, which in the case of the polycrystalline QDSL (Ti_3Si) was not the expected phase TiSi_2 . Theoretical studies should be performed in order to analyze the effect of silicide phases others than TiSi_2 on the thermal conductivity reduction.

3.3 - Ti-based QDSL: p-doped samples

3.3.a - Monocrystalline QDSL

Consider now the monocrystalline Ti-based “p”-doped QDSL. The results for the Seebeck coefficient and electrical resistivity measurements are presented in Figure 3.29.

In the case of these samples, a difference on the electrical resistivity was observed between the reference sample and the QDSL due to the difference on the carrier’s

concentration (Table 3.5). Actually it was not possible to reduce the carriers concentration for the reference sample since a gas flow rate of 5 sccm is the minimum flow rate possible for our CVD tool.

Similarly, a difference on the Seebeck coefficient was observed for both samples. If only the Seebeck coefficient was considered, one could conclude that here again the QD inclusion produced an increase of the material's Seebeck coefficient.

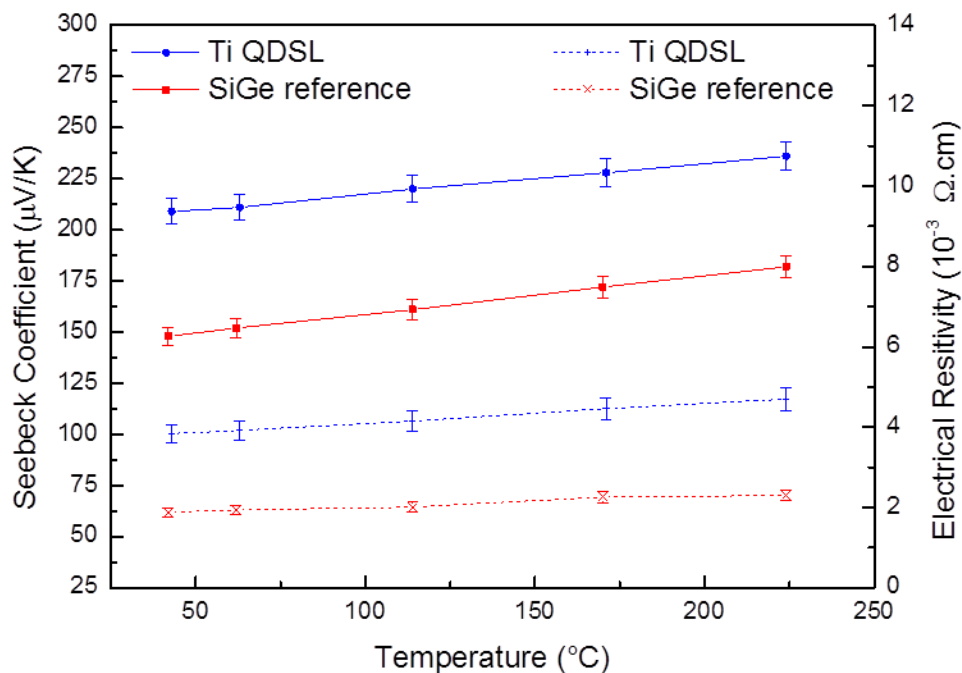


Figure 3.29: left axis: Seebeck coefficient of the p-doped monocrystalline Ti-based QDSL (blue circles) and of the SiGe reference (red squares). Right axis: electrical resistivity of the p-doped monocrystalline Ti-based QDSL (blue crosses) and of the SiGe reference (red X).

However, by looking at Figure 3.30 it can be seen that the power factor does not change up to 200 °C after the inclusion of QD. By looking at Figure 1.13 (Chapter I) it can be seen there is a range corresponding to the carriers' concentration where the power factor is maximum. This range corresponds to the doping employed in this work, i.e., 10^{19} - 10^{20} cm⁻³. Inside this zone, even if a sample has a lower carrier concentration and thus a higher electrical resistivity, the Seebeck coefficient compensates this difference and the final power factor is the same.

This is the same behavior observed for the monocrystalline "p"-doped samples. The difference on the measured Seebeck coefficient and electrical resistivity comes from the difference of doping level, and not from the QD inclusion effect. A discussion will be performed at the end of this section in order to understand the possible

reasons why QD inclusion on the “p” and “n” doped samples did not present the same effect on the Seebeck coefficient.

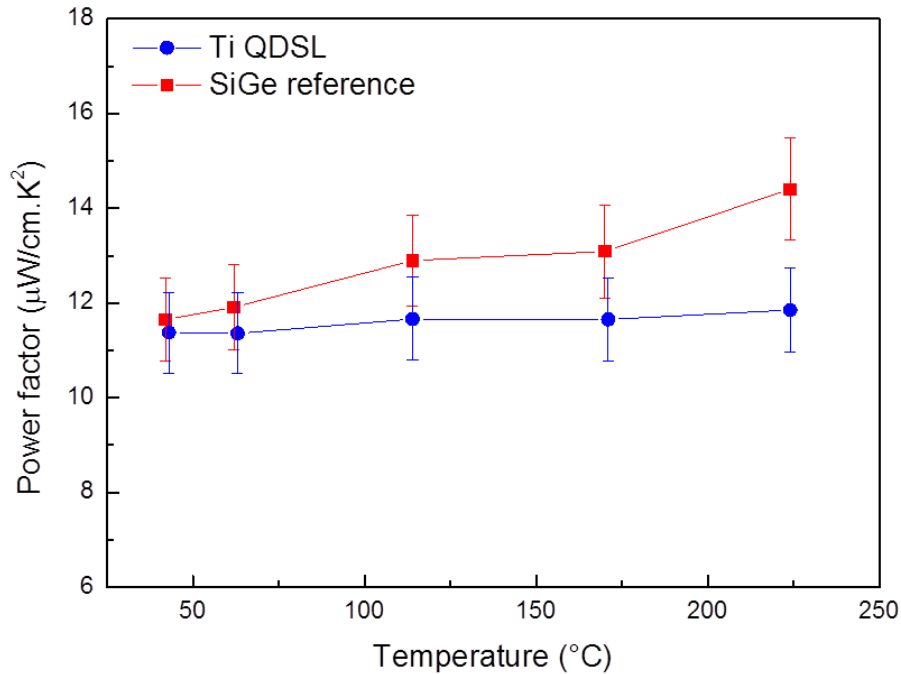


Figure 3.30: Evolution of the thermoelectric power factor with the temperature for the monocrystalline Ti-based “p”-doped QDSL (blue circles) and for its SiGe reference (red squares).

The obtained power factor values correspond to the values measured by Joshi et al. for bulk “p”-doped $\text{Si}_{80}\text{Ge}_{20}$ samples in [14]. The authors measured values between 10 and 20 $\mu\text{W}/\text{cm.K}^2$ at room temperature, which is in the same order of magnitude of the results obtained during this thesis, a power factor around 11,5 $\mu\text{W}/\text{cm.K}^2$ (Figure 3.30).

In Table 3.5 are presented the results of the Hall effect and thermal conductivity measurements for these samples. Considering the carriers mobility, both the QDSL and the sample presented a similar value. Since the carriers mobility is reduced when a higher dopant concentration is employed (which is the case of the SiGe reference for this study), it is not possible to determine if the dopant accumulation produced an overall increase of the mobility for these samples. Considering the mobility values obtained, they are close to the values calculated for Si for a similar dopant concentration, which is around 50 $\text{cm}^2/\text{V.s}$. The same is valuable for the electrical resistivity, which is around 2×10^{-3} for the SiGe reference and around 1×10^{-3} for the calculated Silicon.

Considering the thermal conductivity, in this case no reduction was observed after the QD inclusion inside the matrix. A possible reason for this is the lower QD volumetric density $v_{\%}$ for this sample compared to the “n”-doped monocrystalline sample. This lower density probably reduces the observed nanometric effect up to a point where it is no longer detectable.

Table 3.5: Additional measured properties of the Ti-based monocrystalline “p”-doped QDSL and its SiGe reference.

	carriers conc. (cm^{-3})	carriers mobility ($\text{cm}^2/\text{V}\cdot\text{s}$)	dopant flow rate (sccm)	thermal conductivity ($\text{W}/\text{m}\cdot\text{K}$)
QDSL	$4,30\text{E}+19 \pm 0,3$	42 ± 3	10	$5,9 \pm 0,6$
Ref.	$1,10\text{E}+20 \pm 0,1$	35 ± 2	5	$6,4 \pm 0,6$

3.3.b - Polycrystalline QDSL

Concerning the “p”-doped polycrystalline Ti-based QDSL, in Figure 3.31 are presented the results of the measurements of the Seebeck coefficient and the electrical resistivity.

In the case of these samples, only a slight change was observed on the Seebeck coefficient and on the electrical resistivity, and no differences on the calculated power factor were observed (Figure 3.32). This behavior is similar to those for the monocrystalline “p”-doped samples, and here again no increase on the power factor was observed after the inclusion of QD inside the matrix. Similarly to what was observed for the “n”-doped polycrystalline sample, the power factor for these samples was lower (around $6 \mu\text{W}/\text{cm}\cdot\text{K}^2$) than the power factor obtained for the monocrystalline samples (around $11,5 \mu\text{W}/\text{cm}\cdot\text{K}^2$) mostly due to the lower carriers mobility (Table 3.6) caused by grain boundary scattering.

Moreover, the reference and the QDSL samples present the same carriers' concentration and mobility, indicating that the QD produced no effect on the electrical transport.

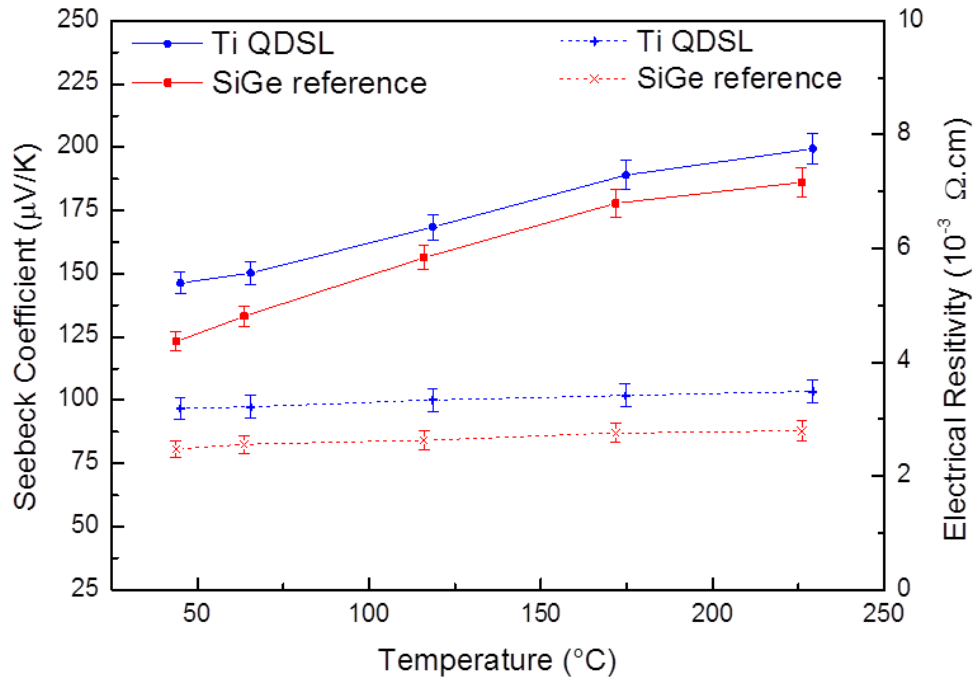


Figure 3.31: left axis: Seebeck coefficient of the p-doped polycrystalline Ti-based QDSL (blue circles) and of the SiGe reference (red squares). Right axis: Electrical resistivity of the p-doped polycrystalline Ti-based QDSL (blue crosses) and of the SiGe reference (red X).

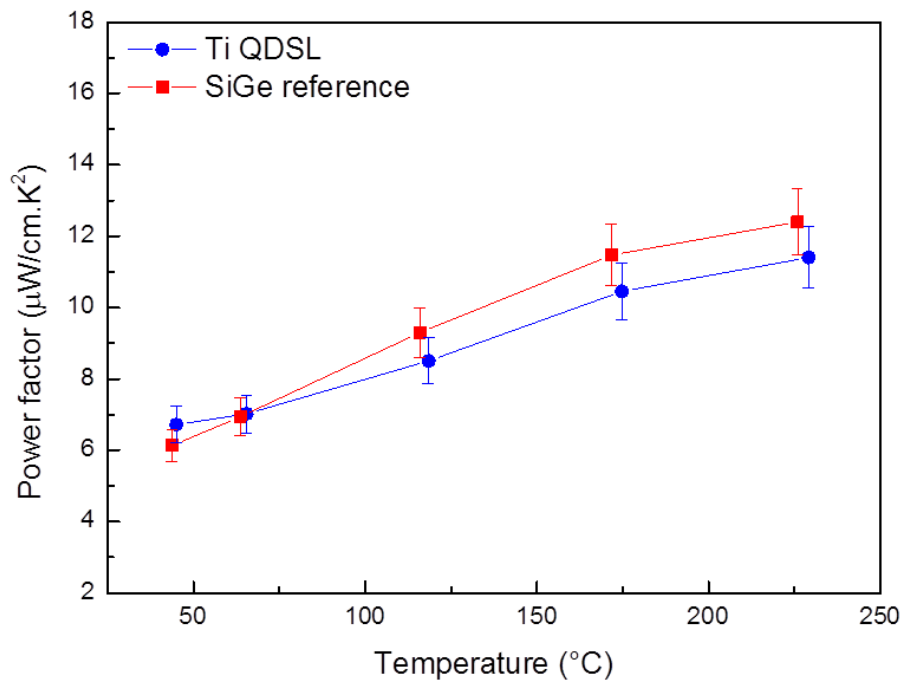


Figure 3.32: Evolution of the thermoelectric power factor with the temperature for the polycrystalline Ti-based “p”-doped QDSL (blue circles) and for its SiGe reference (red squares).

In this table it can also be seen that similarly to the samples characterized until now, a higher amount of dopant (dopant flow rate) is necessary for the QDSL compared to the reference sample due to the dopant accumulation near the QD.

The thermal conductivity measurements were not performed for these samples because of the reasons stated at the beginning of this section.

Table 3.6: Additional measured properties of the Ti-based polycrystalline “p”-doped QDSL and its SiGe reference.

	carriers conc. (cm^{-3})	carriers mobility ($\text{cm}^2/\text{V}\cdot\text{s}$)	dopant flow rate (sccm)	thermal conductivity ($\text{W}/\text{m}\cdot\text{K}$)
QDSL	$9,50\text{E}+19 \pm 0,6$	20 ± 1	20	-
Ref.	$1,10\text{E}+20 \pm 0,1$	25 ± 1	10	-

3.4 - Discussion about the thermoelectrical characterization results of the Ti-based QDSL

Very interesting results were obtained from the thermoelectric characterization of Ti-based QDSL, and an improvement of the thermoelectric properties after the inclusion of QD was observed.

Following a further discussion concerning the two main thermoelectric properties will be presented, i.e., the observed changes on the power factor and on the thermal conductivity.

At the end of this chapter the main results obtained will be compared with literature results and suggestion for future works will be presented.

- **Power factor increase**

The increase of the samples power factor via an augmentation of the Seebeck coefficient was observed for both the mono and polycrystalline “n”-doped samples.

Two hypotheses can be raised to explain this considerable increase of almost 2 times at room temperature on the Seebeck coefficient. The first one has been discussed on Chapter 1, and is due to a possible changing on the material’s density of

states leading to a greater asymmetry of the differential conductivity and thus a bigger Seebeck coefficient.

The other hypothesis is related to the material's doping characteristics. The dopant accumulation can produce a local doping of the material (modulation doping). This effect has been reported by Yu et al. in reference [4]. Since the dopant atoms are concentrated in few zones rather than fully dispersed inside the material, the charge carriers' will suffer less scattering due to impurity atoms.

This would result on an increased mobility and a similar electrical resistivity can be obtained but with a lower dopant atoms concentration, which would lower the Fermi level inside the conduction band and increase the asymmetry of the carriers' energy along it, increasing the Seebeck coefficient.

Another possibility in the case of this thesis is that the TiSi_2 QD could locally dope the material, causing a similar effect.

Considering the "p"-doped material it is not clear why the same effect was not observed. A possible hypothesis has already been cited before, and is related to lower QD volumetric fraction $v_{\%}$ in the case of the "p"-doped samples, which can reduce the nanometric effect produced by the QD.

As a further way to clarify the obtained results, a theoretical study could be made in order to model the effect of both the QD and the dopant accumulation inside the SiGe matrix on the material's density of states, Seebeck coefficient, carrier's mobility and electrical conductivity.

- **Thermal conductivity reduction**

Consider the "n"-doped samples. A 1,25-fold reduction of the material's thermal conductivity was observed for the monocrystalline QDSL sample compared to its reference, proving the effect of Ti-based QD inclusion on the material thermic transport. For the polycrystalline sample no effect was observed, probably because the grain boundaries already act as scattering sites for the phonons, thus masking the effect coming from the QD.

The inclusion of the QD inside the "p"-doped samples apparently did not produce the expected effect on the thermal conductivity, even for the monocrystalline sample. This is probably due to the fact that the QD volumetric fraction for this sample was not high enough to produce a detectable effect.

3.5 - Mo-based QDSL: n-doped samples

3.5.a - Monocrystalline QDSL

In Figure 3.33 are presented the results of the Seebeck coefficient and the electrical resistivity measurements for the “n”-doped monocrystalline sample and its reference.

The electrical resistivity for both samples was the same, but the Seebeck coefficient for the reference sample higher. This produced a calculated power factor (Figure 3.34) higher for the reference sample than for the QDSL.

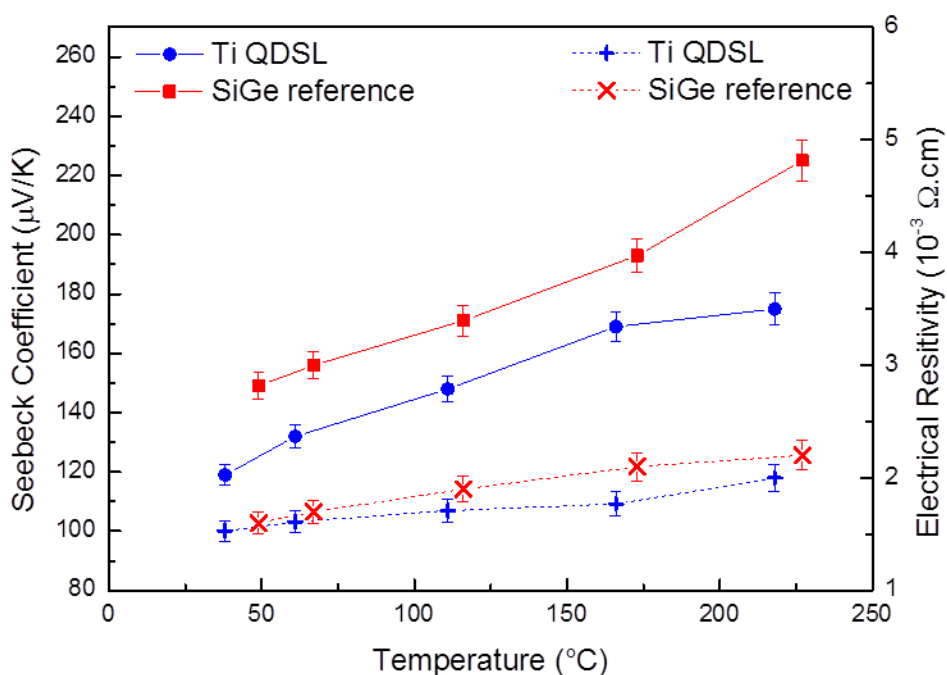


Figure 3.33: left axis: Seebeck coefficient of the n-doped monocrystalline Mo-based QDSL (blue circles) and of the SiGe reference (red squares). Right axis: Electrical resistivity of the n-doped monocrystalline Mo-based QDSL (blue crosses) and of the SiGe reference (red X).

It should be noticed however that between the 100 -175 °C temperature range the values are similar considering the errors bar. Moreover, it is possible that other source of errors exists and was not considered for these measures. It is thus possible that both samples have the same power factors and that the inclusion of Mo-based QD produced no effects on it.

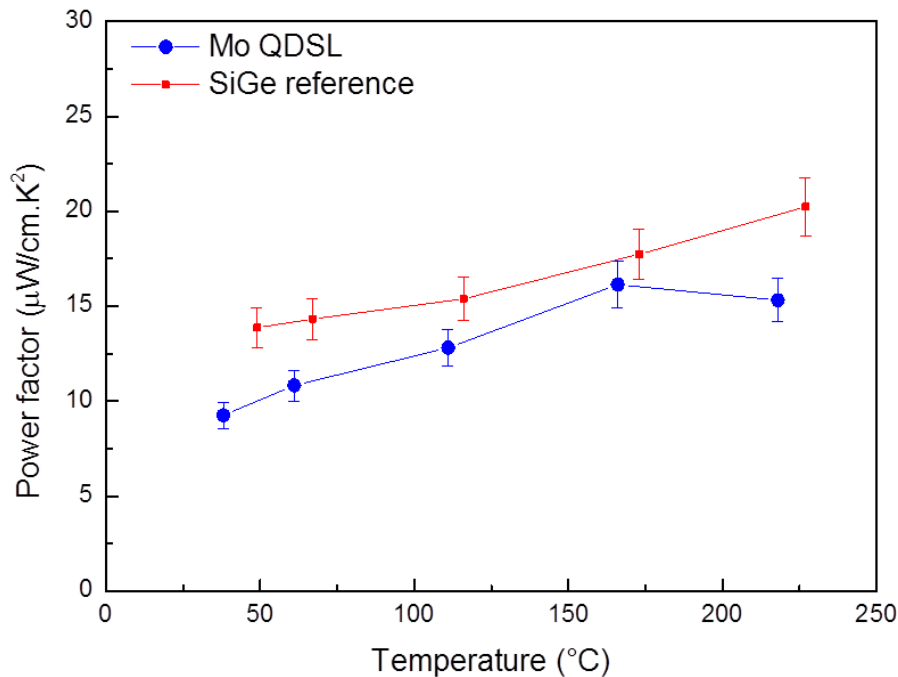


Figure 3.34: Evolution of the thermoelectric power factor with the temperature for the monocrystalline Mo-based “n”-doped QDSL (blue circles) and for its SiGe reference (red squares).

The obtained values of carriers’ mobility (around $77 \text{ cm}^2/\text{V}\cdot\text{s}$) presented in Table 3.7 and room temperature electrical resistivity (around $1,5 \times 10^{-3} \Omega\cdot\text{cm}$) are close to the calculated values for monocrystalline silicon with the same dopant concentration, i.e., a mobility of around $82 \text{ cm}^2/\text{V}\cdot\text{s}$ and a resistivity of around $1,3 \times 10^{-3} \Omega\cdot\text{cm}$. The power factor as well is of the same order of magnitude as those measured in reference [9].

Considering the thermal conductivity measurements, a 1,4-fold reduction of the thermal resistivity was observed when QD were included inside the SiGe matrix, leading to an improvement of the materials thermoelectric properties. These results prove the effect of Mo-based QD on the phonons scattering and thermal conductivity reduction.

A similar result (1,2-fold reduction) was reported by Favier et al. in reference [2], where a volumetric fraction of 1,3 % of Mo silicide quantum dots were incorporated in a bulk “n”-doped SiGe matrix.

It can also be seen in Table 3.7 that for these samples there was no need to change the dopant gas flow rate to obtain similar final carriers concentration for the QDSL and the reference sample. Even though a certain phosphorus accumulation was observed near the QD (Figure 3.13), this effect is much lower than for the Ti-based samples due to the smaller size of the QD. The dopant concentration in solid solution of the QDSL was thus not influenced by the presence of Mo QD for this sample.

Table 3.7: Additional measured properties of the Mo-based monocrystalline “n”-doped QDSL and its SiGe reference.

	carriers conc. (cm^{-3})	carriers mobility ($\text{cm}^2/\text{V}\cdot\text{s}$)	dopant flow rate (sccm)	thermal conductivity ($\text{W}/\text{m}\cdot\text{K}$)
QDSL	$5,80\text{E}+19 \pm 0,3$	77 ± 5	20	$9,5 \pm 0,9$
Ref.	$6,10\text{E}+19 \pm 0,4$	76 ± 5	20	$13,0 \pm 1,3$

3.5.b - Polycrystalline QDSL

Concerning the polycrystalline “n”-doped Mo-based samples, the Seebeck coefficient and electrical resistivity measurements are presented in Figure 3.35. The calculated thermoelectrical power factor is shown in Figure 3.36.

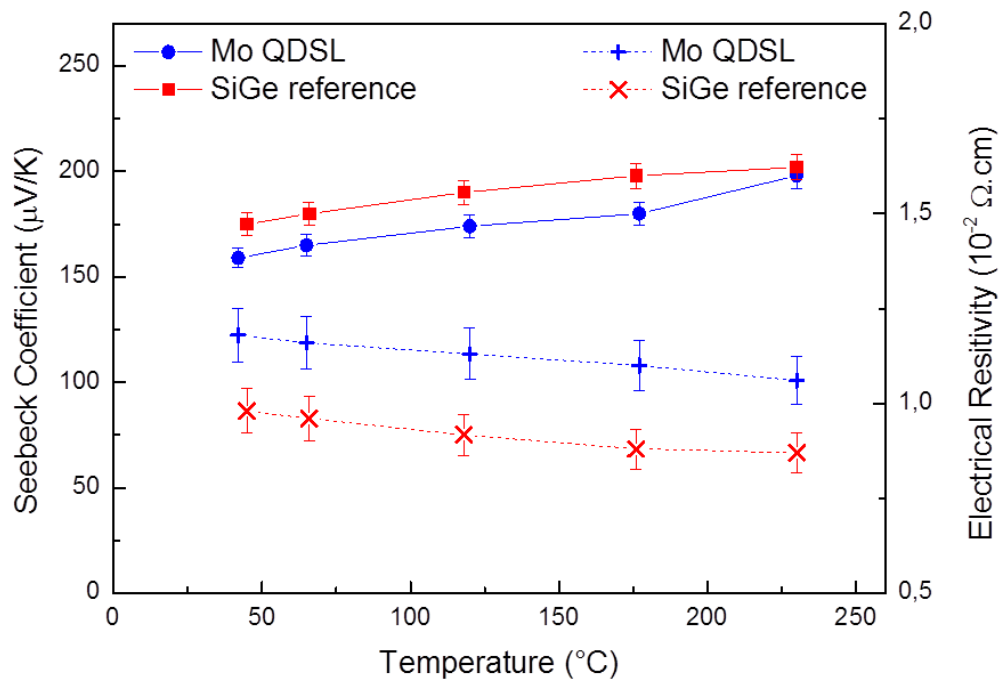


Figure 3.35: left axis: Seebeck coefficient of the “n”-doped polycrystalline Mo-based QDSL (blue circles) and of the SiGe reference (red squares). Right axis: Electrical resistivity of the “n”-doped polycrystalline Mo-based QDSL (blue crosses) and of the SiGe reference (red X).

A small difference on the electrical resistivity of the samples was observed, even though the carriers' concentration and mobility measured was practically the same (Table 3.8). No significant changes on the Seebeck coefficient were observed, though.

This resulted on the obtaining of a higher power factor for the reference sample than for the Mo-based QDSL, similarly to the results for the monocrystalline sample.

Two possibilities exist to explain this phenomenon. The first one has already been cited and is the possibility that the measurement error bar is higher than the calculated, and in this case the Seebeck coefficient and power factor for both samples is the same.

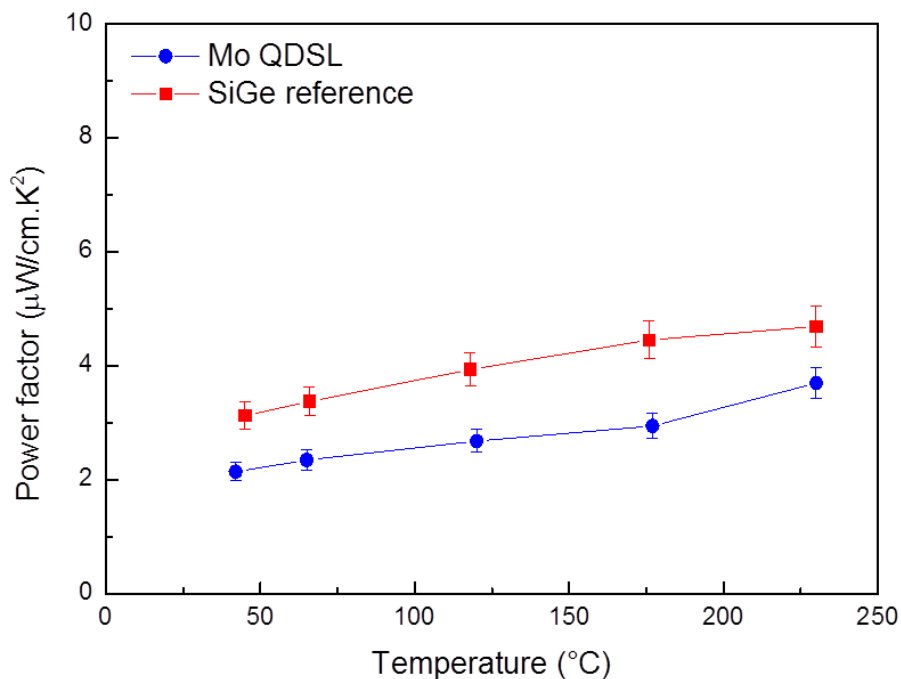


Figure 3.36: Evolution of the thermoelectric power factor with the temperature for the polycrystalline Mo-based "n"-doped QDSL (blue circles) and for its SiGe reference (red squares).

Since the measured carriers concentration and mobility is the same for both samples, the other possible explanation is that indeed the inclusion of Mo-based QD reduces the material's Seebeck coefficient. Further studies should be performed in order to better evaluate and understand the origin of these results.

If these results are compared with the ones for the monocrystalline sample, it can be seen that the power factor is smaller due a reduced carriers' mobility. This is similar to what was observed for the Ti-based samples, where the grain boundaries reduce the material carrier's mobility.

Table 3.8: Additional measured properties of the Mo-based polycrystalline “n”-doped QDSL and its SiGe reference.

	carriers conc. (cm ⁻³)	carriers mobility (cm ² /V·s)	dopant flow rate (sccm)	thermal conductivity (W/m.K)
QDSL	3,80E+19 ± 0,2	17 ± 1	20	-
Ref.	3,60E+19 ± 0,2	16 ± 1	20	-

Similarly to the monocrystalline sample, no changes on the dopant flow rate were necessary to produce QDSL and reference samples with the same dopant concentration, indicating that a lower dopant accumulation exists compared to Ti-based samples.

No information exists concerning the thermal conductivity for these samples, since it was not possible to perform the thermo-reflectance measurements for these samples due to the unavailability of the equipment.

3.6 - Mo-based QDSL: p-doped samples

3.6.a - Monocrystalline QDSL

The electrical resistivity and Seebeck coefficient measurements for the “p”-doped Mo-based monocrystalline sample and its reference are presented in Figure 3.37 and calculated power factor in Figure 3.38.

In the case of these samples, the electrical resistivity was slightly different when the QDSL and the reference samples are compared due to a different dopant concentration (Table 3.9). However this difference was compensated by the Seebeck coefficient as observed for the monocrystalline p-doped Ti-based QDSL in section 3.3.a

This resulted on a power factor value (Figure 3.38) very similar for the QDSL and for the reference sample up to 150 °C and for higher temperatures the same value was obtained considering the error bar.

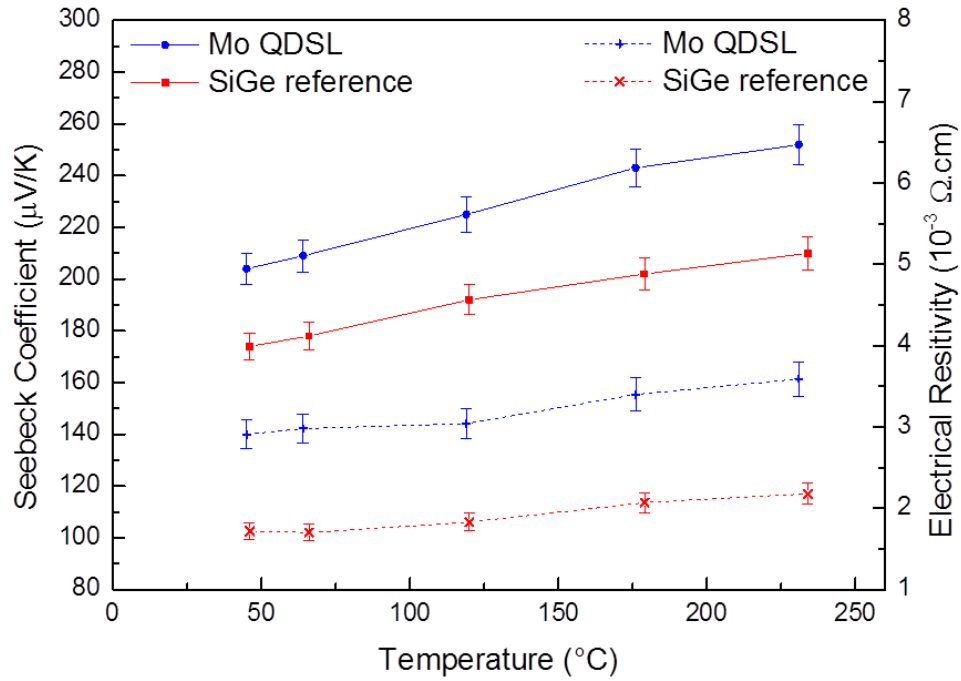


Figure 3.37: left axis: Seebeck coefficient of the “p”-doped monocrystalline Mo-based QDSL (blue circles) and of the SiGe reference (red squares). Right axis: Electrical resistivity of the p-doped monocrystalline Mo-based QDSL (blue crosses) and of the SiGe reference (red X).

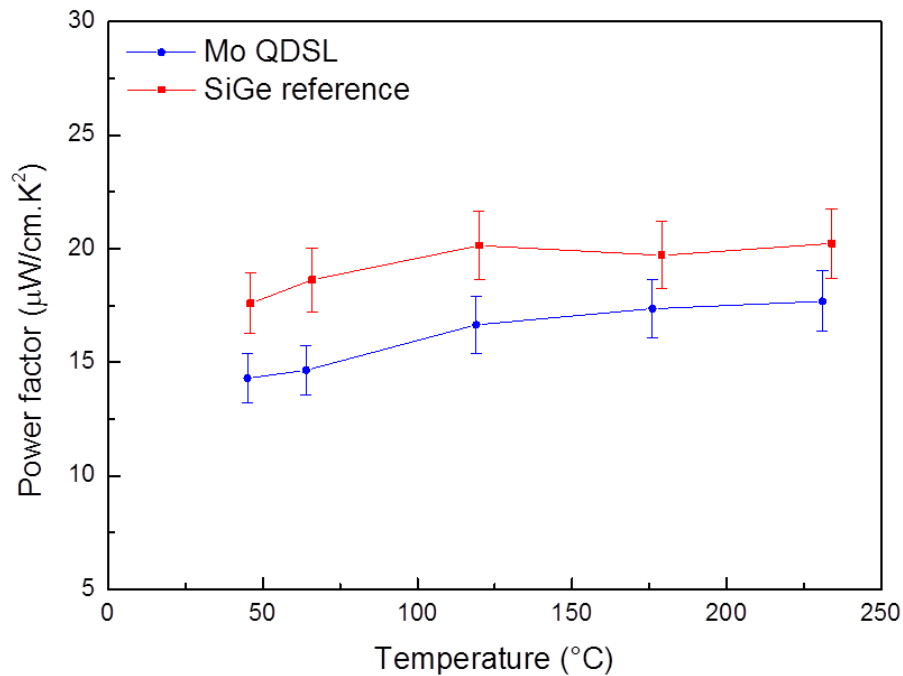


Figure 3.38: Evolution of the thermoelectric power factor with the temperature for the monocrystalline Mo-based “p”-doped QDSL (blue circles) and for its SiGe reference (red squares).

Both samples presented a power factor value between 15 and 20 $\mu\text{W}/\text{cm}\cdot\text{K}^2$ at room temperature, which is comparable to the literature results reported by Wang et al. in [9].

Table 3.9: Additional measured properties of the Mo-based monocrystalline “p”-doped QDSL and its SiGe reference.

	carriers conc. (cm^{-3})	carriers mobility ($\text{cm}^2/\text{V}\cdot\text{s}$)	dopant flow rate (sccm)	thermal conductivity ($\text{W}/\text{m}\cdot\text{K}$)
QDSL	5,80E+19 \pm 0,4	41 \pm 2	20	-
Ref.	9,20E+19 \pm 0,5	41 \pm 2	20	-

The mobility values for both samples corresponds to the values obtained for the monocrystalline p-doped Ti-based QDSL samples and with the calculations for Si with an equivalent dopant concentration. Similarly to the monocrystalline n-doped Mo-based sample and its reference, here again the QD inclusion did not change the carriers' mobility.

Considering the thermal conductivity, no information is available because of the lack of availability of the thermo-reflectance equipment.

3.6.b - Polycrystalline QDSL

In Figure 3.39 are presented the electrical and Seebeck measurements for the “p”-doped polycrystalline Mo-based samples. A small difference on the carrier's concentration between the QDSL and the reference was observed, resulting on a slight difference of the electrical resistivity.

The obtained Seebeck coefficient was higher for the QDSL compared to the reference and the calculated power factor Figure 3.40 showed an increase of the properties when a QDSL is produced compared to pure SiGe.

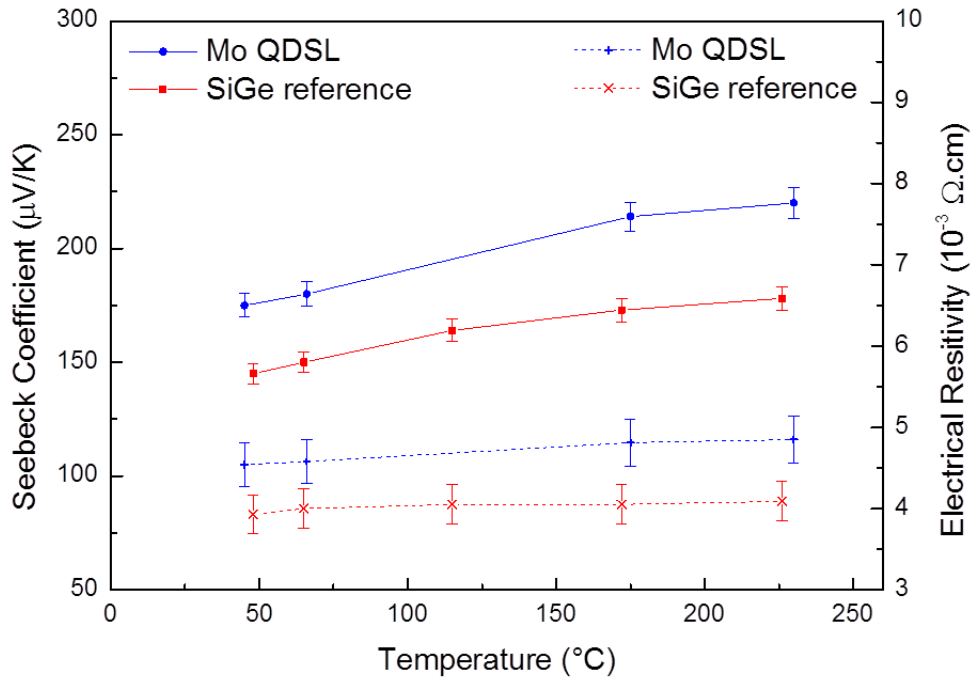


Figure 3.39: left axis: Seebeck coefficient of the “p”-doped polycrystalline Mo-based QDSL (blue circles) and of the SiGe reference (red squares). Right axis: Electrical resistivity of the “p”-doped polycrystalline Mo-based QDSL (blue crosses) and of the SiGe reference (red X).

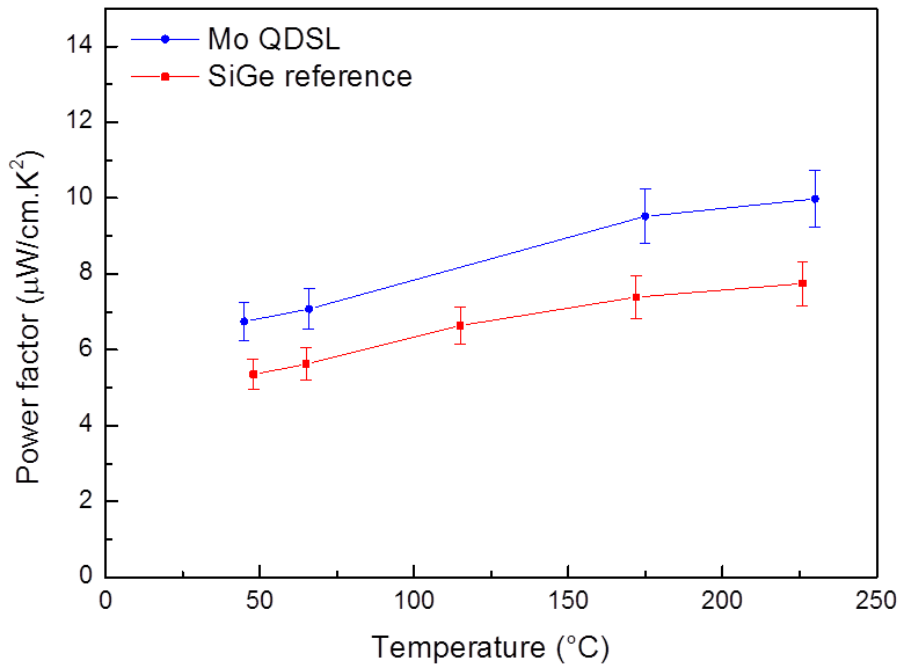


Figure 3.40: Evolution of the thermoelectric power factor with the temperature for the polycrystalline Mo-based “p”-doped QDSL (blue circles) and for its SiGe reference (red squares).

This was the only Mo-based QDSL to present an increase of the power factor. Here again care should be taken in order to explain this phenomena because the power factor values are very close between the QDSL and the reference sample.

By further looking at Table 3.10 it can be seen that for this sample a difference on the dopant gas flow rate was employed to produce a similar value of carrier concentration between the QDSL and the reference sample. This indicates a higher dopant aggregation near the QD, and may be the reason why in this case a higher power factor is obtained for the QDSL sample.

Table 3.10: Additional measured properties of the Mo-based polycrystalline “p”-doped QDSL and its SiGe reference.

	carriers conc. (cm ⁻³)	carriers mobility (cm ² /V·s)	dopant flow rate (sccm)	thermal conductivity (W/m.K)
QDSL	5,40E+19 ± 0,3	25 ± 1	20	-
Ref.	7,60E+19 ± 0,5	21 ± 1	10	-

Concerning the carrier’s mobility the same pattern observed for the other polycrystalline samples was observed here, i.e., the mobility was reduced by the grain boundary scattering resulting on a lower power factor compared to the monocrystalline samples.

No results concerning the thermal conductivity were available for these samples.

3.7 - Discussion about the thermoelectrical characterization results of the Mo-based QDSL

In this section a discussion considering the obtained thermoelectric results will be presented. As it was made for the Ti-based samples, the discussions will be divided in two main parts, one considering the effect of the QD on the thermal conductivity and the other considering the QD effect on thermoelectric the power factor.

At the end of Chapter 3, a global conclusion will be presented as well as summary of the obtained thermoelectric properties and their comparison to reference works.

- **Thermal conductivity reduction**

Considering the thermal conductivity measurements, thermo-reflectance measurements were only performed for one sample, the monocrystalline “n”-doped QDSL.

For this sample a reduction of the thermal conductivity from 13,0 W/m.K to 9,5 W/m.K was observed after the inclusion of QD inside the SiGe matrix. These results prove the effect of Mo-based QD on the phonons scattering and thermal conductivity reduction, as predicted by Mingo et al.

The 1,4-fold reduction is coherent with the results observed for the monocrystalline “n”-doped Ti-based QDSL. The value of the thermal conductivity measured for the Mo-based sample is however higher than the obtained values for the Ti-based samples because of the lower Ge content of the former. These results are consistent with what was expected, since a lower Ge content results on lower alloy phonons scattering and thus on a higher thermal conductivity.

- **Power factor increase**

The observed results for the changes on the power factor after the inclusion of Mo-based QD inside the SiGe matrix are less straight-forward to analyze than the results for the Ti-based samples.

For the both the “n” and “p”-doped monocrystalline samples, it seems that no effect was observed after the inclusion of QD. The small variation between the measured values from the reference and the QDSL may come from an underestimated error bar due to unconsidered errors sources such as sample inhomogeneity, punctual defects or others.

For the polycrystalline samples, it seems that the power factor was reduced after the inclusion of QD inside the “n”-doped sample, even if no particular changes on the carrier’s mobility was observed. Here again this difference could be due to an underestimated error bar.

For the “p”-doped polycrystalline sample the opposite effect was observed, and a small increase of the Seebeck coefficient was observed. In this case, however, a higher gas flow rate was necessary to dope the QDSL in the same way than the reference, indicating that a higher dopant accumulation occurred. This may have produced a modulation doping as discussed for the Ti-based samples and may be the origin of the increase on the Seebeck coefficient observed.

4 - Conclusion

In this chapter were presented the results concerning the structural and thermoelectrical characterization of the produced QDSL and their SiGe references. Three main properties were studied, i.e.: the dopant employed (“n” and “p”-doping); the crystallinity (mono and polycrystalline) and the nature of the QD inclusions (Ti and Mo-based QD).

By analyzing the obtained TEM images it was possible to confirm the presence of silicides inclusions inside all of the analyzed samples. As expected, the metallic QD reacted with Si atoms to form the expected TiSi_2 and MoSi_2 phases, except for one sample, composed of TiSi_3 inclusions.

It was possible to identify the behavior of the QD during the growth, and for the Ti-based inclusion a coalescence phenomenon was observed. This produced a change on the expected diameter of the QD, but with no apparent effect on the thermoelectric properties. A more important feature was the relation between the QD diameters and the layer thickness, described by the volumetric fraction $\%_v$ of the QD inside the matrix.

When the results of the thermal conductivity measurements of the monocrystalline “n” and “p”-doped Ti-based QDSL are compared, it appears that the lower volumetric fraction $\%_v$ the “p”-doped sample is responsible to the fact that no reduction on the thermal conductivity is observed.

Within the samples that presented the layers composing the QDSL too thick compared to the QD no effects on the thermoelectric power factor was observed.

An interesting feature observed on the TEM images was the formation of QW structures. The growth mechanism for these structures was identified as being due to the catalyst effect of the QD on the SiH_4 pyrolysis during the QDSL growth.

Concerning the thermoelectrical characterization results, the measured values were summarized in tables and compared to literature results. For the Ti-based QDSL the results were compared to the works of Joshi et al. and Wang et al, already cited in Chapter 1. The results for the Mo-based samples were compared to the results obtained by Favier, who also investigated the inclusion of Mo-based QD in SiGe.

In Table 3.11 are presented the results concerning the “n”-doped Ti-based samples. These results are among the best obtained during this work. Both the mono and polycrystalline QDSL presented an increase on their power factor after the inclusion of the QD. This produced a power factor up to 4 times higher for the monocrystalline sample compared to the SiGe reference and 2,3 times for the polycrystalline sample. The possible reasons for this have already been discussed previously. Moreover, the monocrystalline sample also presented a reduction of its thermal conductivity due to the QD inclusion.

The results show that a great improvement of the material thermoelectric properties are obtained by including QD in a “n”-doped SiGe matrix. The obtained results are of the same order of magnitude as those presented by Wang et al. in [9] and for the RTG material. It should be noticed that both the RTG and the results presented by Wang et al. concerned samples with 20% of Ge, whereas the presented QDSL had around 10% of Ge. This explains the lower values of thermal conductivity obtained by these authors.

Table 3.11: Overall thermoelectric results of the “n”-doped Ti-based samples, the SiGe references and literature results.

<u>sample</u>	<u>thermal conductivity</u>	<u>thermal conductivity reduction ($\lambda_{\text{alloy}}/\lambda_{\text{nano}}$)</u>	<u>power factor</u>	<u>power factor increase ($S_{\text{nano}}/S_{\text{alloy}}$)</u>
Ti-n-MONO	6,8	1,25	11	4
SiGe reference	8,5		3	
Ti-n-POLY	4,6	-	3,5	2,3
SiGe reference	4,2		1,5	
Wang et al. (nanosctrutured)	2,5	1,8	14	0,8
RTG (reference SiGe)	4,5		17	

Concerning the “p”-doped Ti-based material, the overall results can be seen in Table 3.12. In this case, no effect was observed on the power factor after the inclusion of QD. A possible reason for this has already been discussed, and is related to the lower volumetric fraction of QD in this sample. The same argument can be employed to explain why in this case no reduction on the thermal conductivity was observed.

In the case of this sample the reference literature results are also in the same order of magnitude of the results for the produced QDSL.

Further studies should be performed in order to increase the QD volumetric fraction to analyze the Ti-based QD effect in “p”-doped samples.

Table 3.12: Overall thermoelectric results of the “p”-doped Ti-based samples, the SiGe references and literature results.

<u>sample</u>	<u>thermal conductivity</u>	<u>thermal conductivity reduction ($\lambda_{\text{alloy}}/\lambda_{\text{nano}}$)</u>	<u>power factor</u>	<u>power factor increase ($S_{\text{nano}}/S_{\text{alloy}}$)</u>
Ti-p-MONO	5,9	-	11,3	-
SiGe reference	6,4	-	11,6	-
Ti-p-POLY	-	-	6,4	-
SiGe reference	-	-	6,1	-
Joshi et al. (nanosctrutured)	2,5	2	12	0,9
RTG	4,9	-	13,5	-

In Table 3.13 are presented the results of the “n”-doped Mo-based samples. The results were compared with the results reported by Favier in [15], who employed a volumetric fraction of around 1,3 % of Mo silicide in a SiGe matrix.

Table 3.13: Overall thermoelectric results of the “n”-doped Mo-based samples, the SiGe references and literature results.

<u>sample</u>	<u>thermal conductivity</u>	<u>thermal conductivity reduction ($\lambda_{\text{alloy}}/\lambda_{\text{nano}}$)</u>	<u>power factor</u>	<u>power factor increase ($S_{\text{nano}}/S_{\text{alloy}}$)</u>
Mo-n-MONO	9,5	1,4	10	0,8
SiGe reference	13	-	13	-
Mo-n-POLY	-	-	2	0,7
SiGe reference	-	-	3	-
MoSi _x + SiGe (Favier)	5,1	1,2	12,5	1,25
SiGe reference (Favier)	5,9	-	10	-

It can be seen that the inclusion of Mo-based QD produced a reduction of the material's thermal conductivity, as predicted by the theory. This reduction was of the same order of magnitude as the one found by Favier.

A small difference on the power factor was observed after the inclusion of the QD, but it is not clear whether this difference comes from difference on the materials or due to measurements errors. Further studies should be performed, notably theoretical study to evaluate the role of Mo silicide QD on the material's properties. A possible reason to explain the difference on the power factor has been suggested by Favier, where the QD could act as "counter dopants" annihilating the dopant effect and reducing the material's power factor.

In Table 3.14 are presented the results concerning the "p"-doped Mo-based samples. No information is available concerning the thermal conductivity. For the monocrystalline sample, a reduction of the power factor is observed, where for the polycrystalline an increase is observed. For the monocrystalline sample, this reduction is of the same order of the one observed by Favier, and the reason presented is related to the "counter doping". It is not clear however why the polycrystalline sample did not follow the same pattern.

Table 3.14: Overall thermoelectric results of the "p"-doped Mo-based samples, the SiGe references and literature results.

<u>sample</u>	<u>thermal conductivity</u>	<u>thermal conductivity reduction ($\lambda_{\text{alloy}}/\lambda_{\text{nano}}$)</u>	<u>power factor</u>	<u>power factor increase ($S_{\text{nano}}/S_{\text{alloy}}$)</u>
Mo-p-MONO	-	-	14	0,8
SiGe reference	-	-	17,5	
Mo-p-POLY	-	-	7	1,4
SiGe reference	-	-	5	
MoSi_x + SiGe (Favier)	3,2	1,8	12,5	0,8
SiGe reference (Favier)	5,7		15	

Globally, very interesting results were obtained from the thermoelectric characterization of both Ti and Mo-based samples.

The effect of the silicide QD inclusion on the thermal conductivity was demonstrated, and matches the theory predicted results. The observed reduction is no as bit as the maximum 4-fold reduction expected by Mingo et al in [1], but improvements on the material could be tested, such as increasing the Ge content of the films up to 50% and increasing the QD volumetric fraction.

Moreover, a considerable increase on the Seebeck coefficient was observed for certain samples, which can lead, together with the reduction of the thermal conductivity to a great improvement of the material's ZT.

This is the first time that the growth and characterization of $\text{TiSi}_x/\text{SiGe}$ and $\text{MoSi}_x/\text{SiGe}$ QDSL is reported. As it is normal to be expected in such cases, there are still few points that are still not clear in order to fully understand the effect of the silicide QD inclusion in the materials. Hopefully, this work will serve as a model and starting point for future works dedicated to elucidate the mechanisms and physical phenomena taking place.

REFERENCES

- [1] N. Mingo, D. Hauser, N. P. Kobayashi, M. Plissonnier, and A. Shakouri, “‘Nanoparticle-in-Alloy’ Approach to Efficient Thermoelectrics: Silicides in SiGe,” *Nano Lett*, vol. 9, no. 2, pp. 711–715, 2009.
- [2] K. Favier, G. Bernard-Granger, C. Navone, M. Soulier, M. Boidot, J. Leforestier, J. Simon, J.-C. Tedenac, and D. Ravot, “Influence of in situ formed MoSi₂ inclusions on the thermoelectrical properties of an N-type silicon–germanium alloy,” *Acta Mater.*, vol. 64, pp. 429–442, Feb. 2014.
- [3] C. J. Vineis, A. Shakouri, A. Majumdar, and M. G. Kanatzidis, “Nanostructured Thermoelectrics: Big Efficiency Gains from Small Features,” *Adv. Mater.*, vol. 22, pp. 3970–3980, Sep. 2010.
- [4] B. Yu, M. Zebarjadi, H. Wang, K. Lukas, H. Wang, D. Wang, C. Opeil, M. Dresselhaus, G. Chen, and Z. Ren, “Enhancement of Thermoelectric Properties by Modulation-Doping in Silicon Germanium Alloy Nanocomposites,” *Nano Lett.*, vol. 12, no. 4, pp. 2077–2082, Apr. 2012.
- [5] L. J. van der Pauw, “A method of measuring specific resistivity and Hall effect of discs of arbitrary shape,” *Philips Res. Rep.*, vol. 13, 1958.
- [6] W. Limmer, “Hall Effect in Semiconductors.” *Ulm University*, 2013.
- [7] S. Dilhaire, J.-M. Rampnoux, S. Grauby, G. Pernot, and G. Calbris, “Nanoscale Thermal Transport Studied With Heterodyne Picosecond Thermoreflectance,” *ASME 2009*, pp. 451–456, Jan. 2009.
- [8] G. Pernot, H. Michel, B. Vermeersch, P. Burke, H. Lu, J.-M. Rampnoux, S. Dilhaire, Y. Ezzahri, A. Gossard, and A. Shakouri, “Frequency-Dependent Thermal Conductivity in Time Domain Thermoreflectance Analysis of Thin Films,” *MRS Online Proc. Libr.*, vol. 1347, p. null–null, 2011.
- [9] X. W. Wang, H. Lee, Y. C. Lan, G. H. Zhu, G. Joshi, D. Z. Wang, J. Yang, A. J. Muto, M. Y. Tang, J. Klatsky, S. Song, M. S. Dresselhaus, G. Chen, and Z. F. Ren, “Enhanced thermoelectric figure of merit in nanostructured n-type silicon germanium bulk alloy,” *Appl. Phys. Lett.*, vol. 93, no. 19, p. 193121, Nov. 2008.
- [10] BRIGHAM YOUNG UNIVERSITY, Resistivity & Mobility Calculator for Various Doping Concentrations in Silicon.[Online] .Available: <http://www.cleanroom.byu.edu/ResistivityCal.phtml>
- [11] G. Savelli, M. Plissonnier, V. Remondière, J. Bablet, and J.-M. Fournier, “An innovating technological approach for Si–SiGe superlattice integration into thermoelectric modules,” *J. Micromechanics Microengineering*, vol. 18, no. 10, p. 104002, Oct. 2008.
- [12] W. H. Nam, Y. S. Lim, S.-M. Choi, W.-S. Seo, and J. Y. Lee, “High-temperature charge transport and thermoelectric properties of a degenerately Al-doped ZnO nanocomposite,” *J. Mater. Chem.*, vol. 22, no. 29, p. 14633, 2012.
- [13] J. Y. W. Seto, “The electrical properties of polycrystalline silicon films,” *J. Appl. Phys.*, vol. 46, no. 12, pp. 5247–5254, Dec. 1975.
- [14] G. Joshi, H. Lee, Y. Lan, X. Wang, G. Zhu, D. Wang, R. W. Gould, D. C. Cuff, M. Y. Tang, M. S. Dresselhaus, G. Chen, and Z. Ren, “Enhanced thermoelectric figure-of-merit in nanostructured p-type silicon germanium bulk alloys,” *Nano Lett.*, vol. 8, no. 12, pp. 4670–4674, Dec. 2008.
- [15] K. Favier, Étude de matériaux composites à base de nanosiliciures de métaux de transition pour la thermoélectricité. *ICGICMCM Montpellier 2*, 2013.

Conclusion

The main objective of the work presented in this document can be resumed on first producing Quantum Dots Superlattices (QDSL) made of Ti and Mo silicides Quantum Dots (QD) inside a doped SiGe matrix and later to characterize the morphology and thermoelectrical properties of the obtained materials.

In order to accomplish this, it was first necessary to present the thermoelectric effect and thermoelectric materials commonly employed. These informations were presented in Chapter I, followed by a discussion on the expected increase on the thermoelectric properties via the nanostructuration. It was seen that two effects are possible and have already been reported on the thermoelectric properties after the inclusion of QD. The first one is the increase of the material's power factor due to quantum confinement effects and/or local doping and the second is related to the thermal conductivity reduction due to phonon scattering.

Once the theoretical background was established, in the second chapter the main strategy to include metal silicide QD in a SiGe matrix was presented. This consisted on producing a QDSL thin film material using the Chemical Vapor Deposition (CVD) technique. In order to accomplish this, an evaporator/sublimation system was developed and adapted to an industrial CVD tool. A series of preliminary studies was performed in order to validate the deposition system employing liquid (TiCl_4) and solid (MoCl_5) precursors.

This work was motivated by a theoretical study where the ideal volumetric fraction and diameter of silicides QD in a SiGe matrix in terms of increase of thermoelectric properties was established. Thus, the first step in order to grow the QDSL was to produce QD with a controllable diameter and surface densities. This was achieved through a complete study where the role of the growth parameters such as deposition temperature, duration and substrate Ge content was related to the QD morphological properties. The obtained results allowed to classify the growth parameters into two distinct classes. The first contains the variables that play a role on the surface diffusion of deposited species and is composed notably by the deposition temperature and substrate Ge content. By increasing these parameters, a higher surface diffusion occurs resulting on the growth of fewer quantum dots with higher diameters. The second class contains the variables that only play a role on the quantity of matter deposited, such as the precursor partial pressure and deposition duration. By increasing these variables independently, there is an increase of the QD diameter but no changes on the particles surface density is observed until the coalescence occurs. During the surface deposition it was observed that the Ti deposition employing the evaporator system was very reproducible in long-term. The sublimation system

employed for Mo deposition, however, was less stable at long-term due to the conception of the apparatus.

These studies allowed to determine the optimal deposition parameters both for the Ti and Mo-based QD. The continuation of Chapter II considered the embedding of the QD by depositing a SiGe layer onto the QD. Concerning the low temperature embedding of Ti-based QD it was observed that the particles catalyzed the growth of nanowires by the Vapor Solid Solid (VSS) mechanism. To prevent this, higher Ge contents or higher temperatures have to be employed in order to equilibrate the growth rate near the QD and on the SiGe substrate. Moreover, it was observed that the Ti-based QD are highly mobile inside the SiGe matrix and that a fraction of the QD diffuses up to the material's surface. These effects were not observed for the Mo-based QD and can be explained due to the lower mobility of the heavier Mo atoms compared to Ti.

Once the feasibility of the embedding of the metal QD by the SiGe was determined, different QDSL were produced, both based on Ti or Mo, "n" and "p"-doping, and mono or polycrystalline matrix. The results of the characterization of these materials were presented in Chapter III. Concerning the nature of the QD, it was determined by X-Ray Diffraction (XRD) and Transmission Electronic Microscopy (TEM) analyses that at the early deposition stages there is the formation of metallic nano-islands that which the QDSL growth react with Si atoms from the substrate or from the SiH₄ precursor employed along with GeH₄ to embed the nano-islands. These nano-islands form spherical silicide QD inside the material. The phase of these QD was determined by measuring the planes distance through High Resolution TEM (HRTEM) images and when possible using an EDX technique coupled to the TEM apparatus. It was seen that the expected phase TiSi₂ and MoSi₂ was obtained in the majority of the samples. TEM images also allowed to measure the final QD diameter and the thickness of each QDSL layer, essential to estimate the changes on the volumetric fraction of QD inside the matrix. Another important observation obtained with the TEM analysis is the dopant accumulation near the QD.

The final part of the work consisted in measuring the thermoelectric power factor of the obtained QDSL, i.e., measuring the in-plane Seebeck coefficient and electrical conductivity. Concerning the Ti-based QDSL very interesting results were obtained. For both the mono and polycrystalline "n"-doped samples, an increase of the Seebeck coefficient was observed as well of the carrier's mobility when compared to a pure SiGe reference sample. This resulted on a 4-fold increase of the thermoelectric power factor for the monocrystalline sample and over a 2-fold increase for the polycrystalline material. Different hypotheses exist to explain this, and the most probable is the modulation doping, where the accumulation of dopant atoms near the quantum dots reduces the carriers scattering and thus increases the mobility. This phenomenon was not observed for the "p"-doped Ti-based samples, probably because of the lower

volumetric fraction of QD in this case. Concerning the thermal conductivity measurement, a reduction of 20 % was observed for the monocrystalline “n”-doped sample, validating the phonon scattering theory. The same effect was not observed for the polycrystalline and for the monocrystalline “p”-doped samples. The reason concerning the polycrystalline samples is that the grain boundaries already act as phonons scattering sites, masking the QD effect. For the monocrystalline “p”-doped sample the reduction on the thermal conductivity is probably not observed due to the lower volumetric fraction of QD of this sample.

Concerning the Mo-based QDSL, the results of the power factor were not as conclusive as those for the Ti-based samples. For all the samples tested, only a slight difference was observed for some samples and can be due to an underestimation of the measurement error bars. It is possible that the very low volumetric concentration of these QD did not produce a noticeable effect on the material’s power factor.

The thermal conductivity was only obtained for the “n”-doped monocrystalline QDSL, and an effect similar to the one observed for the Ti-based sample was observed, with a change from 13 W/m.K of the SiGe reference sample to 9,5 W/m.K for the QDSL, i.e., a significant reduction of 27 %.

It is the first time that the growth of metal silicide and SiGe-based QDSL is reported. The characterization results showed that these materials are good candidates for improving the thermoelectric properties of the SiGe material. Further experiments and measurements should be encouraged in order to best understand the effect of the QD inclusion inside thin films, particularly the effect of it on the material’s power factor. These further studies could also be useful to determine the maximum possible improvement obtained by the inclusion of QD in order to evaluate industrial applications for these new materials.

APPENDIX A

Estimative of the Quantum Dots diameter after reaction with Si

As it was shown in Chapter II, both the metallic nano-islands and the silicide quantum dots diameters were considered to be the same for the volumetric fraction calculations. The following calculations are presented in order to support this assumption.

Take as an example the Ti-based materials. It can be seen in the Atomic Force Microscopy (AFM) in Figure A.1 that a nano-island with a diameter " d_{NI} " of around 20 nm has a thickness " t " of around 4 nm.

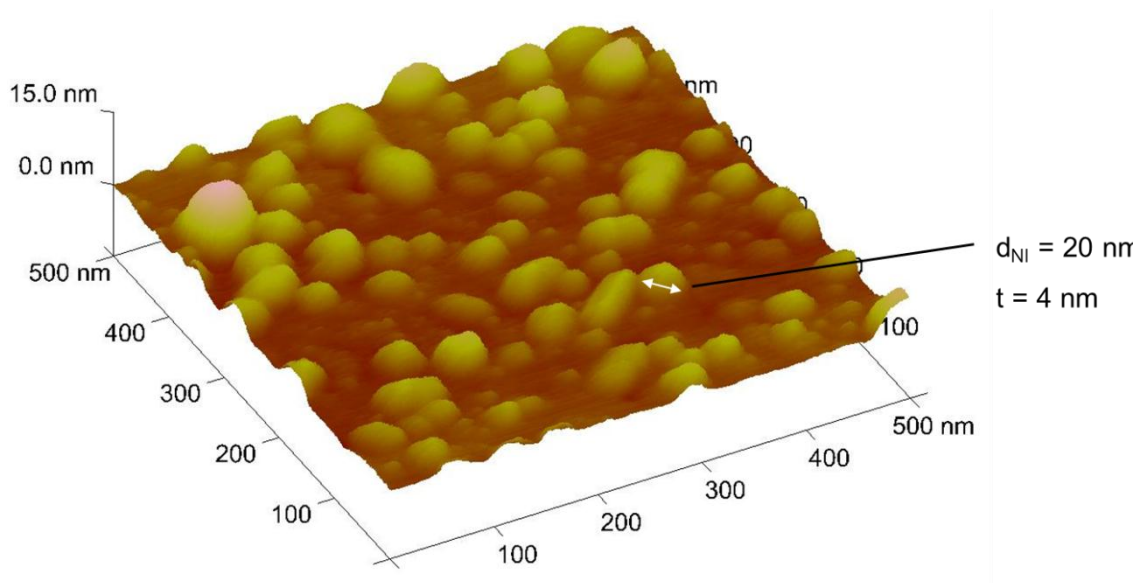
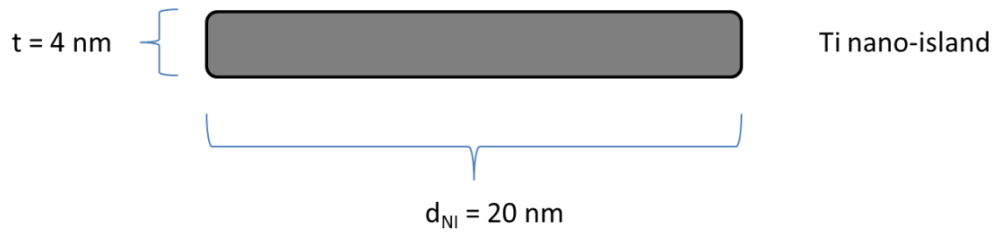


Figure A.1: AFM image of a surface deposition of Ti nano-islands onto a SiGe thin film substrate. This technique allowed to measure the nano-island diameter and thickness.

As it was seen in the TEM images presented in Chapter III, the final obtained QD are spherical. In Figure A.2 is represented the morphological changes between the metallic nano-island and the spherical quantum dot. It is necessary thus to estimate what is the final QD diameter after the metallic nano-islands discs react with Si atoms to form the silicide phase.

a.



b.

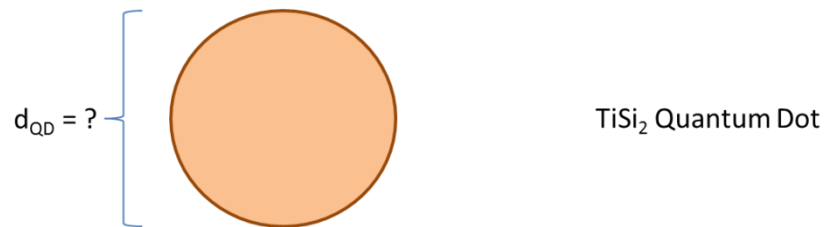


Figure A.2: Schematic representation showing a Ti nano-island of diameter = 20 nm and thickness = 4 nm (a) and of the same nano-island after the reaction with Si and formation of a spherical silicide QD or diameter d_{QD} .

In order to accomplish this, first consider the unit cell volume for both Ti (V_{Ti}) and for TiSi_2 (V_{TiSi_2}). The values are approximately 35 \AA^3 and for TiSi_2 is 339 \AA^3 for metallic Ti and TiSi_2 respectively. Furthermore, the number of atoms per unit cell for Ti (N_{Ti}) is 2 and for TiSi_2 (N_{TiSi_2}) is 24. As Ti atoms represent 1/3 of the total atoms of TiSi_2 , the number of Ti atoms per unit cell of TiSi_2 is 8.

The methodology employed here is based on the changes of the total volume of the particles after the Ti atoms react with Si, i.e., the same amount of Ti atoms on the nano-island will produce a QD with a higher volume.

The unit cell volume per Ti atom for the metallic nano-islands (V_{Ti}^*) can be calculated as follows:

$$V_{\text{Ti}}^* = \frac{V_{\text{Ti}}}{N_{\text{Ti}}} = \frac{35}{2} = 17,5 \quad [\text{\AA}^3] \quad \text{A.1}$$

The same can be made for TiSi_2 , as shown above.

$$V_{TiSi2}^* = \frac{V_{TiSi2}}{N_{TiSi2}} = \frac{339}{8} = 42,4 \quad [\text{\AA}^3] \quad \text{A.2}$$

Thus, a volume increase of " $\frac{42,4}{17,5} = 2,4$ " is observed when a metallic nano-island is transformed into a silicide quantum dot.

Now consider the volume of the disc (nano-island) represented in Figure A.2-b. It can be calculated by considering the nano-island thickness "t" which is 4 nm and the diameter $d_{NI} = 20$ nm. The nano-island volume V_{NI} is thus:

$$V_{NI} = \pi \cdot \left(\frac{d_{NI}}{2}\right)^2 \cdot t = 1256,6 \quad [\text{nm}^3] \quad \text{A.3}$$

By considering the volume increase after the reaction with Si, the final QD volume will be:

$$V_{QD} = V_{NI} \cdot 2,4 = 3015,8 \quad [\text{nm}^3] \quad \text{A.4}$$

Finally, considering the Quantum Dot as a sphere, the calculated radius is:

$$R = \sqrt[3]{\left(V_{QD} \cdot \frac{3}{4} \cdot \frac{1}{\pi}\right)} \cong 9 \quad [\text{nm}] \quad \text{A.5}$$

A QD radius "R" of around 9 nm is obtained, thus the QD will present a diameter of 18 nm after the formation of the silicide phase. This value is very close to the measured initial nano-island diameter of 20 nm.

It can be seen thus that for the conditions present on this work (nano-island thickness of around 4 nm) no significant changes are observed between the observed nano-island diameter and the final QD diameter.

